Thermal Conductivity of Sea Ice and Antarctic Permafrost

Daniel James Pringle

A thesis submitted for the degree of
Doctor of Philosophy.

School of Chemical and Physical Sciences.
Victoria University of Wellington
Wellington, New Zealand

18 October 2004

Supervised by Prof. H.J. Trodahl

This thesis was typeset with LaTeX 2ε, using the American Geophysical Union 2001 style files, and 2004 referencing convention.

Abstract

We present results from measurements of the thermal conductivity of sea ice, k_{si}, using two different techniques. In the first, ice temperatures were measured at 10 cm and 30 minute intervals by automated thermistor arrays deployed in land-fast first-year (FY) and multi-year (MY) ice in McMurdo Sound, Antarctica, and in FY ice in the Chukchi Sea and shallow Elson Lagoon, near Point Barrow, Alaska. Conductivity profiles through the ice were calculated from the coupled time- and depth- dependence of the temperature variations using a conservation of energy analysis, and a graphical finite difference method. These profiles show a reduction in the conductivity of up to 25% over the top $\sim$ 50 cm, consistent with similar previous measurements. From simulations and a detailed analysis of this method, we have clearly identified this reduction (for which physical explanations had previously been invoked) as an analytical artifact, due to the presence of temperature variations with time scales much less than the 30 min sampling interval. These variations have a penetration depth that is small compared with the thermistor spacing, so the effect is shallow. Between 50 cm and the depth at which the method becomes noise-limited, we calculate average conductivities of $2.29 \pm 0.07\,\mathrm{W/m\,^{\circ}C}$ and $2.26 \pm 0.11\,\mathrm{W/m\,^{\circ}C}$ at the FY McMurdo Sound and Chukchi Sea sites, and $2.03 \pm 0.04\,\mathrm{W/m\,^{\circ}C}$ at the MY site in McMurdo Sound.

Using a parallel conductance method, we measured the conductivity of small (11×2.4 cm diameter) ice cores by heating one end of a sample holder, and with the other end held at a fixed temperature, measuring the temperature gradient with and without a sample loaded. From several different cores in each class, we resolved no significant difference, and certainly no large reduction, in the conductivity of FY surface (0-10 cm) and sub-surface (45-55 cm) ice, being $2.14 \pm 0.11\,\mathrm{W/m\,^{\circ}C}$ and $2.09 \pm 0.12\,\mathrm{W/m\,^{\circ}C}$ respectively. The conductivity of less dense, bubbly MY ice was measured to be $1.88 \pm 0.13\,\mathrm{W/m\,^{\circ}C}$. Within measurement uncertainties of about $\pm 6\%$, the values from our two methods are consistent with each other and with predictions from our modification of an existing theoretical model for $k_{si}(\rho, S, T)$. Both our results and previous measurements give conductivity values about 10% higher than those commonly used in Arctic and Antarctic sea ice models. For FY ice, we tentatively propose a new empirical parameterisation, $k_{si} = 2.09 - 0.011\,T + 0.117\,S/T$ [$\mathrm{W/m\,^{\circ}C}$], where T is temperature [$^{\circ}$C] and S salinity [$^{0}/_{00}$]. We expect this parameterisation to be revised as thermal array data from other researchers are made available.

We also report thermal array measurements in ice-cemented permafrost at Table Mountain in the Antarctic Dry Valleys, between November 2001 - December 2003. From 13 months of temperature data with a sampling interval reduced from 4 hours to 1 hour (November 2002 - December 2003), we have modified some aspects of an already published initial analysis [*Pringle et al.*, 2003]. Using thermal diffusivity profiles calculated from measured temperatures, and a heat capacity estimated from recovered cores, we have determined thermal conductivity profiles at two sites that show depth- and seasonal- variations that correlate well with core compositions, and the expected underlying temperature dependence. The conductivity generally lies in the range $2.5 \pm 0.5\,\mathrm{W/m\,^{\circ}C}$, but is as high as $5.5 \pm 0.4\,\mathrm{W/m\,^{\circ}C}$ in a quartz-rich unit at one site. The wintertime diffusivity is $4 \pm 7\%$ higher than the summertime value, which we understand to reflect the underlying temperature dependence. In this analysis we find our graphical finite difference method more versatile and more accurate than common 'Fourier' time-series methods.

Acknowledgements

There are many people that I would like to thank for their part in what has been a very rewarding and enjoyable project for me. I have learned scientific and personal lessons from all of you. To Joe Trodahl, thank you so much for everything from getting me on board, to helping me along with good humour and gentle prodding. I know that I will continue to appreciate your significant scientific and personal influence well beyond this work. To Hajo Eicken, thank you for the fantastic opportunities to visit, work with, and learn about sea ice from you and your group at the University of Alaska Fairbanks, for making unpublished data and measurements available to me, and for the support during the completion of this dissertation. To Warren Dickinson, thank you for the opportunity to become involved in the Table Mountain project, and for the amazing opportunity of field work in the Dry Valleys. To Tim Haskell, thank you for your organisational and experimental support, and for your great company in Antarctica, 2002 and 2003.

Alan Rennie in particular, and Dave Gilmour, deserve special thanks for their expert machining of the thermal arrays and vacuum chamber. Thanks to Eric Broughton and Alex Pyne who assembled the Table Mountain arrays, to Alex and Warren for installing them, and to Alex for discussions about equipment. Thanks also to Mark McGuinness for helpful mathematical assistance and discussions. I received fantastic scientific support from Scott Base technicians Tim Kerr, Shane Thomson, Margaret Auger and Jamie Plowman, and winter-over science staff Johno Leitch, Craig Purdie and Greg Leonard.

In the course of this study I was hosted three times by Hajo Eicken and his sea ice group at UAF. Thank you to everyone involved in making these trips scientifically exciting and stimulating, and for welcoming me into your lives in Fairbanks. This group was shocked by the tragic death of Karoline Frey in March 2002. I acknowledge with sadness but gratitude Karoline's contribution to my field work, her observations and insights, her unpublished data, and her lasting personal influence. Thank you Andy Mahoney, Craig Zubris, Lars Backström and Meg Smith for your help with my field work, and along with Tina Tin, Alain Burgisser, Tanja Petersen, and the rest of the UAF crew, for receiving me so warmly. Thanks also to Cliff Atkins, Paul Callaghan, Mark Hunter, Ocean Mercier, and the friendly Scott Base 'beakers' and staff for your parts in my Antarctic experience. Respect and good luck to Alex, Steve and all the guys at Cornell Physics.

For their administrative help over the last three years I am very grateful to Margaret Brown, Barry Lewis, Maureen Penning and particularly Celia Simpson.

Special thanks to Gazza and Angela, DC and Ang, Paddy and Julz, Lloyd and Briony, Buckey, and Bakie. Thank you Mum and Dad for your continued support and love.

Above all, thank you so much Lisa for your continual support, love, patience, encouragement, example and inspiration. Thanks so much for abiding my trips, all the late nights, and my early-onset absent mindedness. It means the world to me.

This work was funded through the New Zealand Public Good Science Fund, and a Victoria University Targeted Postgraduate Scholarship. Antarctica New Zealand provided logistic, and scientific support at Scott Base. NSF-funded support furnished by the Barrow Arctic Scientific Consortium (BASC) is gratefully acknowledged.

With thanks to those who continue to provide inspiration.

Contents

List of Figures

List of Tables

Chapter 1

Introduction

Sea ice forms annually when the surface of high latitude sea water freezes in the autumn and winter. A large fraction of sea ice survives less than one year, typically growing to less than 2 m thick before melting in the following spring or summer. However some ice survives to become second-year or multi-year sea ice, forming part of the pack ice around Antarctica or in the Arctic basin. The areal extent of sea ice cycles annually between about 4 and 19 million km^2 in the Antarctic and between 9 and 16 million km^2 in the Arctic [*Dieckmann and Hellmer*, 2003]. These cycles are amongst the largest annual variations on the planet and lead to a maximum sea ice coverage of about 10% of the world's oceans. Through its huge area and volume and the large heat, fresh water and salt fluxes associated with its growth and decay cycle, sea ice is a significant component in the earth's heat balance and global climate system. Sea ice models form an integral part of General Circulation Models (GCMs) used to forecast the global climate response to changes in climate forcing.

Through a variety of feedback mechanisms, that primarily alter the ocean-atmosphere heat exchange, sea ice acts as both an indicator and amplifier of climate change [*Eicken and Lemke*, 2001; *Dieckmann and Hellmer*, 2003]. These effects include the ice-albedo effect, thermal buffering, and the thermal insulation of the oceans. The ice-albedo effect is perhaps most well known; compared with water, the higher albedo of sea ice, and the snow cover it can support, decreases the amount of shortwave energy absorbed in the polar regions. This process constitutes a positive feedback, as an increase in sea ice extent leads to a decrease in short wave energy absorbed in the region, and therefore to a further increase in ice growth. Similarly, the high latent heat required to melt ice enhances the thermal buffering effect of the oceans which

is due to the large heat capacity of water. This is a positive feedback because a reduced sea ice cover requires less energy to melt, and re-partitioning of the heat budget leads to a warmer ocean, and therefore less ice formation the following season. Sea ice forms both a mechanical and thermal barrier between the cold atmosphere and relatively warm oceans. In the absence of sea ice, the ocean warms the atmosphere largely through turbulent heat exchange, but also by long wave radiation [*Dieckmann and Hellmer*, 2003]. Neglecting the turbulent flux, a sea ice cover of 1 m can reduce the conductive and radiative flux by more than 50%. In regions of high turbulent flux, this decrease can be as high as 90%. This causes a negative feedback; less ice leads to greater heat loss, and therefore enhanced ice growth.

In reality the interplay of the various feedback mechanisms over a range of temporal and spatial scales is very complex, and accurate modelling of them requires an accurate representation of both thermodynamic and dynamic aspects of the ocean-ice-atmosphere interaction. Accurate observations of sea ice extent have become available only since the satellite era, limiting the time scales of trend analysis. Ice thickness measurements are harder yet to obtain, and remain an area of current focus. Furthermore, the natural variability and large amplitude of the annual cycles (and other cycles eg. decadal oscillations) makes interpretation of the data difficult [*Eicken and Lemke*, 2001]. Observational sea ice scientists are seeking to improve the knowledge of sea ice physics through both a better understanding of the interactions, and better measurements of processes and properties. As modelling capabilities advance, these results can be incorporated into the models.

Sea ice is a complex heterogeneous material. It is composed of pure ice, and air bubbles and brine inclusions trapped during freezing. In compositional models it is assumed that the brine inclusions are always at their salinity-dependent freezing point and in thermal equilibrium with the surrounding ice. When the ice is cooled, a small amount of pure ice freezes out of the inclusions to raise the salinity and lower the freezing point of the brine accordingly. Similarly when the temperature is increased, the inclusions are diluted by melting [*Maykut and Untersteiner*, 1971]. This equilibrium creates a salinity- and temperature- dependence in the physical properties of sea ice. Furthermore sea ice structure and processes display large ranges of length scales, from microns to hundreds and even thousands of kilometres [eg. *Dieckmann and Hellmer*, 2003]. These factors lead to rich geophysical behaviour making sea ice a material that is both interesting to study and difficult to model over geographical scales. As technology has evolved, sea ice has been analysed in an increasingly sophisticated manner. Laboratory microscopy has led to a better understanding of the

microstructure and small scale physical properties [*Light et al.*, 2003a,b]. The SHEBA (Surface HEat Budget of the Arctic) project has recently provided rich information on the spatial and temporal variability in the year-round ice response and surface processes [eg. *Perovich et al.* [2003], and papers in SHEBA Special Section, *J. Geophys. Res.*, *107(C10)*, 2002].

A crucial parameter in sea ice models is the thermal conductivity k_{si}, which characterises the conductive heat flow through the ice between ocean and atmosphere. It controls the rate of ice growth which is limited by the rate at which the latent heat of freezing released at the water/ice interface can be conducted away through the ice, and it similarly controls the rate of decay, and equilibrium thermodynamic thickness. It is also commonly used to calculate the 'apparent thermal conductivity' of snow on sea ice via a quasi-static analysis [eg. *Sturm et al.*, 2002]. The thermal conductivity has proven so difficult to measure that most models use either a single constant value or the empirical parameterisation originally proposed by *Untersteiner* [1961, 1964], and implemented in the seminal thermodynamic sea ice model of *Maykut and Untersteiner* [1971]. Several theoretical models deriving the conductivity from first principles were published about the same time, [*Anderson*, 1958; *Schwerdtfeger*, 1963; *Ono*, 1968], but the result of *Untersteiner* [1964] has remained popular because it captures the first-order temperature and salinity dependence in these more sophisticated models, but is simpler to implement [*Maykut and Untersteiner*, 1971]. We discuss this parameterization in more detail below.

The roughly four-fold difference in thermal conductivity between ice and brine leads to the prediction that the thermal conductivity of sea ice is strongly dependent on salinity and temperature. Therefore accurate measurements must involve minimal disturbance to the ice structure. The difficulties associated with such measurements mean that of the few made prior to the 1990's only those of *Lewis* [1967] claim the accuracy to compare with the theoretical predictions [*Trodahl et al.*, 2000]. In fact the temperature-dependent thermal conductivity of fresh ice, k_i, required to model k_{si}, has itself only been measured to an accuracy of approximately $\pm 5\%$, with $k_i(0\,^\circ\mathrm{C}) \approx 2.1 \pm 0.1\,\mathrm{W/m\,^\circ C}$, see Chapter 2.

In recent years the measurement problem has been addressed by Trodahl, McGuinness and co-workers [*Trodahl et al.*, 2000, 2001; *McGuinness et al.*, 1998; *Collins*, 1998] who began the program culminating in the present work. Using thermistor strings they made high resolution *in situ* measurements of the temperature profile in first year sea ice in McMurdo Sound, Antarctica. The

analysis of these measurements suggested some departures from the predicted behaviour of k_{si}. The most notable was a near-surface reduction with up to $\sim 25\%$ lower values over the top $\sim 50\,\mathrm{cm}$. It was proposed that this reduction might be due to very small crystal size in the near-surface frazil ice causing an enhanced scattering of phonons, the elemental excitations involved in the heat transport [*Trodahl et al.*, 2001]. An apparent increase in the conductivity with depth was also resolved and thought to be associated with convective transport in the brine fraction, which increases with temperature and hence depth. Possible signatures of non-linear heat flow were also identified at lower depths in the ice [*McGuinness et al.*, 1998; *Collins*, 1998]. These measurements are summarised in Chapter 2. In this thesis we present results from similar thermistor array measurements after modifications to the arrays, data logging and analysis scheme. As a ground-truth experiment a different method was developed to measure the thermal conductivity of small sea ice cores drilled from the surface and sub-surface at one first-year and one multi-year array site.

In addition we present a thermistor array study of the near-surface thermal regime of dry, cold, perennially frozen permafrost in the Antarctic Dry Valleys. The Dry Valleys have recently attracted increased scientific interest for two main reasons. The first is the indirect dating in 1995 of the oldest ice on earth [*Sugden et al.*, 1995]. The second is the current interest in exploration and remote sensing of Mars, because the Dry Valleys are one of the best earthly analogues of the martian environment. Furthermore Dry Valley permafrost represents a little-studied, very cold and very dry end-member of the permafrost family [*Putkonen et al.*, 2003] and our work represents the first dedicated study of the near-surface temperature regime and thermal properties. Using equipment and analysis adapted from our sea ice measurements we have resolved the depth- and time- dependence of the ground thermal properties of two nearby sites at Table Mountain. This work was performed in conjunction with researchers from the Antarctic Research Centre of Victoria University, as part of an ongoing interest in the geomorphology and near-surface processes in the Dry Valleys. This study was motivated by a desire to examine the near-surface thermal regime and to investigate a factor-of-three difference in the size of polygonal ground patterning at these two sites. We defer further discussion of this project to Chapter 7.

In the remainder of this introductory chapter we next discuss heat flow near the earth's surface, and then effective-medium properties of composite materials, of which sea ice and ice-cemented permafrost are both examples. This is followed by a sea ice overview, focussing on heat flow. Finally we describe the structure

of the following chapters.

1.1 Heat Flow near the Earth's Surface

Heat flow near the earth's surface arises due to both internal and external processes. Variations in the surface heat balance (on many different time scales) cause temperature disturbances which propagate to depth, and heat flows upward from the earth's warmer interior. The primary component of this upwards flow is conductive, the so-called 'terrestrial heat flow', but there are also convective and advective components, for example fluid migration and volcanism. The terrestrial heat flow is a quasi-static process whereby the local heat flux $\mathbf{J_Q}$ [W/m^2] is given by the product $\mathbf{J_Q} = -k\nabla T_g$ where k [W/m °C] is the thermal conductivity and ∇T_g [°C/m] the geothermal gradient at the same site [1]. On the other hand the propagation of surface temperature disturbances is a dynamic process described by the thermal diffusivity, D [m^2/s] defined by $D = k/c$, where c [J/m^3] is the volumetric heat capacity.

A formal discussion of heat conduction is presented in Chapter 2. To describe the propagation of surface temperature variations we discuss two well-known results here. These are solutions to the one-dimensional heat equation in a uniform, semi-infinite half space of diffusivity D, for two different boundary conditions. The first is a sinusoidal surface temperature, $T(0,t) = T_0 cos(\omega t)$. For mean surface temperature T_m and geothermal gradient $\frac{\partial T}{\partial z}_g$ the temperature field is given by:

$$T(z,t) = T_m + \frac{\partial T}{\partial z}_g z + T_0 e^{-z/d} cos(\omega t - z/d) \quad , \tag{1.1}$$

where $d = (2D/\omega)^{1/2}$ is the penetration depth. Equation (1.1) shows that the sinusoidal surface temperature propagates downwards with a frequency-dependent attenuation and phase lag given by d.

The second readily-solved boundary condition is an instantaneous step in the surface temperature. For a step of magnitude ΔT_0 the temperature profile at a time t later is:

$$T(z,t) = T_m + \frac{\partial T}{\partial z}_g z + \Delta T_0 erfc\left(\frac{z}{2\sqrt{Dt}}\right) \quad , \tag{1.2}$$

[1] In general the thermal conductivity is a tensor quantity so the direction of heat flow is not necessarily the direction of the temperature gradient, but in this work we consider 1-D heat flow, so k is a scalar, and we write temperature gradients as $\frac{\partial T}{\partial z}$.

where $erfc(x) = (2/\sqrt{(}\pi)) \int_x^\infty exp(-s^2)ds$ is the complementary error function.

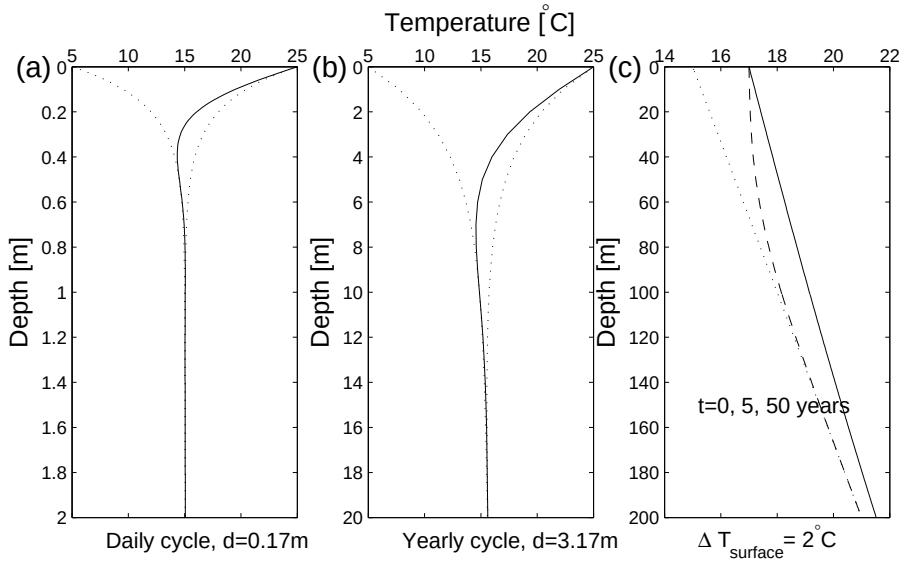

Figure 1.1: Different perturbations to the geothermal gradient. Here $\frac{\partial \mathrm{T}}{\partial \mathrm{z}} = 30\,\mathrm{m}\,^\circ\mathrm{C/m}$ and $D = 1 \times 10^{-6}\,\mathrm{m^2/s}$ for (a) 10 °Camplitude daily cycle, (b) 1 °C amplitude yearly cycle, (c) an instantaneous 2 °C increase in surface temperature. The dashed lines in (a,b) give the envelope of temperature variations, and the solid line is T(z) when the surface temperature is maximum, equation (1.1). The dotted, dashed and solid lines are for immediately before the surface temperature step, and 5 and 50 years after it.

Figure (1.1) illustrates the effect of these disturbances on a 100m deep profile for an average surface temperature $T_m = 15\,^\circ\mathrm{C}$, $\frac{\partial T}{\partial z}_g = 30\,\mathrm{m}\,^\circ\mathrm{C/m}$, and $D = 1 \times 10^{-6}\,\mathrm{m^2/s}$ (similar to that of ice). Note the different depth scales. Figures 1.1(a,b) show the penetration of 10 °C amplitude daily and yearly cycles respectively. The dashed lines mark the envelope of temperature variations, and the solid line is the temperature profile when the surface temperature is maximum, according to equation (1.1). Figure 1.1(c) shows the much deeper and slower temperature response of an instantaneous 2 °C step in the surface temperature. Dotted, dashed and solid lines correspond to immediately before the step, and 5 and 50 years after, as per equation (1.2).

Our thermistor array experiments involve high-precision temperature measurements over small depth intervals and short time intervals, from which we analyse the coupled time- and depth- variations in temperature. Because

there are experimentally confirmed theoretical expressions for the heat capacity of sea ice we are able to analyse what is essentially a thermal diffusivity experiment, to instead determine the thermal conductivity (see Chapter 4). In our permafrost measurements there is no such equilibrium property so we solve directly for the thermal diffusivity. The thermal conductivity is then calculated using the heat capacity calculated from the composition of recovered cores.

In the study of both surface heat balance and terrestrial heat flow, accurate measurement (or estimation) of the thermal conductivity remains a challenge [*Jessop*, 1990]. This is largely due to the highly variable, heterogeneous nature of the geophysical materials involved. For such composite materials the thermal conductivity (and other transport properties) depend on the volume fractions of constituent phases, their geometrical arrangement, and orientation with respect to the direction of heat flow. Variations in the microstructure and porosity of rocks can be caused by diagenetic and environmental factors. These variations coupled with the need to preserve sample conditions makes measurement of the thermal conductivity problematic. The same reasons make theoretical estimates of a given rock type, in the absence of measured characterisation, accurate to only about 25% [*Jessop*, 1990].

More generally, we note thermal conductivity measurements are much more difficult to perform than seemingly analogous electrical conductivity measurements. In each case a potential drop (temperature, or electric potential) is measured in the direction of a known current (thermal or electrical). Both measurements require that the current is confined to the sample with no extraneous paths. This is much more easily achieved in the electrical case,as insulators can have conductivities many orders of magnitude smaller than reasonably good conductors. The range of thermal conductivities is much smaller. The thermal conductivity of copper is only 2 orders of magnitude greater than ice, which is only 2 orders of magnitude higher than air.

1.2 Effective Medium Properties of Composite Materials

The geophysical materials studied in this work, sea ice and ice-cemented ground, are both heterogeneous composite materials. Within a pure ice matrix sea ice contains brine inclusions and air pockets ranging in size from microns to cm's, brine tubes 10's of cm's long, and vertical structural variations over metre- and

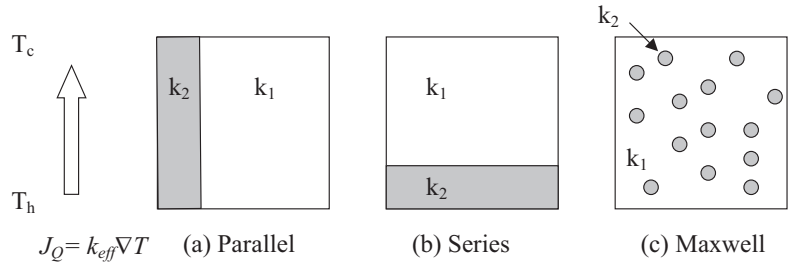

Figure 1.2: Simple heat flow geometries for k_{eff} in a two-phase system. (a) parallel flow; (b) series flow; (c) Maxwell random small inclusion model. See text for expressions for k_{eff} in each case.

sub-metre- scales. The frozen ground we studied is an ice-cemented diamict - a geological unit with a similar matrix-like structure - containing clasts, pebbles, sands and clays as well as stratigraphic structure with length scales ranging from sub-mm to metres.

For 1-D heat flow in a homogeneous material the thermal conductivity is given by the magnitude of the heat flux per unit temperature gradient, $k = J_Q/|\frac{\partial T}{\partial z}|$. For a heterogeneous material the heat flow is characterised by an effective-medium thermal conductivity, for which we use the notation k_{eff}, or just k when it is not ambiguous. Computationally the effective conductivity can be predicted by specifying the phase fractions and geometry of the individual phases and assuming thermal equilibrium between the components. Outer bounds on the effective conductivity of a two component system are parallel and series heat flow shown in figure (1.2). For heat flow along parallel components subject to the same temperature gradient, k_{eff} is given by the thermal conductivity of each phase weighted by its area fraction, which for a parallel arrangement is equal to the volume fraction ϕ, giving

$$k_p = \sum_i = \phi_i k_i \quad . \tag{1.3}$$

For series heat flow it is the thermal resistivity (reciprocal of thermal conductivity) that adds in this way and the effective conductivity is therefore given by

$$k_s = \left(\sum_i \frac{\phi_i}{k_i} \right)^{-1} \quad . \tag{1.4}$$

A variety of models have been proposed for specified arrangements of phases,

including random and unknown geometries. Four commonly used results are:

1. Geometric Model. The simplest model for random inclusions is the 'geometric mean' model in which the effective conductivity is given by the geometric mean of the volume-weighted component conductivities [*Jessop*, 1990]:

$$k = \prod_i {k_i}^{\phi_i} = exp\left(\sum_i \phi_i ln(k_i)\right) \quad . \tag{1.5}$$

2. Maxwell model. For a random distribution of small inclusions (k_2) in a matrix (k_1) as in figure 1.2(c) the effective thermal conductivity is given by Maxwell's expression, originally derived for the effective electrical conductivity for the same geometry:

$$k = k_1 \frac{2k_1 + k_2 - 2\phi_2(k_1 - k_2)}{2k_1 + k_2 + \phi_2(k_1 - k_2)} \quad . \tag{1.6}$$

Although derived in the assumption that that ϕ_2 is small, this result is often applied across the range $0 < \phi_2 < 1$.

3. Hashin-Shtrikman bounds. The Hashin-Shtrickman (H-S) bounds give the tightest possible bounds for a disordered, isotropic material when there is no precise knowledge of the geometric arrangement of components (two-point correlation function unknown). Isotropic here means that there are no extended paths in the direction parallel or perpendicular to the direction of heat flow [*Landauer*, 1978], so the H-S bounds lie inside the extreme bounds of series and parallel heat flow. For a 2-component system with higher conductivity k_1, and lower conductivity k_2 the upper and lower H-S bounds, related by the substitution $k_1 \leftrightarrow k_2$, and $\phi_1 \leftrightarrow \phi_2$, are [*Hashin and Shtrikman*, 1968; *Tuch et al.*, 2001],

$$k_u = k_1 \frac{k_1 + k_2 + \phi_2(k_2 - k_1)}{k_1 + k_2 - \phi_2(k_2 - k_1)} \quad , \tag{1.7}$$

$$k_l = k_2 \frac{k_1 + k_2 + \phi_1(k_1 - k_2)}{k_1 + k_2 - \phi_1(k_1 - k_2)} \quad . \tag{1.8}$$

Here $\phi_2 + \phi_1 = 1$ are the volume fractions of the components. The arithmetic mean of these bounds can be taken as a best-estimate of the conductivity [*Jessop*, 1990].

Figure 1.3 shows the above results for a two-component system with conductivity values approximating ice $k_1 = 2.1$ W/m °C, and brine, $k_2 = 0.5$ W/m °C.

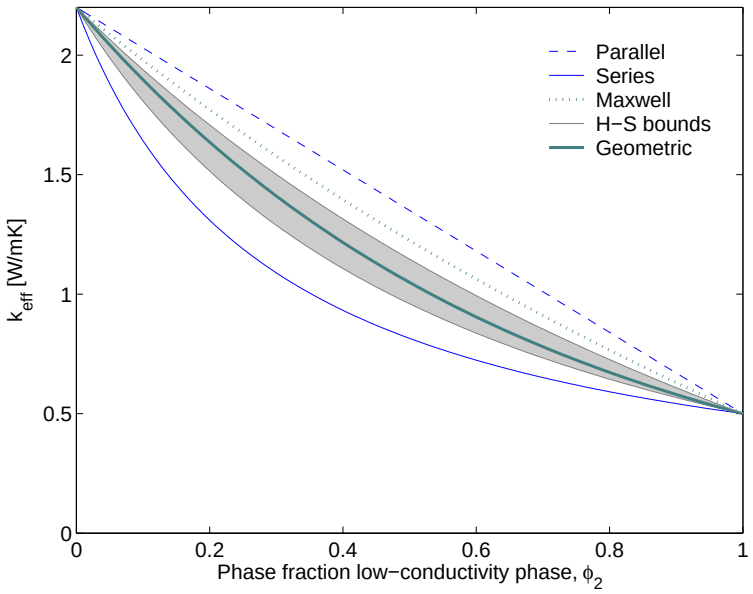

Figure 1.3: Geometric bounds on effective thermal conductivity k_{eff} in a two-phase system. Here $k_1 = 2.1$ W/m °C, and $k_2 = 0.5$ W/m °C correspond to the approximate values of ice and brine. Analytical expressions for the curves are found in the text.

It is important to consider the sample heterogeneity when measuring the effective thermal conductivity of composite materials because an accurate measurement requires that the measured sample is representative of the bulk average. The size of samples should be large compared with the length scale of any compositional variations. This point is relevant to the interpretation of the diffusivity and conductivity profiles at the Table Mountain sites and is discussed more in Chapter 6.

A further complication is that the above models assume a static temperature profile, so that the components are in thermal equilibrium. For time varying temperatures, it is the thermal diffusivity (via its dependence on the heat capacity) that determines the rate of temperature response. Temperature equilibrium will exist only for variations with a characteristic period larger than the response time of the system, $t > L^2/D$ where L is a local length scale. In the thermal array 'diffusivity' measurements in this work, we assume thermal equilibrium between constituent components, and use a theoretical equilibrium heat capacity expression to determine the conductivity. The heat capacity depends only on the volume fractions of ice, and brine and air inclusions and not also their arrangement. Because it is an equilibrium property its measurement

is more straightforward than the thermal conductivity. As discussed in Chapter 2, experimental and theoretical values of $c_{si}(S,T)$ are in good agreement.

1.3 Sea Ice Overview

As heat is extracted from the relatively warm water into the colder atmosphere the sea water first cools to its bulk freezing point, suppressed below 0 °C by the presence of dissolved salts, and then freezes upon the removal of more heat. The salinity of sea ice $\sigma = m_s/m_{si}$ is the mass of salt per unit mass of sea ice. Sea ice salinities are typically expressed in parts per thousand (ppt, or $^0/_{00}$), $S = 1000\,\sigma$. When we write S, it is salinity in parts per thousand. The freezing point-salinity relation for sea water is approximately $T_f \approx -55\,S$ and for typical seawater with salinity $34\,^0/_{00}$ is $T_f = -1.87\,^\circ$C. Whereas fresh water has a density maximum ($T_{\rho\,max} = 4\,^\circ$C) above its freezing point, for sea water of $S > 27$, density is still increasing with decreasing temperature when the freezing point is reached. Therefore convective over-turning occurs as the atmosphere-cooled surface waters are denser than the warmer underlying water, creating a layer of water at its freezing point. Ice formation now begins at the surface and continues as heat is conducted away from the ice/water interface through the ice to the atmosphere. The growth rate slows as the thermal gradient over the ice decreases with increasing ice thickness and the maximum thermodynamic ice thickness is given by the balance of heat conduction away from the ice/water interface and the oceanic heat flux supplied from below. When the oceanic flux exceeds the conductive flux, the onset of melting occurs.

Different environmental conditions during growth and decay cycles give rise to a variety of ice types and features. An overview of these features and associated nomenclature including pictures is presented by *Eicken* [2003]. The primary categorisation of sea ice is age. Ice yet to experience a full melt season is called first year (FY) sea ice. Second year ice has survived one melt season, and multi year (MY) ice more than one. This thesis is largely concerned with first year ice. However we do present results for MY ice from both of our methods. Through the seasonal growth cycle FY ice constitutes a very large fraction of the total sea ice cover, especially in the Antarctic, and therefore plays a significant role in the total heat balance. Furthermore the structure of FY ice is well related to growth processes, whereas older MY ice, with unknown thermal and mechanical histories, displays a larger variance in microstructure. The correlation between measured properties and underlying microstructure is therefore possible in FY ice, and the measured conductivity is applicable to

a large fraction of the ice cover.

We note that sea ice models have historically addressed the Arctic sea ice cover, and therefore often use properties relevant to MY ice. We return to this point in the final, conclusions chapter.

1.4 Heat Flow in Sea Ice

To model the atmosphere-ice-ocean interactions involved in and affected by sea ice growth and decay requires a quantitative heat flux analysis. *Maykut* [1986] and *Steele and Flato* [2000] present this analysis in some detail, and *Eicken* [2003] provides a summary. Factors contributing to the overall heat balance are shown schematically in figure (1.4). Advective and convective heat transport are not usually separated from conductive heat flow and the 'conductive heat flux' $F_c(z) = -k_{si}(z)(\partial T/\partial z)|_z$ represents the total heat flow in the ice at a given depth [2]. Some care must be taken when discussing the total heat flow if not diffusive heat transport is involved. Strictly, the 'thermal conductivity' includes only diffusive transport, whereas what is important in modelling sea ice, and what may be determined from *in situ* measurements, is the effective linear heat flow coefficient. As far as we know, all models parameterise heat flow only in terms of the intrinsic sea ice thermal conductivity, k_{si}, whose accurate measurement is the primary focus of the present work.

The total heat balance problem is non-linear and the ice temperature profile, and growth and decay, are usually modelled numerically. Conceptually the ice temperature profile and ice thickness $H(t)$ are established by various physical processes which serve to balance the heat fluxes at both the top and bottom surfaces. The conductive flux at the surface $F_c(0)$ can be considered a residual term whose value is such to achieve this balance at the upper surface [*Lewis*, 1967; *Eicken*, 2003]. The rate of growth or decay of ice at the ice/water interface then arises in order balance the conductive heat flux at the interface $F_c(H)$ and the oceanic flux F_O represented heat supply from the warmer ocean. For latent heat of fusion L [J/g] the thickness change dH/dt for ice with density ρ is,

$$F_c(H) + F_O = -\rho L \frac{dH}{dt} \quad . \tag{1.9}$$

Here $F_c(H) = -k_{si}(H)(\partial T/\partial z)_H$ is by definition negative for a flow of heat

[2] We here follow the conventional notation in the sea ice literature, in which fluxes are denoted with an 'F'.

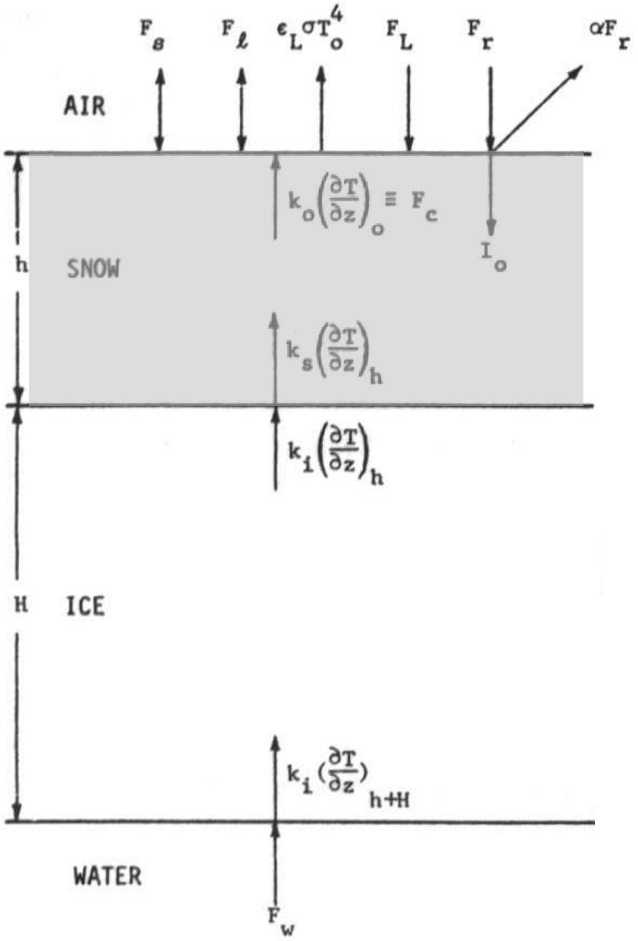

Figure 1.4: Simplified schematic diagram of heat balance of sea ice (with snow cover), slightly modified from *Maykut and Untersteiner* [1971]. The surface fluxes are: turbulent latent heat F_l, and sensible heat F_s; down-welling longwave radiation F_L; re-radiated longwave radiation $\epsilon_L \sigma T^4$; down-welling shortwave radiation F_r; reflected and scattered shortwave radiation αF_r; surface-penetrating shortwave radiation I_0. Oceanic flux is here represented by F_w. Conductive fluxes at various positions are represented by $k(\partial T/\partial z)$. Freezing/melting of ice at the surface, and other effects associated with melt ponds and brine drainage are not represented.

away the ice/water interface, ie. up through the ice. The relative magnitude of the oceanic and conductive fluxes therefore limits the maximum ice thickness from thermodynamic growth possible in a single growth season. For example the maximum thermodynamic thickness of Arctic ice is given by models run

over several years as approximately 3.5 m [*Maykut and Untersteiner*, 1971], although convergent dynamic processes such as ridging and rafting can pile up floes much thicker than this.

A thorough understanding of the factors maintaining heat balance at both the top and bottom ice interfaces is essential in understanding sea ice mass-balance and predicting its response to future climate variability. Numerous studies have been undertaken in the Arctic and Antarctic in order to measure the variability in the heat flux components at the top and bottom ice surfaces. The SHEBA project has led to the systematic study of many processes in the surface heat balance in the Arctic. These include the thermal conductivity of snow [*Sturm et al.*, 2002], the effect of the evolution of surface melt ponds on the total albedo [*Eicken et al.*, 2004], melt water circulation and permeability [*Freitag and Eicken*, 2003]. Complementing these measurements is our present work on thermal conductivity, which because of measurement difficulty, has seen little previous experimental attention.

We note two studies which identified departures from the simple thermal conduction picture of heat flow in sea ice. The study of *Lytle and Ackley* [1996] identified convective heat transport in MY ice in the Weddell Sea, Antarctica. In this case, heavy snow loading lead to surface flooding and formation of a slush layer at the snow/ice interface in early autumn (February/March). Over a 2-3 week period, snow ice formed and the cold dense brine rejected in this process drained through the existed brine tube network, replaced by less saline, warmer water from the upper ocean, constituting a convective contribution to the heat flow from the ocean to ice surface. This process is relevant only in MY ice with a negative freeboard due to heavy snow loading.

The impact of solar radiation on the heat flow in fresh Antarctic plateau ice and sea ice was examined by [*Weller*, 1967]. Using harmonic analyses, Weller observed an unphysical depth-dependence in the apparent thermal diffusivity of both ice types, associated with the effect of solar radiation. We discuss this work further in Chapter 2.

In sea ice models the thermal conductivity is typically represented by the approximate formula of *Untersteiner* [1964], used in the seminal thermodynamic sea ice model of *Maykut and Untersteiner* [1971],

$$k_{si} = k_{i,0} + \frac{\beta S}{T} \quad . \tag{1.10}$$

Here $k_{i,0}$ is the conductivity of fresh ice, S is salinity [$^0/_{00}$], β is a fitted constant, and T temperature [°C]. Particularly since its use by *Bitz and Lipscomb*

[1999], equation (1.10) with $k_{i,0} = 2.03$ W/m °C and $\beta = 0.117 W/m\,{}^0/_{00}$ is firmly established in sea ice models. It is used in the following ice and coupled climate models: Los Alamos Sea Ice Model (CICE) ; (American) National Center of Atmospheic Research (NCAR) Community Atmosphere Model (CAM2); Community Climate System Model (CCSM3.0); Canadian Ice Service Community Ice-Ocean Model (CIOM); Bohai and Baltic Sea Ice models [*Cheng*, 2002].

Untersteiner [1961, 1964] originally used units of [g/cm^3] for salinity in equation his version of equation (1.10). Converting from the original c.g.s. units, equation (1.10) should be written $k_{si} = 2.03 + 0.117\,\rho S/T$ [W/m °C] if ρ [g^{c}m^3] and S [$^0/_{00}$] have their presently conventional units. *Untersteiner* [1964] assumed a constant density of 0.9 g/cm^3. Subsequent papers have either overlooked this density dependence or omitted it for simplicity, and typically use $k_{si} = 2.03 + 0.117\,S/T$ [W/m °C]. This difference is becomes noticeable only for temperatures near the melting point, and for $S = 6\,{}^0/_{00}$ amounts to at most a 1% change in k_{si} for $T < -4$ °C. As this is less than the roughly ±5% uncertainty in k_i (see below), this difference is perhaps not important. Reference in the literature to the parameterisation of equation (1.10)is variously cited as *Untersteiner* [1961], *Untersteiner* [1964], or *Maykut and Untersteiner* [1971]. Hereafter, we use the latter, which reflects the small departure from the original form, and the importance of the *Maykut and Untersteiner* [1971] paper in the development of sea ice modeling. Note that *Maykut* [1986] gives $\beta = 0.13\,W/mppt.$, which differs from both the original, and the commonly used value. We can only speculate that this reflects either an error in division by ρ rather than multiplication, or a typographical error.

Following the 'zero layer' thermodynamic models of *Semtner* [1964] and *Parkinson and Washington* [1979], some models use just Untersteiner's constant term, 2.03 [W/m °C]. Such models have tended to be those concerned with large scale coupling to atmospheric forcing, including the Antarctic sea ice models of *Wu et al.* [1997] and *Lemke et al.* [1990]. The US Navy Polar Ice Prediction System (PIPS 2.0) model uses the constant value 2.1656 [W/m °C].

Our interest lies in measuring and understanding heat flow in sea ice. Our study is not concerned with, or directly relevant to models that treat the thermal conductivity as a tunable parameter. These tend to be coupled models, and in order to accommodate many complex interactions desire the simplest parameterisation of the thermodynamics that still gives accurate model output [eg. *Gough*, 2001]. For example, the thermal inertia (heat capacity) can be set to zero and the thermodynamics treated as quasi-static by tuning the conduc-

tivity (see *Steele and Flato* [2000] discussion of so-called 0-layer models, *Gough* [2001] and references therein). In such cases parameter tuning is performed by constraining model output with observations. With increased modelling capability, most large scale community models do not use this approach now.

Further to its application to sea ice modelling, the thermal conductivity remains one of the least well measured properties of sea ice, and its accurate measurement presents an experimental challenge in itself.

1.5 Structure of Thesis

The body of this thesis is as follows. Background to theoretical and experimental determinations of the thermal conductivity and heat capacity is presented in Chapter 2. In Chapter 3 we provide a full description of the thermal arrays used in our sea ice and permafrost measurements. In Chapter 4 we discuss conductive heat flow and show how our temperature measurements can be analysed to determine the thermal conductivity of sea ice, and thermal diffusivity of permafrost. All details of our analysis method are presented and the method's performance is assessed from an analytical basis and via simulations. We relate the these results to the previous conductivity results of *Trodahl et al.* [2000, 2001] and *McGuinness et al.* [1998]. In Chapter 5 we describe our sea ice array measurements in Antarctica and Alaska, and present results of these experiments. Chapter 6 contains full details of our direct measurement of the thermal conductivity of small cores of sea ice using a new method. At the end of this chapter we discuss the results of our two methods and compare them with theoretical predictions and the parameterisation of *Maykut and Untersteiner* [1971]. We present all aspects of the Dry Valley permafrost project in Chapter 7. Conclusions from this work are presented at the end of this chapter. Then in Chapter 8 we summarise the key results of our sea ice measurements. Conclusions are drawn, including recommendations for the future parameterisation of k_{si} in sea ice models, and possible future work discussed.

Chapter 2

Background

In this chapter we present background to both the theoretical modelling and measurement of the thermal properties of sea ice. We are primarily concerned with the thermal conductivity, k_{si}, but also discuss the heat capacity, c_{si}, because we require an expression for $c_{si}(S,T)$ in the data reduction of our temperature array measurements (see Chapter 4). The thermal properties, like other bulk properties of sea ice, can depend strongly on composition because of large contrasts in the physical properties of the pure ice, brine and air components. In developing theoretic models of sea ice thermal properties there is a progression of increasing complexity: the heat capacity depends only on composition, density requires knowledge of the air content, and thermal conductivity (and therefore diffusivity) requires information on the spatial distribution of phases [*Yen*, 1981]. We therefore first present an overview of the composition and empirical phase relations of sea ice, before discussing theoretical results for k_{si} and c_{si}. We then summarise the approach, analysis and results of previous measurements of k_{si}.

2.1 Composition and Phase Relations

When sea water freezes the salt ions are not incorporated into the ice crystal lattice but are instead rejected into the melt. Brine inclusions form when the lamellar ice-growth interface 'pinches off' small volumes of the melt, and air bubbles, which are trapped in ice grain boundaries as the interface advances into the melt *Weeks and Ackley* [1986]; *Light et al.* [2003a, eg.]. For the brine and ice fractions to remain in phase equilibrium, differential melting or freezing

of pure ice occurs at the inclusion boundaries so that the salinity-dependent freezing point of the inclusions is adjusted to the ice temperature. With further temperature reduction various salts precipitate out of the brine, lining the inclusions.

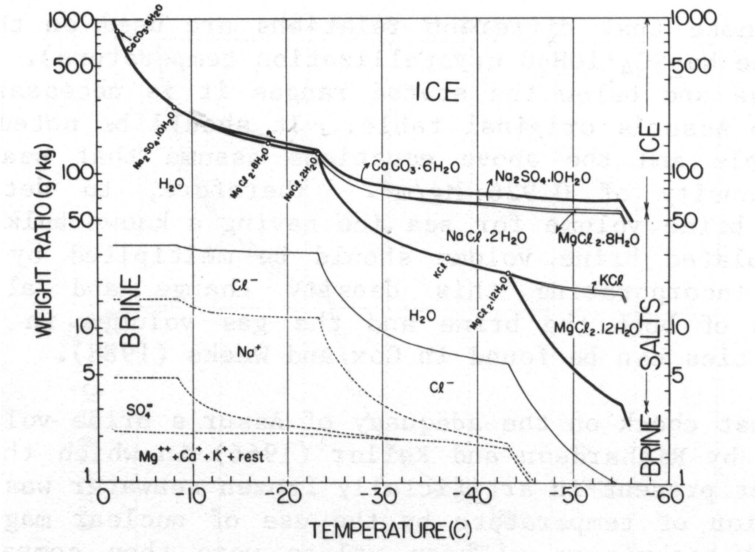

Figure 2.1: Phase relations for 'standard' sea ice. Circles on the brine-salt line indicate temperatures at which solid salts precipitate. Several but not all of these points coincide with kinks in the upper curve. Figure from *Assur* [1958], reproduced from *Weeks and Ackley* [1986].

The mass fractions of ice, pure water, and dissolved and precipitated salts is represented in figure (2.1), the 'standard sea ice' phase diagram of *Assur* [1958] reproduced from *Weeks and Ackley* [1986]. Note the log-linear axes. 'Standard sea ice' is sea ice with composition such that its meltwater has the same relative concentration of ions as normal sea water [*Assur*, 1958]. Barely visible on the upper ice/brine equilibrium line are the temperatures at which various salts precipitate.

Figure (2.2) shows more clearly the salt content dependence of the freezing temperature, T_f, and the onset of salt precipitation. The vertical axis of this phase diagram is not salinity, but instead is fractional salt content, s, defined as the mass of salt divided by the mass of water: $s = m_s/m_w$. (Salinity is the mass of salt per unit mass of sea ice $\sigma = m_s/m_{si}$.) Fractional salt content is used here only because T_f shows linear trends in s rather than σ. For $T > -8\,^\circ\mathrm{C}$, $s \propto T$, and equilibrium is maintained by freezing/melting of

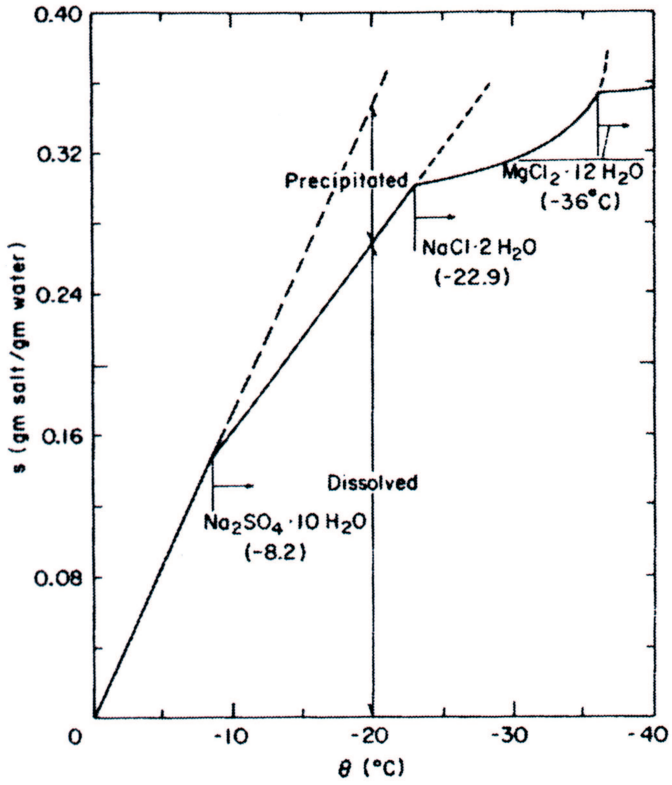

Figure 2.2: Freezing point of brine as a function of fractional dissolved salt content (see text). Solid dots, data from *Nelson and Taylor* [1954]; open circles computed from *Ringer* [1906]; dashed line, possible path if salts precipitate in a different order. Reproduced from *Yen* [1981], after *Schwerdtfeger* [1963].

ice. At approximately $-8\,^{\circ}\mathrm{C}$ mirabilite ($Na_2SO_4 \cdot 10H_2O$) starts to precipitate. The precipitate fraction $p = m_p/m_w$ is a linear function of temperature down to approximately $-23\,^{\circ}\mathrm{C}$ at which point hydrohalite, ($NaCl{\cdot}2H_2O$) also starts to precipitate, then $MgCl_2 \cdot 2H_2O$ at $-36\,^{\circ}\mathrm{C}$. We note that there is some discrepancy in reported values of the precipitation onset temperatures and slopes of lines in the (s, T) diagram. For $T \gtrsim -8\,^{\circ}\mathrm{C}$ we use the result of *Schwerdtfeger* [1963],

$$s = \alpha T, \quad \alpha = -0.01848\,^{\circ}\mathrm{C}^{-1} \quad . \tag{2.1}$$

As discussed below the precipitates play a negligible role in the thermal properties so any small differences in these parameters are unimportant in the present work.

To model the thermal properties of sea ice the volume fractions of the components that are required. For $T > -8\,^{\circ}\mathrm{C}$ all salts are dissolved, in 1 gram of sea ice there are σ grams of salt and σ/s grams of water. The mass of brine is $\sigma(1 + 1/s)$ and its density is $\rho_w(m_w + m_s)/m_w = \rho_w(1 + s)$ so the volume of brine is $v_b = \sigma/(s\rho_w)$, where ρ_w is the density of pure water. The mass of ice in 1 gram sea ice is $1 - \sigma - \sigma/s$ and the ice volume is $(1 - \sigma - \sigma/s)/\rho_i$. Making the substitution $s = \alpha T$, the fractional volumes for brine, ice and air (volume in unit volume of sea ice) are therefore [*Yen*, 1981]:

$$v_b = \frac{\rho_{si}}{\rho_w}\frac{\sigma}{\alpha T} \quad , \tag{2.2}$$

$$v_i = \frac{\rho_{si}}{\rho_i}\left(1 - \sigma - \frac{\sigma}{\alpha T}\right) \quad , \tag{2.3}$$

$$v_a = 1 - \rho_{si}\left(\frac{\sigma}{\alpha T \rho_w} + \frac{1 - \sigma - \sigma/\alpha T}{\rho_i}\right) \quad . \tag{2.4}$$

2.2 Theoretical Thermal Conductivity of Sea Ice

To model the effective-medium thermal conductivity of sea ice, one requires a model for the geometry of ice, brine and air components as well as the temperature-dependence of the component conductivities. *Yen* [1981] describes the slightly different models of *Anderson* [1958], *Schwerdtfeger* [1963] and *Ono* [1968] and presents graphs of $k_s i(\rho, S, T)$ based on Schwerdtfeger's approach but using results for component conductivities not available to Schwerdtfeger. Schwerdtfeger's model considered a matrix of 'bubbly ice' enclosing parallel, vertically-oriented bubbly-brine cylinders. The air bubbles were considered to be randomly distributed through the ice component and Maxwell's result, equation (1.6), applied [*Schwerdtfeger*, 1963]. Ono instead considered the air bubbles to be dispersed uniformly through both the ice and brine [*Ono*, 1968]. Recent work by Light and co-workers on the temperature-dependent micro-structure of FY Arctic sea ice using modern image processing methods, has shown air bubbles only in (present or previous) brine inclusions and not originating in the ice itself [*Light et al.*, 2003a]. They determine a power-law air bubble size distribution, and a bubble number density (number per unit volume) only $\sim 5\%$ of the brine inclusion number density. Schematic representations of Schwerdtfeger's and Ono's models are shown in Figure (2.3) together with an image from *Light et al.* [2003a].

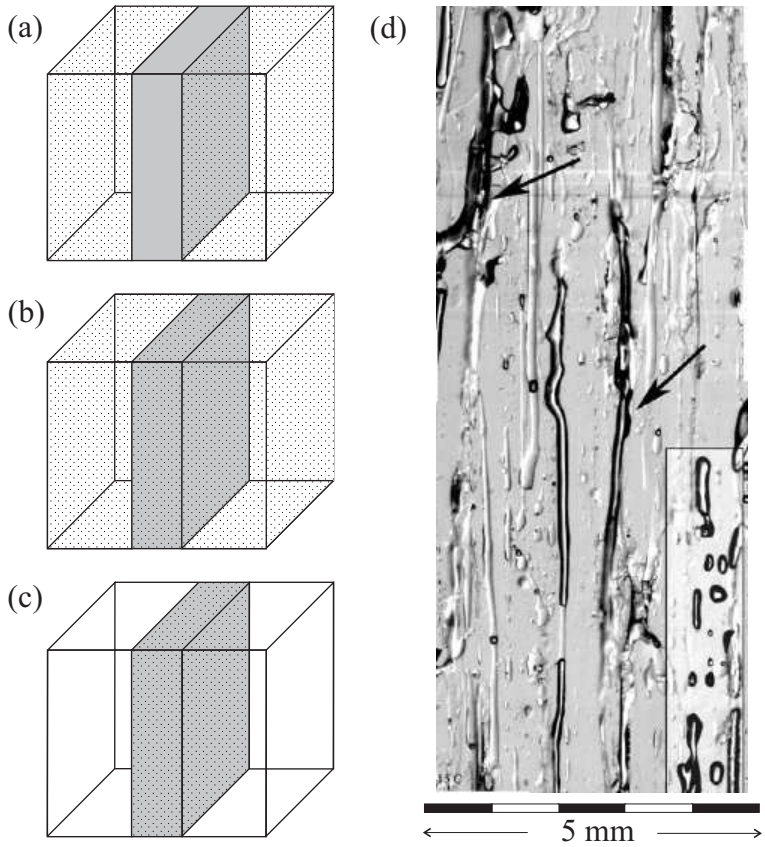

Figure 2.3: Highly simplified sea ice structure for thermal conductivity models: (a) *Schwerdtfeger* [1963] model: bubbly ice and brine; (b) *Ono* [1968] model, bubbly ice and bubbly brine; (c) our model, ice and bubbly brine; and (d) photograph of first year sea ice at $-15\,^{\circ}\mathrm{C}$ from *Light et al.* [2003a]. For parallel heat flow, only the volume fractions are important in (a,b,c) so the brine component does not need to be represented as tubes. In (d) the vertical brine tubes are a darker gray, and the edge of air bubbles are dark. The arrows point to drained brine tubes, and the insert shows several 'inactive' air bubbles.

With these results of *Light et al.* [2003a] in mind, we have modified Yen's adaptation of Schwerdtfeger's model, by considering parallel components of pure ice and 'bubbly brine'. We use Maxwell's result for the conductivity of the bubbly brine,

$$k_{bb} = k_b \frac{2k_b + k_a - 2v_a(k_b - k_a)}{2k_b + k_a + v_a(k_b - k_a)} \quad . \tag{2.5}$$

For k_b, we here use the same result as Yen, the thermal conductivity of NaCl

and Na_2SO_4 solutions ($S < 150\,{}^0/_{00}$) as measured by *Lange and Forke* [1952],

$$k_b = 0.4184(1.25 + 0.030\,T + 0.00014\,T^2) \quad [\mathrm{W/m\,^\circ C}] \quad . \tag{2.6}$$

For the thermal conductivity of air we use a temperature-dependent expression not used by Yen (who used $k_a = 0.0251\,\mathrm{W/m\,^\circ C}$) [*Di Nello*, 1995],

$$k_a = 0.0277 + 0.00010\,T \quad [\mathrm{W/m\,^\circ C}] \quad . \tag{2.7}$$

The dominant term in modelling k_{si} is the conductivity of fresh ice, $k_i(T)$, which in fact is not well known at all. There is good agreement on the temperature coefficient of $k_i(T)$ but $k_i(0\,^\circ\mathrm{C})$ has been determined only to an accuracy of about 5%, or 0.1 $\mathrm{W/m\,^\circ C}$. Reviews of previous measurements of $k_i(T)$ have been made by *Slack* [1980] and *Yen* [1981]. From a graph of several data sets, displaying a scatter of approximately ±15%, Yen gives the following best fits,

$$k_i(T) = 9.828e^{-0.0057\,T[K]} \quad [\mathrm{W/mK\,^\circ C}] \quad (\mathrm{all\,T}) \quad , \tag{2.8}$$

$$k_i(T) = 6.727e^{-0.0041\,T[K]} \quad [\mathrm{W/m\,^\circ C}] \quad (\mathrm{T} > 195\,\mathrm{K}) \quad . \tag{2.9}$$

From Yen's figure (14), the all-temperature fit is clearly too steep for $T > 195\,\mathrm{K}$, reflecting a bias from a large scatter in data below 150 K. For the temperatures that we are interested in, equation (2.9) is the best estimate of $k_i(T)$ with this functional form. Despite this, Yen uses equation (2.8) to model k_{si}. Between 0 °C and −30 °C these two fits are well described by the linear fits:

$$k_i(T) \approx 2.07 - 0.013\,T \quad [\mathrm{W/m\,^\circ C}] \quad (\mathrm{all\,T}) \quad , \tag{2.10}$$

$$k_i(T) \approx 2.19 - 0.01\,T \quad [\mathrm{W/m\,^\circ C}] \quad (\mathrm{T} > 195\,\mathrm{K}) \quad . \tag{2.11}$$

These linear forms show a $\sim 6\%$ difference in $k_i(0\,^\circ\mathrm{C})$, and both values are larger than $k_{i,0} = 2.03\,\mathrm{W/m\,^\circ C}$ originally adopted by *Untersteiner* [1961].

Slack [1980] addresses the underlying mechanisms of heat transfer in ice and seeks to analyse previous conductivity results based on then recent measurements and calculations of the phonon-dispersion curves. He rejects some of the data Yen included in his curve-fitting exercise, and rather than fit an equation to the still quite scattered data, Slack tabulates 'best estimates' of $k_i(T)$ from 0 °C down to 10 K for which he quotes an accuracy of 10%. [1]Of the many references available for $k_i(T)$He gives a higher precision estimate of $k_i(0\,^\circ\mathrm{C}) = 2.14\,\mathrm{W/m\,^\circ C}$. A linear interpolation of Slack's best estimates for 0 °C and −30 °C gives,

$$k_i(T) = 2.14 - 0.011\,T \quad [\mathrm{W/m\,^\circ C}] \quad . \tag{2.12}$$

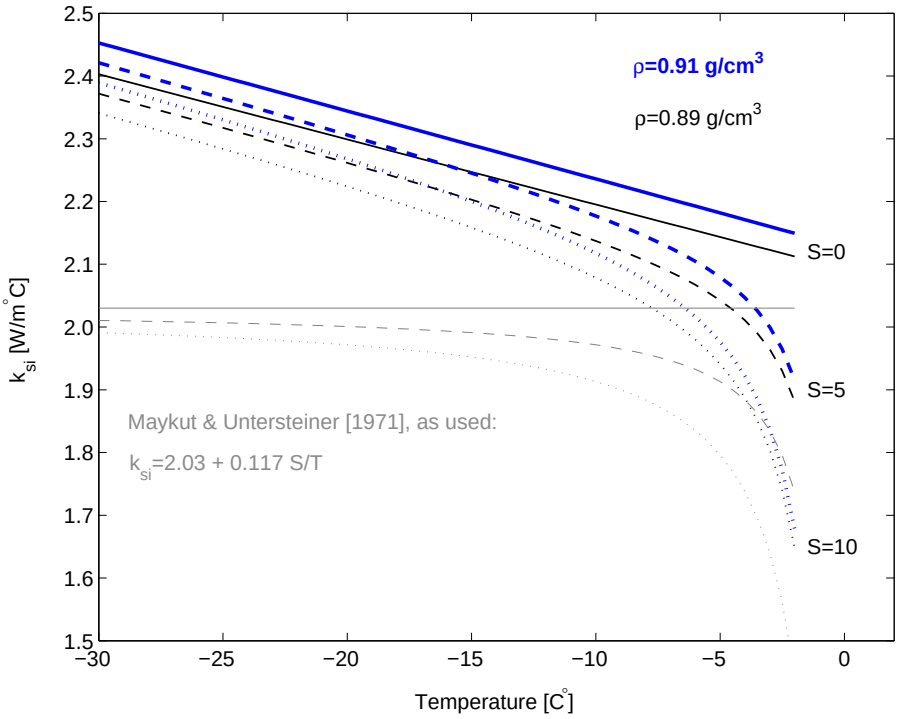

Figure 2.4: Modelled sea ice thermal conductivity, $k_{si}(\rho, S, T)$, for parallel conduction along pure ice and bubbly brine. Adapted from *Yen* [1981] for salinities and densities appropriate to FY ice, see text for details. Upper curves, $S = 0$, 5, 10 and densities $\rho = 0.89$, $0.91\,\mathrm{g/cm^3}$. Grey lower curves: parameterisation used in *Maykut and Untersteiner* [1971].

A translated version of the Russian text 'Sea Ice' [*Doronin and Kheisin*, 1977] gives the following relation for pure ice, from the measurements Nazintsev,

$$k_i(T) = 2.22 - 0.035\,T \quad [\mathrm{W/m\,^\circ C}] \quad . \tag{2.13}$$

This temperature gradient is more than twice that of the other results, but may be a typographical error as there are others in the same chapter of that book. The original reference could not be acquired either in Russian or in translation.

We consider equation (2.12) to be the best estimate of $k_i(T)$, and use it in our model of $k_{si}(T)$. The temperature gradient is similar to the linearisations of Yen's fits, and Slack specifies the 0 °C value to a higher precision that his other

[1] In support of Slack's tabulated values, the 2005 CRC Handbook of Physics and Chemisty [*Lide*, 2005] quotes them for the thermal conductivity of ice.

values indicating a greater degree of confidence. We have therefore modified the Yen/Schwerdtfeger model by considering bubbly brine in parallel with pure ice and by using different expressions for $k_i(T)$ and $k_a(T)$. Figure 2.4 shows $\mathrm{k_{si}}(\rho, \mathrm{S}, \mathrm{T})$ from evaluating equation (1.3) with equations (2.5, 2.7, 2.12). From the uncertainty in $k_i(0\,^\circ\mathrm{C})$ the underlying absolute accuracy of this model is about $\pm 0.1\,\mathrm{W/m\,^\circ C}$.

Structural models could be developed to include the size- and number- distributions of air bubbles and brine inclusions measured by *Light et al.* [2003a] from which effective medium parameters (electrical, and mechanical as well as thermal) could be predicted. However these refinements would result in changes in the predicted parameters that are likely below the present experimental resolution, and at a cost of increased mathematical complexity. Given the natural variability in sea ice microstructure this level of sophistication is probably not justified.

2.3 Theoretical Specific Heat of Sea Ice

The specific heat of sea ice differs from non-saline ice because the saline brine inclusions contribute a 'distributed latent heat' below the bulk freezing point. At low temperatures the brine volume is small and the specific heat of sea ice approaches the temperature-dependent specific heat of fresh-ice. However just below the freezing point the strongly temperature-dependent brine volume results in a strong temperature-dependence in the heat capacity. Because it is an equilibrium property the heat capacity is much easier to both model and measure than the thermal conductivity, and there has been good agreement between theoretical and experimental results.

Schwerdtfeger [1963] incorporated the sea ice phase diagram of *Assur* [1958] (figure 2.1), and from first principles derived models of the specific heat, density, and thermal conductivity of sea ice. Within uncertainties his own measurements of $c_{si}(S,T)$ in the Canadian Arctic were consistent with his theoretical results. A small error in his theoretical treatment was corrected by [*Ono*, 1968] who produced a series of papers on the thermal properties of sea ice including both theoretical modelling and experimental results from Mombetsu Harbour in the Okhotsk Sea at the far north of Japan [*Ono*, 1965, 1967, 1968]. Schwerdtfeger took the heat required for differential melting/freezing of ice mass δm to be $\delta Q = \delta m L_0$, for all temperatures, where L_0 is the latent heat of fresh ice at $0\,^\circ\mathrm{C}$. Correcting this to account for the temperature-

dependence of the internal energy of water and ice, *Ono* [1968] obtained $\delta Q = \delta m(L_0 + (c_w - c_i)T)$.

Ono's work is now the standard reference for the heat capacity of sea ice. For $T \gtrsim -8\,^\circ\mathrm{C}$ in which there are no precipitated salts, his result for the specific heat of sea ice is:

$$c_{si} = c_i + \sigma(c_b - c_i) - \frac{\sigma}{\alpha T}(c_w - c_b) - \frac{\sigma}{\alpha T^2}L_0 \quad . \tag{2.14}$$

Here m_i and $m_b = m_s + m_w$, are the mass of ice and brine in one gram sea ice, c_i, c_b, c_w are the specific heat of fresh ice, brine and water respectively and L_0 is the latent heat of fresh ice at $0\,^\circ\mathrm{C}$. Because there is no salt precipitation in this temperature range the mass of dissolved salt per unit mass sea ice equals the mass of total salt per unit mass sea ice, σ and the mass of water per unit mass of sea ice is $w = \sigma/s = \sigma/\alpha T$ according to the salt-content/temperature equilibrium line in figure 2.2. We use the results in *Ono* [1967], *Pounder* [1965] and *Nazintsev* [1964], here in SI units,

$$\text{Pure ice} \qquad c_i = 2.113 + 0.0075\,T \quad [\mathrm{J/g\,^\circ}C] \tag{2.15}$$

$$\text{Pure water} \qquad c_w = 4.205 - 0.008\,T \quad [\mathrm{J/g\,^\circ}C] \tag{2.16}$$

$$\text{Brine} \qquad c_b = 4.205 + 0.092\,T \quad [\mathrm{J/g\,^\circ}C] \quad . \tag{2.17}$$

With these and $\alpha = -0.01848\,^\circ\mathrm{C}^{-1}$, equation (2.14) gives [2],

$$c_{si} = 2.113 + 0.0075T - 0.0034S + 0.00008ST + 18.04\frac{S}{T^2} \quad [\mathrm{J/g\,^\circ C}] \quad , \tag{2.18}$$

for S [$^0/_{00}$] and T [$^\circ$C].

Ono did not consider the effect on the specific heat of salt precipitation below $-8\,^\circ\mathrm{C}$, probably because these temperatures are rarely reached at Mombetsu. Schwerdtfeger did this calculation for $-8\,^\circ\mathrm{C} < T < -23\,^\circ\mathrm{C}$ by assuming a linear rate of precipitation of $Na_2S0_4 \cdot 10H_20$. The dashed line in figure (2.2) shows the line $s + p_1 = \alpha T$ where p_1 is the fractional content precipitate. Applying Ono's correction to Schwerdtfeger's treatment leads to the following result,

$$\begin{aligned} c_{si} \;=\; & c_i + \sigma(c_b - c_i) - \frac{\sigma}{\alpha T}(c_w - c_b) - \frac{\sigma}{\alpha T^2}L_0 + \ldots \\ & \ldots - \frac{\sigma}{\alpha T}\sum_{j=1,2}(p_j\beta_j c_i + p_j c_b - p_j(1 + \beta_j c_{pj})) \quad . \end{aligned} \tag{2.19}$$

[2]Note that Ono used slightly different notation to Schwerdtfegers's convention that we are using here: $\alpha_{Ono} = -1/\alpha = 54.11\,^\circ\mathrm{C}$, equivalent to $\alpha = -0.01848\,^\circ\mathrm{C}^{-1}$.

Here $j = 1, 2$ indexes the precipitates mirabilite and hydrohalite, p_j the mass of precipitate j, c_{pj} their specific heat, and β_j is the ratio of water of hydration to salt mass. The relevant properties are,
(i) $T \leq -8\,^{\circ}\mathrm{C}$, $Na_2SO_4 \cdot 10H_2O$: $\beta_1 = 1.27$, $c_{p1} = 2.11\,\mathrm{J/g\,^{\circ}C}$, $\mathrm{p_1} = \alpha'(\mathrm{T} + 8\,^{\circ}\mathrm{C})$, $\alpha' = -0.01\,^{\circ}\mathrm{C}^{-1}$.
(ii)$T \leq -23\,^{\circ}\mathrm{C}$, $NaCl \cdot 2H_2O$: $\beta_2 = 0.67$, $c_{p2} = 0.75$ $\mathrm{J/g\,^{\circ}C}$, $\mathrm{p_2} = \alpha''(\mathrm{T} + 23)$, $\alpha'' = -0.007\,^{\circ}\mathrm{C}^{-1}$.
Evaluated with these parameters the precipitate (last) term in equation (2.19) is about $0.5\,\sigma c_i$ for $-8\,^{\circ}\mathrm{C} \leq T \leq -23\,^{\circ}\mathrm{C}$, and $0.45\,\sigma c_i$ for $-23\,^{\circ}\mathrm{C} \leq T \leq -30\,^{\circ}\mathrm{C}$. These corrections are very small. In his original paper *Schwerdtfeger* [1963] neglected the term $\sigma \mathrm{c_i}$. And at low temperatures $c_{si}(T) \rightarrow c_i(T)$ so the fractional size of the term σc_i is $0.5 - 1\%$ for $\sigma = 5 - 10\,{}^{0}/_{00}$. As these variations are below the experimental resolution of our array measurements, we neglect the effect of precipitation on c_{si}, and in our conductivity analysis described in Chapter 4, apply (2.18) at all temperatures.

2.4 Previous Experimental Results

We present here the methods and results of previous experimental results for the thermal conductivity of sea ice. We describe in detail the various experimental methods, and the data analysis used to calculate the conductivity.

2.4.1 Stefan, 1873

The first experimental value for the sea ice thermal conductivity was determined by *Stefan* [1891] from an analysis of ice thickness measurements from British Arctic surveys in the Canadian archepeligo from 1829-1853 [*Malmgren*, 1927]. From the rate of ice growth, assuming constant specific heat, density and a latent heat of fusion, Stefan found an average conductivity of $k = 1.7\,\mathrm{W/m\,^{\circ}C}$. The validity of this analysis has been questioned due to the expected salinity of the ice [*Malmgren*, 1927], and possible departures in the ocean heat flux from that assumed in the analysis [*Wettlaufer*, 2001].

2.4.2 Malmgren, 1927

Malmgren [1927] wrote the first comprehensive report on the thermal properties of sea ice based on experiments performed adrift on the 'Maud' during the Norwegian Arctic expedition, 1922-25. He reported experimental work on the density, salinity profile, specific heat and thermal conductivity of various sea ice types. He measured thermal conductivity with three methods: two from the analysis of $T(z,t)$ data, and an independent hot-wire method.

Malmgren Method I: 1-D Heat Flow Analysis

Malmgren's first temperature profile measurements were made in multi-year ice from October 1922 - August 1923. Four Ni resistance thermometers were placed at different depths, one in each of four bore-holes in a straight line. The laterial separation of the holes was 50 cm. They were back-filled with water and temperatures were read manually via a galvanometer once per day.

Malmgren considered the net 1-D heat flow into a cylinder of ice. If over a period of time t the average temperature of the ice changes from T_1 to T_2 the heat balance is given by,

$$\left(k_1 \frac{dT}{dz}_1 - k_2 \frac{dT}{dz}_2 \right) t = h\rho c \, (T_1 - T_2) \quad . \tag{2.20}$$

Here h, ρ and c are the height, average density and average specific heat of the cylinder over the interval t, and k_1 and k_2 the thermal conductivity at the top and bottom depths. If the temperature record shows times over which $T_1 = T_2$ equation (2.20) becomes:

$$k_1 \frac{dT}{dz}_1 = k_2 \frac{dT}{dz}_2 \quad . \tag{2.21}$$

Malmgren analysed the temperature record to find periods for which the temperature difference $(T_1 - T_2)$ was large ($\sim \pm 10\,^\circ$C), and those when it was zero. Equations (2.20, 2.21) were then applied to find the temperature-averaged conductivity at each measurement depth. Temperature gradients were found from interpolation of the measured temperatures. The results were shown in Table (2.1).

This method suffers from several short comings including coarseness in the analysis scheme, and time and depth resolution. The thermometers were arranged in separate bore holes, so the assumption of 1-D heat flow must

Depth [m]	T range [°C]	ρ [g/cm^3]	S [$^0/_{00}$]	k (meas) W/m °C	k (model) W/m °C
0.00	-8 to -17	0.89	0	1.0 ± 0.1	2.22 ± 0.05
0.25	-8 to -17	0.89	0	1.3 ± 0.1	2.22 ± 0.05
0.50	-4 to -19	0.91	1.5	1.7 ± 0.1	2.21 ± 0.10
1.25	-4 to -19	0.91	1.5	1.8 ± 0.1	2.21 ± 0.10

Table 2.1: Conductivity results for MY ice using from Malmgren's first method described above [*Malmgren*, 1927]. See text for details. $k(model)$ indicates the value predicted by our modifation to the Schwerdtfeger model for the measured ρ and S (see section 2.2).

hold over the total horizontal separation of 2m. In ice with uneven surface- and/or bottom- topology, this assumption doesn't hold.

Malmgren Method II: 1-D Heat Flow, Monthly Analysis

Between November 1923 - May 1924, a second set of temperature measurements were made in second-year ice with possibly the earliest forerunner of modern thermal arrays. Temperatures were measured with an array of 6 copper-constantan thermocouples mounted on a wooden board, positioned vertically down one water back-filled bore hole. Manual temperature measurements were made daily with a galvanometer. As the gradients were better known this year a more robust but computationally intensive adaption of the previous method was used in which monthly calculations were made.

Depth [m]	T range [°C]	ρ [g/cm^3]	S [$^0/_{00}$]	k (meas) W/m °C	k (model) W/m °C
0.00	-16 to -23	0.89	0	0.7 ± 0.2	2.30 ± 0.03
0.25	-9 to -16	0.89	0	1.4 ± 0.2	2.23 ± 0.04
0.75	-9 to -16	0.9	0.8	1.9 ± 0.1	2.23 ± 0.04
1.25	-6 to -14	0.9	2.2	2.1 ± 0.1	2.18 ± 0.04

Table 2.2: Conductivity results for 2nd year ie using Malmgrens's second method described above. $k(model)$ as in table (2.1).

Two thermo-piles were also installed during the second measurements. These consisted of a 'large number of series-coupled copper-constantan thermocouples' giving a direct measurement of the temperature difference over 10 cm to within 0.05 °C. Centered at depths of 25 and 200 cm, these provided a more direct and accurate measurement of the temperature gradient at these depths. The period of reliable data was short however. Using the ratio of $k_{0.25m} = 0.772\, k_{1.25m}$ from table (2.2), the average conductivities from the directly measured gradients are $\mathrm{k}_{0.25} = 1.5\,\mathrm{W/m\,^{\circ}C}$ and $\mathrm{k}_{1.25} = 2.0\,\mathrm{W/m\,^{\circ}C}$.

Compared with the values predicted by our model, Malmgren's conductivity values using Methods I and II are all very low. Intriguingly, they show a surface reduction that is similar to that observed by Trodahl and McGuinness, see below.

Method III Hot Wire Method

Malmgren also performed a direct 'hot wire' measurement with the equipment sketched in figure (2.5). He stretched tight the thermocouple wires and hot wire on a wooden frame to maintain the distances a (wire to centre of thermocouple) and Δa (spacing of thermocouple wires) and froze the frame into 'young ice'. The heating wire (AB) and the two thermocouple wires were arranged radially. For a current I the heat dissipated per cm is $A = I^2R$, where R is the wire resistance per cm. Eventually all of the applied heat will have passed through the cylinder with axis AB and radius a. The heat through each square centimeter is then $Q = A/(2\pi a)$, and as this heat flows outwards there will be a variation in the temperature gradient at radius a. The total heat flow is given by,

$$\frac{A}{2\pi a} = k \int_{t_0}^{\infty} \left.\frac{dT}{dz}\right|_a dt \quad . \tag{2.22}$$

Replacing the integral by the average value over the time interval Δt of measured non-zero temperature gradient $\Delta T/a$ gives,

$$k = \frac{A}{2\pi a \Delta t < \frac{\Delta T}{a} >} \quad . \tag{2.23}$$

One set of measurements was made in 'young ice' giving $k = 2.1\,\mathrm{W/m\,^{\circ}C}$ at a depth of 35 cm. This value is high compared with Malmgren's other results but no uncertainty is quoted, and he reported no repeat measurements to assess reproducibility.

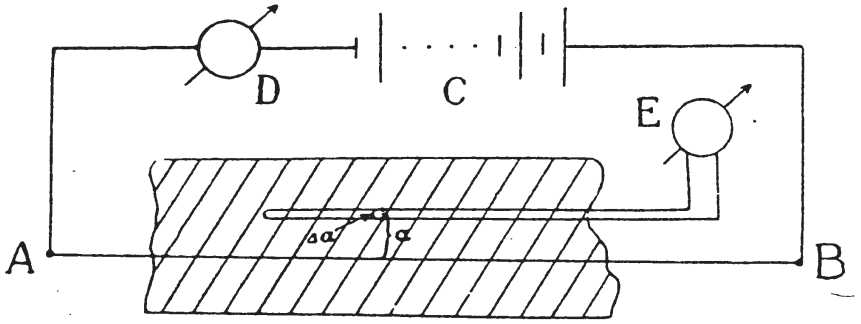

Fig. 11. Arrangement for experimental determinations of heat-conductivity of sea-ice.

Figure 2.5: Geometry for Malmgren's hot wire method for measuring thermal conductivity. Figure from original paper [*Malmgren*, 1927]. Hot wire is AB. Galvanometer E is connected to thermocouple, see text.

2.4.3 Nazintsev, 1950-60s

Before the cold war era, the sea ice research community in the Soviet Union was more active than that in the west [*Dieckmann and Hellmer*, 2003]. Unfortunately, work from that time, including that on the thermal properties of sea ice is still difficult to obtain either in translation, or in the original Russian. Nazintsev made laboratory and field measurements on the thermal properties of porous ice and sea ice in the late 1950s and 1960s (references in *Doronin and Kheisin* [1977]). He reported calorimetric measurements of the heat capacity and thermal diffusivity ('thermometric conductivity') made on the drifting station Noth Pole-4 in 1957 [*Nazintsev*, 1959]. The specific heat of 'young', first-year and second year sea ice with salinity $1.5 - 6\,{}^{0}/_{00}$ was measured over the range -2 to $-19\,^{\circ}$C. The thermal diffusivity was determined from the temperature change in ice samples immersed in a well-stirred isothermal alcohol bath. The diffusivity was determined from the rate of change of the ice temperature, and by 'normalising' with the results of pure ice samples.

For the two samples for which both the specific heat c and diffusivity D were measured, we have calculated the thermal conductivity as $k = \rho c D$. Table (2.3) shows the resulting conductivity using either the theoretical heat capacity, or by interpolating Nazintsev's heat capacity measurements, which were generally made at different temperatures than the diffusivity measurements. Nazintsev does not present density values, we here use $\rho = 0.91\,\mathrm{g/cm^3}$. Full

data and analysis of the diffusivity measurements are not presented, and Nazintsev himself notes that the diffusivity results 'must be regarded as somewhat approximate' [*Nazintsev*, 1959].

T [°C]	D 10^{-3}[cm^2/s]	$c_{Meas}{}^a$ [J/g °C]	$c_{Model}{}^b$ [J/g °C]	$k(c_{meas})$ [W/m °C]	$k(c_{model})$ [W/m °C]
'Young ice', 10 cm depth, S=3.59 $^0/_{00}$, small air pores					
-5	5.2	4.2	4.67	2.0	2.21
-10	8.7	2.2	2.69	1.7	2.13
-15	11.3	2.1	2.29	2.2	2.35
FY ice, 170 cm depth, S=3.86 $^0/_{00}$					
-5	4.6	4.6	4.67	1.9	1.95
-10	8.4	2.3	2.69	1.8	2.05
-15	10.6	2.1	2.29	2.1	2.21

Table 2.3: Thermal conductivity calculated from the thermal diffusivity measurements of *Nazintsev* [1959]. [a] Interpolation from Nazintsev's specific heat measurements.[b] Model of *Schwerdtfeger* [1963]. A density $\rho = 0.91\,\mathrm{g/cm^3}$ was assumed in the conductivity calculations.

Figure (2.6) shows other results of Nazintsev reported in *Doronin and Kheisin* [1977] from which the figures have been slightly reformatted. Subplot (a) shows $k(T)$ from 'laboratory specimens of ice' with salinity $4.7\,^0/_{00}$. Subplot (b) shows k as a function of relative depth (z/z_0) for field results. Regrettably no absolute values of the depth are presented in *Doronin and Kheisin* [1977], and neither are experimental details. The reduction near the surface is attributed to increased porosity (lower density) and that at depth to the increasing brine component [*Doronin and Kheisin*, 1977].

2.4.4 Ono, 1960s

Ono [1965] developed a method for extracting the thermal diffusivity from temperature measurements in sea ice which is also outlined in *Yen* [1981]. Due to the mild climate at his field site in Mombetsu Harbour (Sea of Okhotsk) Ono used artificial heat sinks to drive the surface temperatures and produce

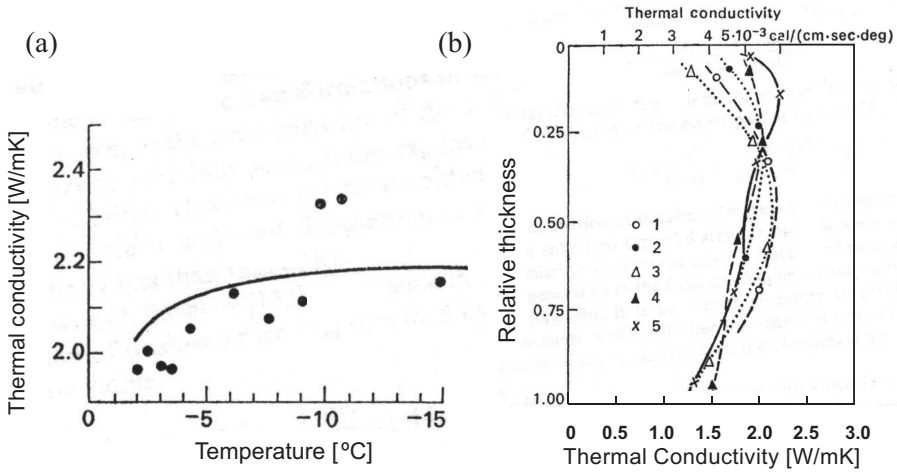

Figure 2.6: Russian k_{si} results. Both figures from Nazintsev, reproduced and modified slightly from *Doronin and Kheisin* [1977]. (a) $k_{si}(T)$ for $S = 4.7\,{}^{0}/_{00}$ laboratory specimens; (b) $k_{si}(z/z_0)$ for field results from floating ice stations:1 - one-year ice (SP-4, 1957); 2 - two-year ice (SP-4, 1957); 3 - one-year ice (SP-5, 1956); 4 - two-year ice (SP-5, 1956); 2 - multi-year ice (SP-5, 1956).

temperature variations large enough for his analysis. From temperatures measured at 2, 4, 7 cm, the conductivity calculated from the measured diffusivity at these depths was estimated to be in the range 1.84 - 1.97 W/m °C [*Ono*, 1965]. The temperature range was -1 to -8 °C.

2.4.5 Schwerdtfeger, 1960s

To compliment his theoretical formulation of the thermal properties of sea ice *Schwerdtfeger* [1963] measured the thermal conductivity of sea ice with two methods. The first was a comparison of the temperature gradients in sea ice and a $1.5 \times 1.5 \times 0.3\text{m}^3$ reference block of fresh ice embedded in the sea ice. The conductivity of the reference block was calculated with Schwerdtfeger's model using measured salinity and density and $k_{i,0} = 2.09\,\text{W/m}\,^{\circ}\text{C}$. Over two months, the conductivity of sea ice between $10 - 30\,\text{cm}$ with mean temperature $-7\,^{\circ}\text{C}$, density $0.91\text{g/cm}^3$and salinity S=6, was determined to be $k = 2.00 \pm 0.30\,\text{W/m}\,^{\circ}\text{C}$. Schwerdtfeger's model gives a theoretical value of $\text{k} = 2.0\text{W/m}\,^{\circ}\text{C}$.

In the second method the average thermal conductivity of the entire sheet was

determined via a modified form of Stefan's simple ice growth model in which the growth rate was related to the surface temperature history and the time lag for heat flow between the surface and interface accommodated. For the cover as a whole with mean temperature $-5\,^{\circ}\mathrm{C}$, density 0.915 g/cm^3 and S=6 the experimental conductivity was $k = 2.05 \pm 0.20\,\mathrm{W/m\,^{\circ}C}$. For these parameters Schwerdtfeger's theory gives 1.97 W/m °C. Within quite large experimental uncertainties there is good agreement between Schwertdfeger's experimental and theoretical results.

2.4.6 Lewis, 1966

Lewis [1967] reported temperature measurements in winter sea ice in Cambridge Bay, North Western Territories, Canada (69° 04′ N, 105° 00′ W). He deployed 5 vertical thermistor chains in a linear array with 10 m lateral spacings. Each chain consisted of 13 thermistors separated vertically by 15 cm, but no other details of the array construction are presented. An automated data logging system read the chain every hour for 800 hours (33 days, 8 hours) to a reported accuracy of $\pm 0.01\,^{\circ}\mathrm{C}$.

Lewis calculated the ice thermal conductivity at the ice/water interface form the ice growth rate and its depth profile through the ice using heat flow analysis based on the heat balance shown schematically in figure (2.7). Lewis's heat flow analysis is quite complicated and ultimately relies on an assumption of 'monochromatic' heat flow. For completeness, we include a full description of this method. [3] Analytically the heat balance in figure (2.7) is given by

$$F(z,t) = F_L(z,t) + F_O(z,t) + F_U(z,t) \quad , \tag{2.24}$$

where z is depth beneath the surface, $F_L(z,t)$ is heat flow associated with Latent heat released, $F_O(z,t)$ is heat flow associated with sensible oceanic heat flux, and $F_U(z,t)$ is heat flow associated with changes in internal energy in the ice sheet, ie. via the temperature and heat capacity.

Both analysis methods, presented in more detail below, required a value for the oceanic heat flux at the interface, F_O. Assuming no advective ocean currents at this site (one of the reasons for choosing it) and correlating the heat loss from the water column, calculated from 70 m deep water temperature profiles, with ice formation over a 23 day period, Lewis estimated $F_O = 0.2\,\mathrm{cal/cm^2/hr} = 2.3\,\mathrm{W/m^2}$.

[3] Note that Lewis used 'Q' for heat fluxes [W/m^2]. In keeping with current sea ice usage, we use 'F'.

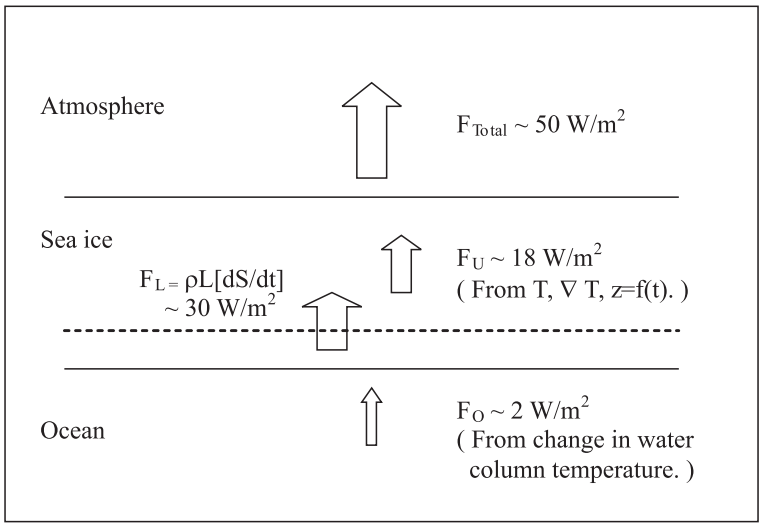

Figure 2.7: Heat flux balance through sea ice, after *Lewis* [1967]. Values are particular to his experimental site, see text.

Both methods are computationally intensive, requiring accurate estimation of several quantities from the temperature record, and in the second case, an assumption regarding the heat flow which is really accurate only in the first order.

Lewis Method I: Ice interface conductivity

At the water/ice interface z=H the net heat balance is associated with a change of phase, not a change of temperature, and the heat balance given by,

$$k_{int} \left. \frac{\partial T}{\partial z} \right|_{z=H} = \rho L \frac{dH}{dt} + F_O(H,t) \quad , \tag{2.25}$$

where k_{int} is the thermal conductivity at the interface. The rate of growth of the interface can be estimated from the temperature derivatives at the interface,

$$\frac{dH}{dt} = - \left[\frac{\partial T/\partial t}{\partial T/\partial z} \right]_{z=H} \quad . \tag{2.26}$$

Lewis calculated $\frac{\partial T}{\partial t}|_H$ from the rate of temperature change as the interface grew past successive sensors, and $\frac{\partial T}{\partial z}|_H$ from a quadratic fit to temperatures of the four bottom-most thermistors in the ice. The interface depth H was calculated as the intercept of this quadratic with $T = -1.56\,^{\circ}\mathrm{C}$ (the temperature of sensors in the water column just below the interface), and $\frac{\partial T}{\partial z}|_H$ evaluated

from the quadratic fit at this depth. Table (2.4) gives the thermal conductivity calculated using this method for the four functional thermistor strings, as the interface advanced past $z = 165$ cm.

Chain No.	$\partial T/\partial z\|_S$ °C/m	$\partial T/\partial t\|_H$ 10^{-6} °C/s	dH/dt 10^{-6}m/s	$F_L(H,t)$ W/m^2	F_O W/m^2	$F(S,t)$ W/m^2	k_{si} W/m °C
10	14.2	-1.44	0.102	26.2	2.3	28.5	2.01
30	16.3	-1.94	0.119	30.8	2.3	33.1	2.03
40	12.1	-0.92	0.076	19.7	2.3	22.0	1.82
50	11.4	-0.75	0.066	17.0	2.3	19.3	1.69

Table 2.4: Calculated values of k_{si} at ice/water interface from *Lewis* [1967]. Values here converted to SI units.

Lewis estimates an uncertainty, derived mainly from estimating $\frac{\partial T}{\partial t}|_H$, of ± 0.04 W/m °C, except for string '10' which due to temperature 'instabilities', was considered less reliable. A weighted average of strings 30, 40, 50 gives $k_{int} = 1.85 \pm 0.02$ W/m °C. Without a measured density theoretical comparison cannot be made. Derived from a heat flow perspective, this *in situ* measurement potentially captures any convective contribution to the heat flow in the mushy layer at the base of the ice [*Worster and Wettlaufer*, 1997]. However the method is sensitive to the value of F_O, and it is unclear how sensitive it is to the temperature extrapolations involved.

Lewis Method II: conductivity profile in ice

The second approach used by Lewis was to analysis the propagation of heat through the ice sheet, by following peaks or troughs in the measured temperature field $T(z,t)$. Identifying peaks in the temperature field with extrema in ∇T and therefore the heat flow, Lewis makes the 'monochromatic' assumption that *all* heat flow is associated with the peaks, whose paths can be tracked in the (z,t) plane through the temperature record. In this monochromatic assumption, all heat flow associated with a temperature feature at the surface at time t_1 occurs along this path for which F_L and F_O are considered constant. By combining equations (2.24, 2.25) the heat flow along this path $z(t)$ from

z_1, t_1 to H, t_2, is given by

$$F(z_1,t_1) = F(H,t_2) + F_U(z_1,t_1) \quad , \tag{2.27}$$

$$\delta F_U = \delta F = \left(\frac{\partial F}{\partial z}\delta z + \frac{\partial F}{\partial t}\delta t\right)_{z=f(t)} \quad . \tag{2.28}$$

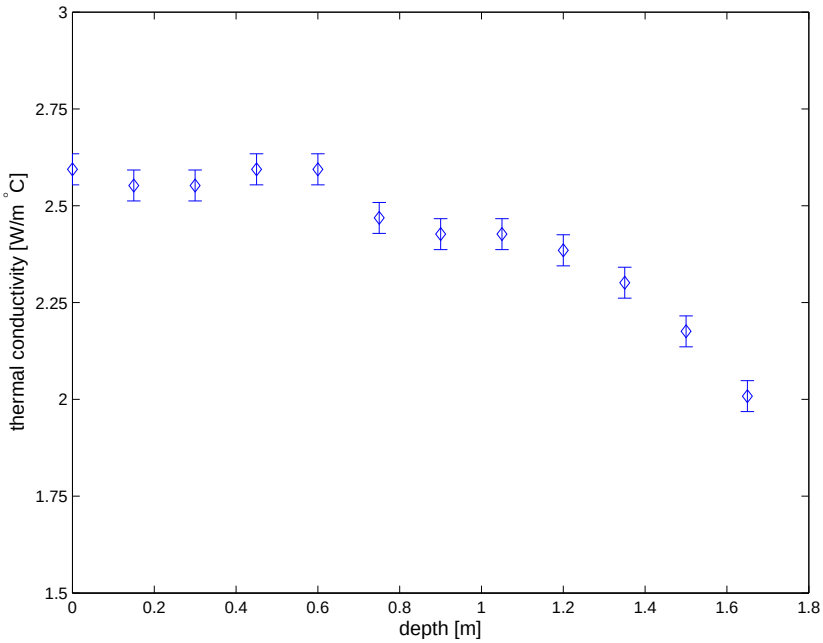

Figure 2.8: Thermal conductivity profile from thermal array measurements of *Lewis* [1967], using monochromatic heat flow analysis. Conductivity values have been recalculated in SI units by the present author, see text.

Equation (2.28) follows for F_L and F_O constant along the heat flow path z(t). Combining equations (2.25, 2.26, 2.27, 2.28) gives,

$$\begin{aligned} F(z_1,t_1) &= F(H,t_2) + \int_{z=f(t)} \left(\frac{\partial F}{\partial z}\delta z + \frac{\partial F}{\partial t}\delta t\right) \quad , \\ &= F_L(H,t_2) + F_0(H,t_2) + \int \left(\rho c \frac{\partial T}{\partial z}\delta z + k\frac{\partial}{\partial t}\left[\frac{\partial T}{\partial z}\right]\delta t\right) \quad , \\ &= -\rho L \left[\frac{\partial T/\partial t}{\partial T/\partial z}\right]_{z=H} + F_0(H,t_2) + \int \left(\rho c \frac{\partial T}{\partial z}\delta z + k\frac{\partial}{\partial t}\left[\frac{\partial T}{\partial z}\right]\delta t\right). \end{aligned} \tag{2.29}$$

The path $z(t)$ is determined as the locus of points (z_i, t_i) which mark a propagating temperature peak, so the last integral is evaluated as a sum over the

intervals $\Delta z_i, \Delta t_i$ between these points. Equation (2.29) becoming:

$$k\nabla T = -\rho L \left[\frac{\partial T/\partial t}{\partial T/\partial z}\right]_{z=H} + F_O(H,t_2) + \sum_{(z_1,t_1)}^{(z,t)} \rho c(\overline{T_i}) \frac{\partial T}{\partial z}\Delta z_i + \sum_{(z_1,t_1)}^{(z,t)} k\frac{\partial}{\partial t}\left[\frac{\partial T}{\partial z}\right]\Delta t_i. \tag{2.30}$$

The derivatives in equation (2.30) were estimated from finite difference estimates from the temperature record. As k appears in the last term on the RHS, equation (2.30) is really an iterative scheme for finding k. For this RHS term, Lewis used Schwerdtfeger's modelled $k_{si}(T)$, using the average temperature of each δz, δt interval, ranging from 2.01 W/m °C at the ice/water interface to 2.51 W/m °C at the top surface. Lewis measured the salinity profile and used the heat capacity of *Schwerdtfeger* [1963], and $L_f = 67.5$ cal/g (282 kJ/kg) and $\rho = 0.915\,\mathrm{g/cm^3}$. Figure (2.8) shows $k(z)$ from one thermistor chain. These values are the highest reported anywhere. Aside from the error introduced in the monochromatic assumption in deriving equation (2.30) errors in the terms in equation (2.30) are compounded in the sums along the path $z(t)$. We note that these values have been recalculated by the present author using equation (2.30) iteratively. The values differ from Lewis's original values by only $\sim$ 1-2 %.

2.4.7 Weller, 1965-68

The 1960's represented a busy era for members of the Australian Antarctic Division, who made glaciological and meteorological measurements on plateau and sea ice in the Mawson Base area of Antarctica. From temperature borehole measurements *Weller* [1967] determined the apparent diffusivity in plateau ice and sea ice. His analysis, and particularly that of *Budd* [1967], illustrated that ignoring the effect of absorbed solar radiation, leads to systematic errors when the thermal diffusivity is calculated using Fourier methods. This effect can lead to erroneous diffusivity values as deep as 6 m ($\sim$ 2 penetration depths for the annual cycle) in plateau ice, due to absorption of the annual annual insolation cycle.

In the case of sea ice, *Weller* [1967] measured daily (midnight) temperatures between May and November with thermocouples at depths of (0, 15, 30, 45, 60, 80, 100) cm, and obtained heat flow measurements with a heat flux plate at 30 cm. Hourly measurements were made at least for October.

Weller calculated the diffusivity using the daily heat flux and temperature

amplitudes at 30 cm using the semi-infinite analysis of *Lettau* [1954]. This first required a correction for the effect of the daily radiation cycle on these measurements. This was done with a trial and error method, in which the amplitude of the total daily radiative perturbation was varied (its phase fixed by solar noon). The phase and amplitude of the unperturbed daily temperature and heat flux cycles were then varied so that once combined with the effect of the radiation, observed variations were reproduced. The unperturbed cycles were found to be $\pi/4$ out of phase as expected. This analysis required a heat capacity value for which the model of *Schwerdtfeger* [1963] was used with the average measured October values of 0.9 g/cm^3, S=6, $T = -12\,^\circ$C, giving (in SI units) $c = 2.80\,J/g\,^\circ$C). The calculated conductivity and diffusivity were $k = 1.80\,\mathrm{W/m\,^\circ C}$, and $D = 0.72 \times 10^{-6}\,\mathrm{m^2/s}$. Schwerdtfeger's model predicted $k = 1.96\,\mathrm{W/m\,^\circ C}$, and $D = 0.78 \times 10^{-6}\,\mathrm{m^2/s}$.

Considering this as a good agreement, *Weller* [1967] remarks that "Radiation effects seem therefore to have been successfully eliminated". This conclusion surely reflects the low accuracy of conductivity measurements available at that time; we consider a value of $k = 1.80\,\mathrm{W/m\,^\circ C}$ to be unexpectedly low.

Weller [1967] also calculated the diffusivity profile $D(z)$ from the propagation through the ice of an approximately sinusoidal '50-day period warm wave'. This wave was centered in mid August, when solar radiation levels were very low. Ignoring radiation, Weller graphically fit the amplitude decay and phase lag of the wave to the solution for the harmonic surface-driving of a finite slab [*Carslaw and Jaeger*, 1959], and compared them with the predictions of *Schwerdtfeger* [1963]. This analysis yielded diffusivity values very sensitive to uncertainties in the measured temperatures, with uncertainties in the experimental values larger than 50 %. For these temperatures, the predicted values are highly sensitive to salinity and temperature.

Weller's results illustrate two points. Firstly, daily radiation effects do perturb the heat flow near the surface, rendering even sophisticated harmonic analysis complicated and of limited accuracy. Secondly, even in the absence of the daily cycle, both experimental values obtained from harmonic analysis, and theoretical predictions of the thermal diffusivity are highly sensitive to measurement errors.

A noteworthy aspect of this work was the automated, mechanical thickness measurements made with a Schwerdtfeger-designed hot-wire device. These were used to investigate the time-lag between heat flux variations (at 30 cm) and the rate of growth at the base. *Schwerdtfeger* [1966] introduced a 'lag coefficient' between surface temperatures and basal growth rate, expected to

be inversely proportional to the diffusivity. It seems that the intended use of this as a simple ice-growth forecasting parameter was not adopted.

2.4.8 Trodahl and co-workers, 1996-

In the 1990's Trodahl and co-workers from Victoria University of Wellington established an experimental programme to measure the thermal properties of sea ice. This thesis represents the completion of that program. Full details of the measurement methods and analysis as used in the present work, are presented in chapters 3 and 4 respectively. We here provide a brief overview of the earlier measurements and results of this program.

Johnson and co-workers first measured the heat capacity of artificial and natural sea ice and demonstrated excellent agreement with Ono's theoretical expression evaluated as equation (2.18) [*Johnson*, 1989]. See figure 2.9(a) (over page). This was followed by the first thermal array measurements in which the vertical temperature profile in the top 2 m was measured at 10 cm intervals over several months. The thermal conductivity was determined from a conservation of energy analysis analysis according to which the rate of change of the internal energy density was related to the temperature curvature by

$$\rho \frac{\partial U}{\partial t} = k \frac{\partial^2 T}{\partial z^2} \quad . \tag{2.31}$$

Here $\rho\,[\mathrm{g/cm^3}]$ is density, and U [J/g] is internal energy density. We fully describe this analysis in Chapter 4. On the basis of the excellent agreement between theoretical and experimental results in figure 2.9(a), and elsewhere, U was calculated by integrating equation (2.18) [*Trodahl et al.*, 2000]. The thermal conductivity was determined as the best-fit slope to scatter-plots of finite difference estimates of the partial derivatives in equation (2.31). Figure 2.9(c) shows a vertical conductivity profile, $k(z)$ calculated from scatter plots at successive depths in the ice. The temperature-dependence of the conductivity $k(T)$ was obtained from data at all depths, although cold temperature data naturally originate exclusively from near the ice surface, and warm temperature data from near the ice/water interface. See figure 2.9(d).

The depth profiles $k(z)$ showed variations other than those predicted by the models. From several years' of array experiments, a 25-50% reduction in the conductivity over the top $\sim 50\,\mathrm{cm}$ was resolved, as was an apparent increase with depth [*Collins*, 1998; *McGuinness et al.*, 1998; *Trodahl et al.*, 2000, 2001]. It was proposed that the reduction in near-surface conductivity might

be caused by to enhanced phonon scattering, due to very small crystal size, in the frazil ice at these shallow depths [*Trodahl et al.*, 2001]. The increase in conductivity with depth was associated with the possibility of heat flow arising from convection within brine tubes [*McGuinness et al.*, 1998; *Collins*, 1998]. It is clear from figures 2.9(c,d) that the depth-dependence is dominating the expected temperature-dependence.

The present work was in part motivated by the desire to understand the large apparent near-surface reduction observed by Trodahl and co-workers. We note that a strong near-surface reduction was resolved by Malmgren (methods I, II above) and Nazintsev (figure 2.6(b)), and Weller's value at 30 cm is low. On the other hand Lewis derived a higher conductivity near the surface.

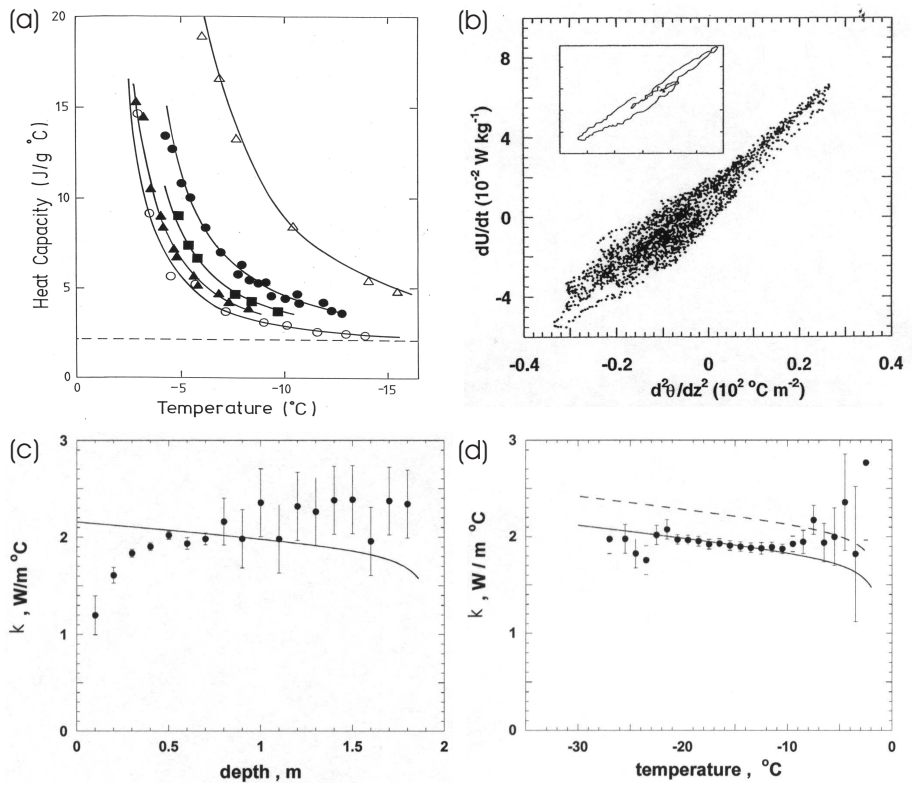

Figure 2.9: Figures from Victoria University sea ice programme.
(a)Measured sea ice heat capacity from *Johnson* [1989]. Artificial (NaCl) ice: $S = 4.6$ (O), $S = 37.6$ ($\triangle$). Natural sea ice, $S = 6.2$ ($\blacktriangle$), $S = 8.4$ ($\blacksquare$), $S = 13.2$ ($\bullet$), from respective depths 570-620 mm, 339-380 mm, 0-50 mm in a 1700 mm ice cover, McMurdo Sound. Uncertainty bars, omitted for clarity, are 5% at most. Solid line, Ono's prediction, equation (2.18).
(b)Example of finite difference graph, the best fit slope is k. Inset shows a counter-clockwise loop in the data [*Trodahl et al.*, 2000].
(c)Depth-dependence of k in FY McMurdo sea ice (1999). Solid line is Yen/Schwertdfeger model for depth-dependent average temperature but reduced by 10% [*Trodahl et al.*, 2001].
(d)Temperature-dependence of k in FY McMurdo sea ice (1999). Data from all depths, but cold temperatures exclusively from surface ice and warm temperatures from near ice/water interface. Dashed line is Yen/Schwertdfeger model, and and solid line the same reduced by 10% [*Trodahl et al.*, 2001].

Chapter 3

Array Measurements

Using thermistor arrays and automated data loggers, we have recorded the temperature profile in sea ice for up to 6 months, and in permafrost continuously for 2 years. In this chapter we present all aspects of the equipment involved in these measurements, and their installation. Following an overview, we present details of the individual array components, including thermistors, measurement circuitry and data loggers. We then describe the site assembly and installation. This chapter enlarges on, and goes beyond, such aspects of these experiments previously published by the Victoria University group, [*McGuinness et al.*, 1998; *Collins*, 1998; *Trodahl et al.*, 2000, 2001; *Pringle et al.*, 2003].

3.1 Overview of Experiment

In these experiments we measure the sea ice temperature profile as a function of time. Similar ground temperature measurements have been used for many years to estimate ground thermal diffusivities [*DeVries*, 1963]. These latter measurements are most readily processed by applying Fourier analysis schemes, and solving for an apparent thermal diffusivity. It is usually assumed that the diffusivity is constant and uniform. We discuss such analysis schemes in the context of our permafrost measurements in Chapter 6. They are problematic in sea ice because the thermal diffusivity is a strong function of temperature over the range of measured temperatures, and because of the finite-thickness, constant-temperature lower boundary condition of the ice. Instead, we recast the analysis in terms of energy conservation and exploit the

Figure 3.1: The author with a thermal array installed in MY ice, in McMurdo Sound, 2003.

known temperature-dependence of the internal energy of sea ice, to solve directly for the thermal conductivity [*Trodahl et al.*, 2000]. This analysis is fully presented and discussed in Chapter 4.

Temperature measurements were made with thermistors positioned at 10 cm intervals inside a 2 m long vertically oriented 'thermistor string' or 'array' embedded vertically in the ice by coring a 5 cm diameter hole and freezing it in. A data logger and multi-plexor were used to sequentially measure the electrical resistance of the thermistors using a bridge circuit. The whole array was read in this way with a measurement interval of either 30 minutes or 1 hour, and the results saved to memory. Data analysis involved first converting the resistance values to temperature, and then calculating the thermal conductivity from the coupled time- and depth- variations in the temperature.

Figure (3.1) shows an assembled site at McMurdo Sound, Antarctica. The thermistor string is frozen into the ice and only its red connector is visible at the ice surface, joining the cable leading to the data logger housed inside the polycarbonate box, attached to the frame. The multiplexor and batteries

are also inside this box. The frame is about 2 m long and 0.8 m tall, and is anchored to the ice with thin steel cables and ice screws. By elevating the instrumentation box onto a frame, we eliminate the thermal disturbance that would result from the box sitting on the ice surface, due both to the insulating effect of the box itself and also the accumulation of wind-blown snow. The snow cover is generally very thin in open sections of wind-swept McMurdo Sound.

Our thermal arrays have been designed with the aim that the measured temperature profile is as close as possible to the temperature profile that would exist in the ice if the array were not there. Not only must the individual temperature measurements be accurate, but the perturbation to the local heat flow, both laterally and vertically, must be minimised. This has resulted in several departures from industry-standard design.

3.1.1 Array Construction

Figure (3.2) shows the inner thermistor string, thin-walled stainless steel tube and connector that comprised the body of the thermal array. Twenty thermistors were positioned in small notches 10 cm apart down a 3 mm diameter teflon 'spaghetti'. Enameled high-resistance constantan wire was used for all connections inside the array. This minimised the thermal conductance between the thermistors and surface. The measurement circuitry is shown in figure (3.4) and discussed fully below; for now we concentrate on the construction and physical properties of the array. A full wiring diagram is shown in Appendix A.

Physical protection for the wiring and connections was provided by heat shrink around the teflon spine. Small notches were cut in the heat shrink around the thermistors to enable good thermal contact between the thermistors, standing proud from the teflon spine, and the stainless steel tube. The constantan wires were soldered into a military-specification waterproof connector, and the heat shrink-stiffened thermistor string was slid into the tube. The fit was snug.

The small volume left inside the tube was in-filled with sunflower oil, which pours readily at room temperature but freezes to a viscous gel at our measurement temperatures. This maximises the thermal contact of the thermistors with the tube by eliminating air space, and eliminates air-cell convection within the tube. With the tube held in a vertical position ,and the top connector not attached, an O-ring sealed set screw at the bottom of the tube was

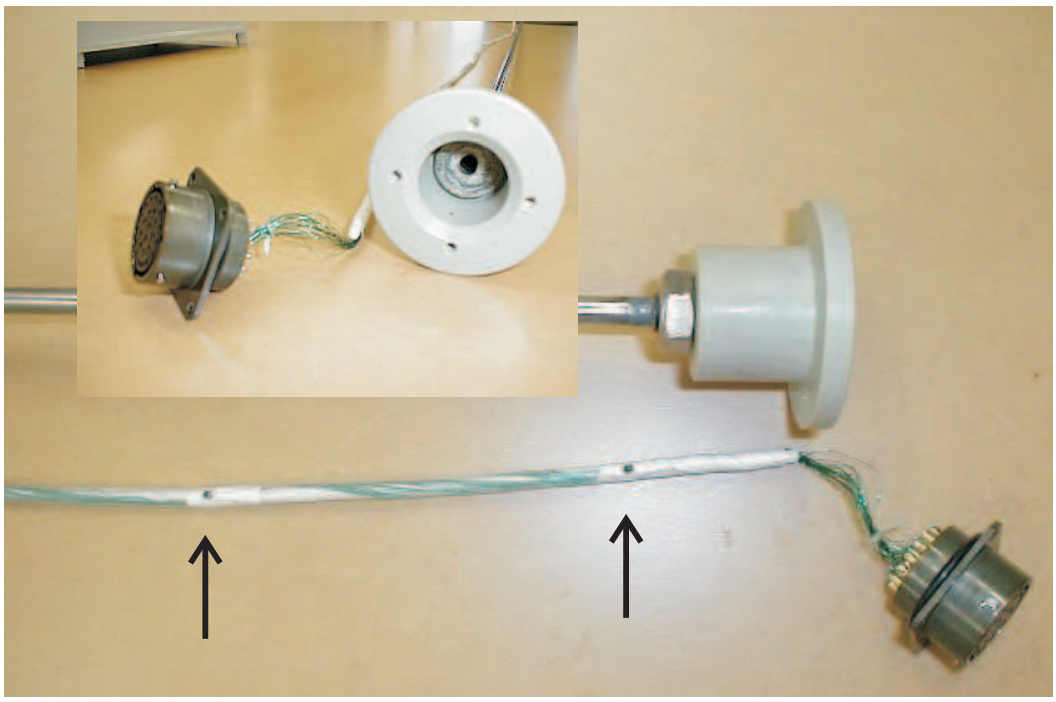

Figure 3.2: Detail of a thermal array later installed in FY sea ice Antarctica, 2002. This array has clear heat shrink tubing through which the green, enamelled constantan, wiring can be seen, wound around the white teflon rod. Arrows point out two thermistor beads.

opened and sunflower oil gravity-fed into the tube from the bottom up over approximately 12 hours. This prevented air bubbles being trapped in the tube. When the tube was completely filled, the bottom screw was replaced and the O-ring sealed top connector attached. This displaced a small amount of oil, ensuring that no air was trapped in the top of the tube.

Using a stainless steel tube has allowed us to make a considerably narrower array than standard arrays which are typically durable plastics, eg. polycarbonate-polyethylene [eg. *Frey et al.*, 2001]. Our cross sectional area is $\sim 0.4\,\mathrm{cm}^2$ compared with $\sim 4\,\mathrm{cm}^2$ for other designs. To minimise the perturbation to local heat flow, the thermal conductance of the array must be well-matched to the thermal conductance of the ice that it displaces. Although the thermal conductivity of stainless steel is higher than ice, the figure of merit is the thermal conductance per unit length of the enitre array. For parallel heat flow up the tube, teflon spine, wiring and grease, this is calculated by summing the

conductivity-area products kA for each component. Stainless steel is an alloy with a thermal conductivity lower than pure metals. For 316 stainless steel $k(-10\,^{\circ}\mathrm{C}) \approx 14.8 \pm 0.1\,\mathrm{W/m\,^{\circ}C}$ [*Atlas*, 2003], only about factor of 6 more than ice. Table (3.1) summarises the areas, and conductivities in the calculation of the thermal conductance per unit length of the array.

Material	k [W/m °C]	A [mm^2]	kA [μWm/ °C]
Teflon + heat-shrink[a]	0.2	12.6	2.51
Sunflower Oil gel[b]	0.18	16.2	2.91
Constantan Wiring[c]	22	0.38	8.81
(i)SS Tube measured[d]			30.8 ± 1.6
(ii)316 Stainless steel[e]	14.8 ± 0.1	2.53	37.4 ± 0.8
(i)kA_{array} (k_{SS} meas)	$46 \pm 3\,\mu$Wm/ °C		
$d_{eq,\,ice}$	5.1 ± 0.3mm		
(ii)kA'_{array} (k_{SS} specs)	$53 \pm 3\,\mu$Wm/ °C		
$d_{eq,\,ice}$	5.5 ± 0.2mm		

Table 3.1: Conductivity and areas of components in thermal array tube.[a] Heat shrink given same value as Teflon (PTFE). [b] Value for Vaseline [*Weast*, 1971]. [c] Area is for 26 wires, 0.15mm diameter. [d] Measured, see text. [e] Manufacturers specifications, [*Atlas*, 2003].

Values for the thermal conductivity of heated heat-shrink and sunflower oil could not be found. As the values of most plastics vary by less than a factor of 2, we have used the teflon value also for the heat shrink. Similarly, electrically insulating gels show only a week variation in thermal conductivity, so for the congealed sunflower oil, we have used the value for the similarly viscous Vaseline. As justification of these choices, we note that the total contribution to the kA_{array} is at the level of the uncertainty, see table (3.1). We give two values for the thermal conductance per unit length of the stainless steel tube in table (3.1). The first derives form an indirect measurement of the thermal conductance of identical stainless steel tubes. In metals the thermal conductivity k and electrical resistivity ρ are related by the Weidemann-Franz Law, according to which $k = L_0 T/\rho$ where $L_0 = 2.45 \times 10^{-8}\mathrm{W}\Omega/\mathrm{K}^2$ is the Lorenz number [*Ashcroft and Mermin*, 1976]. We measured the average electrical resistance of two 2 m lengths to be $R = 0.48 \pm 0.01\Omega$, giving $kA_{SS} = L_0 T L/R = 30.8 \pm 1.6\,\mu$Wm/ °C. From the two estimates of kA_{array} in

table (3.1), and using $k_{si} = 2.2\,\mathrm{W/m\,^\circ C}$, the 6.35 mm diameter array therefore has the thermal conductance per unit length of an ice cylinder with diameter $d_{\mathrm{eq,\,ice}} = 5.1 \pm 0.3\,\mathrm{mm}$, and $d'_{\mathrm{eq,\,ice}} = 5.5 \pm 0.2\,\mathrm{mm}$ respectively. This results may seem surprising; despite the stainless steel outer, the array as a whole has a thermal conductance per unit length about 30% less than the ice it replaces.

Estimating the thermal perturbation in the heat flow near the array due to this slight mismatch is difficult to determine. *Trodahl et al.* [2000] provides one estimate by assuming unperturbed temperature variations at a radius which is intermediate between the radius of the probe and the depth of the ice. For the ice-equivalent thermal diameter of the array calculated above, and for thermal driving of period $\sim$ 1 week, the perturbation to the amplitude of temperature variations at the probe radius is of the order of 10^{-4}. This asymptotic solution does not apply very close to the top of the array though. The relevant boundary conditions are harmonic driving in the $z = 0$ plane, and a conductance mismatch between ice and array in the radial direction. For such a cylindrical geometry, we have been unable to find an analytical solution in the heat conduction literature, and were unsuccessful in finding an analytical solution ourself. A separation of variables approach is stymied as the boundary conditions cannot be separated. A numerical approach is considered necessary (Mark McGuinness, personal communication, 2004 [1]).

Ideally the temperature of each thermistor is the same as the ice at that depth. This assumes not only no thermal disturbance due to the array but also negligible thermal resistance between the thermistor and adjacent ice. The spacing between a thermistor and the inner stainless steel wall is not precisely known on account of the string being slid into the tube. However the fit is tight, indicating probable contact between the protruding thermistors and the inside wall. A conservative (over-) estimate of the thermistor to tube distance, or the thickness of sunflower grease between them is $\delta z \sim 0.5\,\mathrm{mm}$. For $k_{\mathrm{grease}} \approx 0.2\,\mathrm{W/m\,^\circ C}$ this corresponds to a maximum thermal conductance of $K \approx 0.2\,\mathrm{mW/\,^\circ C}$. The thermal resistance of the 0.1 mm thick stainless steel tube in series with the grease can be neglected here. The conductance of the wires connected to the thermistor up the array can be estimated from the Weidemann-Franz law, according to which $K = L_0 T/R$, where T [K] is absolute temperature and $L_0 = 2.45 \times 10^{-8}\mathrm{W/K^2}$ is the 'Lorenz number'. [2]

[1] After finding an explanation for the near surface conductivity reduction resolved by the present and previous array measurements, in the finite difference analysis, this question was not pursued any further.

[2] The Weidemann-Franz law is usually expressed in terms of the electrical conductivity, σ_e as $k/\sigma_e T = L_0$. A quantum mechanical treatment of electron transport predicts $L_0 =$

For two 1 m lengths of constantan wire, of resistance $R = 17\,\Omega$ at $-10\,^{\circ}\mathrm{C}$, the thermal conductance is $K' = 0.4\,\mu\mathrm{W/m\,^{\circ}C}$, approximately three orders of magnitude smaller than the lateral conductance to the ice. The temperature difference to a depth of 1m down the array is about $5 - 10\,^{\circ}\mathrm{C}$. From the ratio of vertical to lateral conductance, $K/K' \sim 1000$ the maximum estimated temperature difference between the thermistor and adjacent ice is $\sim 5 - 10 \times 10^{-3}\,^{\circ}\mathrm{C}$, comparable to the noise level of our measurements.

3.1.2 Thermistors

We used high-resistance, negative temperature coefficient YSI 55031 thermistors. Thermistors are preferable in our measurement because their large temperature coefficient allows better temperature resolution than thermocouples would. Their higher electrical resistance also makes lead resistance less problematic, which is particularly important as we used high-resistance wiring to minimise thermal conduction from the surface to the thermistors. The 2 mm diameter glass-enclosed thermistors have a fast thermal response, and low self-heating so there is little dissipation of heat to interfere with the measurement.

The temperature rise of the thermistor due to the measurement current is called self heating. The dissipated power given by $P = V_t^2/R$,where V_t is the voltage drop over the thermistor and R its resistance. Typical values of $V_t = \frac{1}{2}V_0 = 0.125\,V$, and $R = 50\,\mathrm{k}\Omega$ give $P = 0.3\,\mu\mathrm{W}$. Taking the thermistor to be a 2.4 mm diameter glass bead, the heat capacity is approximately $mc = 0.01\,\mathrm{J/\,^{\circ}C}$. If all of the dissipated power goes into heating the thermistor, the maximum temperature rise is $\Delta T = P\delta t/mc \approx 4\mu\,^{\circ}\mathrm{C}\,\delta t$, where δt is the time in seconds for which this power is dissipated. In each measurement, current flows through each thermistor current for only 10 ms in each of the 20 reverse polarity measurements, so neglecting cooling between measurements, the maximum temperature increase is of the order of 10^{-5} °C. Self heating is entirely negligible.

Conversion from resistance to temperature was performed by fitting a calibration curve to resistance/temperature data supplied by the thermistor manufacturer. We used a Steinhart-Hart fit of the form [*Steinhart and Hart*, 1968; *Sapoff*, 1999]:

$$1/T = A + Bln(R) + C(ln(R))^3 \quad . \tag{3.1}$$

$\pi^2k^2/3e^2 = 2.45 \times 10^{-8}\mathrm{W/K^2}$, where e is the electronic charge. For most metals this is accurate to within ±10% between 0 - 100 °C [*Kittel*, 1976].

This functional form is empirical. The quadratic ln(R) term has been dropped only because including it was originally not found to improve the accuracy of the fit [*Sapoff*, 1999]. We found that including the quadratic term compounded computational errors resulting in a less accurate temperature inversion. The manufacturers' data and our calibration curve are shown in figure (3.3) over the temperature range $-50\,^{\circ}\mathrm{C} - +5\,^{\circ}\mathrm{C}$. This exceeds our range of interest to eliminate end-effects in the fitting. Converting to degrees Celsius, $T[\,^{\circ}\mathrm{C}]$ this fit is:

$$T = 1 \times 10^6/(0.15714(ln(R))^3 + 238.93\,ln(R) + 1030.72) - 273.15 \quad . \quad (3.2)$$

This was used for all of our measurements with YSI 55031 thermistors. Over the range $-40\,^{\circ}\mathrm{C} - 0\,^{\circ}\mathrm{C}$, the standard deviation between the data and curve is $0.002\,^{\circ}\mathrm{C}$ Furthermore, as we are interested in evaluated small differences in temperatures, or temperature-dependent properties, it is the even smaller variation in the fit over small temperature intervals that is important.

For small temperature ranges, the thermistor response is well described by the simpler expression

$$R = R_0 exp\left(\frac{\beta}{T}\right) \quad , \quad (3.3)$$

where T is absolute temperature [K], and R_0 and β are fitted parameters. We stress that equation (3.1) has always been used for resistance-to-temperature conversions. Equation (3.3) simplifies the mathematics when assessing thermistor characteristics below.

Thermistor manufacturers typically quote a 'tolerance' in the expected fractional variation in resistance between individual thermistors in a batch. For YSI 55031 thermistors it is $0.75 - 0.5\%$ from -20 to $0\,^{\circ}\mathrm{C}$. When converted directly to temperature, this equates to an 'interchangeability' of approximately $\pm 0.1\,^{\circ}\mathrm{C}$. The usual approach is to perform a 'one-point calibration' by measuring the resistance at a common temperature and then apply a constant temperature offset to each thermistor. This is justified only if the temperature offset between individual thermistors remains constant. The difference between individual thermistors is listed by the manufacturers as a multiplicative factor in R. With respect to equation (3.3) it is most likely that fractional variations in resistance originate in the shape factor R_0, rather than in β which represents an intrinsic property of the thermistor bead material. Writing $R_0 = R_0(1+\epsilon)$ where $\epsilon \lesssim 1\%$ and solving equation (3.3) for T to first order in ϵ gives:

$$T = \frac{\beta}{ln\left(\frac{R}{R_0}\right)}\left(1 + \frac{\epsilon}{ln\left(\frac{R}{R_0}\right)}\right) \quad . \quad (3.4)$$

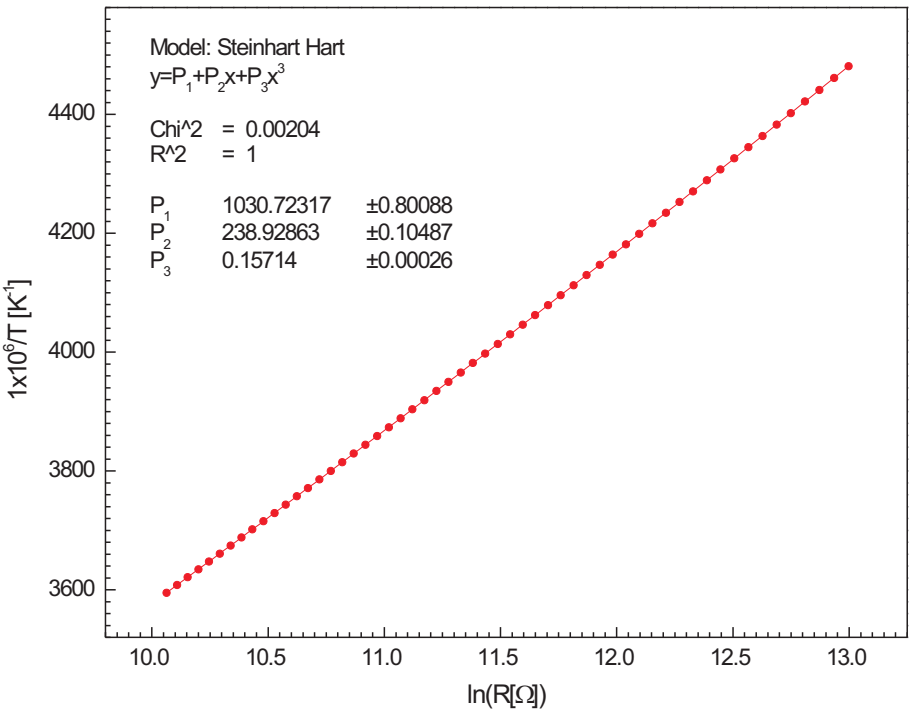

Figure 3.3: Calibration curve for YSI 55031 thermistors. Points from product specifications, and line from Steinhart-Hart fit listed.

Between $-5\,^{\circ}\mathrm{C}$ and $-25\,^{\circ}\mathrm{C}$ and for $\epsilon = 0.75\%$ this gives temperature offsets vary between $0.16\,^{\circ}\mathrm{C}$ and $0.14\,^{\circ}\mathrm{C}$. This shows that the approximation of a constant temperature offset, and therefore the accuracy of a one-point calibration, is good to about $\pm 0.01\,^{\circ}\mathrm{C}$ over this temperature range.

We have not performed such one-point calibrations for our arrays. Because we examine temperature *differences*, our analysis naturally accommodates constant temperature offsets between individual thermistors, so performing such a 'one point calibration' would not alter our analysis or results [*Trodahl et al.*, 2000; *Pringle et al.*, 2003]. An accurate full temperature range calibration of individual thermistors is cost prohibitive for the number of thermistors involved in this study. In some of our sea ice measurements, we have performed a one-point calibration of the thermistors initially below the ice/water interface by assuming an isothermal water column. These thermistors were not used in

conductivity calculations, and these calibrations used only in our discussion of water temperature variations, see Chapter 5.

3.1.3 Measurement Circuitry

Figure (3.4) shows a simplified representation of the bridge circuit for each thermistor, and a schematic diagram of the array wiring when connected to a Campbell Scientific CR10X data logger, and AM16/32 multiplexor (timing wiring not shown). As well as the 20 thermistors, we also measured two low-temperature coefficient, precision 'standard resistors', in order to monitor the logger performance. These standard resistors were chosen to approximately span the range of resistance values the thermistors take, $33\,\mathrm{k}\Omega \sim -2\,^{\circ}\mathrm{C}$ and $67\,\mathrm{k}\Omega \sim -17\,^{\circ}\mathrm{C}$. These resistors were positioned approximately 2 cm from the end of the array, as this provides the quietest temperature environment. The intrinsic measurement noise and temperature resolution/discretisation were established from the variations in the equivalent temperature of these resistors.

The entire array was read by sequentially selecting each thermistor, and exciting the voltage divider circuit shown schematically in figure 3.4(a). Further details for the CR10X and custom built loggers are discussed below.

Accounting for the lead resistance, R_L, the resistance of each thermistor using the CR10X circuit in figure 3.4(b) is

$$R = (R_{ref} + R_L)\left(\frac{V_0}{\overline{V}_m} - 1\right) - R_L \quad . \tag{3.5}$$

This measurement will have an uncertainty arising from noise in the excitation voltage V_0 and measurement uncertainty in V_m.

We have optimised R_{ref} to minimise the final uncertainty in δT averaged over the measured temperature range, due to the uncertainty in measuring R. Details are presented in Appendix A. The result is

$${R_{ref}}^* = \left(\frac{{R_2}^2 - {R_1}^2}{2ln(R_2/R_1)}\right)^{1/2} \quad . \tag{3.6}$$

For $R_1 = 30\,\mathrm{k}\Omega$ and $R_2 = 80\,\mathrm{k}\Omega$, ${R_{ref}}^* = 52\,\mathrm{k}\Omega$. We used high-precision, low-temperature coefficient resistors with nominal values ${R_{ref}}^* = 52.3\,k\Omega$. For all such resistors in our arrays we made direct measurements of the resistance.

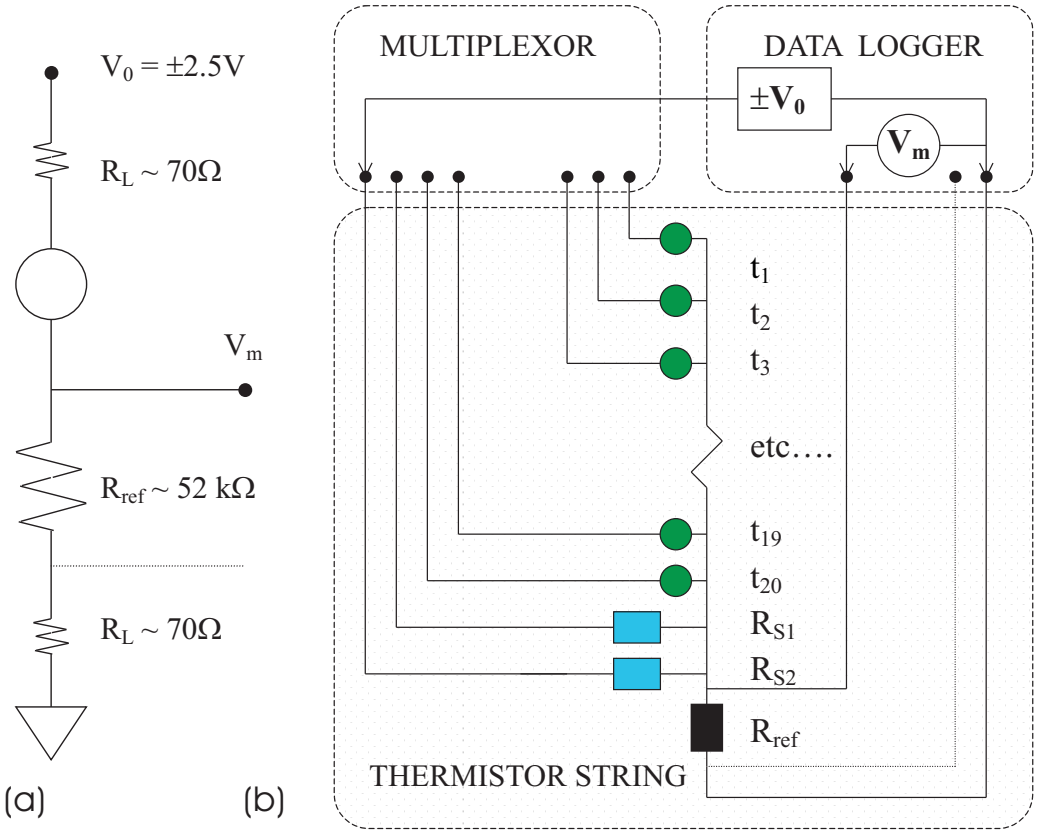

Figure 3.4: Schematic diagram of measurement circuit for thermal arrays: (a) bridge circuit for each measurement; (b) schematic diagram of wiring inside tube, and connections with multiplexor and data-logger. The same length of wire was used in each thermistor circuit from multiplexor back to data logger. The large dashed box in (b) shows the components inside the array tubes: the reference and standard resistors R_{ref}, R_{S1}, R_{S1}, and thermsitors t1 ... t20. Thin dotted line below R_{ref} in both figures is the separate signal ground, used with our custom built loggers.

3.2 Data Loggers

In our experiments we used two different measurement systems. (i) commercial Campbell Scientific Instruments CR10X data logger and CSI AM16/32 multiplexor; (ii) custom-built units including logger and relay-switching multiplexor.

3.2.1 Campbell CR10X Loggers

Campbell CR10X data loggers are industry standard devices for remote logging applications. In the experiments in Alaska (2000/01, 2003), and in MY ice in Antarctica (2003) we used an CR10X with 2 Mb of internal memory and extended temperature testing (rated to -55 °C). Data was stored on board and also output to a SM4M (4Mb) storage module for easy on-site data retrieval. Our CR10X program and pin-out/connections for the array, logger and multiplexor are included in Appendix A.

The RC time constant of our thermistor measurement circuit was measured to be $\tau \approx 0.15$ ms. To allow for capacitive delays in establishing the excitation voltage, measurements were made with an 'excite, delay, measure' procedure with a delay time of 10 ms. To eliminate the effect of thermo-electric voltages reverse polarity measurements were made using $V_0 = \pm 2.5$ V. The average absolute value of 10 forward and 10 reverse measurements for each sensor, $\overline{V}_m$, was output to final storage in the data logger.

The CR10X manual gives the resolution of single ended voltage measurements as $\delta V_m/V_0 = 1/3750$ [*Campbell Scientific, Inc.*, 2001] . For $V_0 = 2.5\,V$ this gives $\delta V_m \approx 0.66$ mV, and a temperature resolution of $\delta T \approx 0.02\,^{\circ}$C. By averaging over 20 reverse polarity measurements we have reduced the temperature discretisation to $\delta T \approx 0.001\,^{\circ}$C, and the random measurement noise to $\sigma_T \approx 0.005\,^{\circ}$C. See Chapter 5.

3.2.2 Custom Built Loggers

To exceed the resolution of the CR10X loggers, custom built data loggers were designed and built by electronics technician Rod Brown of the School of Chemical and Physical Science at Victoria University of Wellington. We refer to these loggers hereafter as 'RB' loggers. These loggers were superior to the CR10X loggers both in terms of lower measurement noise, and, by virtue of a 17-bit ADC, better resolution.

The RB loggers performed a bridge measurement similar to the CR10X loggers. Reverse polarity measurements were made with an excitation voltage $V_0 = \pm 512\,$mV which, in contrast to the CR10X loggers, was *measured* for each excitation. The logger averaged 20 measurements (10 of each polarity) of the fractional voltage drop over the reference resistor, V_m, and wrote the average value of $\eta = (V_m/V_0)$ to on-board flash memory. These loggers could be

downloaded to a laptop running custom software via a serial port interface.

The voltage drop over the reference resistor was measured with a separate 'measurement ground' line so neither measurement lead was current-carrying and the measurement not at all sensitive to lead resistance. Data were processed accordingly. The separate measurement ground is shown in figures 3.4(a,b) as an unconnected dashed line. All thermal arrays were built with this line so they could be used interchangeably with the two logging systems, and it was left unconnected in the CR10X configuration.

In our sea ice arrays read by RB loggers, we measured a temperature discretisation of $\delta T \approx 3 \times 10^{-5}\,^{\circ}\mathrm{C}$, and the random measurement noise to $\sigma_T \approx 0.0012\,^{\circ}\mathrm{C}$. The RB loggers have achieved a factor of 30 improvement in resolution and factor of 4 improvement in noise. This has improved the accuracy of our thermal conductivity analysis and extended the depth into the ice that we can calculate the conductivity before the analysis becomes noise-limited.

3.3 Site Assembly and Installation

The array sites were installed in Alaska by the author and colleagues from University of Alaska Fairbanks, and in Antarctica by scientific support staff from New Zealand's Scott Base. In the latter case they could only be installed once FY ice had grown to thickness considered safe for ice travel, usually greater 1 m.

For FY ice, the smallest available augur (5 cm diameter), was used to drill through the ice thickness to the sea below. The thermistor string was connected to the quite rigid cable leading to the data logger box, and in this way held in a vertical position while the water which had reflooded the hole refroze. One or two days after installation, the freeboard ($\sim 10\,\mathrm{cm}$) was filled with water to create a level ice surface. The ice which refreezes in the hole encasing the thermistor string freezes faster than the ice that was removed so will have a higher salinity than the surrounding ice [eg. *Weeks and Ackley*, 1986; *Eicken*, 2003]. In our one Antarctic MY site, a 2 m hole was drilled into the 4 m thick ice, and the array positioned vertically as above. The hole was then refrozen with low salinity water so that the resulting ice around the array would more closely resemble the surrounding low salinity ice.

3.4 Experimental Uncertainty in Δz, Δt

The experimental uncertainty in the measurement interval Δt is established by the accuracy of the data logger clocks, and we neglect it entirely. Both the exact positioning of the thermistors, and any overall tilt of the array, introduce an uncertainty in the vertical spacing Δz. From the finite thickness of the thermistor bead and the array construction, we estimate the uncertainty in individual thermistors to be $\pm 0.25\,\mathrm{mm}$, and a separation uncertainty of $\pm 0.5\,\mathrm{mm}$. For an array tilt of θ degrees, the error in the vertical separation between thermistor pairs is $(1-cos\theta)\Delta z$; a 2.5° tilt giving an error of $-0.1\,\mathrm{mm}$. The conductivity (or diffusivity) will be underestimated if adjacent spacings are both too large, and underestimated if they are both too small. If the errors are of the opposite sense then the curvature estimate varies, being too small or too large, depending on the value of the curvature. Numerical propagation of these uncertainties through the full analysis show that for the *worst case scenario* of adjacent errors with opposite sign, $\pm 0.5\,\mathrm{mm}$ and $\mp 0.5\,\mathrm{mm}$, the final uncertainty in the geometric mean slope is $\pm 3\%$. We consider a $\pm 1\%$ to be a reasonable estimate of this effect.

Chapter 4

Analysis of Temperature Array Data

In this chapter we present details of the finite difference time-series analysis used to extract the thermal conductivity from measured sea ice temperatures, and the thermal diffusivity from measured permafrost temperatures. We start the chapter with an overview of thermal properties and conductive heat flow. This establishes the basis and conditions for applying this method. Implementation details are discussed, and we then assess the expected performance of this method using an analytical approach, and by processing simulated temperature fields.

4.1 Conductive Heat Flow in Sea Ice

The three fundamental thermal parameters are the thermal conductivity k, specific heat c, and density ρ. The thermal diffusivity (sometimes referred to as thermometric conductivity) is defined in terms of the previous parameters as $D = k/\rho c$. The thermal conductivity k [W/m °C] is defined by Fourier's equation as the proportionality constant between a conductive heat flux, $\mathbf{J_Q}$ [W/m^2] and the temperature gradient driving that heat flow:

$$\mathbf{J_Q} = -k\nabla T \quad . \tag{4.1}$$

Any heat flow for which the heat flux is proportional to the temperature gradient, is termed 'linear'. In addition to conduction there is the possibility of a

convective contribution to the linear heat flow in sea ice. What our measurements resolve is the effective linear heat flow coefficient. In the bulk of the ice we expect this to equal the conductivity, but near the ice/water interface *Collins* [1998] and *McGuinness et al.* [1998] claim to have identified signatures of convective transport the ice/water interface where the brine volume is large. Thermal conductance, K [W/ °C] is the extensive variable relating (in the scalar case) heat flow Q [W] along a temperature difference ΔT.

$$K = \frac{Q}{\mid \Delta T \mid} \quad . \tag{4.2}$$

The specific heat c [J/g °C] is defined as the heat δQ required to induce a temperature change δT per unit mass of a material,

$$c = \frac{\delta Q}{\delta T} \quad . \tag{4.3}$$

Equivalently, it parameterises the storage of internal energy per unit temperature increase,

$$c\rho = \frac{d\mathcal{U}_V}{dT} \quad , \tag{4.4}$$

where $\mathcal{U}_V$ [J/m^3] is the internal energy density of the material, and ρ is the density. The product ρc [J/m^3 °C] is the volumetric heat capacity.

The rate of change of internal energy density, is given by the negative divergence of the heat flux, $-\nabla \cdot \mathbf{J_Q}$, plus any contribution from heat sinks or sources, $\dot{Q}_S$ [W/m^3],

$$\frac{d\mathcal{U}_V}{dt} = -\nabla \cdot \mathbf{J_Q} + \dot{Q}_S \quad . \tag{4.5}$$

Putting equations (4.1, 4.4) into equation (4.5) gives the general heat equation

$$\rho c \frac{\partial T}{\partial t} = \nabla k \cdot \nabla T + k \nabla^2 T + \dot{Q}_S \quad . \tag{4.6}$$

For a medium with constant and uniform conductivity ($\nabla k = 0$) with no heat generation ($\dot{Q}_S = 0$), the heat equation takes the simplified form,

$$\frac{\partial T}{\partial t} = D \nabla^2 T \quad , \tag{4.7}$$

where $D = k/\rho c$ [m^2/s] is the thermal diffusivity. The thermal diffusivity is therefore associated with the propagation of temperature variations through a medium whereas the thermal conductivity is associated with the conductive heat flux.

Analytical solutions to equation (4.7) that allow D to be resolved from temperature records exist only for certain boundary conditions. Because we make use of it in simulations below, we briefly discuss the solution for a uniform semi-infinite half-space ($z > 0$), where D is constant and uniform. For harmonic surface temperature $T(0,t) = T_0 e^{i\omega t}$, the solution is

$$T(z,t) = T_0 e^{-z/d} e^{i(z/d - \omega t)} \quad . \tag{4.8}$$

Here $d = (2D/\omega)^{1/2}$ is the penetration depth for a harmonic wave of frequency ω. Complex notation is mathematical convenient here, but it is understood that the temperature is given by the real part of this expression,

$$T(z,t) = T_0 e^{-z/d} cos(z/d - \omega t) \quad . \tag{4.9}$$

As equation (4.7) is linear a general surface temperature can be represented as a Fourier integral over frequency components, which propagating according to equation (4.8). The diffusivity D can then be determined from the amplitude decay and/or phase shift of a given frequency component with depth. The assumption of constant and uniform thermal properties cannot be made in our case because the thermal diffusivity of sea ice is a strongly varying function of temperature in our measurement range, so such Fourier methods are inappropriate. To accommodate this we recast equation (4.6) in terms of conservation of energy [*Trodahl et al.*, 2000],

$$\rho \frac{\partial U}{\partial t} = -\nabla \cdot \mathbf{J_Q} = k \nabla^2 T \quad . \tag{4.10}$$

Here U [J/g] is the temperature-dependent internal energy per unit mass of sea ice. The left hand side of this equation accommodates a temperature-dependent heat capacity $c(T) = \partial U/\partial T$ but the right hand side still assumes $\nabla k = 0$. As the vertical thermal gradients far exceed the lateral ones, we assume one-dimensional heat flow, giving

$$\rho \frac{\partial U}{\partial t} = k \frac{\partial^2 T}{\partial z^2} \quad . \tag{4.11}$$

Within an additive constant, which is unimportant as we are interested only in variations, U is given by integrating Ono's result for the heat capacity for sea ice (equation (2.18)) giving

$$U = (2.113 - 0.033S)T + (0.00375 + 0.0004S)T^2 - 18.04S/T^2 \quad . \tag{4.12}$$

Here S is salinity [$^0/_{00}$] and T is Celcius temperature [°C].

4.2 Overview of Graphical Finite Difference Analysis

We have determined the thermal conductivity from our sea ice temperature measurements by estimating the derivatives in equation (4.11) and calculating k as the gradient of a scatter plot of $\rho\partial U/\partial t$ vs. $\partial^2 T/\partial z^2$. Without an internal energy relation for the permafrost, we instead calculate the diffusivity from plots of $\partial T/\partial t$ vs. $\partial^2 T/\partial z^2$. We now present full details of this method. In Chapter 7 we also discuss some other time series methods which have been applied to ground temperature measurements and apply them to our Antarctic permafrost temperature data.

We approximate the derivatives in equation (4.11) by centered finite differences between measurements at adjacent depths and times,

$$\frac{\partial U(z,t)}{\partial t} = \frac{U(z,t+\Delta t) - U(z,t-\Delta t)}{2\Delta t} \tag{4.13}$$

$$\frac{\partial^2 T(z,t)}{\partial z^2} = \frac{T(z+\Delta z,t) - 2T(z,t) + T(z-\Delta z,t)}{\Delta z^2} \quad . \tag{4.14}$$

For the permafrost we calculate $\partial dT/\partial t$ as:

$$\frac{\partial T(z,t)}{\partial t} = \frac{T(z,t+\Delta t) - T(z,t-\Delta t)}{2\Delta t} \quad . \tag{4.15}$$

By determining the conductivity (or diffusivity) as the best-fit slope of scatter plots of $\rho\partial U/\partial t$ (or $\partial T/\partial t$) vs. $\partial^2 T/\partial z^2$, we avoid known short-comings of previous finite difference methods, in which the diffusivity has been calculated as a time average of point-by-point values of the ratio $\partial T/\partial t$ to $\partial^2 T/\partial z^2$ [eg. *Zhang and Osterkamp*, 1995; *Westin and Zuidhoff*, 2001]. Our approach is insensitive to thermistor-to-thermistor calibration offsets which, among other problems, render such methods unreliable [*Hinkel*, 1997; *Fuhrer*, 2000; *Pringle et al.*, 2003].

Our method assumes only that the thermal conductivity (diffusivity) varies little over the vertical separation between the three thermistors used to estimate the temperature curvature. It provides a robust resolution of the *average apparent* conductivity (diffusivity) in each three-thermistor interval ($2\Delta z$) and for the time interval for which data are included in the analysis. By repeating this procedure for each thermistor, a depth-dependent apparent conductivity profile $k(z)$ (or diffusivity profile $D(z)$) can be constructed [*Trodahl et al.*, 2000; *Pringle et al.*, 2003]. Figure (4.1) shows an example scatter-graph and best-fit line from sea ice data recorded at McMurdo Sound, Antarctica 2002.

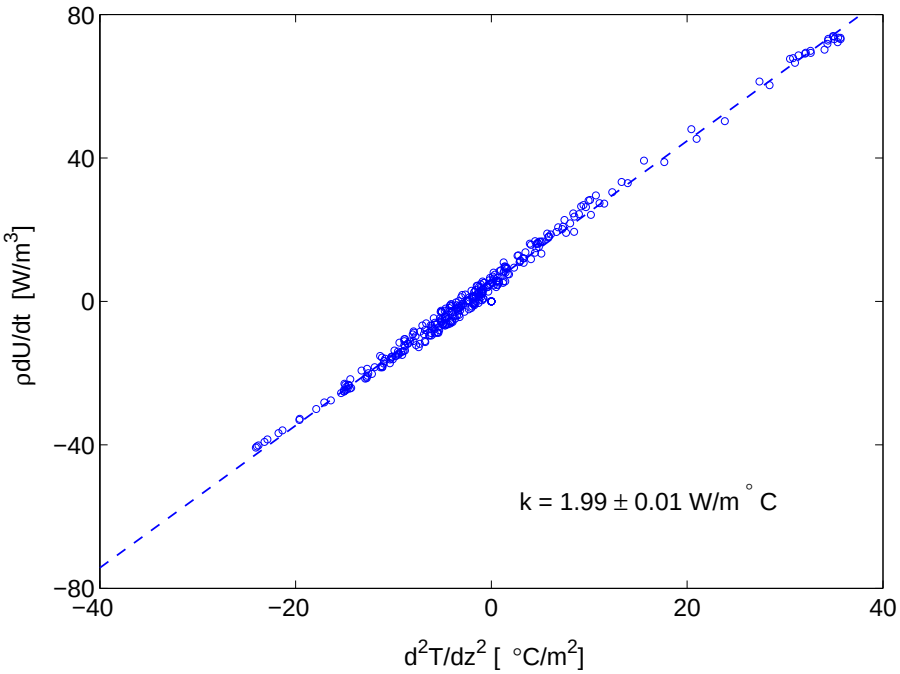

Figure 4.1: Example of a finite difference scatter plot. Data from FY, McMurdo Sound sea ice Antarctica, 2002, at a depth of 40 cm. The dashed line is the geometric-mean least squares fit, see section (4.3), and the slope is $1.99 \pm 0.01\,\mathrm{W/m\,^{\circ}C}$.

We now present a detailed analysis of two aspects of our finite difference analysis. These effects establish the limitations of the method and under what conditions extra care must be exercised in applying it. They also explain two signatures seen in the experimental conductivity profiles. These are both related to the finite difference estimates of the plotted variables. first aspect is the effect of measurement noise, and the second is the effect of the finite sampling intervals Δt and Δz.

4.3 Effect of Measurement Noise

Linear regression in the presence of random errors in the variable treated as independent leads to a slope which is underestimated by the factor that depends on the 'relative error' in that variable [*Fuller*, 1987]. In our case we have errors associated with both plotting variables deriving from the temper-

ature measurements. Considering our sea ice measurements, the least squares slope m_1 from a regression of $\rho\partial U/\partial t$ against $\partial^2 T/\partial z^2$ will underestimate the value of the thermal conductivity k. Similarly, the slope m_2 determined from a regression of $\partial^2 T/\partial z^2$ against $\rho\partial U/\partial t$ will underestimate the value of k^{-1}.

We show in Appendix B that the geometric mean of these two k estimates, $m_{gm} = (m_1 m_2^{-1})^{1/2}$ is biased by the difference in the relative errors in the two variables. We show this is true for the two cases in which the plotted variables are distributed as (i) a gaussian distribution with superimposed, normally distributed noise, and (ii) a uniform distribution. In both cases the geometric mean least-squares estimate of the gradient is

$$m_{gm} = \beta_1 \left(\frac{1+\delta_Y}{1+\delta_X} \right)^{1/2} \quad , \tag{4.16}$$

$$\approx \beta_1 \left(1 + \frac{1}{2}(\delta_Y - \delta_X) \right) \quad , \tag{4.17}$$

to first order in δ. Here δ_Y and δ_X measure the 'relative error' in the variables plotted on the Y and X axes. They measure the noise in the measured value compared with the range of measured values, and are defined for the two cases below.

A correlation coefficient $0 < r < 1$ can also be be determined from the two least squares gradients as $r = (m_1/m_2^{-1})^{1/2}$,

$$r = ((1+\delta_X)(1+\delta_Y))^{-1/2} \tag{4.18}$$

$$\approx 1 - \frac{1}{2}(\delta_X + \delta_Y) \quad . \tag{4.19}$$

For perfect correlation, $m_1 = m_2$ and $r = 1$. For $r \approx 1$ the sum $\delta_Y + \delta_X$ is small and therefore so is the difference $\delta_Y - \delta_X$, implying little difference between the two gradient estimates, and an accurate geometric-mean gradient estimate. However low r-value fits imply a large value of $\delta_Y + \delta_X$ in which case $\delta_Y - \delta_X$ may now be large, admitting the possibility of a large error in the slope estimate and these estimates must be treated with caution.

4.3.1 Gaussian Noise and Data Distribution

In this section we consider both plotted variables to be normally distributed, each with a normally distributed measurement noise. A full derivation of the results above, equations (4.16) and (4.18) are included in Appendix B. Take

the measured values of $\partial^2 T/\partial z^2$ to be normally distributed with a mean 0 and variance σ^2_{xx}. Here σ^2_{xx} characterises the distribution, or range of $\partial^2 T/\partial z^2$ values - it is in no way associated with any error or uncertainty. When $\partial^2 T/\partial z^2$ values from this distribution are measured they are corrupted with a normally distributed measurement noise with mean 0 and variance σ^2_{uu}. We define the relative error δ_X as,

$$\delta_X = \frac{\sigma^2_{uu}}{\sigma^2_{xx}} \quad . \tag{4.20}$$

Similarly for the Y axis variable we have,

$$\delta_Y = \frac{\sigma^2_{ee}}{\beta_1^2 \sigma^2_{xx}} \tag{4.21}$$

where σ^2_{ee} is the noise associated with the measurement of the Y variable, and $\beta_1^2\sigma^2_{xx}$ is the variance of the distribution of Y- values.

The plotted variables are calculated from the same temperature measurements. We now show how their relative errors (due to measurement noise) are related to the relative size of the sampling intervals Δt and Δz and the underlying measurement noise.

For the sea ice measurements we associate $Y \leftrightarrow \rho\partial U/\partial t$, $X \leftrightarrow \partial^2 T/\partial z^2$, and $\beta_1 \leftrightarrow k$, the thermal conductivity. If the errors in the temperature measurements have a gaussian distribution, mean 0, variance σ^2_T, then the propagation of measurement error leads to a variance in $\partial^2 T/\partial z^2$ values given by

$$\sigma^2_{T''} = \left(\frac{1}{(\Delta z)^2}\right)^2 \left(\sigma^2_T + (-2\sigma_T)^2 + \sigma^2_T\right) \quad , \tag{4.22}$$

$$\sigma^2_{T''} = \frac{6\,\sigma^2_T}{(\Delta z)^4} \quad . \tag{4.23}$$

This analysis assumes no correlation between the errors in $T(z_1, t)$ and $T(z_2, t)$, or between $T(z, t_1)$ and $T(z, t_2)$. In order to similarly calculate the errors in $\rho\partial U/dt$ (but not in the conductivity calculations) we make the assumption that the heat capacity varies little between successive measurements and write

$$\rho\frac{\partial U}{\partial t} = \rho\frac{U(z, t+\Delta t) - U(z, t-\Delta t)}{2\Delta t} \tag{4.24}$$

$$= \rho c(\overline{T})\frac{T(z, t+\Delta t) - T(z, t-\Delta t)}{2\Delta t} \quad . \tag{4.25}$$

In this case we get,

$$\sigma^2_{\rho\dot{U}} = \left(\frac{\rho c}{2\Delta t}\right)^2 \left(\sigma_T^2 + (-\sigma_T)^2\right) \quad , \tag{4.26}$$

$$\sigma^2_{\rho\dot{U}} = \frac{(\rho c(T))^2 \sigma_T^2}{2(\Delta t)^2} \quad . \tag{4.27}$$

The terms $\sigma^2_{\rho\dot{U}}$ and $\sigma^2_{T''}$ correspond to σ^2_{ee} and σ^2_{uu} respectively so that the ratio of relative errors $\delta_Y/\delta_X = \sigma^2_{ee}/\beta_1^2\sigma^2_{uu}$ is given by,

$$\frac{\delta_Y}{\delta_X} = \frac{(\rho c)^2(\Delta z)^4}{12\,k^2(\Delta t)^2} = \frac{(\Delta z)^4}{12\,D^2(\Delta t)^2} \quad . \tag{4.28}$$

From equation (4.16), the geometric-mean slope is unbiased when $\delta_Y = \delta_X$, which is satisfied for

$$\frac{(\Delta z)^4}{12\,D^2(\Delta t)^2} = 1 \quad . \tag{4.29}$$

Note that this result only applies when the sole source of scatter in the plotted variables derives from a constant measurement noise σ_T. The value of $(\Delta z)^4/12\,D^2(\Delta t)^2$ for our four experimental cases using appropriate average diffusivity values are shown in Table (4.1).

Experiment	Δt [hr]	Δz [m]	D [10^{-6} m^2/s]	$\frac{(\Delta z)^4}{12D^2(\Delta t)^2}$
Sea Ice I [a]	1	0.1	1.15	0.5
Sea Ice II [b]	0.5	0.1	1.15	1.9
Table Mtn. I	4	0.135	1.5	0.1
2001-02			3.0	0.02
Table Mtn. II	1	0.135	1.5	1.0
2003			3.0	0.2

Table 4.1: Finite intervals for our different experiments. Ideally the last column should equal 1 (see text). The two D values for the Table Mountain cases span the range of experimentally resolved values. [a] Measurements in 1996, 1997, 1999 reported by *McGuinness et al.* [1998]; *Collins* [1998]; *Trodahl et al.* [2000, 2001]. [b] Measurements reported here.

All of these experiments were completed prior to the above analysis. The time intervals for the earliest sea ice measurements were chosen to give approximately the same resolution in depth and time [*McGuinness et al.*, 1998;

Trodahl et al., 2000]. The 1 hour interval was reduced to 30 minutes in the design of our custom built loggers. A 30 minute interval was also used for our Arctic sea ice measurements. The time interval of 4 hours for the 2001-02 Table Mountain measurements was dictated by limited data storage capacity over the Antarctic winter, during which no site servicing could be made. With increased storage capacity this interval was reduced to 1 hour for November 2002 - December 2003, see Chapter 7.

4.3.2 Uniform Measurement Noise and Data Spread

In Appendix B we also consider the case of a uniformly distributed scatter plot. In this case, the relative error is defined by $\delta_X = \sigma_x^2/\Delta_x^2$ where σ_x^2 is the width of the $\partial^2 T/\partial z^2$ distribution, and Δ_x^2 the range of the $\partial^2 T/\partial z^2$ values; and similarly for δ_Y. Figure (4.2) illustrates how these parameters are defined for the X axis variable: We show in Appendix B that with these

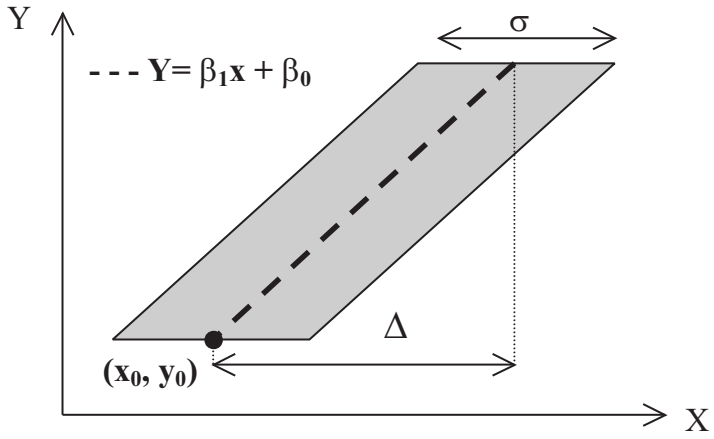

Figure 4.2: Definition of uniform distribution parameters for analysis of the effect of relative errors on least squares gradient fitting. There are errors only in the X values here.

definitions the geometric mean gradient has the same form as the gaussian case, equation (4.16). Whilst we don't expect our experimental noise to obey one of these specific distributions, this common result suggests that, to a good approximation, the geometric mean gradient of our experimental scatter plots will be biased by one half the difference in the relative errors.

4.4 Effect of Finite Sampling Intervals

As well as intrinsic measurement noise, scatter in these plots can also derive from systematic effects in the calculation of the finite difference estimates,

The accuracy of the finite difference estimates of the temperature derivatives, equations (4.13, 4.14, 4.15) depends on the sampling intervals Δz and Δt. Qualitatively, these estimates will be most accurate when Δz is small compared with the penetration depth d, and when Δt is small compared to $1/\omega$. In this section we present analytical results for the error in these finite difference estimates due to finite sampling intervals, for harmonic surface driving of a semi-infinite homogeneous medium. Our analytical results and output from simulations clearly demonstrate that the near-surface conductivity shows an apparent reduction in the presence of components for which $\omega\Delta t$ is large.

Using complex notation, harmonic surface driving is $T(0,t) = T_0 e^{i\omega t}$, and the solution to the infinite half space problem given by equation (4.8). Analytical expressions for $\partial T/\partial t$ and $\partial^2 T/\partial z^2$ are,

$$\frac{\partial T}{\partial t} = i\omega T_0 e^{-(1+i)z/d} e^{i\omega t} = i\omega T(z,t) \quad , \tag{4.30}$$

$$\frac{\partial^2 T}{\partial z^2} = \frac{2i}{d^2} T_0 e^{-(1+i)z/d} e^{i\omega t} = \frac{2i}{d^2} T(z,t) \quad . \tag{4.31}$$

The real parts of these expressions, giving the observable temperature and derivatives are,

$$T(z,t) = T_0 e^{-z/d} cos(\omega t - z/d) \quad , \tag{4.32}$$

$$\frac{\partial T}{\partial t} = -\omega T_0 e^{-z/d} sin(\omega t - z/d) \quad , \tag{4.33}$$

$$\frac{\partial^2 T}{\partial z^2} = \frac{-2}{d^2} T_0 e^{-z/d} sin(\omega t - z/d) \quad . \tag{4.34}$$

A parametric plot of $\partial T/\partial t$ vs. $\partial^2 T/\partial z^2$ as a function of time therefore traces up and down a straight line of slope D and intercept zero.

Evaluating the finite difference estimate of $\partial T/\partial t$, using the analytical temper-

ature solution, equation (4.8), shows the effect of the finite sampling interval:

$$\begin{aligned}
\left.\frac{\partial T}{\partial t}\right|_{FD} &= \frac{T(z,t+\delta t)-T(z,t-\delta t)}{2\Delta t} \quad , \\
&= T_0 e^{-z/d} e^{i(\omega t - z/d)} \frac{(e^{i\omega\Delta t} - e^{-i\omega\Delta t})}{2\Delta t} \quad , \\
&= T_0 e^{-z/d} e^{i(\omega t - z/d)} \frac{\sinh(i\omega\Delta t)}{\Delta t} \quad , \\
&= i\omega T(z,t) \left(\frac{\sin(\omega\Delta t)}{\omega\Delta t}\right) \quad . \qquad (4.35)
\end{aligned}$$

Equation (4.35) approaches the analytical result (4.30) as $\omega\Delta$t $\rightarrow 0$. Starting from equation (4.14) and using a similar approach, the finite difference estimate of ∂^2T/∂z^2 is

$$\begin{aligned}
\left.\frac{\partial^2 T}{\partial z^2}\right|_{FD} &= \frac{T(z+\delta z,t) - 2T(z,t) + T(z-\delta z,t)}{(\Delta z)^2} \quad , \\
&= \frac{T_0 e^{-z/d} e^{i\omega t - z/d}}{(\Delta z)^2} \left(e^{-(1+i)\Delta z/d} - 2 + e^{(1+i)\Delta z/d}\right) \quad , \\
&= \frac{2T(z,t)}{(\Delta z)^2} \left[\cosh\left((1+i)\frac{\Delta z}{d}\right) - 1\right] \quad . \qquad (4.36)
\end{aligned}$$

Equation (4.36) is compactly written as:

$$\left.\frac{\partial^2 T}{\partial z^2}\right|_{FD} = \frac{2i}{d^2} T(z,t) \left[\frac{\sinh\left((1+i)\frac{\Delta z}{2d}\right)}{\left((1+i)\frac{\Delta z}{2d}\right)}\right]^2 \quad , \qquad (4.37)$$

or it can be expanded to separate the real (in phase) and imaginary (out of phase) contributions:

$$\left.\frac{\partial^2 T}{\partial z^2}\right|_{FD} = \frac{2i}{d^2} T(z,t) \left[\frac{\sinh(\frac{\Delta z}{d})}{(\frac{\Delta z}{d})} \frac{\sin(\frac{\Delta z}{d})}{(\frac{\Delta z}{d})} + i\,\frac{\cosh(\frac{\Delta z}{d})\cos(\frac{\Delta z}{d}) - 1}{(\frac{\Delta z}{d})^2}\right] \quad . \qquad (4.38)$$

When Δz/d $\rightarrow 0$ the term in square brackets in equation (4.38) reduces to 1 + 0i , and this finite difference estimate approaches the analytical result (4.31).

The real parts of equations (4.35) and (4.38) can be expressed in terms of the driving frequency ω by substituting the penetration depth $d = (2D/\omega)^{1/2}$,

giving

$$\left.\frac{\partial T}{\partial t}\right|_{FD} = -\omega\left(\frac{sin(\omega\Delta t)}{\omega\Delta t}\right)T_0 e^{-z/d} sin\left(\omega t - z/d\right) \quad , \tag{4.39}$$

$$\left.\frac{\partial^2 T}{\partial z^2}\right|_{FD} = \frac{-2}{d^2}\left(a^2+b^2\right)^{1/2} T_0 e^{-z/d} sin\left(\omega t - z/d + \tan^{-1}\left(\frac{b}{a}\right)\right) \tag{4.40}$$

$$a = \frac{\sinh(\Delta z\sqrt{\frac{\omega}{2D}})\sin(\Delta z\sqrt{\frac{\omega}{2D}})}{(\Delta z)^2\frac{\omega}{2D}} \quad , \tag{4.41}$$

$$b = \frac{\cosh(\Delta z\sqrt{\frac{\omega}{2D}})\cos(\Delta z\sqrt{\frac{\omega}{2D}}) - 1}{(\Delta z)^2\frac{\omega}{2D}} \quad . \tag{4.42}$$

For finite Δz the phase shift in equation (4.40) means that in a plot of $\partial T/\partial t|_{FD}$ vs. $\partial^2 T/\partial z^2|_{FD}$ the locus of points will not describe a straight line of slope D, but instead a Lissajous figure, ie. an ellipse. Such ellipses will be traced out once per period in a counter-clockwise fashion. They are probably the origin of features previously observed in similar plots for sea ice, and attributed to hysteretic effects [*Collins* [1998]; *Trodahl et al.* [2000]; Karoline Frey, personal communication, 2002].

Figure (4.3) shows modelled examples of such Lissajous figures for diffusivity $D = 1\times10^{-6}\,\mathrm{m}^2/\mathrm{s}$, $\Delta z = 0.1$ m, $\Delta t = 30\,\mathrm{min}$ and driving periods P= 4, 12, 24 hours and 1 week. These parameters are typical of our field measurements enabling an examination of how significant these effects might be. The curves show the Lissajous ellipses from parametric plots of (4.39) vs. (4.40), and the circles are points sampled along these ellipses at the measurement interval Δt. Measurements from successive periods overlay each other here as the driving period is an integer multiple of the sampling time. As the driving period decreases the ellipses become more open (smaller eccentricity) and the departure from ideal behaviour is more pronounced. This broadening occurs for increasing values of $\omega\Delta t$ and/or $\Delta z/d = \Delta z\sqrt{(\omega/2D)}$. As well as this broadening the ellipses also tilts towards the X-axis. This is mainly due to the decrease in the pre-factor of $\sin(\omega\Delta t)/\omega\Delta t$ in $\partial T/\partial t|_{FD}$, see equation (4.39).

Towards identifying possible effects in our experimental results, we now consider more than one frequency component. Figure (4.4) shows two examples with the same driving but different measurement intervals. In both case the surface driving is a 10 °C amplitude daily cycle, and a 5 °C cycle with 4 hour period. In figure 4.4(a), $\Delta t = 1$ hr and $\Delta z = 0.1$ m. The small, open ellipses from the 4 hour cycle are positioned along the essentially flat ellipse from the daily cycle. In figure 4.4(b), $\Delta t = 4\,\mathrm{hr}$ and $\Delta z = 0.135\,\mathrm{m}$ the sampling inter-

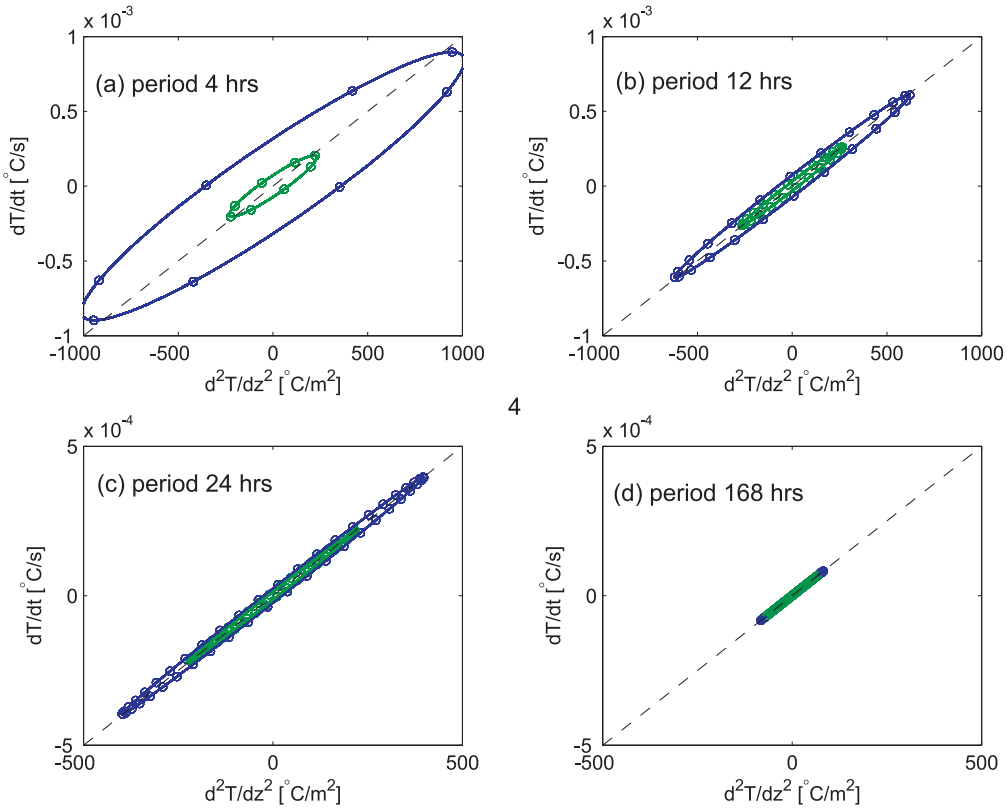

Figure 4.3: Analytical results for the effect of finite sampling intervals on finite difference scatter plots. Values of $\partial T/\partial t$ and $\partial^2 T/\partial z^2$ calculated with equations (4.39) and (4.40) for $D = 1 \times 10^{-6}\,\mathrm{m}^2/\mathrm{s}$, $\Delta t = 30$ min, $\Delta z = 10$ cm. Blue lines and points, $z = 10$ cm; green, $z = 20$ cm. Results for harmonic forcing with periods shown, see text for discussion.

vals at Table Mountain 2000-02. In this extreme case the 4 hour component is always sampled at the same point in its cycle. The blue line shows where these points might lie along the two-frequency Lissajous figure depending on when in the cycle measurements are made.

The two cases shown in figure (4.4) clearly show that the scatter plots can be artificially broadened by high frequency components for which $T << \Delta t$. When the points are irregularly distributed like this it is unclear how the geometric-mean least squares estimate will perform, although we expect that an increased spread, and therefore relative error, in the x-axis variable will lead

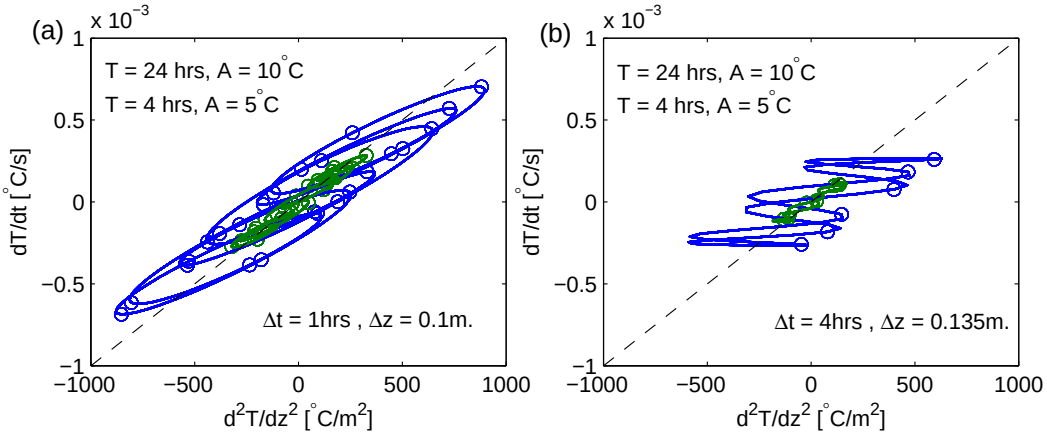

Figure 4.4: Analytical results for the effect of finite sampling intervals on finite difference scatter plots with two frequency components. Values of $\partial T/\partial t$ and $\partial^2 T/\partial z^2$ calculated with equations (4.39) and (4.40) for $D = 1 \times 10^{-6}$ m^2/s, for surface temperature components and sampling intervals shown on figures. Surface temperature components shown on figures. Curves are analytical Lissajous figures, and symbols the points sampled along the curves at time intervals Δt. Blue lines and symbols, $z = 10$ cm; green, $z = 20$ cm.

to an underestimation of the gradient using our least squares method. We now examine this expectation.

4.5 Simulations of Many-Component Driving

We have applied our finite difference analysis to calculate the diffusivity profile $D(z)$ from artificial temperature sets. Temperature fields $T(z,t)$ were generated for a uniform half-space with constant diffusivity $D = 1 \times 10^{-6}\,\mathrm{m}^2/\mathrm{s}$. The surface temperature $T(0,t)$ was prescribed as a sum of up to seven different frequency components. The sub-surface temperature is given by the sum of these components which each propagate to depth according to equation (4.32). Temperature 'measurements' were made by sampling this analytical temperature field at measurement intervals Δt and Δz. To further mimic our experimental conditions a normally-distributed random noise, σ_{noise}, was added to individual temperature measurements. We also set a measurement precision, δT, analogous to the digitization level of the data logger ADC: temperature measurements were rounded to the nearest multiple of the precision,

eg. $\delta T = 0.001\,^{\circ}\mathrm{C}$. Finite difference derivatives were calculated from the sampled temperatures using equations (4.14) and (4.15) from which scatter plots were drawn for inspection, and the thermal diffusivity profile calculated as the geometric-mean least squares gradient.

The simulations illustrate the following two effects, which we explain below:

- The diffusivity is underestimated near the surface due to scatter in $\partial^2 T/\partial z^2$ values arising from components for which $\omega \Delta t$ is large.
- Correlation coefficients (r-values) are low at depths where the variations become comparable to the underlying precision, and the diffusivity is either under- or over- estimated depending on whether the value of $(\Delta z)^4/12D^2(\Delta t)^2$ is less than or greater than 1.

4.5.1 Simulation Details

For Simulation 1 the temperature components were a $15\,^{\circ}\mathrm{C}$ amplitude yearly cycle, and $10\,^{\circ}\mathrm{C}$ amplitude daily cycle and several $5\,^{\circ}\mathrm{C}$ amplitude low-period components: T = $(5, 1.9, 1.13, 0.51)$ hours. Figure (4.5) shows the simulation output for: $\Delta t = 1$ hr, $\Delta z = 0.1$ m, $\delta T = 0.001\,^{\circ}\mathrm{C}$, $\sigma_{noise} = 0.001\,^{\circ}\mathrm{C}$.

Figure 4.5(d) shows the diffusivity profile (circles, left axis) and correlation coefficient (diamonds, right axis) for the least squares fits. The first depth at which D can be calculated is the second thermistor in the ice, here 15 cm. Two deviations in the diffusivity profile are evident. D is underestimated near the surface, and also below about 1m. In both cases the correlation coefficient is reduced, particularly below 1 m where it decreases dramatically. The discretization of points in the scatter plots in figure 4.5(c) is due to the sampling precision. From equations (4.15) and (4.14) the smallest increments in $\partial T/\partial t$ and $\partial^2 T/\partial z^2$ values are $\delta T/(\Delta z)^2 = 0.1\,^{\circ}\mathrm{C/m}^2$ and $\delta T/2\Delta t = 1.4 \times 10^{-7}\,^{\circ}\mathrm{C}/s$, as seen.

Figure 4.5(e-h) shows the output for Simulation 2 which differs from Simulation 1 only in that the daily cycle has been replaced by a weekly cycle of the same amplitude ($10\,^{\circ}\mathrm{C}$), and the phase of the yearly cycle has been shifted by 6 months. The surface is now colder than the ground below so that the temperature trace for upper-most thermistor shown (T2, $z = 15$ cm) is bottom-most in figure 4.5(e). The weekly oscillation ($d = 62$ cm) clearly causes significant disturbance over the top metre. The diffusivity profile in figure 4.5(h)

is now accurately resolved over all thermistors below 1m but the near-surface reduction is greater and extends deeper than in figure 4.5(d).

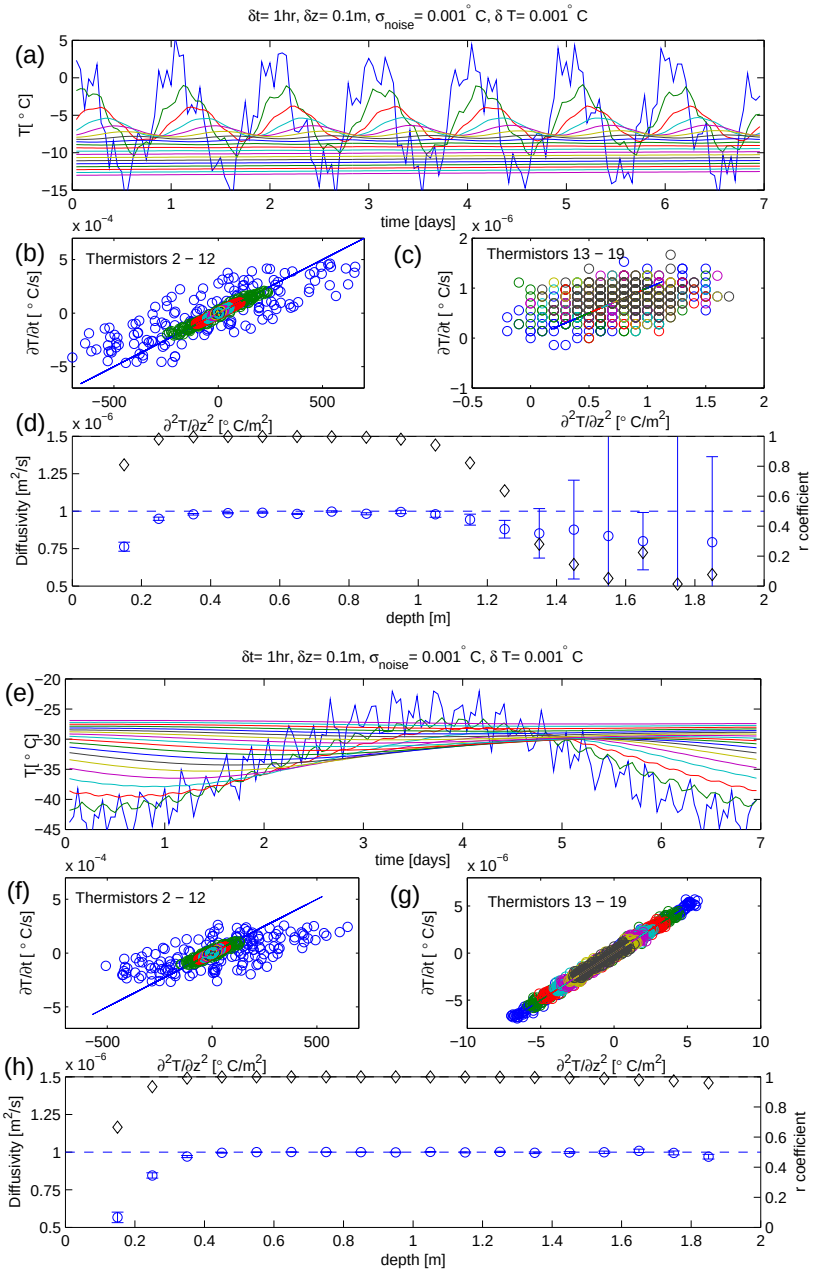

Figure 4.5: Top: Simulation 1. See text for simulation details. (a) Sampled temperatures. (b,c) Scatter plot of finite difference estimates. Lines are analytical results and points of each colour are the calculated values for individual thermistors, largest amplitudes from top thermistors. (d) Left axis: Calculated geometric-mean diffusivity profile; right axis: correlation coefficient (r-value). Bottom: (e-h) Similarly for simulation 2.

4.5.2 Interpretation of Simulation Results

Variations in the diffusivity profiles returned by these simulations are fully explained by the effects of finite sampling intervals, and the relative errors in the plotted variables biasing the geometric-mean least squares gradient estimate. This highlights that these factors must be carefully considered in the analysis of our experimental data.

Equation (4.16) shows that when the relative error in the X variable, δ_X^2, is greater than that in the Y variable, δ_Y^2, then the geometric-mean gradient will be an underestimate. This is precisely what occurs in the near-surface reduction in these simulations. The high-frequency components contribute a high level of scatter to the $\partial^2 T/\partial z^2$ values but not to the $\partial T/\partial t$ values. This scatter arises because the sampling interval Δz exceeds the penetration depth of the high frequency components. The high frequency variations measured in the top thermistor, T1, do not propagate to the third thermistor T3, which creates scatter in the $\partial^2 T/\partial z^2$ values. Such scatter does not arise in the corresponding $\partial T/\partial t$ values because they are calculated at just one depth, and because high frequency components are largely damped over the one thermistor spacing $\Delta z > d$ between the top and middle thermistor. As the high-frequency components responsible for this conductivity reduction attenuate over the top few 10's of cm, so does the magnitude of the effect.

It is the relative errors which are important here. In the two simulations above the high-frequency components are the same, so the difference lies in the size of the $\partial^2 T/\partial z^2$ variations. From equation (4.34) the amplitude of $\partial^2 T/\partial z^2$ at depth z is $(2/d^2)e^{-z/d} = \omega e^{-z/d}$. Although the penetration depth of the yearly cycle is a factor of $\sqrt{52} \sim 7$ greater than that of the weekly cycle the amplitude of $\partial^2 T/\partial z^2$ disturbances it produces is much smaller at a depth of 1-2 m on account of its factor-of-52 lower frequency. The frequency giving rise to the largest amplitude $\partial^2 T/\partial z^2$ variations is $\omega_c = 8D/z$. For $z = 0.5$ m, 1 m and 2 m, and $D = 1.15 \times 10^{-6}\,\mathrm{m^2/s}$, $\omega_c = 4$, 8, and 16 days.

In Simulation 2 the weekly cycle is in fact quite close to ω_c for 1 m, and contributes a larger amplitude $\partial^2 T/\partial z^2$ variation. As the scatter in both cases is the same the weekly driving produces lower relative errors and the diffusivity is better-predicted by the geometric mean in simulation 2. In Chapter 7 we show how this effect is manifest in our permafrost measurements. In that case spread or noise in $\partial^2 T/\partial z^2$ values is roughly constant throughout the year, but larger $\partial^2 T/\partial z^2$ values occur in the winter, making the relative error smaller, and the method more accurate, than in the summer.

That the diffusivity is underestimated below 1 m in simulation 1, but not in simulation 2, is due to the *relative* size of the sampling intervals. At these depths the high-frequency component responsible for the near-surface reduction have been damped right out and it is the measurement noise and precision which cause the scatter. In this case the ratio of relative errors in $\partial T/\partial t$ and $\partial^2 T/\partial z^2$ is given by equation (4.29). For the parameters here ($\Delta t = 1$ hr, $\Delta z = 0.1$ m, $D = 1 \times 10^{-6}\,\mathrm{m}^2/\mathrm{s}$), we find $\delta_Y^2 \approx 0.6\,\delta_X^2$. As this is less than 1, the geometric mean will underestimate the scatter plot gradient according to equation (4.16). Simulations with all parameters identical except $\Delta t = 0.5$ hr, gives $\delta_Y^2 \approx 2.6\,\delta_X^2$ gave an *overestimate* below 1 m as expected on this basis. Figure (4.6), discussed below, illustrates this effect.

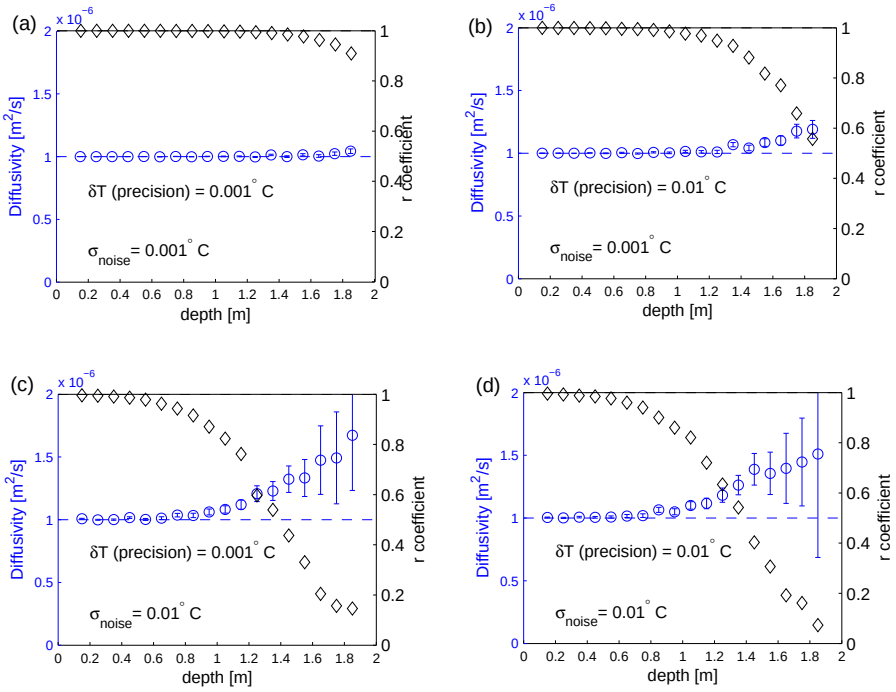

Figure 4.6: Simulated effect on diffusivity profile of the measurement precision, δT, (or 'discretisation') that temperature measurements are rounded to by logging electronics, and σ_{noise} the amplitude of normally distributed temperature measurement noise. Left hand axis (blue circles), $D(z)$ profile; right hand axis (black diamonds), correlation coefficient ('r-value').

Figure (4.6) shows the effect of increased measurement noise, σ_{noise}, and measurement precision, δT , on the diffusivity profile from Simulation 2, but here with $\Delta t = 0.5$ hr. For $\delta T = \sigma_{noise} = 0.001\,^{\circ}\mathrm{C}$ there is little error in the diffusivity profile right down to 2 m. But for a factor of 10 worse signal to noise

caused either by decreasing the precision or increasing the noise, the profile is accurate only to about 1 m. With our sampling intervals, the accuracy of our finite difference method below 1 m relies on temperature measurements with noise and precision of the order of 0.001 °C.

4.5.3 Effect of Data Smoothing

We expected that the near-surface diffusivity reduction returned by our analysis routine could be removed by low-pass filtering the simulated temperature data. We tested this expectation by time-domain filtering the sampled temperatures before the calculation of the finite difference derivative estimates. The results for identical parameters as in figure (4.5) are shown below in figure (4.7). The smoothing was performed by numerically convoluting the temperature time-series $T(z_i, t)$ of each thermistor with a gaussian window with a width of 7 hours (7 measurements) and standard deviation 1.4 hours, effectively removing components with $T < 5$ hours.

Compared with figure (4.5), figure (4.7) shows that filtering has removed the discretisation in the scatter plots for the deeper thermistors, resulting in a slight improvement in the accuracy of the diffusivity profile at these depths. The depth-extent of the near-surface diffusivity reduction has also been reduced, although somewhat surprisingly, a diffusivity reduction was still observed at z = 15 cm despite the filtering. Similar behaviour is seen in figure (4.7). The depth-extent of the near-surface reduction has been decreased but the reduction at 15 cm is actually *larger*. This is not fully understood, but it is an important result for interpreting our experimental results. It shows that despite appropriate filtering the geometric-mean least squares gradient can still be biased downwards near the surface.

These simulations have shown that combined effects of measurement noise, high-frequency noise and the size of the sampling intervals must be carefully considered. We have demonstrated that these effects can cause a near-surface reduction in the geometric-mean least squares gradient. In Chapters 5 and 7 we refer back to the results of this chapter in order to distinguish analytical artifacts from physical effects when we discuss the variations resolved in our conductivity and diffusivity profiles.

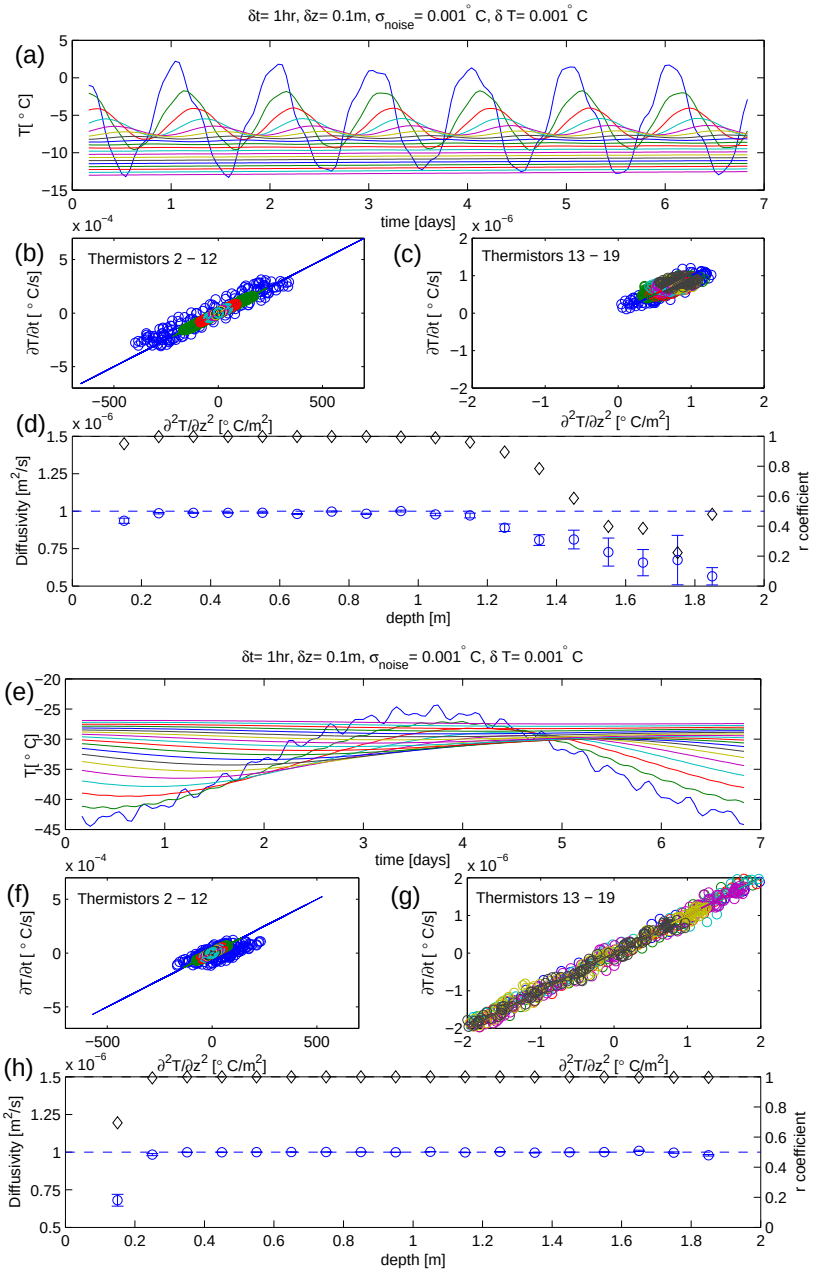

Figure 4.7: As for Figure (4.5) but after time-domain filtering. Temperatures at each depth were convoluted with a discrete gaussian window of width $7\Delta t$ and standard deviation $1.4\Delta t$, effectively removing components with periods less than 5 hours. Otherwise all parameters are identical to those in Figure (4.5).

Chapter 5

Sea ice Thermal Array Measurements

In this chapter we report sea ice thermal array measurements made in Antarctica and Alaska using the equipment described in Chapter 3. The measured temperatures have been analysed with the finite difference method described in Chapter 3. We present and discuss results for the depth-and temperature-dependence of k_{si} from the different sites. We first present measurements in FY and MY ice in McMurdo Sound, Antarctica. We then describe similar measurements in FY ice in both the Chukchi sea and Elson Lagoon near Point Barrow, Alaska. In all cases the ice was land-fast. In both MY Antarctic and FY Arctic measurements, our temperature record continued far enough into the melt season to identify daily solar heating events, the phase of which is different to expected. We observe semi-diurnal variations in the water temperature in the shallow Elson lagoon and correlate them with flushing from the tidal cycle.

5.1 McMurdo Sound, Antarctica 2002

Two thermal arrays were installed in FY land-fast ice in McMurdo Sound, Antarctica by Scott Base science technician Tim Kerr, on 10 July 2002. The sites were positioned south of the Delbridge islands, and West of the Erebus Glacier tongue, and separated by 100 m. The site location is marked as FY02 in figure (5.1). The two sites were MCM1, S 77° 43′ 926″; E 166° 26′ 491″ and MCM2, S 77° 43′ 938″; E 166° 26′ 426″. The arrays were read with the custom-

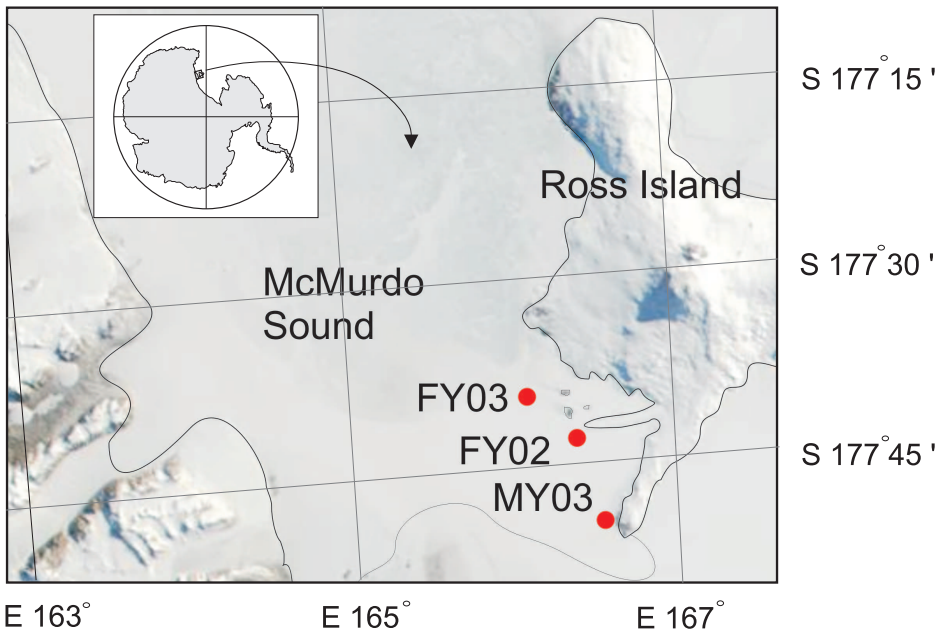

Figure 5.1: Location of thermal array sites, McMurdo Sound, Antarctica 2002, 2003. Two arrays in FY ice 2002 (FY02); one array in FY ice, 2003 (FY03); one array MY ice, 2003 (MY03). Faint dotted line near the bottom marks the edge of the Ross Ice Shelf.

built RB loggers every 30 minutes. See Chapter 3 for details of the logger operation. The thermistor spacing was 10 cm, and two reference resistors were included in each array to assess logger performance. A thermal array of different design, and an electrical permittivity array from the University of Alaska, Fairbanks were installed very near by. This site was approximately 1 km beyond the edge of the MY ice that had survived the previous summer. At the time of installation the ice was 142 cm thick at site MCM2. The whole area was flat with only a thin (1 cm) layer of snow on the surface.

When the arrays were removed, 11 November 2002, the ice thickness at a core site between the two arrays was 240 cm. There was a level fairly even snow cover of 20 cm. The salinity profile, determined from the electrical conductivity of melted core samples from this time, is shown in figure (5.2), which also core photos from this time.

Temperatures recorded at site MCM2 are shown in figure (5.3). Each curve shows the temperature-time trace for a given thermistor. The bottom trace in this figure shows the coldest temperatures recorded at the top thermistor

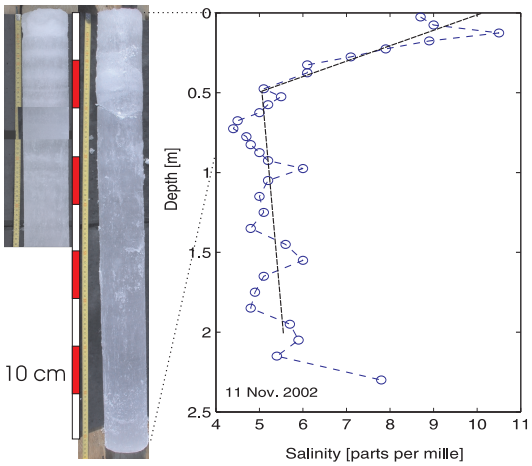

Figure 5.2: Three-photo collage 0-49 cm, and single photo 0-92 cm from two cores at site FY02. Salinity profile from halfway between the two array sites. Dashed lines is salinity profile used in conductivity analysis. (Photos and measurements by Hajo Eicken and Lars Backström, 11 November 20002.)

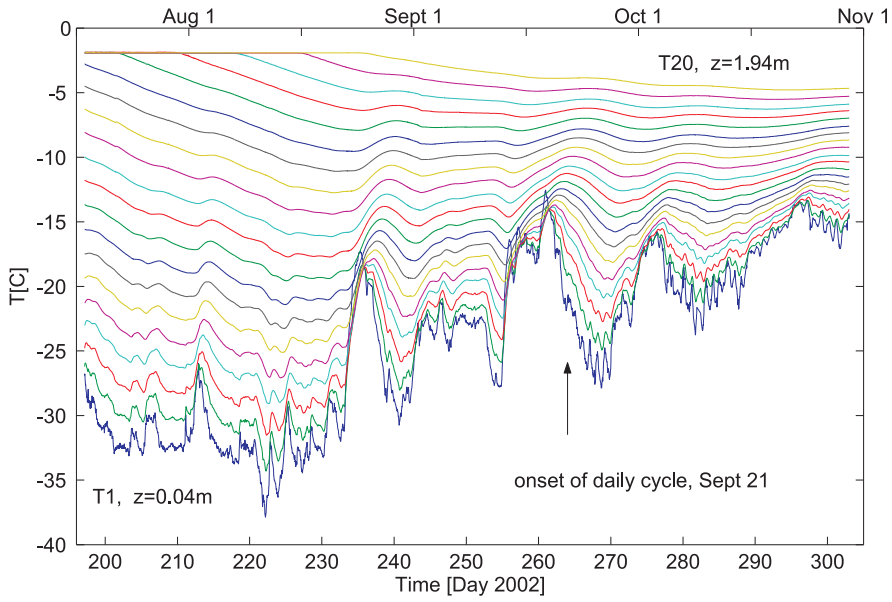

Figure 5.3: Temperature record from site FY02 (array MCM2), FY ice, McMurdo Sound, Antarctica. Lines show $T(t)$ for thermistors separated by 10 cm. The coldest temperature trace is the uppermost thermistor at a depth of 4 cm. See text for discussion.

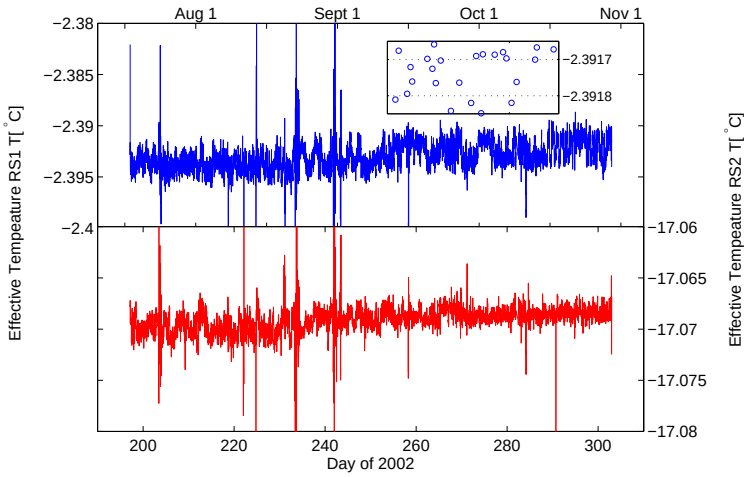

Figure 5.4: Noise in temperature measurements as shown by equivalent temperature of two low temperature-coefficient standard resistors, FY02 (array MCM2). Excluding outliers, the standard deviation of the variations is $\sigma_T = 0.0012$ °C. Inset shows discretisation level, $\delta T \approx 3 \times 10^{-5}$ °C.

(T1, $z = 4$ cm). Initially the bottom 5 thermistors were below the ice/water interface, recording the water temperature $T_w \approx -1.9$ °C. As the interface grows past these thermistors their temperature curves successively drop below the water temperature. In mid winter (mid July - mid August) surface temperatures are the most stable, and the average temperature gradient largest, $|\partial T/\partial z| \sim 20\,°\text{C/m}$. Pronounced warming events are superimposed on the gradual surface warming in September and October. Signs of the daily insolation cycle are identified first on September 21. By the start of November, the temperature gradient has reduced to about 5 °C/m. The melt season was not recorded due to the need to dismantle the sites in early November. The temperature record from site MCM1 (not shown) is virtually identical.

The temperature resolution of our measurements is indiacted in figure (5.4) where we plot the equivalent temperature of the two standard, low-temperature coefficient resistors, positioned near the bottom of the array. Excluding occasional outliers the standard deviation in these values is $\sigma_T = 0.0012$ °C for the temperature range -2 to -17 °C. A gradual increase of about 0.002 °C is observed at both sites over the duration of the experiment. The inset shows the very low discretisation level of the data, $\delta T \approx 3 \times 10^{-5}$ °C.

Thermal conductivity profiles have been calculated using the finite difference analysis described in Chapter 4. Temperature data were first smoothed in

the time domain by numerical convolution with a gaussian filter. The full width of the filter was one day, and the half width half maximum of the filter's power spectrum was 12 hours, effectively removing components, with periods smaller than this. The internal energy density was calculated from the measured temperatures using the salinity profile shown in figure (5.2). Finite difference estimates of the derivatives $\rho\,\partial U/\partial t$ and $\partial T^2/\partial z^2$ were calculated using equations (4.12, 4.13) and (4.14), using a value of $\rho = 0.92\,\mathrm{g/cm^3}$. The conductivity was then calculated as the geometric mean of the two best fit slopes to these ($\rho\partial U/\partial t$, $\partial T^2/\partial z^2$) data obtained by treating each derivative as the independent variable (see Chapter 4). Statistical outliers were removed first by rejecting data pairs if either derivative exceeded a cut-off value, and by processing the data twice. In the first pass we calculated the best fit line, and the standard deviation (σ_1) in the vertical separation between each point and the best fit line. Points were excluded from the second pass if their vertical separation was greater than $2\sigma_1$. From the second pass we calculated three variables for each thermistor depth: the geometric mean conductivity, the standard deviation in this value , and the correlation coefficient.

Temperature data were processed in blocks of 10-20 days in order to monitor the evolution of $k(z)$ through the season. Time-dependent factors include the ice thickness, temperature profile and variations in the dominant frequencies of the surface driving. Figure (5.5) shows two $k(z)$ profiles from each site, and the corresponding scatter plots. The r-coefficient profiles (black diamonds, right axis) are also shown with the conductivity profiles (blue circles, left axis). The first and last thermistors at which $\partial^2 T/\partial z^2$ could be calculated were the second thermistor into the ice, and second thermistor above the ice/water interface. This boundary changes as the ice grows so we included a warm temperature cut-off; the temperature derivatives were not calculated if the next thermistor down was above $-5\,^{\circ}\mathrm{C}$. Estimating changes in the highly salinity-dependent internal energy is very sensitive to the input salinity profile at these temperatures.

In general, the conductivity profiles in figure (5.5), and similar plots not shown, display several features similar to results previously reported by *Collins* [1998]; *McGuinness et al.* [1998]; *Trodahl et al.* [2000], and *Trodahl et al.* [2001]. Firstly, a near surface conductivity reduction is observed in which $k(14\text{ cm})$ is much lower than the expected value. Secondly, the conductivity is relatively constant over the central depths of the ice. Thirdly, close to the ice/water interface the conductivity profiles show an upturn. As demonstrated below, our interpretation is that analytical artifacts have caused the first and third effects, and that the most reliable best conductivity values are returned in the

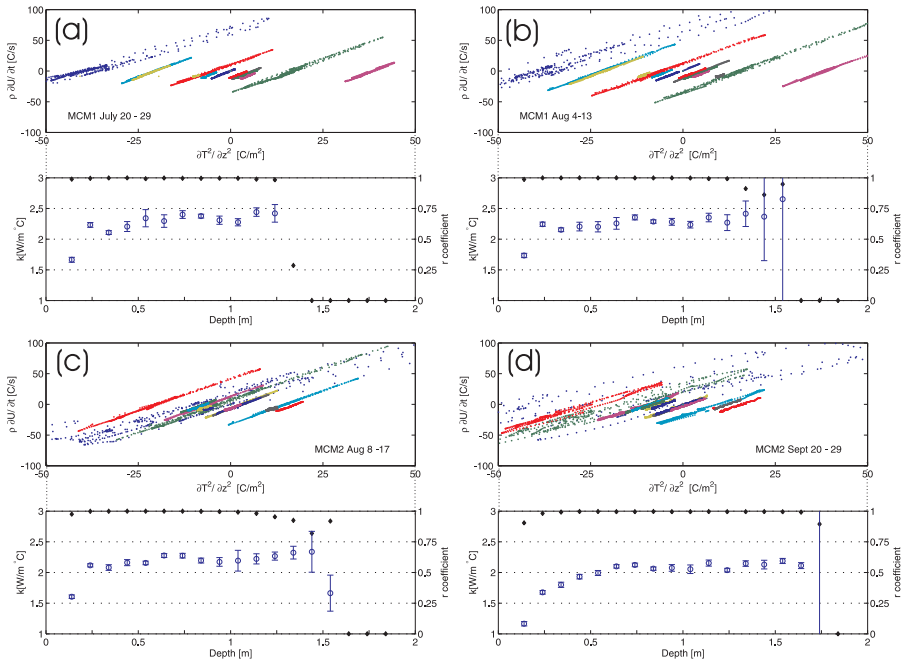

Figure 5.5: Scatter plots and thermal conductivity profiles $k(z)$, FY ice, McMurdo Sound 2002, (a,b) MCM1, and (c,d) MCM2. In the scatter plots each cluster of coloured points is from one thermistor. The scatter plots do not pass through the origin because of the small temperature offsets between thermistors but this does not affect the conductivity value, determined as the best-fit slope. In the profiles, blue circles are conductivity values (left axis), and black diamonds are r-coefficients (right axis).

central depths.

The near-surface reduction was the most puzzling feature in the previous work. One proposed explanation was that the crystal size of the surface frazil ice was comparable with the phonon mean free path, causing enhanced scattering [*Trodahl et al.*, 2001]. We now believe that this effect is an analytical artifact. The conductivity profiles in subplots (a,b) show a reduction only at one thermistor (14 cm). The reduction extends deeper in subplot (c), and even more so in subplot (d) when the surface temperature undergoes abrupt warming and cooling.

Two results form Chapter 4 are relevant to these results. Firstly, in Chapter 3 we identified two scenarios, with recognizable signatures in the scatter plots, that lead to the geometric-mean conductivity being underestimated. These

were (i) high frequency driving causing loops in the scatter plots [1], (ii) and a relative error in $\partial^2 T/\partial z^2$ greater than that in $\rho\,\partial U/\partial t$. Both loops and a wide lateral spread in the data are apparent in the scatter plots for the top thermistor (T1(4 cm), blue symbols) in plots (a-c). They are present in the next two thermistors too, but less visible in this figure. In subplot (d) these effects are clearly visible in the top four thermistors (blue, red, green, cyan symbols), which all show a decreased conductivity compared with (c).

Secondly, the conductivity reduction near the surface is similar to that seen in both the previously reported array measurements of *Collins* [1998]; *McGuinness et al.* [1998]; *Trodahl et al.* [2000, 2001], and in the simulations reported in Chapter 4. In the present analysis and in those simulations, temperatures were filtered to remove high frequency components ($T \leq 5$ hours). We do not fully understand this reduction in the simulations, but it clearly shows that in the presence of high-frequency components, our analysis routine returns an underestimated conductivity very close to the surface despite appropriate filtering. In the experimental case there is the additional possibility that the array caused a perturbation to the local heat flow. Such an effect will be largest near the surface. As the temperature recorded at the very top thermistor (T1(14 cm)) is used to calculate the temperature curvature at T2, making the conductivity calculated at this depth the most prone to such an effect.

At depths near the ice/water interface the temperature derivatives have small values, the scatter plots are quite clustered, and our analysis method becomes noise limited. For $\Delta t = 30$ minutes and $\Delta z = 0.1\,\mathrm{m}$, the figure of merit $(\Delta z)^4/(12D^2(\Delta t)^2) = 1.9$ and a conductivity overestimate is expected if the dominant source of scatter is intrinsic measurement noise (see section 4.3). Such an increase is observed. We note that by increasing the width of the gaussian filter used to 'smooth' the data, this upturn can be reduced. This apparent increase is associated with proximity to the ice/water interface, and as the ice thickens through the growth season it moves deeper. McGuinness and co-workers observed this effect too, and identified it with possible enhancement of the heat transport due to convection within the brine volume. They also examined the correlation coefficient profile, and interpreted r-values decreasing with depth as a possible signature of non-linear heat flow. We believe now that the largest factor influencing the r-values is the measurement signal-to-noise. Decreasing r-values are entirely expected as the temperature variations attenuate closer to the isothermal ice/water interface.

We believe that the best estimates of the conductivity are found in the fairly

[1] 'High frequency' here means $\omega\Delta t >> 1$.

flat central third of the $k(z)$ profiles where neither of the above two effects occur. In this region the subplots in figure (5.5) do show some small variations from thermistor to thermistor. By moving the 10 day data period forward by one day and therefore changing the distribution of scatter plot points, can, in some cases, change the conductivity values below about 125 cm by up to $\pm 0.1\,\mathrm{W/m\,^{\circ}C}$. The average conductivity between 50-125 cm for the four subplots shown are (a) $2.36 \pm 0.06\,\mathrm{W/m\,^{\circ}C}$, (b) $2.28 \pm 0.05\,\mathrm{W/m\,^{\circ}C}$, (c) $2.22 \pm 0.05\,\mathrm{W/m\,^{\circ}C}$, (d) $2.07 \pm 0.05\,\mathrm{W/m\,^{\circ}C}$. For the reasons discussed above the value for (d) is thought to be an underestimate. In this depth range the mean (and standard deviation) conductivity value for the FY columnar ice at these sites is $k = 2.29 \pm 0.07\,\mathrm{W/m\,^{\circ}C}$.The temperature range for these measurements is approximately -25 to $-10\,^{\circ}\mathrm{C}$.

In the depth-dependence, $k(z)$, we expect contributions from both the intrinsic temperature dependence, and any (micro-) structural variations. The temperature dependence predicts a conductivity that decreases with depth. Our results show the opposite effect. To examine the temperature-dependence we have binned the temperatures measured at each thermistor by temperature, and calculated $k(T)$ for each temperature bin. Figure (5.6) shows results from both arrays for the period July 20 - July 30, 2002. Except for the upper few thermistors, the temperature range measured by one thermistor is typically less than 5 °C so many thermistors are required to span a wide temperature range. The small diamonds are the conductivity for each temperature bin for individual thermistors, and the larger blue circles are the average of these values. The dashed line is the overall average listed in each figure. The variation from thermistor to thermistor is larger than any temperature variation.

By increasing the time period considered, the temperature range of each thermistor may be extended. However in this case the temperature dependence is dominated by time-dependent effects, for example, a reduction is measured for the temperatures measured during the pronounced warming and cooling events in the spring. This approach is limited because of the small range of temperatures measured by each thermistor, but also in a more fundamentally aspect. We have observed loops and other non-ideal features in the scatter plots. Lines fitted to subsets of these data, binned by temperature, will be more sensitive to the spread in data than fitting all of the data together. For these reasons we believe that this approach is ultimately unable to resolve the temperature dependence of the conductivity for the small range of temperatures spanned.

From -25 to -15 °C the conductivity of fresh ice is expected to decrease by approximately $0.1\,\mathrm{W/m\,^{\circ}C}$. This is comparable to the uncertainty in the av-

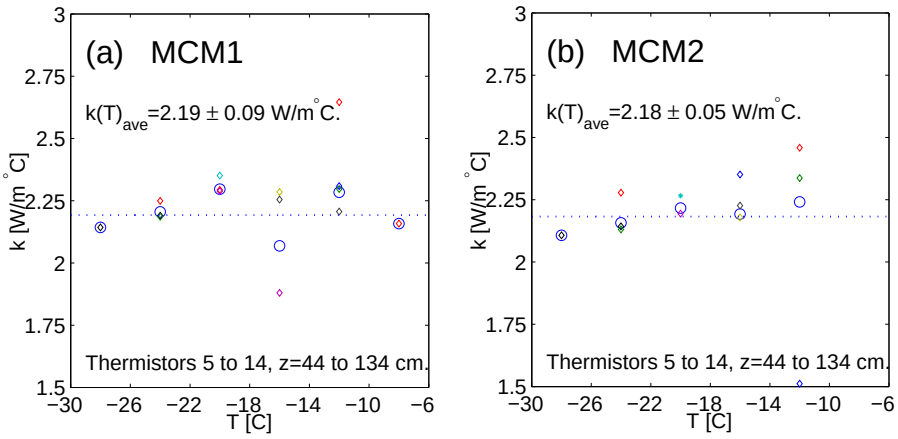

Figure 5.6: Temperature dependence of k from McMurdo Sound arrays, 2002. (a) MCM1, and (b) MCM2, both for data from July 20 - July 30. Coloured diamonds from individual depths, and larger blue circles are averages of these results, for each temperature bin. Dashed line is overall average value, as listed.

erage value over this range (see figure 5.6). Unstersteiner's parameterisation gives an increase of less than 0.02 W/m °C. We conclude that we have been unable to resolve the temperature dependence of $k_{si}(T)$ with this analysis of these measurements. We are experimentally limited by the small temperature range that each thermistor spans, and by thermistor-to-thermistor variations in the conductivity that are greater than the expected temperature variation. Given the loops and spread observed in these scatter plots, it is perhaps unreasonable to expect systematic variations in the slope of subsets of these scatter plots binned by temperature.

5.2 MY ice McMurdo Sound, Antarctica 2003

Thermal arrays were installed at one FY and one MY site in McMurdo Sound, July 2003. One array was new, and the other reconditined from 2002, but otherwise the equipment was identical to 2002. Unfortunately a data logger fault just before installation has meant that we have not been able to recover the data from either site. However, measurements were made between 7 November 2003 - 10 January 2004 with a swapped-in CR10X logger.

The MY site was about 1km west of Arrival Heights, near McMurdo Station.

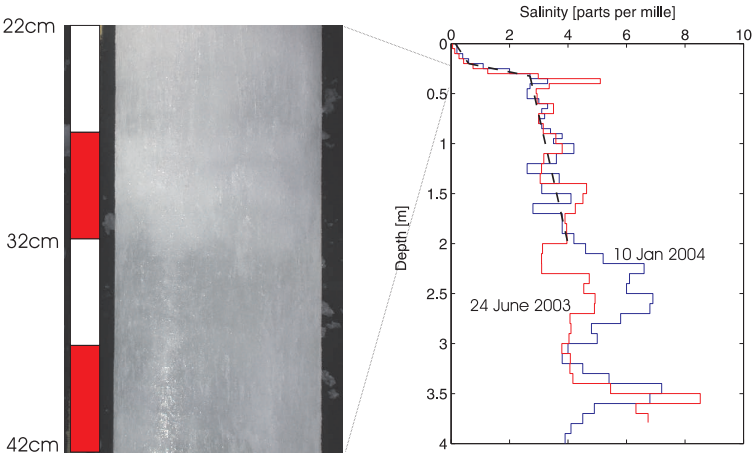

Figure 5.7: Photograph and salinity profiles of MY ice, McMurdo Sound, 2003 (site MY03). The photo shows the transition between highly light scattering, low-salinity surface ice above, to less scattering higher salinity ice below. Red salinity profile, 24 June 2003; blue profile 10 January 2004. Dashed line, salinity profile used in conductivity analysis.

The location of this site, labelled MY03 in figure (5.1), was S 77° 50′ 19″, E 166° 36′ 78″. When the CR10X logging system was installed on 7 November 2003, the site was free of snow, and the slippery and undulating surface seen in figure (3.1) suggested surface ablation. The surface ice was sampled for the experiment reported in the next chapter, and over the top 10 cm found to have salinity $0.2\,{}^{0}/_{00}$ and density $0.82 \pm 0.02\,\mathrm{g/cm^3}$. The image in figure (6.4) shows the high bubble content. This is likely to be refrozen snow melt.

Salinity profiles were measured when the site was installed and dismantled. The profile from a core extracted on 24 June 2003, when the ice was 3.79 m thick is shown in red in figure (5.7). This profile was measured by Scott Base winter-over staff and scientists, Margaret Auger, Johno Leitch, and Greg Leonard. The blue line is the profile from a site 15 m away when the array was dismantled on 10 January 2004. At this time the ice at the array site was 4.16 m thick, with an uneven snow cover of about 10 cm snow cover and 37 cm free board. For floating ice, these depths indicate an average density of 0.91 g/cm^3. This profile was measured by Hajo Eicken, and Lars Backström from the University of Alaska, Fairbanks (UAF). The salinity peaks at approximately 2.5 and 3.5 m indicate periods of fast ice growth in the coldest part of successive growth seasons/winters. It is likely that this ice is at the end of its third growth season.

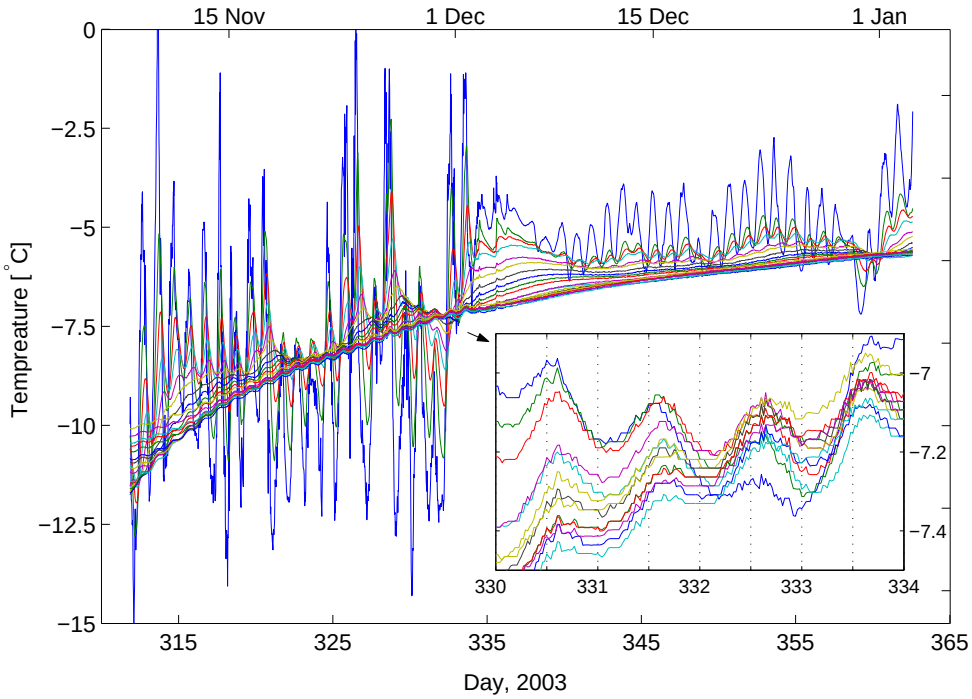

Figure 5.8: Temperatures measured with CR10X data logger in MY ice 1km off shore of Arrival Heights, McMurdo Sound, Antarctica. High snow fall between December 1-3 attenuated the daily temperature variations as well preventing direct solar heating of the ice after this time. Inset shows solar heating peaks in the deep thermistors before the snow fall.

Figure (5.8) shows the ice temperatures measured at this site with the CR10X logger during November and December. Initially there was no snow cover and the top thermistor was above the local ice surface due to melting around the array, making it very sensitive to the daily insolation cycle. The inset in figure (5.8) shows 24-hr peaks in thermistors T8 -T20 (74-194 cm). These variations are not due be conductive heating because they are well below the penetration depth of the daily cycle. Although the changing temperature baseline does make comparison difficult, these peaks are found to be in-phase with maxima at about 3-4 pm local time, and show no clear attenuation with depth. We find similar peaks in our data from the Chukchi Sea, near Pt. Barrow in Alaska, and in previous data from a nearby site (Karoline Frey, unpublished, 2002). We identify these peaks with direct solar heating of the ice, and discuss this more after we have presented the Chukchi data. A strong blizzard in the Hutt Point area between December 1-3, resulting in about 20

cm of fresh snow fall and large snow accumulation in the area (Alex Pyne, personal communication, 2004). The main graph in figure (5.8) clearly shows both the insulating effect and high albedo of this snow cover. The daily cycle is greatly attenuated after the snow fall, and the 24 hr oscillations disappear respectively. The gradual increase in the amplitude of the daily cycle through December suggests a reduction in the snow cover over this time.

Both the strong solar heating and the very strong daily temperature cycle mean our conductivity analysis cannot be used before the snow fall. Even after the snow fall, the insulating effect of the snow, and relatively stable surface temperatures mean that the temperature variations are large enough for our analysis only over the top 50 cm. We used the salinity profile shown with the dashed line in figure (5.9). The density profile is constrained only by the small sample surface measurement ($0.82 \pm 0.01\,\mathrm{g/cm^3}$), the average value of $0.91\,\mathrm{g/cm^3}$ implied by the thickness and freeboard measurements, and the expectation that a depth of 2 m it takes a value of approximately $0.92\,\mathrm{g/cm^3}$. In his review of sea ice density, *Timco and Frederking* [1996] note that the density profile of MY ice in particular is difficult to predict. For MY ice he tabulates previous measurements between 0.8 - 0.94 $\mathrm{g/cm^3}$, with lower values above the freeboard, and an average value at depth of 0.91 $\mathrm{g/cm^3}$. We have used a density profile scaled between these limits by the salinity profile.

Conductivity profiles for four 6-day periods between December 4-27 are shown in figure (5.9). As the uppermost thermistor was very close to the surface, $\partial^2 T/\partial z^2$ could not be accurately estimated at the second thermistor, (11 cm), so these profiles start at 21 cm.

All of the temperatures analysed at MY03 are above $-7\,^\circ\mathrm{C}$ where the heat capacity varies strongly with salinity. Using the average density and salinity, rather than the measured profile, gives a conductivity at 21 cm up to $0.4\,\mathrm{W/m\,^\circ C}$ higher. Although the two salinity profiles are in good agreement near the surface, the steep salinity gradient makes the conductivity calculation here quite sensitive to the input salinity. Our calculated conductivity is proportional to the input density, so the error bars in figure (5.9) include a 1% contribution for the uncertainty in density. For lower depths the temperature derivatives are small due to the insulating effect of the snow. Due to the small temperature variations these conductivity profiles do now show a clear plateau region between the near-surface reduction and the depths at which the goodness of fit deteriorates. These variations were large enough for a reliable estimate of $k(51\,\mathrm{cm})$ only in the last 6 day period. The average conductivity for depths 31-41 cm, over the four profiles, is $k_{MY} = 2.03 \pm 0.04\,\mathrm{W/m\,^\circ C}$. This

range is shown by the dashed lines in figure (5.9).

This value is lower than the average value in FY ice found above. Physically a decreased conductivity is expected for low salinity, low density and high temperatures, all of which apply here. However, as calculations were only possible for a short period at one site, and because of the sensitivities described above, we consider this estimate less reliable than the FY values.

From the equivalent temperature of the low temperature-coefficient standard resistors, the noise in these measurements is $\sigma_T \approx 0.005\,^{\circ}\mathrm{C}$, and the temperature resolution, or discretization level, $\delta T \approx 0.001\,^{\circ}\mathrm{C}$. As this is below the level expected for one-off single-ended measurements using the CR10X, confirming that the averaging of 20 repeated measurements in the data logging program has improved the ultimate resolution.

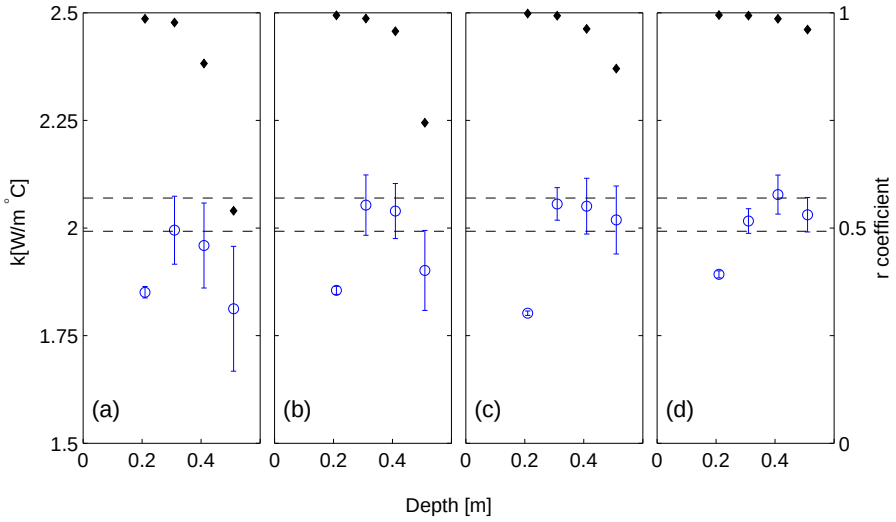

Figure 5.9: Conductivity profiles in MY ice, 1km off shore of Arrival Heights, McMurdo Sound, Antarctica 2003 (site MY03). (a) Dec 4-9, (b) Dec 10-15, (a) Dec 16-21, (b) Dec 22-27. Dashed lines show limits of average conductivity for 31-41cm, $k_{MY} = 2.02 \pm 0.07\,\mathrm{W/m\,^{\circ}C}$.

5.3 Chukchi Sea, Alaska 2002/03

Through a collaboration the Geophysical Institute, University of Alaska, Fairbanks (UAF), we also made array measurements near Point Barrow, Alaska.

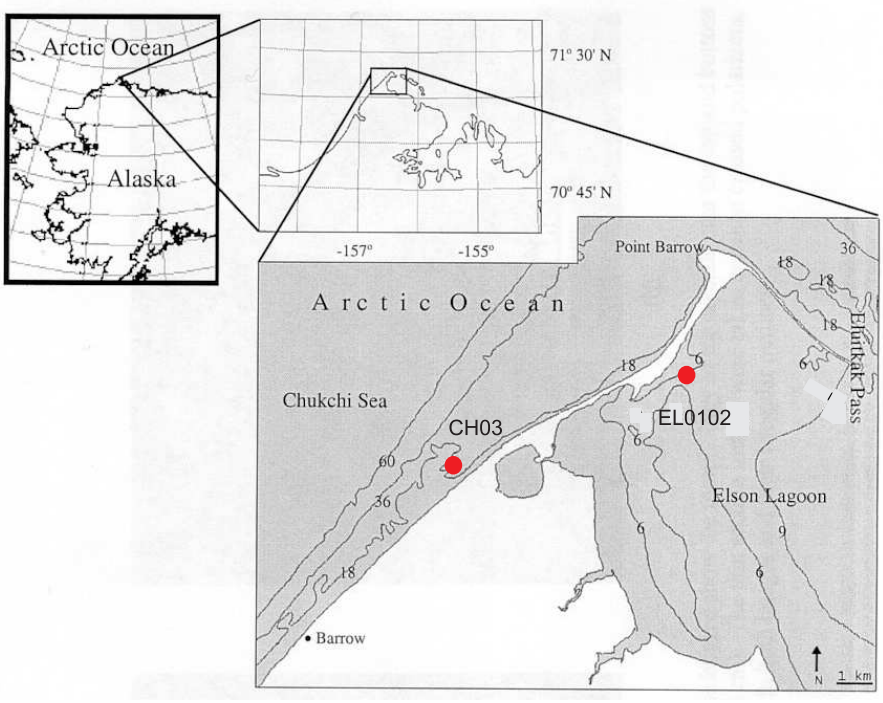

Figure 5.10: Location of thermal array sites in Chukchi Sea 2003 (CS03), and Elson Lagoon 2001/02 (EL0102, near Point Barrow, Alaska. (Maps with permission from *Stierle and Eicken* [2002])

Similar array measurements were made in the shallow tidal Elson Lagoon, November 2001 - May 2002, and in the Chukchi Sea, February - June 2003. We first present results from the more successful Chukchi experiment.

Array MCM1 used in McMurdo Sound FY ice 2002 was reconditioned and retested in New Zealand. It was then deployed with a CR10X data logging system in FY ice in the Chukchi Sea, near Barrow, by Andy Mahoney and Lars Backström from UAF. The location of the site, labeled CH03 in figure (5.10), was N 71° 20′; W 156° 41′. Temperature measurements were made between 4 February and 10 May, 2003, by which time the temperature was above $-2\,^{\circ}\mathrm{C}$ through the entire thickness of the ice. Ice grew to a maximum depth of about 135 cm, freezing only 13 thermistors into the ice.

Figure (5.11) shows the recorded temperatures. The temperature time series for thermistors T5 and T6 (44, 54 cm) are missing in subplot (a) because these thermistors and T20 (194 cm) short-circuited when the array was first installed. There had been no short circuit in testing the previous day. This

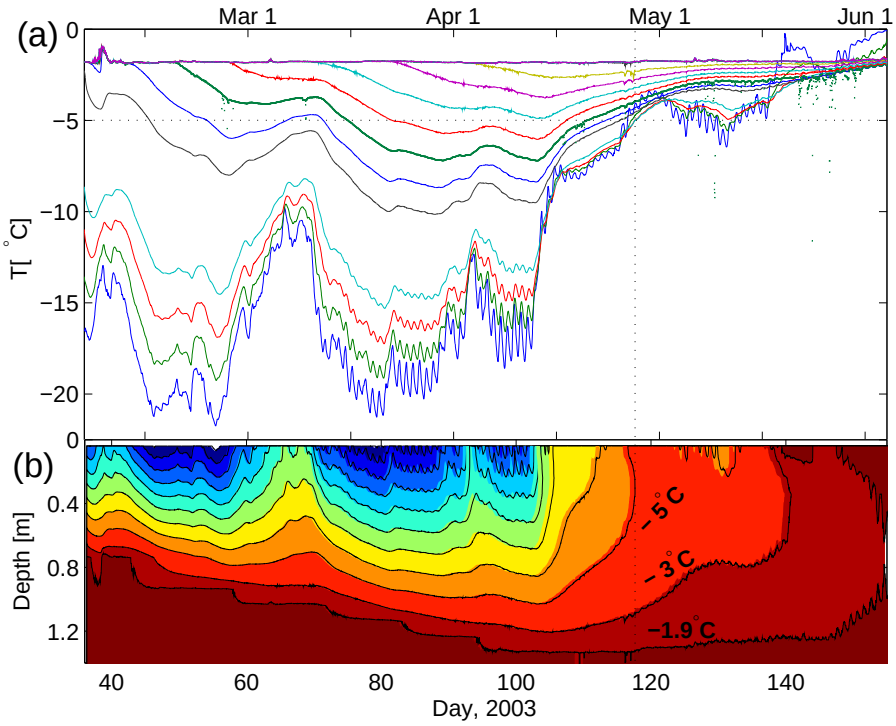

Figure 5.11: Temperatures measured at site CH03 in FY ice, Chukchi Sea, Point Barrow, 2003. (a) Temperature-time traces for thermistors 10 cm apart; traces at 44 and 54 cm are missing due to short circuit. (b) Colour reconstruction of temperature field. Isotherm increments are 2 °C except the −1.9 °C isotherm which gives the approximate position of the ice/water interface until about day 145, see text.

array suffered a kink near the connector during shipping, which we suspect led to sea water leakage. The sun was above the horizon for all of this period, having risen on 21 January. The upper thermistors do not show strong 24 hour periodicities until mid-March, presumably due to a decrease in the thickness of the initial snow cover of 11 cm. Responding to a 10 °C surface temperature increase on April 12, the ice warms very quickly, and is above −5 °C at all depths after April 27 (day 118).

The thermistors between 84-194 cm were all below the ice interface when the array was installed. A half day period of relatively stable water temperatures enabled calculation of the relative temperature offsets of these thermistors. For this time the average water temperature over these thermistors was −1.79 °C. We assumed an isothermal water column over these depths, and applied a

constant temperature shift to calibrate these thermistors to this temperature.

From the equivalent temperature of the low temperature-coefficient standard resistors, the noise in these measurements is $\sigma_T = 0.005\,^{\circ}\mathrm{C}$, and the temperature resolution, or discretization level, $\delta T \approx 3 \times 10^{-4}\,^{\circ}\mathrm{C}$, again below the expected logger resolution, and showing the benefit of averaging multiple measurements.

5.3.1 Conductivity Analysis

The missing data at 44 and 54 cm meant that $\partial^2 T/\partial z^2$ could not be calculated as above for thermistors T4 - T7 (34 - 64 cm). However, using a finite difference estimate for uneven separations we were able to calculate the average conductivity in the middle of this range. For separations Δz_1 and Δz_2 between thermistors labelled i-1, i, i+1, the curvature, to order $O(\Delta z_2 - \Delta z_1)$, is given by [*Zhang*, 1993],

$$\frac{\partial^2 T}{\partial z^2} = \frac{\frac{T_{i-1}}{\Delta z_1} + \frac{T_{i+1}}{\Delta z_2}}{\frac{1}{2}(\Delta z_1 + \Delta z_2)} - \frac{2T_i}{(\Delta z_1 \Delta z_2)} \quad . \tag{5.1}$$

For thermistors as 34 and 64 cm, the adjacent spacings Δz_1, Δz_2 are (10, 30) cm and (30, 10) cm respectively. Compared with nearby values, we found a conductivity systematically about 10%higher at 34 cm and systematically lower by about 10% at 64 cm using equation (5.1). This asymmetry is expected as equation (5.1) is only first order in $(\Delta z_2 - \Delta z_1)$, and its magnitude is not surprising given the factor of three asymmetry in spacings. A non-biased estimate can be made for the intermediate depth of 49 cm by averaging these values at 34 and 64 cm (assuming no other depth dependent effects). We have no salinity profile at this site. However previous measurements in the area, for the time of year analysed, have shown a 'C' shape profile with a bulk salinity of about 5 $^{0}/_{00}$, and an increase to about 7 $^{0}/_{00}$ over the top and bottom $\sim$10 cm of the ice [Andy Mahoney, unpublished data; *Eicken*, 2002]. We have used a constant salinity, S=5.

Figure (5.12) shows the resulting conductivity profile for four 10 day periods between Feb 16 - April 17. Not shown are the profiles for periods with pronounced surface warming or cooling, which, as in figure 5.5(d) have high scatter and reduced conductivities. Subplots (b-d) show a reduction in $k(14\,cm)$ similar to that seen in FY McMurdo Sound ice. Between 49 - 84 cm, the average conductivity (and standard deviation) over these plots is

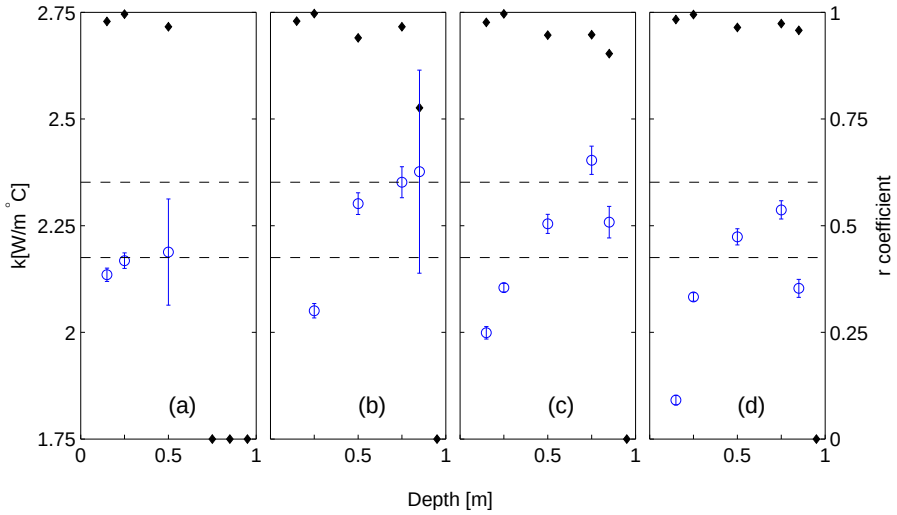

Figure 5.12: Conductivity profiles for site CH03, FY ice Chukchi Sea, Point Barrow, 2003. Blue circles, conductivity (far left axis); black diamonds, r-values (far right axis). 7-17. All subplots have the same left and right axes scales. (a) Feb 16-25, (b) March 18-27, (c) March 28 - April 7, (d) April 8 - 17.

$k_{CH} = 2.26 \pm 0.09\,\mathrm{W/m\,°C}$. Sensitivity to the input salinity value increase with temperature and therefore depth. By increasing the constant salinity by ± 1 to 6 or 4, the conductivity at 49 cm changes by about $\pm 0.1\,\mathrm{W/m\,°C}$, and at 84 m by $\pm 0.15\,\mathrm{W/m\,°C}$. This sensitivity is greater again higher than at site FY02 in McMurdo Sound, due to warmer temperatures.

Comparing figure (5.12) with the FY02 conductivity profiles in figure (5.5), both profiles show lower values near the surface and higher values at depths when the analysis becomes noise-limited. A region of approximately constant conductivity is clear at FY02, but less so at CH03, at least partly due to the much smaller depth range. For this reason, we are less confident in the conductivity values returned at CH03, than in those at FY02.

5.3.2 Other Temperature Features

Figure (5.13) shows three interesting features in the Chukchi 2003 temperature record. Subplot (a) shows a pronounced warming event recorded in the thermistors below the ice/water interface, and in the two thermistors closest to the

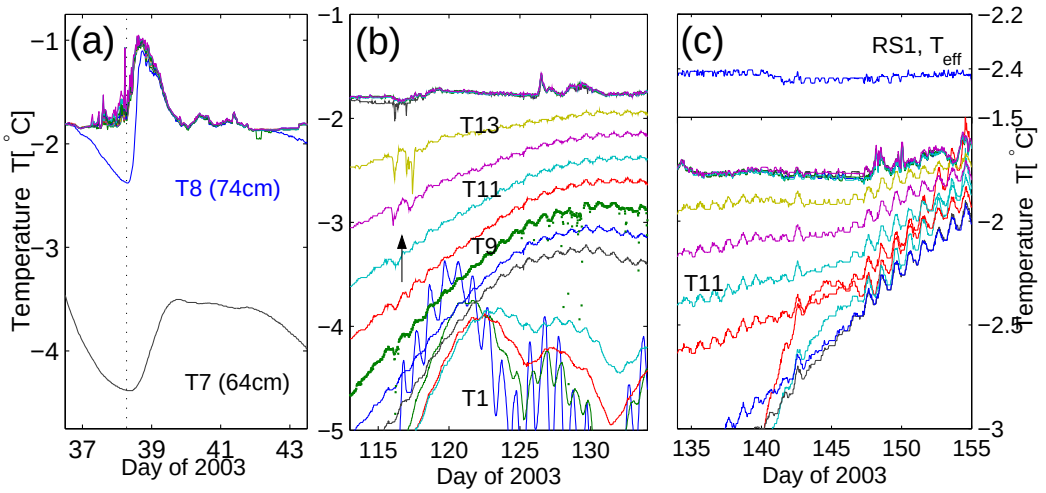

Figure 5.13: Features in the Chukchi temperature record. (a) Basal warming and ablation event. (b) Onset of in-phase 24 hr periodic features. Arrow marks cooling events in lower thermistors. (c) Amplitude increase in 24 hr peaks later in the season. Traces for 4, 14 and 84 cm have been removed for clarity. Top subplot shows the equivalent temperature of standard resistor RS1.

interface. The ice interface melts up past T8, as seen by this temperature trace re-joining those in the water, and not cooling below them again for another 4 days. From the approximate alignment of the pre- and post-warming trajectories of T8 and T7, we estimate a basal ablation of $\sim 10\,\mathrm{cm}$. The dashed line shows that the temperature minimum at T8 is later than the water column warming, but earlier than the minimum of T7 (due to conduction from the surface), so we conclude warming from below the ice. This may be due to heating of the surface water layer, although no other surface warming events in this record are accompanied by such a large water temperature increase.

Late in the season we observe 24-hour period features similar to those seen at the McMurdo MY site MY03. Such peaks have been observed before in similar Chukchi sea thermal array measurements [Karoline Frey, unpublished data, 2002]. The arrays in those measurements were larger polycarbonate-polyethylene conduits with thermistors mounted at the end of 5 cm long protruding 'fingers' [*Frey et al.*, 2001]. It is therefore unlikely that these temperature features are due to aspects of array design.

Figure 5.13(b) shows the first onset of such features. The disturbances at T9 and T11 (84, 104 cm) are in phase and show no amplitude attenuation,

indicating an origin other than conductive heat transport. At this time the temperature at 4 cm has increased above $-6\,^{\circ}$C for the first time, and between 84 - 104 cm it has just exceeded $-5\,^{\circ}$C. Larger temperature disturbances recorded at T12, T14 (114, 134 cm) are reminiscent of features identified by *McGuinness et al.* [1998] as possible over-turning of brine channels in which cold brine is ejected and replaced by warmer brine. In our case there are two cooling events, and in between them a slower warming. After this time, thermistors T4 - T13 (34 - 124 cm) show in-phase 24-hour oscillations with an amplitude of about $\sim 0.02\,^{\circ}$C, although they are sometimes not clear over the changing temperature background. The temperatures at 4 and 14 cm show 24 hour period features too, but with an amplitude attenuation and phase characteristic indicating conduction of daily solar heating. Figure 5.13(c) shows the increase in peak amplitude, to about $0.03 - 0.04\,^{\circ}$C, after day 147 (May 27). At this time the surface temperature (not shown) had just risen above the water temperature. The water column temperature increases gradually over about a week to $-1.6\,^{\circ}$C, suggesting that ice is melting, freshening the water beneath it.

The equivalent temperature of standard resistor RS1 shows weaker and less coherent variations with magnitude $\leq 0.01\,^{\circ}$C, barely above the noise level. This suggests that data logger performance may explain similarly weak variations in the submerged thermistors, but cannot explain the 3-4 times stronger, in phase peaks in the thermistors embedded in the ice.

The tides at Pt. Barrow are semi-diurnal so this behaviour must be driven by the daily insolation cycle. Following the observation of similar variations in FY ice at McMurdo Sound, *Trodahl et al.* [2000] discuss the possibility of solar heating of the ice vs. radiative heating of the probe (of the same construction as the VUW ones used here). They estimate that the radiative heating of the probe should impose an order of magnitude smaller temperature rise than direct heating of the ice. Furthermore the two effects should be identifiable by the phase; the former in phase with the insolation cycle, and the latter approximately $\pi/2$ out of phase. *Trodahl et al.* [2000] report measurements with a phase shift similar to $\pi/2$, or 6 hours. In the Chukchi Sea measurements, both the present measurements and those of Karoline Frey [unpublished data, 2002] show maxima at between 3-4pm local time, corresponding to a phase shift of approximately $\pi/4$. From the analysis of *Trodahl et al.* [2000], this would imply a much larger in-phase absorption in the ice. Materials potentially contributing to enhanced absorption at Barrow include the large amount of sediment entrained in the ice [*Stierle and Eicken*, 2002], and algae. The difference between predicted and observed phase shift warrants some attention, in

terms of both data collection and mathematical treatment. The mathematical problem is presently (2005) being addressed by Mark McGuinness, at Victoria University of Wellington.

5.4 Elson Lagoon, Alaska 2001/02

In the season prior to the Chukchi experiment, temperature measurements were made in the shallow Elson Lagoon, in the lee of Point Barrow. The location of the site, labelled EL0102 in figure (5.10), was N 71° 21′; W 156° 31.5′. Apart from a different array, the equipment was the same as that used at the Chukchi site. The stainless steel tube suffered some kind of corrosion during shipping, resulting in many small pin holes. These were patched by coating with 'JB Weld', a general purpose epoxy suitable for marine applications, and available at short notice in Barrow. When the site was installed on 5 November 2001 the ice was approximately 30 cm thick with a fairly uniform snow cover of 6 ± 1 cm. The depth of the lagoon at the site was just over 2 m.

Recorded temperatures spanning a large fraction of the growth season are shown in figure (5.14). A one-point temperature calibration was made for the thermistors initially below the ice level in a manner similar to that described above for the Chukchi site. It is clear in figure 5.14(a) that the ice/water interface temperature is not stable, particularly just after deployment. This instability is also evident in figure (5.15), in which very large variations are seen in the standard resistors, positioned next to each other near the bottom of the array. Variations in the excitation voltage may be responsible for the similar variations in the equivalent temperatures of the two resistors over the first 40 days, but not the later uncorrelated variations. Late in the season, both resistors showed variations consistent with the noise level observed at the Chukchi site using the same logger the following year, $\sigma_T \approx 0.005\,^{\circ}\mathrm{C}$. We don't have an explanation for the erratic behaviour seen in figure (5.15), but suspect that it may have arisen due to complications from the array repair. In light of this variability we have not conducted a conductivity analysis of these data.

Figure (5.16) shows semi-diurnal, in-phase temperature variations measured by the thermistors below the ice/water interface. In subplot (a) for 28 November - 4 December 2001, their magnitude increases with depth for thermistors T17 - T20 (164 - 194 cm), and occasional peaks are seen in T15 and T16 (144, 154 cm). In subplot (b) for 27 March - 2 April 2002, the variations have a

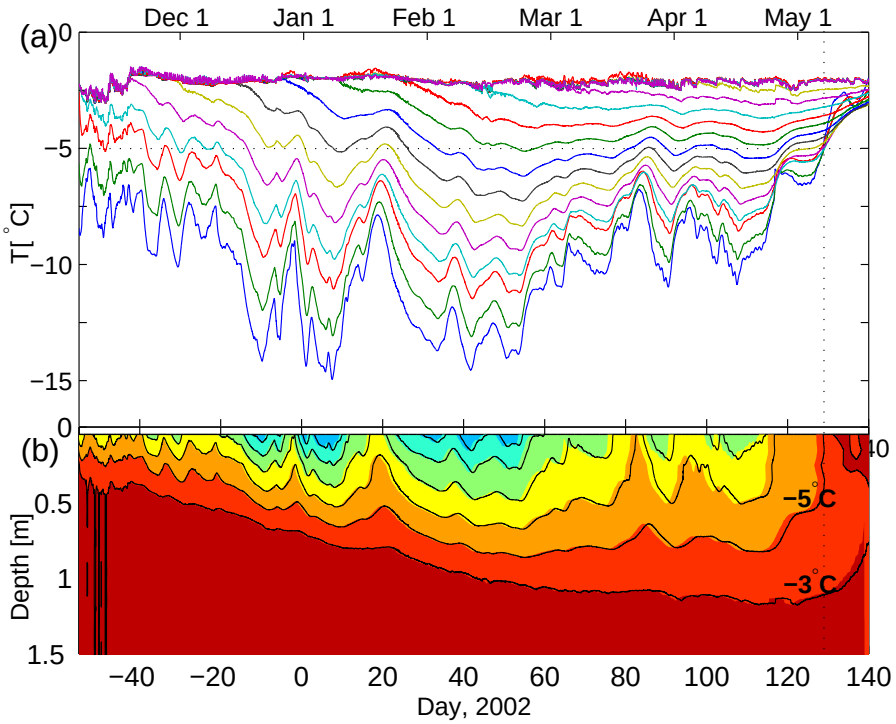

Figure 5.14: Recoded temperatures in FY ice, Elson Lagoon, Barrow, 2001/02. (a) Temperature time series, for thermistors 10 cm apart. (b) Colour reconstruction of temperature field. Isotherm increments are 2 °C. The −3 °C isotherm is slightly above the the ice/water interface, see text.

nearly constant magnitude over all 8 submerged thermistors, T13 - T20 (124 - 194 cm). Over the experiment duration the behaviour varied between these two kinds shown, but the latter was common for the last two months, with peak-to-peak magnitudes of up to 0.35 °C.

The period clearly ties these variations with the semi-diurnal tidal cycle. From tidal predictions for those dates at Pt. Barrow, these temperature maxima occur just after water level maxima [2]. A possible explanation is that the lagoon is being flushed with the high tides, causing a cycle in the salinity, and therefore freezing point. This agrees qualitatively with the relatively warm, less saline water of the Chukchi Sea flushing the Lagoon. Figure (5.16) shows the water temperature base-level in the lagoon to be between −2.1 °C and −2.4 °C, which is colder than the nearby sea water temperature in the Chukchi Sea, at

[2]Tide predictions from http://www.fishingworks.com/tide_prediction_interval.cfm, using (US) National Oceanic and Atmospheric Administration prediction data.

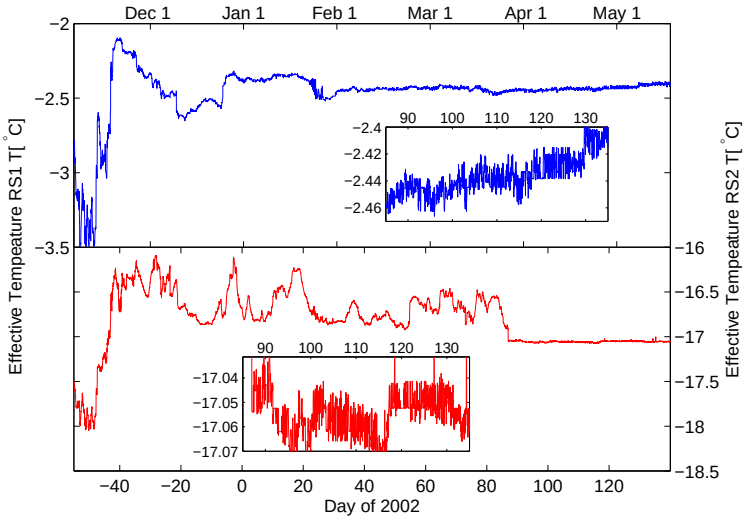

Figure 5.15: Equivalent temperature of low temperature-coefficient standard resistors, Elson Lagoon 2001/02. Top, left axis, RS1. Bottom, right axis, RS2. Insets show intrinsic measurement noise, when other variations are absent.

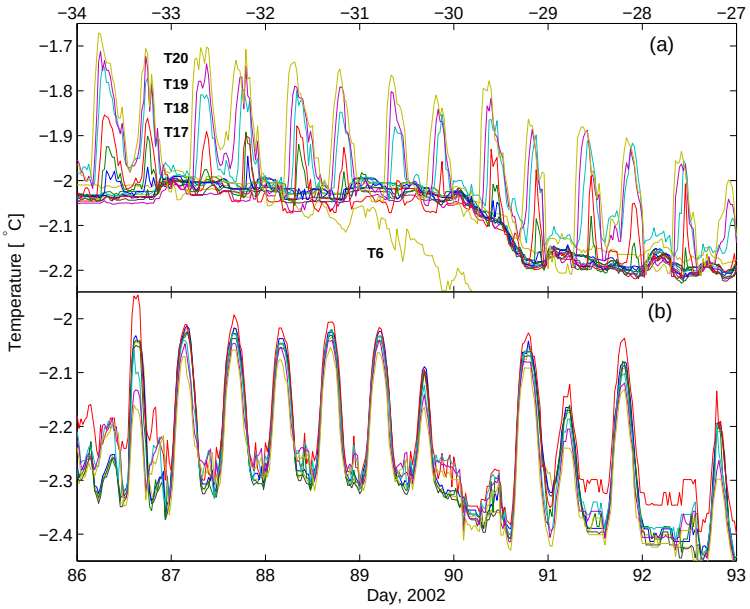

Figure 5.16: Diurnal temperature variations in the submerged thermistors, Elson Lagoon, 2001/02. (a) 28 November - 4 December 2001; (b) 27 March - 2 April 2002.

-1.79 °C. We note that a change in freezing temperature of $\Delta T_f = 0.3\,^{\circ}\mathrm{C}$ would imply a salinity change in the lagoon of about $\Delta S = 5.5$. Accurate

information about the tidal patterns and salinity variations in Elson Lagoon are required to purse these observations further.

5.5 Discussion

We have reported on four thermal array measurements, and calculated the conductivity profile for three of these. Based on a a more thorough understanding of the performance of our finite difference conductivity analysis, our implementation and interpretation differs slightly from the previous work of Trodahl and co-workers. As with their results, we resolve a near-surface reduction in the conductivity at all sites, and an apparent increase near the ice/water interface. Based on the analysis in Chapter 4, we can explain these effects. However, because we cannot predict the magnitude of them, we are unable to distinguish any physical effects which might also exist. The conductivity calculated in these regions is not considered reliable. We have calculated an average conductivity for the intermediate region between them, which in the case of FY ice is columnar ice, and the region of least structural variability.

Location	Ice Type	k_{si}(meas) [W/m °C]	Depth [m]	Temp. range [°C]
McMurdo Sd.	FY	2.29 ± 0.07	0.5-1.2	-25 to -10 °C
Chukchi Sea	FY	2.26 ± 0.09	0.5-0.8	-15 to -5 °C
McMurdo Sd.	MY	2.03 ± 0.04	0.3-0.4	-6 to -5 °C
McMurdo Sd. [a]	FY	2.17 ± 0.12	0.5-1.5	-19 to -8 °C
McMurdo Sd. [b]	FY	2.0 ± 0.1	-	-21 to -8 °C
McMurdo Sd. [c]	FY	1.95 ± 0.05	> 0.2	-28 to -8 °C

Table 5.1: Thermal conductivity values from the thermal array experiments presented here, top, and from previous work. [a] *Collins* [1998]; [b] *Trodahl et al.* [2000], unknown depth range; [c] *Trodahl et al.* [2001]. NB: the average values for (b,c) have been read from graphs of $k(T)$.

Table (5.1) shows the conductivity values determined above, together with values from previous array measurements. Of these, the value for FY ice in McMurdo Sound (site FY02) is considered the most reliable. Results from two arrays separated by 100 m are in good agreement, and, importantly, the thick

ice and cold temperatures allowed the clear identification of a plateau in the conductivity profile between 50-125 cm. Although in excellent agreement with this value, the conductivity from the Chuckchi Sea site is the average over a smaller depth range, and it is less clear that the conductivity profile flattens out.

We believe our values to be more accurate than the lower values from similar experiments listed in table (5.1), and that due to differences in analysis, the previous values were underestimates. The best agreement is with the value reported by *Collins* [1998], for depths below 50 cm. We believe that the much lower conductivity found in *Trodahl et al.* [2001] is related to a not accounting for now better-understood analytical artefacts.

The uncertainties in the MY conductivity reflect a small variance in the data. However, the small depth range over which these values were determined means it is not clear that the conductivity profile shows a plateau, as clearly seen in the FY McMurdo Sound profiles.

In the next Chapter we present results from a direct measurement of the conductivity of small FY and MY cores. We then discuss the results of both methods, and compare then with each other and theoretical predictions.

Chapter 6

Direct Measurement of Sea Ice Thermal Conductivity

In this chapter we report on a direct measurement of the thermal conductivity of small sea ice samples, performed at Scott Base, Antarctica, in November 2003. The experiment was designed as a ground-truth experiment to investigate the 25-50% reduction in conductivity over the top 50 cm of first year (FY) ice suggested by our thermal array measurements. We measured the conductivity of several samples of three ice types: FY surface (0-10 cm), FY sub-surface (45-55 cm) and MY surface (0-10 cm).

There are two key results of this experiment. Firstly, we did not measure any reduction in the conductivity over the top 50 cm in FY ice. We did measure a 10% reduction in the MY surface ice compared with the FY surface ice, consistent with the lower density of this desalinated, bubbly MY ice. The second key result is that the average conductivity values of the three ice types we examined are, within $\pm 6\%$ uncertainties, all consistent with values predicted by our adaption of the Yen/Schwerdtfeger conductivity model discussed in Chapter 2.

After an overview of the parallel conductance method (PCM), we present full details of our experimental apparatus. This is followed by a heat flow analysis in which we discuss the conductive heat flow that we measure, and in particular how our analysis accommodates radiative heat losses. The samples are characterised and the measurement procedure and results presented and discussed.

6.1 Overview of Parallel Conductance Method

The thermal conductivity is most directly determined in a 1-D experiment from Fourier's law, $J_C = -k\partial T/\partial z$, by measuring the temperature gradient $\partial T/\partial z$ in the direction of a known conductive heat flux J_C. This is most simply realised in a 1-D experiment by placing a heater at one end of a sample, while the other end is held at a constant temperature, and measuring the resulting temperature profile along the sample. Such an approach requires that the conductive heat flow along the sample is precisely known, so care must be taken to eliminate or accommodate any heat flow other than conduction along the sample.

By performing the measurement with the sample and heater in a high vacuum chamber, conductive and convective losses from the sample can be eliminated, however this approach is not straight forward for high vapour pressure materials such as ice. The vapour pressure of fresh ice at $-10\,^{\circ}\mathrm{C}$ is approximately $5\,\tau$ [*Weast*, 1971] [1]. However, because the thermal conductivity of gases is independent of pressure until the gas mean free path is comparable with the vacuum chamber dimensions, very low pressures are required to reduce conductive losses through the chamber. Ice samples exposed to such pressures would sublimate. This problem is overcome by placing high vapour pressure samples in a vacuum-tight sample holder. This eliminates conductive and convective losses from the holder but the heat flow is now along the sample and holder in parallel, and the conductance of the holder must be accounted for.

In our case the holder is a thin-walled stainless steel tube, along which with 5 thermistors are attached to measure the temperature profile. When a sample is loaded, the temperature gradient along the tube gives the total thermal conductance K of the tube plus ice sample, which in the assumption of parallel heat flow add together:

$$K_{ice+holder} = (K_{ice} + K_{holder}) = \frac{P_C}{L \mid \partial T/\partial z \mid} \quad , \tag{6.1}$$

where $P_C = J_C A$ is the conducted power. From a separate tube-only measurement with no sample loaded gives the conductance of the tube is

$$K_{holder} = \frac{P_C'}{L \mid \partial T/\partial z \mid'} \quad . \tag{6.2}$$

The difference between these two measurements is the conductance of the ice,

[1] Pressures are here expressed in torr [τ], $1\,\tau = 1.3\,\mathrm{mbar}$.

from which the ice conductivity is calculated as:

$$k_{ice} = \frac{L}{A_{ice}}(K_{ice+holder} - K_{holder}). \tag{6.3}$$

For no extraneous heat loss the conducted power P_C is equal to the power dissipated by the heater, and the measurements described above would determine the conductance of both the sample and the holder. This is the idealised parallel conductance method.

Using a high vacuum eliminates conductive and convective loss but at our operating temperatures of approximately $-10\,^{\circ}\mathrm{C}$, radiative transfer between the holder and vacuum chamber wallscannot be neglected. We show rigorously in Appendix C, and discuss in section 6.3.1 below, how our analysis does this. To a very good approximation the effect of radiative losses is that equations (6.1, 6.2) overestimate $K_{ice+holder}$ and K_{holder} by the same amount, so that despite this error, equation (6.3) still gives the ice conductivity to $\pm 1\%$.

6.2 Experimental Equipment

Our measurements were performed in an insulated shipping container, converted into a field laboratory, at Scott Base. There are five components of our experimental equipment: (i) a sample holder tube with a heater at its base, and five attached thermistors for measuring the temperature profile along the tube; (ii) a vacuum chamber in which the sample holder and heater were housed; (iii) a turbo-molecular pump, backed with a rotary pump, for maintaining chamber pressures down to $P \sim \mu\tau$; (iv) a circulating cold bath for pumping a temperature-controlled fluid through copper fittings surrounding the vacuum chamber to keep it isothermal; (v) electronics for measuring the thermistors' resistance, and for heater power supply.

The experimental arrangement is shown in figure (6.1). The circulating bath is under the bench, the rotary pump behind it (obscured), and the turbo pump mounted on the frame in the foreground. The vacuum bellows and cooling fluid hoses were fed through a small porthole, obscured by the turbo pump, to the chamber outside. The current supply for the heater and multimeter for reading the thermistor resistance are on the top shelf, and their electric cabling feed through another porthole. Figures 6.1(b,c) show the chamber housing mounted on the outside of the container, the copper top flange of the chamber and circulating cold bath hoses. Schematic diagrams of the vacuum chamber, measurement circuits and vacuum system are shown in figure (6.2).

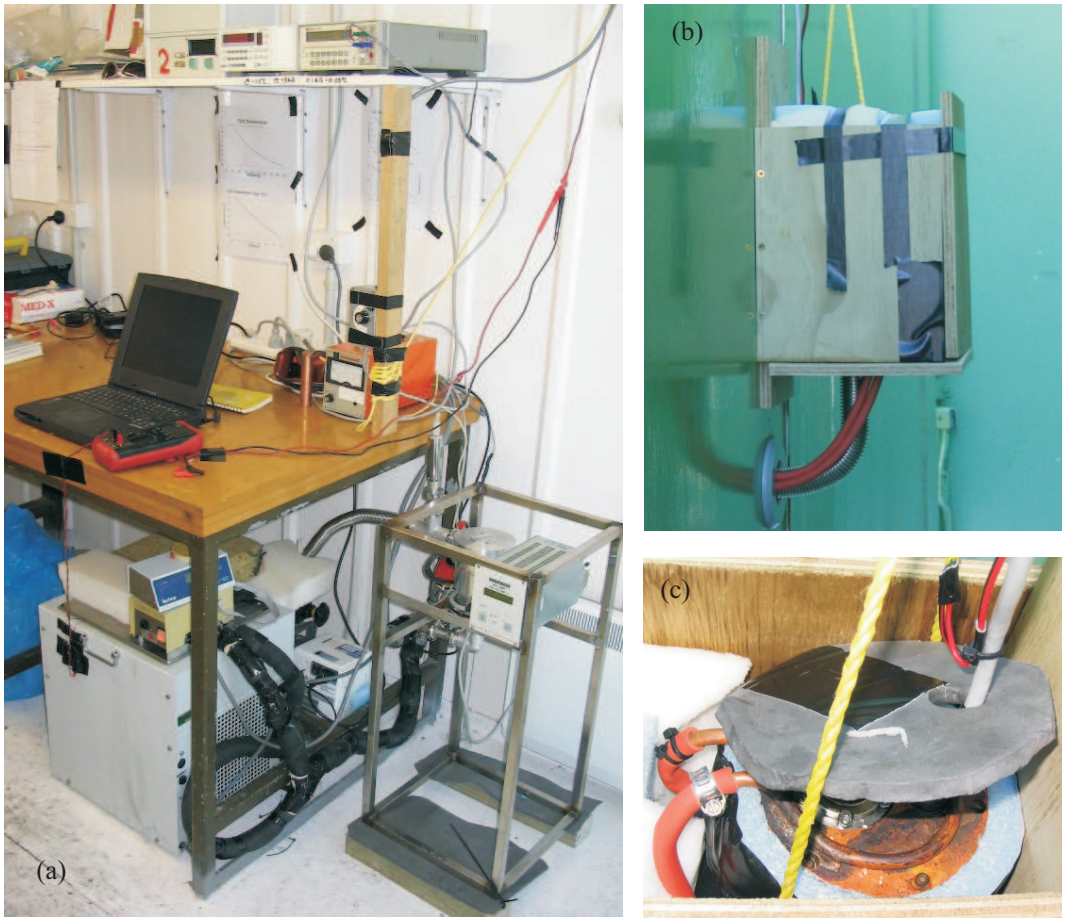

Figure 6.1: (a) Experimental arrangement inside container lab. See section 6.2 for discussion of apparatus. (b) Housing of chamber mounted on outside of container, showing vacuum bellows and circulating bath hoses coming from inside the container. (c) Chamber and electrical cabling inside plywood enclosure. During operation the space in the enclosure around and above the chamber was fully packed with insulating foam.

Figure 6.3(a) shows inside the chamber, with the sample holder tube protruding through the upside-down top flange. The sample holder tube was a 25.4 mm outside diameter, 0.3 mm thick 304 stainless steel tube. The tube was sealed at its base with a raised centre, housing an O-ring-sealed air release screw. A copper blank was placed on top of this to create a bobbin for winding the heater wire, and to provide uniform heating over the base of the tube. The heater was approximately 10 metres of constantan wire, with a total resistance of $340.9 \pm 0.1\,\Omega$, wound in a loop to prevent inductive heating. The

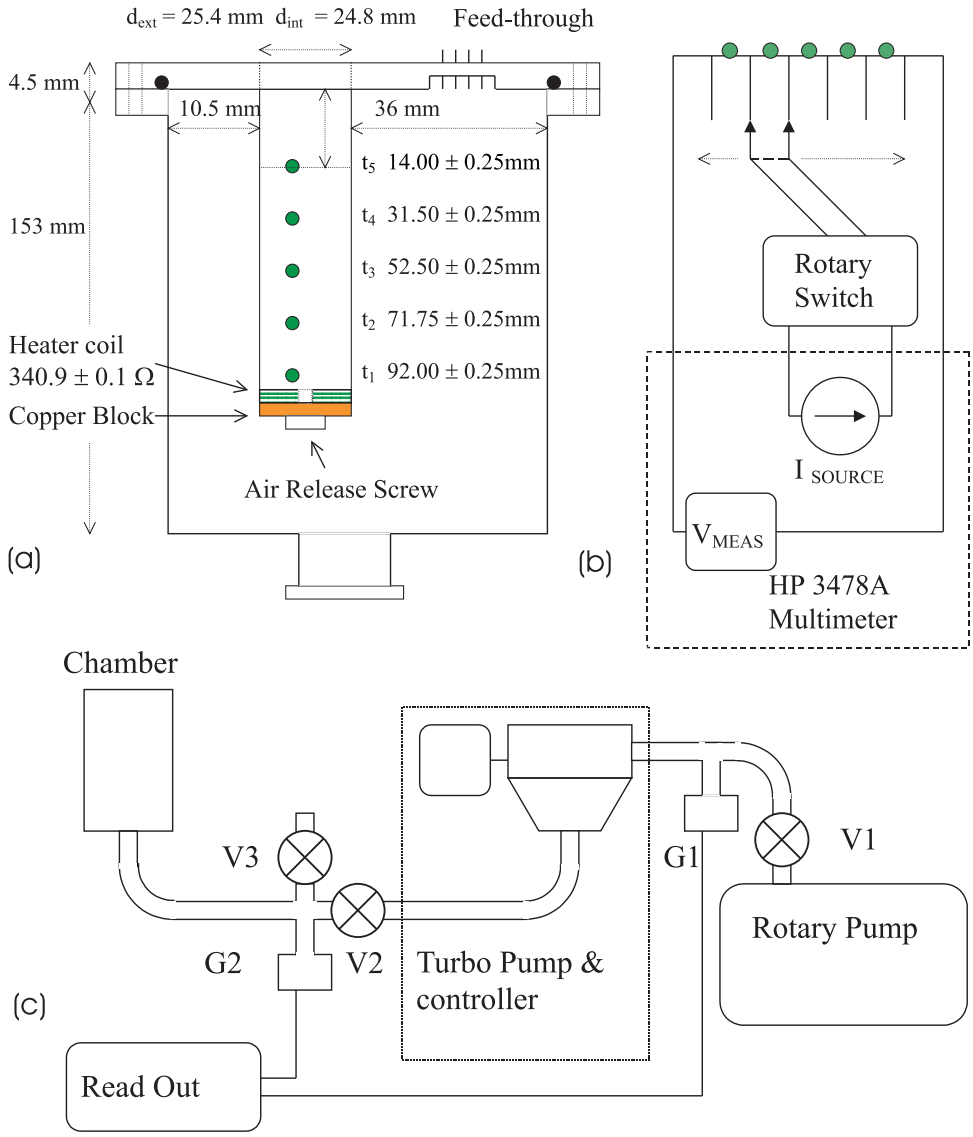

Figure 6.2: Schematic diagrams of experiment. (a) Vacuum chamber showing thermistor positions, chamber dimensions and other features. (b) Thermistor measurement circuit including manual 2-way rotary switch for selecting thermistors. (c) Pumping system. The rotary pump served as roughing and backing pump for the turbo-molecular pump. Needle-valve V3 allowed air-venting of chamber. Ionization gauge is G2 and themistor gauge G1. Dotted box indicates frame for turbo pump and controller.

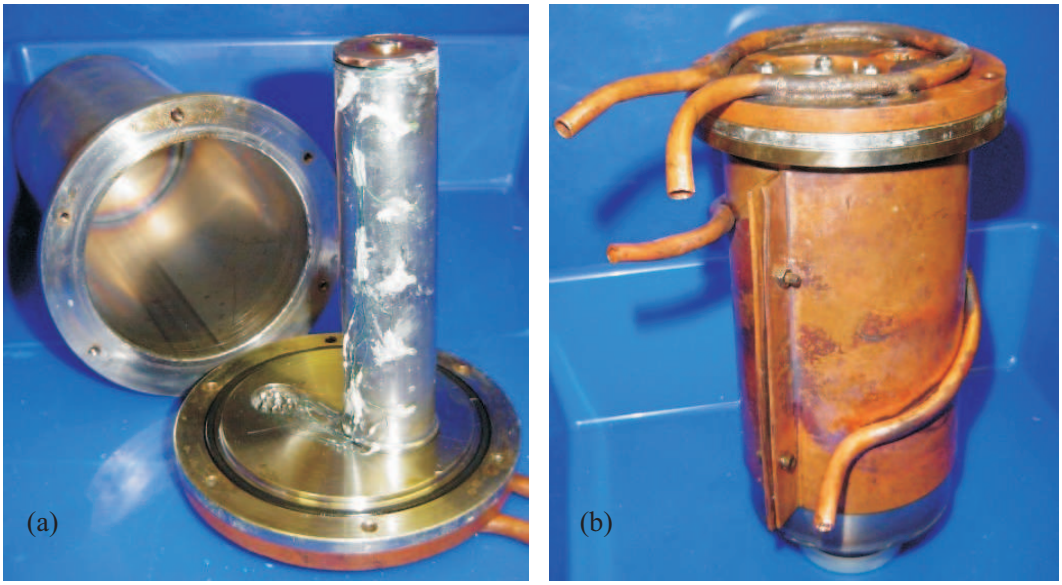

Figure 6.3: Photographs of experimental vacuum chamber. (a) Inside of chamber and sample holder tube. Air-release screw, copper heating plate, and heater wire can be seen on top of the narrow, upright, sample holder tube. Thermistor beads are attached with Torr Seal. The electric feed-through is on the flange to the left of tube. (b) Copper fittings through which cold bath fluid was pumped.

heater current was supplied by a calibrated Yokogawa 7651 precision power supply.

The YSI 55031 thermistors are visible in figure (6.3) as small green beads attached to the sample tube with Torr Seal, a white-coloured vacuum epoxy. Care was taken to ensure a direct tube-to-thermistor contact at the centre of the thermistor beads. Thermistor resistance was measured with a 4-point measurement using a calibrated HP3478A multimeter. The circuit is shown in schematically in figure (6.2). The excitation current is $10\,\mu$A producing negligible thermistor self-heating. After calibration (see section 6.5 below) the resistances were converted to temperatures using the Steinhart-Hart fit described in Chapter 3. These thermistors are from the same batch as those used in the thermal arrays.

Specifications of the constantan wires in the thermistor circuit and copper heater current wires were carefully selected according to two criteria so as to minimise the uncertainty in the power delivered to the tube: (i) less than

1% of the I^2R power dissipated in the heater circuit is dissipated other than in the heater itself (ie. the electrical resistance of the current leads $< 1\%$ electrical resistance of the heater coil); (ii) the thermal conductance of all wiring connecting the sample holder and the chamber top is less than 1% of the thermal conductance of the tube. According to the Weidemann-Franz law (see section 3.1.1), the thermal conductance is inversely proportional to the electrical resistance, so these criteria above impose upper and lower limits on the electrical resistance of the heater supply wires.

We used 0.08 mm diameter enamelled copper wire for the heater supply wires, giving $R = 0.74\Omega$ for both wires in series. This is 0.2% of the total resistance in the heater circuit satisfying the first condition. The two heater input wires give a total parallel thermal conductance of approximately $40\,\mu\Omega$/K. High resistance 33 Ω/m constantan wires were used in the thermistor circuit giving $10\,\mu\Omega$/K for the parallel conductance of the 8 wires. The thermal conductance of the tube was measured to be approximately 7 mΩ/K. Therefore the total thermal 'leak' to the chamber top along all of the wiring is 0.7% of the tube conductance, and 0.2% when an ice sample is loaded, satisfying the second condition in both cases.

We desire an isothermal chamber for two reasons. Disturbances in the chamber top temperature will be conducted down the tube and interfere with the measurement of the equilibrium temperature gradient. Furthermore, an isothermal chamber provides a well-characterised radiative environment, and consistent radiative losses, which are assumed in our analysis below. To achieve this we used a Techne 12-B re-circulating bath continuously pumping a 40/40/20 mixture of ethylene glycol/water/isopropyl alcohol through the chamber's copper fittings shown in figure (6.3). The annular, copper top flange was bolted to the top of the chamber allowing ice samples to be loaded through its hole. The lower jacket was made with a radius of curvature slightly smaller than the outside of the chamber, and clamped tight against it. Silicon vacuum grease was applied between the chamber and copper fittings to optimise thermal contact. The fluid went through the top flange, down through the jacket and then back to the bath. To provide insulation against variations in outside temperature, the chamber was fully wrapped in 20 mm thick high density foam, and housed inside an enclosure of 17 mm plywood, padded with additional foam. See figure (6.1).

The chamber was evacuated with an Alcatel ATP-90 turbo pump backed by a Pascal 2005 SD rotary pump. Backing line pressure was monitored with a thermistor gauge and the chamber pressure with a cold-cathode ion gauge.

Standard measurement pressures were 0.5 - 2 $\mu\tau$. The vacuum set-up is shown schematically in figure 6.2(c). The chamber could be isolated with valve V2 and vented to air pressure with the needle valve V3.

The pumping system, circulating bath, and electronics could not be operated at outside temperatures, so were housed inside the container. A temperature-controlled cold-room, in which the chamber could have been housed, would have been preferable but was not available. The insulated chamber enclosure was shielded from direct sunlight and out of line of sight of the sun for 22 hours a day, but otherwise experienced the local weather at Scott Base. The ambient temperature measured with a thermistor just above the enclosure was mostly in the range -8 °C to -18 °C, and averaged -12 °C.

6.3 Heat Flow Analysis

In equations (6.1-6.3) we assume that all of the heat input is conducted along the tube, and ice if present. Here we first estimate the conductive and radiative losses from the sample tube in our vacuum chamber, then, in the sections below, show that how analysis accommodates the non-negligible radiative loss. A full treatment of the heat flow is presented in Appendix C.

The kinetic theory result for the thermal conductivity of an ideal gas is independent of pressure,

$$k = \frac{1}{3} v \lambda c_v \quad , \tag{6.4}$$

where v is the average molecular speed, λ the mean free path, and c_v the volumetric heat capacity of the gas. Although the mean free path is inversely proportional to density (hence pressure), this pressure-dependence is cancelled by the volumetric heat capacity, which is proportional to density. Equation (6.4) holds until the pressure is so low that the mean free path of gas molecules exceeds the container dimensions. For air at -10 °C in a chamber with typical dimension $L \sim 3$ cm, this occurs at $P_0 \sim 7$ mτ. In the molecular regime, $P < P_0$, collisions with a wall are more probable than with other molecules, and the assumptions of kinetic theory no longer hold. The transport of heat can no longer be considered in terms of inter-molecular collisions, but by molecular flow instead. The effective thermal conductivity is given by [*Gombosi*, 1994]:

$$k = \alpha P L \left(\frac{2 k_B}{\pi m T} \right)^{1/2} , \tag{6.5}$$

where P [Pa] is pressure, L [m] the heat transfer length scale , m [kg] the mass of a single gas molecule and $k_B = 1.38 \times 10^{-23}$ J/K is Boltzman's constant. The dimensionless pre-factor α is of order unity, and depends on the gas and contact surfaces [*Dushman*, 1949; *Gombosi*, 1994].

At our highest operating pressures of $5\,\mu\tau$ the conductivity of the rarefied air in our chamber ($L = 3\,\text{cm}$) is approximately 1500 times smaller than the STP conductivity of air: $k_{air}(\text{STP}) = 0.025\,\text{W/m}\,^\circ\text{C}$ [*Di Nello*, 1995]. The overall thermal conductance of the vacuum surrounding the tube can be estimated as $K_V = k_V A_{tube}/\Delta r$, where Δr is the difference between the chamber and tube radii, giving $K_V \sim 5\,\mu\text{W}/\,^\circ\text{C}$. This is three orders of magnitude smaller than the measured conductance of the ice; the high vacuum has effectively eliminated all conductive heat loss from the sample holder. Convective losses are also eliminated at such pressures. In the molecular regime a gas is not characterised by a temperature-dependent density, so buoyancy or convective effects do not apply.

An order of magnitude estimate of the radiative heat loss can be obtained by considering the tube to be radiating at its average temperature, $\text{T}(\frac{\text{L}}{2})$, into a radiation field at the chamber temperature, assumed to be the bath fluid temperature T_b. The radiative heat flux for this idealisation, which ignores the finite size of the chamber, is:

$$Q_{rad} = \epsilon_{ss}\sigma\left(T(\tfrac{L}{2})^{\,4} - {T_b}^{4}\right) \quad , \tag{6.6}$$

where the Stefan-Boltzman constant $\sigma = 5.67 \times 10^{-8}\,\text{W/m}^2\text{K}^4$, A is the tube area, and ϵ_{ss} is the 300 K, or 'longwave', emissivity of stainless steel, which depends on the surface condition. Values lie in the range 0.05 - 0.25, for polished to rough surfaces respectively. Modelling the temperature profiles for tube-only and ice sample measurements in this experiment, we found a good fit with $\epsilon_{ss} = 0.2$, so we use that value for the estimate here. With $T_b = -15\,^\circ\text{C}$ and the heater delivering 50 mW, we measured $T(\frac{L}{2}) \approx -13.5\,^\circ\text{C}$, giving Q_{rad} ≈10 mW. As this constitutes a 20% heat loss, radiative effects cannot be disregarded.

6.3.1 Parallel Conductance Method with Radiative Losses

In the analysis presented in Appendix C we assume that only radiative losses occur, and solve the problem of conduction along a bar of length L and circumference s with radiative losses from its surface. The boundary conditions

are: (i) the end of the bar is at the chamber temperature set by the circulating bath, $T(L) = T_b$, and (ii) the heat flux into the bar at the heater (z=0) is $(1-\beta)P/A$ where P is the applied power, A the surface area perpendicular to the heat flow, and β is the fraction radiated away from the copper base of the heater. Expressed in terms of the excess temperature, $\theta(z) = T(z) - T_b$ the solution is

$$\theta(z) = \frac{P(1-\beta)}{\alpha L K} \frac{\sinh(\alpha L(1-z/L))}{\cosh(\alpha L)} \quad , \tag{6.7}$$

where αL parameterises the relative strength of radiative loss to conductive flow. For circumference s, length L and thermal conductance K, $\alpha L = (qsL/K)^{1/2}$. Here q is a radiative heat loss coefficient, which we evaluate in Appendix C, assuming an isothermal chamber at T_b, to be $q \approx 3.5\epsilon_{ss}\sigma {T_b}^3$. The finite chamber size has reduced the pre-factor here from 4 to 3.5. For no radiative loss $q = \alpha L = 0$ and an expansion of the hyperbolic functions in equation (6.7) gives a linear profile. For no radiative loss from the heater $\beta = 0$, and the ideal result is recovered, $\theta(z) = (P/K)(1 - z/L)$.

We measure the temperature gradient at the centre of the tube, where boundary effects are least pronounced, and heat flow expected to be most uniform. However radiative losses cause a reduction in the conductive heat flow and therefore in the magnitude of the gradient here, $\mid \frac{\partial T}{\partial z} \mid_{L/2}$. Therefore equation (6.2) overestimates the thermal conductance. In light of this we define the 'apparent conductance' as:

$$K_{app} = \frac{P}{L \mid \frac{\partial T}{\partial z} \mid_{L/2}} \quad . \tag{6.8}$$

In Appendix C we derive an analytical expression for K_{app} by differentiating equation (6.7), expanding to order $(\alpha L)^2$, and substituting $(\alpha L)^2 = (qsL/K)$. The apparent conductance of the tube plus ice, and tube are respectively (equations C.20, C.21):

$$K_{app} = \frac{1}{1-\beta}\left(K_{tube} + K_{ice} + \frac{3}{8}\, q(T_b) sL\right) \quad , \tag{6.9}$$

$$K_{app}{}' = \frac{1}{1-\beta'}\left(K_{tube} + \frac{3}{8}\, q({T_b}') sL\right) \quad . \tag{6.10}$$

Here β and β' are the fraction of heat radiated from the copper heater base, and T_b and T_b' the chamber temperature for the two cases. Expanding to order $(\alpha L)^2$ here introduces an error of less than 0.5%.

Following the ideal parallel conductance method we can calculate the apparent

conductance of the ice by subtracting (6.10) from (6.9):

$$K_{app,ice} = \frac{1}{1-\beta}K_{ice} + \left(\frac{1}{1-\beta} - \frac{1}{1-\beta'}\right)K_{tube} + \frac{19}{16}\left(\frac{{T_b}^3}{1-\beta} - \frac{{T_b}'^3}{1-\beta'}\right). \tag{6.11}$$

Here K_{ice} is the physical conductance of the ice that we would like to determine, and $K_{app,ice}$ the value calculated from the ideal parallel conductance method. For our chamber we calculate $\beta \approx 0.01$, $\beta' \approx 0.02$. With these values and experimental values for K_{app} and ${K_{app}}'$, the second term on the RHS is approximately -0.5% of the first term. As discussed below we have treated together results with T_b in the range -14 to -7 °C. Using the extreme values for T_b and ${T_b}'$ the third term on the RHS is at most ±1% of the first term.

We conclude that although radiative losses cause equations (6.9, 6.10) to overestimate the thermal conductance, the thermal conductance of the ice sample can be calculated as the difference in these apparent conductance values to an accuracy of approximately ±1%. It is convenient to retain the term 'apparent conductance' when discussing this calculation, and particularly when discussing the raw data below, but we stress that it does not represent a physically meaningful thermal conductance, in our case overestimating the actual conductance by approximately 20%. Hereafter we drop the subscript 'app' and K and K' represent the apparent conductance values from the ice and tube-only runs respectively.

6.3.2 Calculating Ice Conductivity and Uncertainties

Values of K and K' were calculated with equation (6.8) using a finite difference estimate of the average temperature gradient in the central third of the tube, $|\frac{\partial T}{\partial z}|_{L/2} = |\,(T_2 - T_4)/(z_2 - z_4)\,|$, and $L = 100\,\mathrm{mm}$. The apparent conductance values discussed below are therefore 'the apparent conductance for a 100 mm length'. The ice conductivity is ultimately calculated using equation (6.3) in which L cancels out with no associated uncertainty. We calculated a thermal conductivity value in this way for each ice sample measurement, and then made a weighted average of the individual runs for the three ice types: FY surface, FY sub-surface, and MY surface. As it is only appropriate to here use weights that derive from random uncertainties, we have distinguished random and systematic uncertainties.

Random uncertainties are those that increase the variance in the conductivity values, and include the run-to-run measured variations in $\Delta\mathrm{T} = (\mathrm{T}_2 - \mathrm{T}_4)$,

the underlying temperature resolution, and the uncertainty in the ice cross section, $\delta A_{ice}/A_{ice} \approx 1\%$ for each run. The individual terms on the RHS of equation (6.11) can vary by approxiamtely $\pm 1\%$ from run to run, so we have included a 1% random uncertainty in applying equation (6.3).

The uncertainties in input power and thermistor spacing are the same for all measurements and contribute systematic uncertainties that do not change from run to run. The finite contact area of the roughly spherical beads limits the precision of the thermistor spacing to $\Delta z = (z_2 - z_4) = 40.25 \pm 0.50\,\text{mm}$, a 1.25% uncertainty. From the analysis of the heater and measurement wire properties above (section 6.2) we use an uncertainty in the heater power $\delta P/P = 0.5\%$, giving a total systematic uncertainty of 1.75%.

6.4 Sample Characterisation

Blocks of ice approximately 450 mm on a side were cut with a chainsaw from sites at which thermal arrays had been installed over the 2003 Austral winter. Two surface blocks (0-450 mm) and one sub-surface block (450-900 mm) were cut from FY sea ice NW of the Delbridge Islands in McMurdo Sound, at array site FY03 (S 77 40.710, E 166 07.817). One surface block was cut from MY ice 1 km off Arrival Heights at site MY02 (S 77 50.189, E 166 36.779). See figure (5.1) for locations.

Small ice samples approximately 110 mm x 24 mm diameter were cored from these blocks with a custom-built coring unit shown in figure (6.4). The corer used three carbide cutters and flute angle of approximately 45°, and was powered by a speed-regulated mains-powered hand drill. Vertical alignment was maintained with a tripod-mounted brass collar. Best results were obtained by rinsing the corer with isopropyl alcohol prior to use. This prevented binding of the ice shavings which otherwise caused the drill to stall, and by lubricating the collar with mineral oil, which reduced vibrations that would otherwise snap the core. Coring created small free-standing ice pillars that were snapped off at their base and extracted with a length of tube identical to the sample holder, see figure (6.4). This tube was pre-cooled to prevent core melting. The cores were stored in zip-lock bags in a chest freezer at $-18\,^{\circ}\text{C}$. Figure (6.4) also shows the drilling set-up and photos of representative samples of the three ice types.

The density of the cores was determined from measurement of sample dimen-

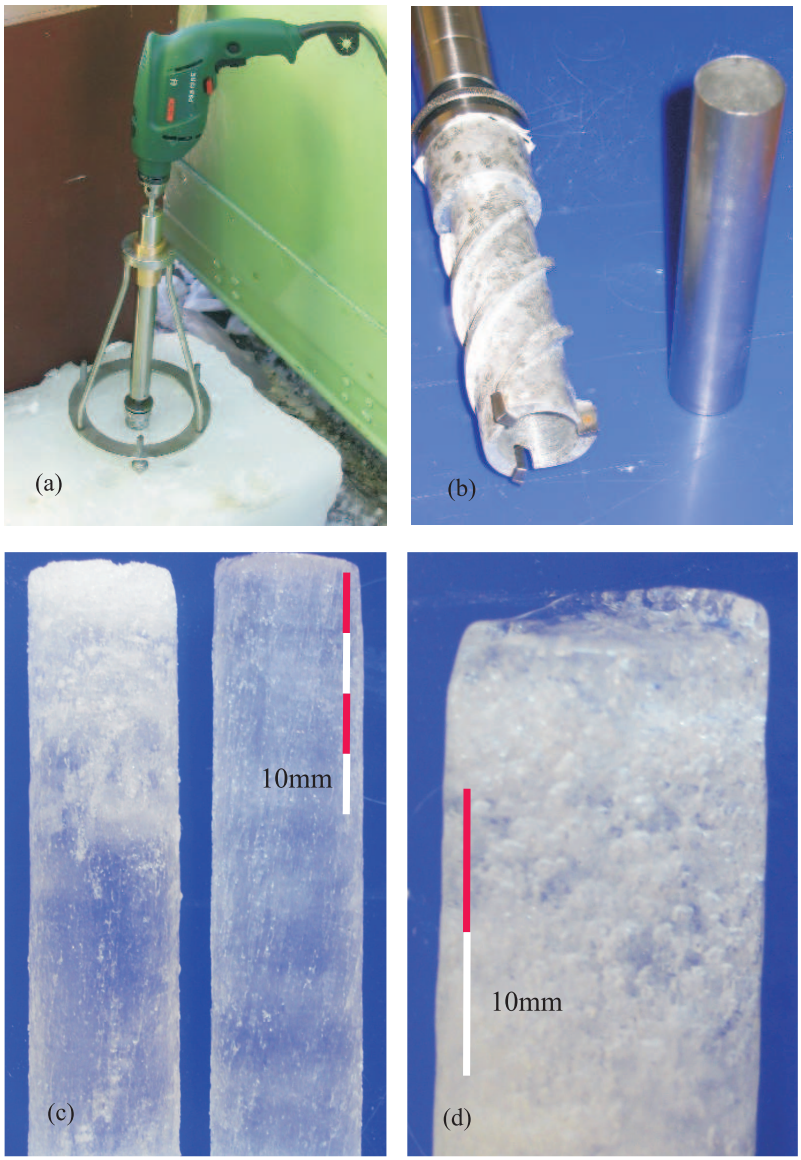

Figure 6.4: Coring equipment and ice cores. (a) Drill set-up, including tripod and drill. (b) Corer and stainless steel tube for core extraction. (c) FY surface core with 40 mm of highly light-scattering frazil ice at the top (left), and more uniform looking FY sub-surface core (right). Some helical striations were created by the drill bits. (d) MY surface core showing high air-bubble fraction. This is the bottom end of a 0-100 mm core which also shows some melting along the edges due to handling; measurements were not made on this core.

sions and mass. Results are shown in table (6.1). Salinity was determined from the electrical conductivity of melted cores measured with a Palintest conductivity probe with automatic temperature compensation. Individual ice cores were placed inside sealed plastic containers and left to melt and equilibrate at room temperature. The ~ 40 ml solutions were individually poured into clean 1 cm diameter test tubes so the conductivity probe could be fully immersed. The probe was flushed with double-purified Scott Base water until the reading in a test tube of this water was 0.01 ± 0.01 mS (milli Siemens) on the scale used for measurements. Measurements were made on two melted cores from each of the three ice types, in a cyclic fashion, to establish the reproducibility of the measurements. The difference in repeated runs was less than the sample to sample variation for the different ice types.

Two conversions were required to determine salinity S from the measured electrical conductivity σ_e. First, the ionic concentration M was calculated from the conductivity using a calibration curve obtained by measuring the salinity of four prepared NaCl solutions. Secondly, salinity, as mass of salts per unit mass of melted core, was determined from the ionic concentration by assuming standard sea-water composition of the cores. Strictly speaking, Oceanographers define the salinity of sea water by the ratio of its electrical conductivity to that of a standard KCl solution [*Eicken*, 2003]. We did not use this approach. We had no standard KCl solution, and the conductivity meter was calibrated only to a level for testing Scott Base water. Rather, we calculated the mass of salts per unit mass of ice, using a standard sea water composition, and by calibrating the meter. Only NaCl was available to prepare solutions for this calibration. Results are shown with the density values in table (6.1).

Ice Type /Depth	**Location**	**Position**	**Density** [$\mathbf{g/cm^3}$]	**Salinity** [$^0/_{00}$]
FY 0-100mm	NW of Tent Is.	S 77 40.710	0.90 ± 0.01	5.3 ± 0.2
FY 450-550mm	McMurdo Sound	E 166 07.817	0.92 ± 0.01	4.5 ± 0.2
MY 0-100mm	1km off Arrival Hts, McM Sd.	S 77 50.189 E 166 36.779	0.82 ± 0.01	0.2 ± 0.2

Table 6.1: Location, density and salinity of the three ice types examined. The FY sub-surface block was taken from directly below the FY surface block.

These salinity and density values agree entirely with the profiles of *Trodahl*

and Buckley [1990] obtained at a nearby site. The slightly higher salinity at the surface is characteristic of the 'C shaped' commonly observed in FY ice [*Weeks and Ackley*, 1986]. The MY ice has undergone brine drainage, as shown by a lower density and salinity than the FY ice. The very high bubble content suggests rapid re-freezing of surface water. This is likely to have been snow melt. The slightly lower density of the FY surface ice is attributed to the presence of frazil ice during the formation of which more air is trapped than in the congelation composing the sub-surface cores. About 40 mm of frazil ice is seen in the FY surface core in figure 6.4. The top 10 mm is particularly granular in appearance. We use these salinity and density values to characterise the ice types and as input for conductivity models to compare with our measured conductivities, not in the calculation of our experimental conductivity values.

6.5 Thermistor Calibration

We calibrated the five thermistors along the sample tube under experimental conditions to get a relative accuracy of 0.005 °C. With the circulating bath on, and the chamber in the insulated enclosure, a tight-fitting copper rod was inserted into the sample holder, and the thermistors read with the heater turned off. The high thermal conductivity of copper ($k_{Cu} \sim 200\,\mathrm{W/m\,^\circ C}$) optimises the uniformity of the tube temperature. Also, the thermal response time to any disturbances in the temperature at the top of the chamber is small due to the high thermal diffusivity of copper. For a length scale of 100 mm and thermal diffusivity of copper at these tempreatures ($D_{Cu} \approx 1.2 \times 10^{-4}\,\mathrm{m^2/s}$), the approximate thermal response time of the system is $t \sim z^2/D = 8\,\mathrm{s}$. Thermistor readings were stable to $\delta R = \pm 5\Omega\,(\pm 0.003\,^\circ\mathrm{C})$ for up to 15 minutes.

The resistive offsets with respect to the bottom thermistor t_1 were measured at $-9.5\,^\circ$C and $-15\,^\circ$C to the nearest $10\,\Omega$, twice the resistance resolution, giving an uncertainty in the temperature offsets of approximately $\pm 0.006\,^\circ$C. The measured resistive offsets, and corresponding calculated temperature offsets are shown in table (6.2). The temperature offsets are the values that must be added in the calibration. The $-9.5\,^\circ$C offsets were reproduced with two trials separated by 4 days with air temperatures $-16\,^\circ$C and $-12\,^\circ$C. The calibration at $-15\,^\circ$C was reproduced in two runs 10 days apart with air temperatures $-11\,^\circ$C and $-13\,^\circ$C.

As discussed in Chapter 3 a 'one point' calibration is often made with such

$\mathbf{T_{bath}}[\,^\circ\mathrm{C}]$	**Offset**	$\mathbf{t_1}$	$\mathbf{t_2}$	$\mathbf{t_3}$	$\mathbf{t_4}$	$\mathbf{t_5}$
$-9.5\,^\circ$C	δR[kΩ]	0	-0.21	-0.23	-0.07	0.01
	$\delta T[\,^\circ\mathrm{C}]$	0	-0.09	-0.10	-0.03	0.00
$-15\,^\circ$C	δR[kΩ]	0	-0.21	-0.22	-0.01	0.08
	$\delta T[\,^\circ\mathrm{C}]$	0	-0.07	-0.07	0.00	0.03
Applied Offsets	δT$[\,^\circ\mathrm{C}]$	0	-0.08	-0.085	-0.015	-0.015

Table 6.2: Measured resistive offsets in the thermistors (t_1 - t_5) at $-9.5\,^\circ$C and $-15\,^\circ$C and corresponding temperature offsets. Bottom line shows temperture offsets applied to all measurements, see text.

thermistors. As seen in table (6.2) we have two such 'one point' calibrations, with slightly different offsets. These differences are as likely to reflect experimental uncertainty as a physical effect, so we have chosen to make the simplest calibration by averaging the two temperature offsets for each thermistor. Over the range $-6.5\,^\circ$C to $-15\,^\circ$C these offsets were added to the temperatures calculated from the measured resistance using equation (3.2). The conductivity calculations involve only the difference $\Delta T = (T_2 - T_4)$. The relative difference between the t_2 and t_4 offsets at the two calibration temperatures is $0.01\,^\circ$C, establishing the ultimate accuracy of ΔT.

6.6 Measurement Procedure

For the tube-only runs, the air-release screw was removed and with the top O-ring sealed cap in place, the chamber and tube were evacuated. For measurements on ice samples the air-release screw was replaced. Samples were removed from the storage freezer and carefully inserted into the tube after silicon vacuum grease had been smeared inside the tube to optimise thermal contact. Aside from these differences the measurement procedure is the same for the tube only- and ice- runs.

When removed from the storage freezer, the ice samples had a uniform temperature or about $-18\,^\circ$C. To reduce the time to reach the equilibrium temperature, profile the heater power was increased above the measurement value for a short time. It was then reduced to the measurement value and the temperature profile monitored over time. When the temperature gradient levelled out

as a function of time, thermal equilibrium was considered to have occurred. A small rate of change in the entire profile was allowed, so long as the temperature difference between successive thermistors remained constant to within $\pm 0.01\,^{\circ}\mathrm{C}$. Uncertainty in determining when equilibrium was reached arose because temperature perturbations propagating down the tube could superimpose a small temperature gradient, disrupting the temperature profile, and potentially causing the $|\frac{\partial \mathrm{T}}{\partial \mathrm{z}}(\mathrm{t})|$ curve to level out even though equilibrium had not been reached. In practise this effect could never be fully excluded, but we sought to minimise it by keeping the chamber as isothermal as possible.

For the ice and no-ice cases, we selected heater powers P and P' respectively, to produce similar temperature gradients. This was done to minimise the influence of any unexpected systematic effects on the heat flow, specifically the radiative losses. From a scientific perspective it would be preferable to make the measurements with the temperature gradient comparable to that which occurs naturally in the ice sheet, $|\frac{\partial \mathrm{T}}{\partial \mathrm{z}}| \sim 10\,^{\circ}\mathrm{C/m}$, giving $\Delta T = 0.4\,^{\circ}\mathrm{C}$ for an inter-thermistor spacing of 40 mm. To reduce the fractional uncertainty in measuring $|\frac{\partial T}{\partial z}|_{L/2}$ we induced gradients of $\sim 35\,^{\circ}\mathrm{C/m}$. No part of any measured sample was warmed above $-5\,^{\circ}\mathrm{C}$. This is the temperature at which the proposed 'percolation threshold' of brine volume fraction $5\,{}^{0}/_{00}$ is reached for ice with salinity $5\,{}^{0}/_{00}$; the rule of fives of *Golden et al.* [1998].

6.7 Results and Analysis

We measured the total and tube-only apparent conductance, K and K', at $T_b = -9.5\,^{\circ}\mathrm{C}$ and $T_b = -15\,^{\circ}\mathrm{C}$, and with heater powers in the range 17 to 68 mW. The results showed no trend in heater power. No such dependence is expected, so we conclude that there are no systematic effects associated with the heat input. In figure (6.5) the apparent conductance of ice and tube-only runs are plotted as a function of $T(\frac{L}{2})$, the temperature at which the conductance was measured. Note that the vertical axis tick-interval is $1\mathrm{mW}/\,^{\circ}\mathrm{C}$ on both axes. Tube conductance measurements were made at $-9.5\,^{\circ}\mathrm{C}$ with chamber pressures $0.5 - 5\,\mu\tau$, and in two cases at $-15\,^{\circ}\mathrm{C}$ with the chamber evacuated but the sample space containing air at 1 atm. After accounting for the conductivity of air in the tube, these measurements were consistent. Any convective contribution was therefore negligible. The different ice categories are shown separately: FY surface, blue triangles; FY sub-surface, open red diamonds; and MY surface black squares. Within each class the scatter is larger than in the tube data, even accounting for the two-fold difference

in magnitude. We return to the possible causes of this scatter later in this section.

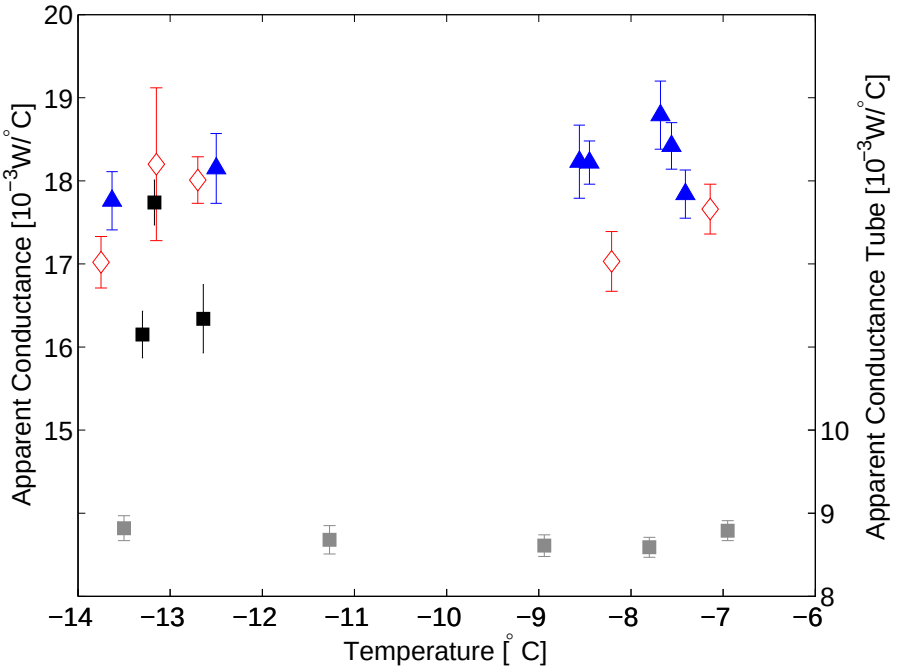

Figure 6.5: Apparent conductance results. Left axis: K, apparent conductance of runs with ice samples loaded: Blue triangles, FY surface; red diamonds, FY sub-surface; black squares, MY surface. Right axis: K', apparent conductance of tube-only runs, grey squares. Note the vertical axis tick-interval is 1 mW/°C for both the left and right axes.

Across the temperature range −14 °C to −7 °C the thermal conductivity of 304 stainless steel increases by approximately 1% [*Atlas*, 2003], which is smaller than the uncertainty in our individual measurements. As we are unable to resolve this variation we have used a weighted average for the apparent conductance of the tube over this temperature range: $K' = 8.70 \pm 0.23\,\mathrm{mW/°C}$. Over this temperature range where the brine fraction is low, the predicted temperature dependence of sea ice thermal conductivity is established by the temperature dependence of the fresh ice component, $k_i(T)$. Combining the expected temperature dependence of $k_i(T)$ and stainless steel, the area-weighted conductance of the tube and ice in parallel is predicted to show a 0.5% decrease from −14 °C to −7 °C, again below our scatter.

An ice conductivity value for each ice run was calculated using equation (6.3)

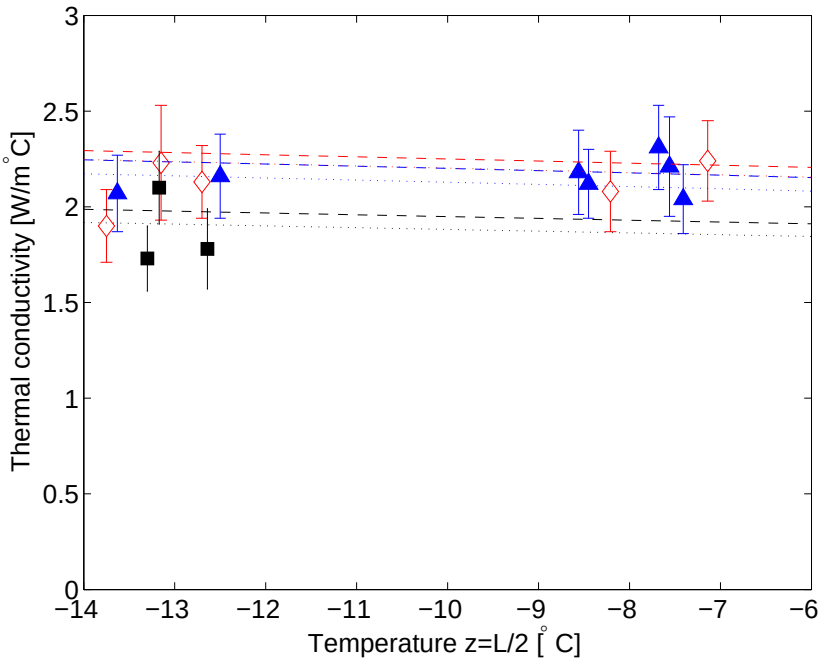

Figure 6.6: Plot of all thermal conductivity values for the three classes: FY surface, blue triangles; FY sub-surface, open red diamonds; black squares, MY surface ice. Lines are predictions of our slight modification to the Yen/Schwerdtfeger conductivity model, for the range of measured density and salinity for each class; same colouring as symbols.

with $K' = 8.7 \pm 0.23\,\mathrm{mW/\,^{\circ}C}$, $L = 100\,\mathrm{mm}$, and $A_{ice} = \frac{\pi}{4} d_{ice}^2$ as measured for each core. The individual conductivity values, along with the weighted ice type averages, are collated in table (6.4) at the end of this section. The final uncertainty in the conductivity of each ice type is the sum of the 1.75% systematic uncertainty discussed above, and a weighting of the random uncertainty for the different runs in each category.

Figure (6.6) shows all of the measured conductivity values and output from our model for k_{si} (see Chapter 2). As in figure (6.5), blue triangles represent FY surface ice, open red diamonds FY sub-surface ice, and black squares MY surface ice. The two lines for the model output for each ice type give the conductivity limits due to he uncertainty in density and salinity. There is good agreement between the measured conductivity and the predicted values in figure (6.6). Furthermore, this figure clearly shows that difference in conductivity between the FY surface and FY sub-surface ice is less than the scatter in each class.

Ice Type/ Depth [cm]	**Density** $\overline{\rho}$**[g/cm^3]**	**Salinity S[‰]**	$\overline{\mathbf{T}}(\frac{\mathbf{L}}{\mathbf{2}})$ [°C]	**Measured k** [W/m °C]	**Modelled k** [W/m °C]
FY $0-10$	0.90 ± 0.01	5.3 ± 0.2	-9.4	2.14 ± 0.11	2.18 ± 0.02
FY $45-55$	0.92 ± 0.01	4.5 ± 0.2	-11.0	2.09 ± 0.12	2.22 ± 0.02
MY $0-10$	0.82 ± 0.01	0.2 ± 0.2	-13.0	1.88 ± 0.13	2.05 ± 0.05

Table 6.3: Comparison of experimental thermal conductivity of the three ice types with predictions of our conductivity model using the measured average density and salinity, and temperature. $\overline{\mathrm{T}}(\frac{\mathrm{L}}{2})$ is the average temperature for runs in each ice type.

Table (6.3) shows a comparison between the ice-type averages and the range of values predicted by our model described in Chapter 2, evaluated at the average temperature for each ice type, $\overline{T}(\frac{L}{2})$, using the range in measured density and salinity values. Within uncertainties, the average conductivity is consistent with the prediction of this model for all three ice types. The overlap is small in each case though, at the upper range of the measured values, and lower end of the modelled values.

Notably, no reduction in conductivity is seen between the FY surface and sub-surface ice. Although the average surface value is slightly higher, this difference is not significant compared with the uncertainties. In fact, omitting the lower, and seemingly outlying value 1.90 W/m °C from the FY sub-surface ice, gives an average of 2.16 ± 0.13 W/m °C. However, despite it improving the comparison, we have no sound basis for discarding this value, so have not done so. Within an overall uncertainty of $\sim 6\%$, we resolve no difference in the conductivity of FY ice from depths of 5 cm and 50 cm. The lower conductivity of the MY surface ice is expected on the basis of its high air volume, hence low density.

Our model predicts a lower range of conductivities for the FY surface ice compared with the FY sub-surface ice because of the approximately 2% lower average density in the surface cores. However, due to 40 mm of frazil ice at the top of the FY surface cores, it is likely that the density in the central third of the FY surface cores - where the conductivity was measured - is slightly higher than the average value of 0.9 g/cm^3. For this reason we expect that the measured conductivity of the FY surface cores to lie near the top of the range of values predicted with $\overline{\rho}$. Using the average salinity $\overline{S}$ as input for the Yen model introduces no similar problems because the salinity at the centre

of the core is well estimated by $\overline{S}$. Furthermore the conductivity model is only weakly dependent on salinity. For salinities and temperatures relevant to these measurements, a salinity variation of $4\,{}^{0}/_{00}$ is needed to produce the same predicted change in conductivity as a density variation of $0.01\mathrm{g/cm}^3$.

The scatter in the ice conductivity values in figure (6.6), and table (6.4) derives largely from scatter in the ice conductance values, which is due to the difficulty in accurately measuring the equilibrium temperature gradient. This scatter is larger than the tube-only runs, cf. figure (6.5), for two main reasons. The first is that when an ice sample is loaded the thermal time constant $\tau \sim z^2/D_{eff}$ increases by a factor ~ 10 due to the decrease in effective thermal diffusivity of the ice and tube system. The volumetric heat capacity $c_{v,eff}$ increases approximately in proportion with the area, a factor of ~ 20, but the conductance increases only by a factor of ~ 2, giving a factor of 10 decrease in $D_{eff} = k_{eff}/c_{v,eff}$. This means that not only is thermal equilibrium approached more slowly with ice samples loaded, but any perturbations to the temperature profile caused by disturbances in the chamber top temperature also propagate more slowly than for tube only runs. Such disturbances disrupt the temperature profile over a longer time and are harder to identify. The temperature profiles were never completely static. For most measurements the temperature difference between adjacent thermistors was constant to within $0.01\,^{\circ}\mathrm{C}$ over 10 minutes. For $|\frac{\partial \mathrm{T}}{\partial \mathrm{z}}| \sim 35\,^{\circ}\mathrm{C/m}$ and thermistor spacings of 40 mm, this equates to a less than 1% uncertainty in $|\frac{\partial \mathrm{T}}{\partial \mathrm{z}}|$.

The second source of enhanced scatter in the ice measurements is the quality of thermal contact between the tube and the ice. It is not quite true that our analysis assumes no thermal resistance between the ice and the tube because a thermal resistance which is constant down the length of the tube will give the same temperature gradient on the outside of the tube as along the ice inside. Despite smearing silicon grease inside the tube there will be unavoidable run-to-run variations not only in the thermal contact but therefore also in how uniform the heat flow is along the ice cores, even in the central third.

Furthermore, there is natural variability in the samples themselves. Variations in density of $\pm 1\%$ are not improbable, resulting in conductivity variations of $\pm 0.02\ \mathrm{W/m\,^{\circ}C}$. As the observed variability is several times larger than this, this is not the main cause of scatter.

Date	**Core**	**P [mW]**	**T_b [°C]**	**T_{air} [°C]**	**k [W/mK]**	**δk_{rand}**	**δk_{sys}**
5-Nov	01-A	66.8	-9.5	-6	2.31	0.18	0.04
6-Nov	01-C	66.8	-9.5	-10	2.21	0.19	0.04
6-Nov	01-C	34.1	-9.5	-11	2.18	0.19	0.04
8-Nov	01-D	66.8	-9.5	-12	2.04	0.15	0.04
8-Nov	01-D	34.1	-9.5	-7	2.12	0.14	0.04
12-Nov	02-A	34.1	-15	-9	2.07	0.16	0.04
12-Nov	02-A	66.8	-15	-9	2.16	0.18	0.04
						0.06	0.04
FY surface					**2.14**	**0.11**	
4-Nov	03-B	66.8	-15	-18	2.23	0.30	0.04
10-Nov	03-C	66.8	-9.5	-6	2.08	0.18	0.04
11-Nov	03-C	34.1	-9.5	-4	2.24	0.17	0.04
12-Nov	03-D	34.1	-15	-12	1.90	0.15	0.03
12-Nov	03-D	66.8	-15	-13	2.13	0.15	0.04
						0.07	0.04
FY sub-surface					**2.09**	**0.12**	
13-Nov	MY-b	66.8	-15	-11	1.78	0.17	0.03
13-Nov	MY-b	49.1	-15	-20	1.73	0.14	0.03
14-Nov	MY-a	49.1	-15	-18	2.10	0.15	0.04
						0.09	0.03
MY surface					**1.88**	**0.13**	

Table 6.4: Measured conductivity values for the three ice types. P [mW] is heater power. T_b is temperature of the recirculating bath fluid, and by assumption, the chamber. T_{air} is air temperature at time of measurement. The last line for each ice type gives the average conductivity (weighted with random uncertainties δk_{rand}) and the total uncertainty - the weighted random uncertainty plus the systematic uncertainty δk_{sys}.

6.8 Discussion of Conductivity Results

In this section we discuss the results from both our thermal array and parallel conductance measurements. We first summarise the results and then compare them, first with each other and previous measurements, and then with the values predicted by our theoretical model and the parameterisation of *Maykut and Untersteiner* [1971].

The conductivity profiles from the analysis of our array measurements show a roughly constant conductivity between a near surface reduction and an increase close to the ice/water interface. This behaviour is opposite to that predicted from the expected temperature-dependence. Models of $k_{si}(T)$ predict a reduced conductivity near the ice/water interface due to the lower conductivity of the increasingly large brine volume, and an increase towards the colder surface due to the temperature-dependence of the conductivity of the fresh ice component. We believe that this discrepancy is due to artifacts in our finite difference analysis method.

We firmly believe that the apparent reduction in the near-surface conductivity of FY sea ice, also observed by *Collins* [1998]; *McGuinness et al.* [1998]; *Trodahl et al.* [2000, 2001], is an artifact of the analysis method. The finite difference estimates of $\partial U/\partial t$ vs. $\partial^2 T/\partial z^2$ become unreliable when their are temperature components for which $\omega\Delta t$, and/or $\Delta z\sqrt{(}\omega/2D)$ is large. These estimates suffer a time lag, resulting in loops in the scatter plots of $\partial U/\partial t$ vs. $\partial^2 T/\partial z^2$, as previously observed and associated with possible hysteric effects within the ice [*Collins* [1998]; *McGuinness et al.* [1998]; *Trodahl et al.* [2000, 2001]; Karoline Frey, personal communication, 2002]. This effect causes larger relative errors in $\partial^2 T/\partial z^2$ than in $\partial U/\partial t$, so the geometric-mean least squares gradient underestimates the conductivity. Simulations show that filtering, via numerical convolution with a gaussian window, does not remove this effect very near the surface. The effect is shallow because the high-frequency components responsible for it have a small penetration depth. Temperatures near the surface are also the most prone to measurement error, due to heat flow perturbation caused by the mismatch between the thermal conductance of the probe and the ice.

We also believe that the observed increase in conductivity near the ice/water interface is an artifact of the analysis, arising because the temperature variations are weak near the isothermal interface and the method becomes noise-limited. *Collins* [1998] and *McGuinness et al.* [1998] have previously associated a reduction in the correlation coefficient (r-value) of the least squares fitting,

with depth, as a signature of increasing non-linearity in the heat flow, and therefore a possible signature of convective heat flow. We consider this an unreliable association because such a reduction naturally occurs with depth as the signal to noise worsens.

The conductivity profiles are approximately level over the depths between about 50 cm and the depth at which the analysis becomes noise-limited. This is clear in the $k(z)$ profiles from two arrays in FY ice in McMurdo Sound (site FY02). Signal to noise was good at this site due to the high precision of our custom built logger and thick ice (deeper isothermal boundary), allowing the conductivity to be determined accurately to greater depth. Between 50 - 125 cm, spanning temperatures between $-25\,^{\circ}\mathrm{C}$ - $-10\,^{\circ}\mathrm{C}$, we found $k = 2.29 \pm 0.07\,\mathrm{W/m\,^{\circ}C}$. At our FY ice site in the Chukchi Sea near Point Barrow, the ice only grew to 130 cm and a plateau in the conductivity profile was less clear. Between 0.49 - 84 cm, and a temperatures range $-15\,^{\circ}\mathrm{C}$ - $-5\,^{\circ}\mathrm{C}$ we found $k = 2.26 \pm 0.11\,\mathrm{W/m\,^{\circ}C}$. At our MY McMurdo site, instrument failure meant that only a short period of data were available, and these were at temperatures close to the maximum allowed in our analysis. We found $k = 2.03 \pm 0.04\,\mathrm{W/m\,^{\circ}C}$ over the small depth range 30 - 40 m and temperature range $-6\,^{\circ}\mathrm{C}$ - $-5\,^{\circ}\mathrm{C}$. As this MY ice has a lower density than the FY ice, this lower conductivity value should not be interpreted as clearly identifying a temperature-dependence.

With our parallel conductance method (PCM) we measured the thermal conductivity of small samples of FY surface (0-10 cm), FY sub-surface (45-55 cm) and MY surface (0-10 cm) sea ice. From several different ice cores for each class, our results for FY surface, and sub-surface ice are $2.14 \pm 0.11\,\mathrm{W/m\,^{\circ}C}$ and $2.09 \pm 0.12\,\mathrm{W/m\,^{\circ}C}$ respectively. For very bubbly, low density MY surface ice we did resolved a 10% reduction, finding $k = 1.88 \pm 0.13\,\mathrm{W/m\,^{\circ}C}$. These results are all within the prediction of our modification of the Yen/Schwertdfeger conductivity model described in section (2.2). More importantly, we resolve no significant difference, and certainly no large reduction, in the conductivity of FY surface (0-10 cm) and sub-surface (45-55 cm) ice. These measurements provide direct evidence that contradicts the near-surface reduction resolved by the array measurements. We believe that the PCM results are most robust, and the array-derived near surface reduction to be erroneous.

Figure (6.7) shows a comparison of the results of both of our methods with historical measurements, our theoretical prediction, and the Untersteiner's parameterisation. Boxes and coloured symbols show results from our thermal array and parallel conductance methods, lines are theoretical results, and grey

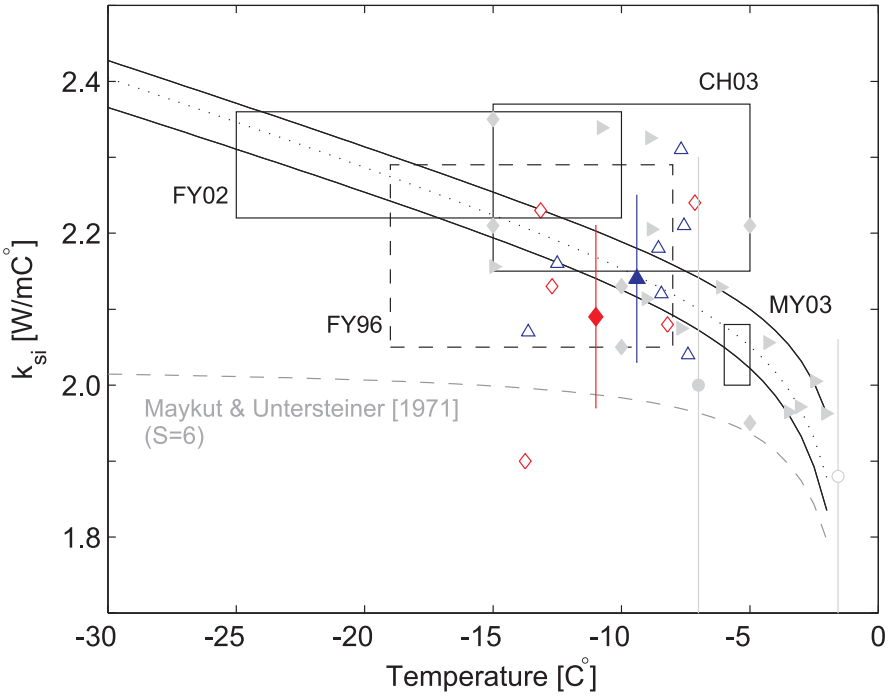

Figure 6.7: Comparison of measured and predicted k_{si} values. Parallel conductance method results: FY surface ice, blue squares; FY sub-surface ice red diamonds; small symbols individual measurements ($\sim \pm 0.15\,\mathrm{W/m\,^{\circ}C}$ error bars omitted), and large symbols averages. Thermal array results: black boxes centered on averaged conductivity value, with width and height giving measured temperature range and conductivity uncertainty. Previous measurements, grey points: solid circle, *Schwerdtfeger* [1963] comparative gradient method (S=6); open circle, *Lewis* [1967] ice interface value; diamonds, values calculated from *Nazintsev* [1959] diffusivity measurements (S=3.6, 3.9); solid triangles, Nazintsev laboratory measurements (S=4.7) *Doronin and Kheisin* [1977]. Lines: solid black, our predicted bounds of k_{si} for $S = 4 - 6$, $\rho = 0.9 - 0.92\,\mathrm{g/cm^3}$; dashed grey, parameterisation of *Maykut and Untersteiner* [1971] for S=6; black dotted, parameterisation suggested in text.

points are previous measurements. Individual measurements with the parallel conductance method are shown as small blue squares (FY surface) and red diamonds (FY sub-surface), where error bars of $\sim \pm 0.15\,\mathrm{W/m\,^{\circ}C}$ have been omitted) and the larger symbols with error bars are the ice-type averages. The black boxes depict the array results. They are centered on the conductivity values listed above, and their width and height indicate the temperature range, and uncertainty. Results are shown for McMurdo sites FY02 and MY03, and

FY Chukchi site CH03. The dashed box shows results from *Collins* [1998] for FY ice in McMurdo Sound, from 1997 temperatures and depths 0.5 - 1.5 m. The previous results shown with small grey symbols are: the ice/water interface value of *Lewis* [1967] (open circle with error bars), the comparative gradient value of *Schwerdtfeger* [1963] (solid circle with error bars), the values calculated from the diffusivity measurements of *Nazintsev* [1959] (diamonds), and Nazintsev's results from artificial sea ice with S=4.7 (solid triangles). See section (2.4) for details of these measurements.

Given the difference in ice, particularly density, the MY values should be considered separate from the FY values. The temperature-dependence of k_{si} is then not well identified by these results. The coldest temperature values are set by our most reliable array measurements at FY02. Measuring the conductivity at low temperatures is hampered by the inapplicability of our analysis near the surface. Similarly, we are unable to measure any decrease as the ice warms above $-5\,^{\circ}\mathrm{C}$ near the ice/water interface where temperature variations are weak, our analysis noise limited, and the internal energy too highly dependent on salinity. Excluding one outlier, our parallel conductance method measurements agree well with our array results. The average values are consistent with our theoretical prediction. The historical data show a similar scatter to our parallel conductance methods measurements, and within this scatter, do overlap quite well.

Overall, our results show a good agreement with the the range predicted by our conductivity model for typical FY parameters, $S = 4 - 6$ and $\rho = 0.9 - 0.92\,\mathrm{g/cm^3}$ (solid black lines). So do the historical data, particularly in the temperature dependence above $-5\,^{\circ}\mathrm{C}$ which we cannot resolve. The deviation from the combined results and the predicted range is about 5%, similar to the uncertainty in the conductivity of pure ice. The value of $k_i(0\,^{\circ}\mathrm{C}) = 2.14\,\mathrm{W/m\,^{\circ}C}$ in our model has an uncertainty of about $\pm 0.05\,\mathrm{W/m\,^{\circ}C}$. Nevertheless, the overall agreement between our experimental methods, the previous measurements, and our theoretical prediction is encouraging.

Both our data and the previous results show a conductivity about 10% higher than that predicted by Untersteiner's parameterisation. We attribute this difference to Untersteiner's low, and temperature-independent value for the conductivity of pure ice, $2.03\,\mathrm{W/m\,^{\circ}C}$. In our model we have used $k_i(T) = 2.14 - 0.011\,T$, where T is temperature [$^{\circ}$C], interpolated from the data compiled more recently by *Slack* [1980]. *Untersteiner* [1964] references only the experimental work of *Malmgren* [1927], who measured quite low conductivity values (section 2.4.2), and the theoretical model of *Schwerdtfeger* [1963] who

used a constant pure ice conductivity, $k_i = 2.09\,\mathrm{W/m\,^\circ C}$. Based on the subsequent experimental results discussed here, and underwritten by the good fit of our modified theoretical result (also based on subsequent $k_i(T)$ values), we considered that this parameterisation of k_{si} needs revisiting, and tentatively propose an alternative. The black dotted line in figure (6.7) shows the equation

$$k_{si} = 2.09 - 0.011\,T + 0.117 S/T \qquad [\mathrm{W/m\,^\circ C}] \quad , \tag{6.12}$$

where T is temperature [°C] and S salinity [$^0/_{00}$]. This form was found by retaining the S/T term from *Maykut and Untersteiner* [1971], and the temperature coefficient from our linear fit to the pure ice data of *Slack* [1980], and adjusting the constant term to lie between the bounds predicted by our model, which fits the experimental results quite well. Equation (6.12) does not represent an analytical result.In the same sense as Untersteiner's original parameterisation, which *pre-dated the availability of all of the data in figure* (6.7), it is an empirical fit to the presently available data. The data in figure (6.7) suggest that it is important to retain both the linear and inverse temperature terms. We imagine that implementing this result in sea ice models, rather than the two-term result used since *Maykut and Untersteiner* [1971], would not add significant computational burden. If a single constant value is required, it should represent an average over the depth of the ice, and we suggest that a value is chosen according to the expected range of local ice temperatures. For Antarctic temperatures, indicated by the range of our array measurements, we propose $2.2\,\mathrm{W/m\,^\circ C}$. A value as low as $2.05\,\mathrm{W/m\,^\circ C}$ may be appropriate for expected temperatures above $-10\,^\circ\mathrm{C}$. The constant value $2.03\,\mathrm{W/m\,^\circ C}$, which is sometimes used, is considered too low for all but the warmest temperatures.

We finally note that the parallel conductance method results for the MY surface ice have been omitted from this comparison. This is only because the very low density of that ice, $0.82 \pm 0.01\,\mathrm{g/cm^3}$ is much lower than the typical densities found in either bulk FY or MY ice. This value does overlap our predicted values (see previous section) but is inappropriate in the present discussion.

Chapter 7

Thermal Properties of Antarctic Permafrost

In this chapter we report on thermal array measurements made in the ice-cemented permafrost at Table Mountain in the McMurdo Dry Valleys of Antarctica. This work was initiated by members of Victoria University's Antarctic Research Centre as part of ongoing geological and geophysical research in the extended Dry Valleys area. They installed thermal arrays similar in design to the sea ice arrays in November 2000. The present author made revisions to the data logging program, serviced the instrumentation site in November 2002, and completed all data analysis. An initial report on this project based on the analysis of temperature data from November 2000 - January 2002 has already been published [*Pringle et al.*, 2003]. In this chapter we call on discussion from that paper and summarise its main results. Between November 2002 - December 2003 the sampling interval was reduced from $\Delta t = 4$ hours to 1 hour, and data averaging in the logger program improved. Together with a better understanding of the analysis scheme, these factors have enabled a more accurate analysis of the new data. This has led to some modification of our initial results and conclusions.

7.1 Dry Valleys Introduction

The extreme climate of the Dry Valleys is characterised by very low precipitation (< 10 cm/year in the form of fine 'diamond dust' snow), low annual mean temperatures (< -20 °C), large annual temperature amplitude (~ 15 °C) and

strong, katabatic winds [eg. *Thomson et al.*, 1971; *McKay et al.*, 1998]. The valleys are not ice covered primarily because the Trans-Antarctic Mountains block ice from the polar plateau flowing into and through the valleys [*McKay et al.*, 1998]. The ground surface is typically an ice-free, rock debris mineral soil, up to 1 m deep, overlying a perennially frozen ice/mineral soil matrix, which us referred to here as 'ice-cement'.

The very cold, very dry Dry Valley permafrost represents a little-studied end member of terrestrial permafrost environments [*Putkonen et al.*, 2003]. Recently there have been two main drivers for increased scientific interest in the region. The region has been identified as the best terrestrial analogue of the Martian polar regions, in which patterned ground is observed and ground ice is likely to exist [eg. *Mellon*, 1997; *Malin and Edgett*, 1998]. There has been a debate surrounding the age and stability of Beacon Valley ground ice which has been indirectly dated as 8.1 My making it the oldest ice on earth [eg. *Sugden et al.*, 1995; *Hindmarsh et al.*, 1998; *Marchant et al.*, 2002]. Attention has also focussed on polygonal patterned ground features, which are found extensively throughout the greater Dry Valley region, ranging in diameter from $1 - 20\,\mathrm{m}$ [*Péwé*, 1959; *Marchant et al.*, 2002; *Putkonen et al.*, 2003; *Sletten et al.*, 2003]. This widespread occurrence of sand-wedge polygons reflects contraction crack networks within the underlying ice-cement (buried ice in the case of Beacon Valley).

Our focus is the thermal regime and properties of two sites, separated by 100 m, at Table Mountain in the Dry Valleys, see figure (7.1). These two sites show different scale surface patterning, and furthermore, one of the sites lies in a debris flow of unknown age or flow mechanism, discussed below. In this chapter we characterise the ground temperatures and the depth-dependent thermal properties at the two sites which we correlate with lithographic and ice-content profiles of the top 2 metres at the sites. In particular we are interested in any differences in thermal properties that might contribute to the factor-of-three difference in polygon diameters between these nearby sites. Previous temperature measurements have been made in near-surface layers in Antarctic permafrost [*Matsuoka et al.*, 1990; *McKay et al.*, 1998], but we believe this is the first in-depth study of the thermal properties of the sub-surface.

Although there is the potential for low-level vapour transport in most soils, with a resulting transfer of latent heat, such transport is expected to be exceedingly small in the ice-rich ground, and due to the very low year round temperatures, there is no expectation of latent heat effects or heat flow other than by conduction. We proceed by this assumption, and from the temper-

ature record examine the depth- and seasonal- dependence of the apparent thermal diffusivity (ATD). One site shows a weakly- and smoothly- varying ATD profile, whereas the other shows an abrupt two-fold increase over a sharp compositional boundary. We present the results of several time series methods for computing the mean ATD profile. In particular, we are interested in the performance of these methods at this abrupt boundary. From heat capacity profiles determined from the composition of cores recovered from each site, and the ATD profiles, we calculate apparent thermal conductivity profiles, which we correlate with core composition.

7.2 Site Details

The experimental sites TM1 (S 77° 57′ 36″; E 161° 57′ 15″, 1840 m above mean sea level) and TM2 (S 77° 57′ 39″; E 161° 57′ 25″, 1852 m asl.) are on the northwest flank of Table Mountain, which is on the south side of the Ferrar Glacier near the eastern margin of the Dry Valleys, see figure (7.1). Table Mountain is made up of sandstones of the Beacon Supergroup which have been intruded by Ferrar Dolerite (Jurassic). These formations are mantled by a linear band (2 × 5 km) of Sirius Group, a glacial till [*Passchier et al.*, 1998] with a probable, but controversial, mid-Miocene age [*Miller and Mabin*, 1998]. Sirius Group sediments crop out in a series of low (< 3 m) ridges and have a hardness of dried mud, but below depths of 0.5 m are generally ice-cemented.

The north-western flank of Table Mountain also has several debris flows that appear to originate from weathered dolerite dikes. Although the age and mechanism by which these debris flows formed are unknown, they are clearly defined by large-scale polygonal ground, see figure (7.1). The debris flow in our study area truncates the Sirius Group which is marked by small scale polygons in figure (7.1). Regardless of the sediment composition and soil horizonation, loose, dry, ice-free permafrost in the vicinity of these sites is 0.10-0.5 m thick and lies on top of the ice-cemented permafrost. The contact between the dry and ice-cemented permafrost is not flat, but undulates depending on the aspect of the ground surface and overlying materials. The depths quoted here are referenced to the level surface at each installation site. Note that the dry permafrost overlying the ice-cemented permafrost is not an 'active layer'. Aside from direct solar heating of surface rocks during the summer, this layer is below freezing year round but is simply ice-free. The sublimation and evaporation rates of the sub-surface ice through such layers is currently under investigation [eg. *Sugden et al.*, 1995; *Hindmarsh et al.*, 1998; *Marchant et al.*, 2002; *Putkonen*

et al., 2003]. A desert pavement of ventifacted dolerite pebbles and cobbles covers the surface at both sites.

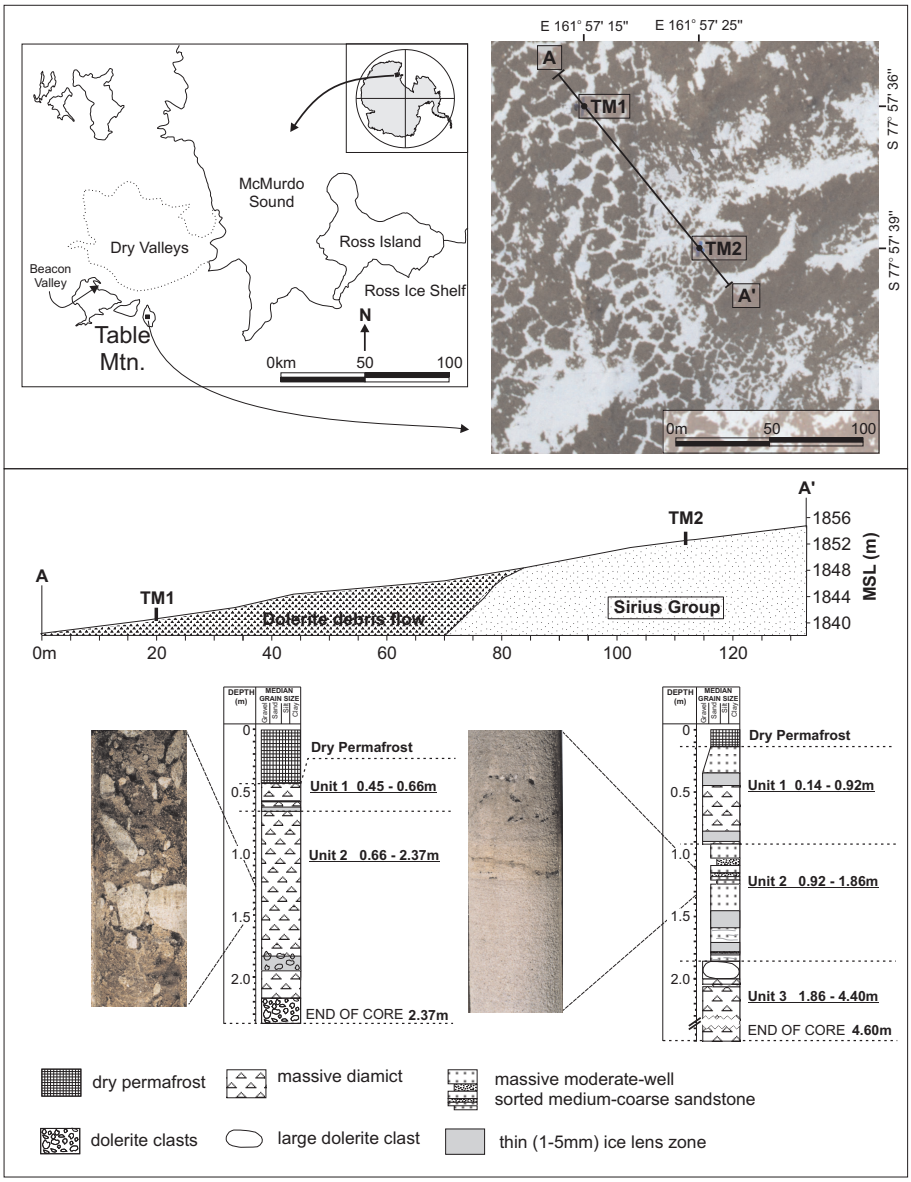

Figure 7.1: Locations, surface features, and core log of Table Mountain sites. Aerial photo (top right) shows different scale polygons, demarcated by snow, and debris flow (left). Middle figure shows the contact between the intrusive Dolerite flow and Sirius. Core stratigraphy and photos from central sections of the cores show the very different composition at the two sites. (Colour version of Figure 1 in *Pringle et al.* [2003].)

At site TM1 the polygons on the surface have an average diameter of 16 m and are demarcated by snow accumulation in the peripheral trenches, which are about 0.5 m below the polygon centres. Sediment at this site originates as a debris flow which contains mostly dolerite as both clasts and matrix. At the installation hole, the dry permafrost is loose to a depth of 0.45 m and consists of very poorly-sorted sediment with about 20% gravel, and 70% sand, silt and clay. The ice cement from 0.45-0.66 m consists of essentially the same material as in the dry permafrost zone but the dolerite clasts are more weathered. Below 0.66 m the sediment comprises about 30% ice, 20% clasts (scattered pebbles and cobbles 3-10 cm diameter) and 50% sand, silt and clay. Clasts in this lower zone are mostly un-weathered and fresh looking.

Polygons at site TM2 have an average diameter of 5 m, but otherwise have a similar morphology to those at site TM1. The dry surface permafrost is light-tan in color and loose to a depth of 0.14 m. It consists of about 40% small dolerite pebbles and 60% sand, silt and clay, which derive mostly from Sirius group facies. Between 0.14-0.92 m the sediment is a moderately sorted, medium to coarse quartz-rich sand with several zones of weathered dolerite clasts ($\sim$ 5 cm diameter) and segregation ice. The overall composition in this unit is about 23% ice, 10% dolerite clasts, and 67% quartz-rich, medium grain sand. Several $\sim$ 0.01 m thick ice lenses occur between 0.7-0.9 m. From 0.92 to 1.86 m is a massive, well-sorted, medium to coarse grained, quartoze sandstone of the Sirius group, cemented by pore ice and fine clays [*Dickinson and Grapes*, 1997], see photo in figure (7.1). The sandstone contains about 15% ice, mostly in pore space. Below this, and extending to the bottom of the thermistor array, is a zone of about 30% dolerite clasts (10 - 15 cm diameter) 50% quartz-rich sand and 20% ice, both in pore-spaces and as ice lenses.

The ice fraction profiles for both sites, are shown in figure 7.2). These were determined from approximately 5 cm long, 6 cm diameter sections from the frozen, and dehydrated weights by Warren Dickinson [*Pringle et al.*, 2003]. Within the ice cement, ice is present as both lenses and pore ice. The length scale of features in the ice-cement, for example ice lenses and pebbles, is comparable with the core section dimensions ($\sim$ 50 mm), so the $\pm$10% variability in ice content over these length scales is not surprising.

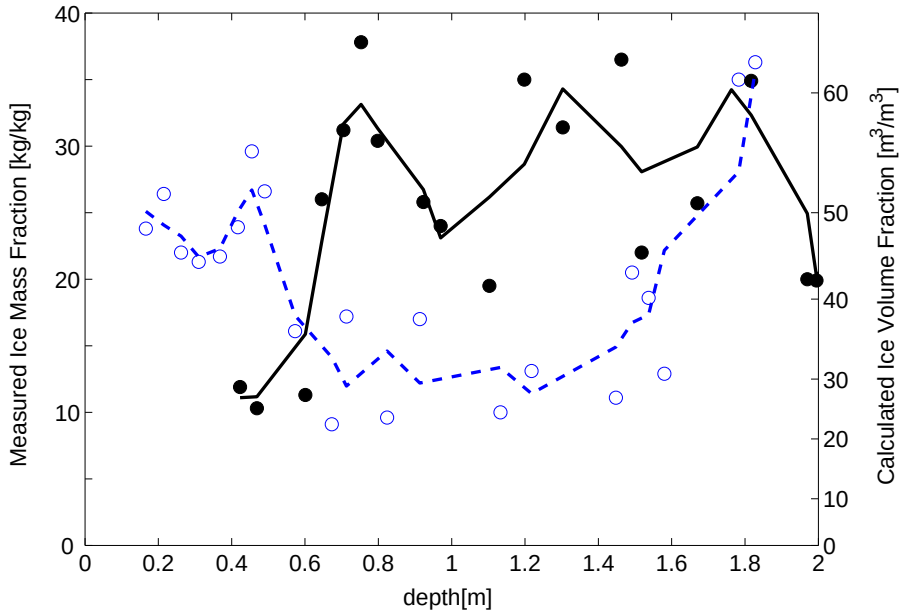

Figure 7.2: Ice content of recovered cores: TM1 (closed black circles) and TM2 (open blue circles); lines, running three point averages (end points not shown). Left hand axis is measured mass fraction, and right hand axis volume fraction calculated using $\rho(\text{ice}) = 0.91\,\text{g/cm}^3$, $\rho(\text{mineral phase}) = 2.65\,\text{g/cm}^3$.

7.3 Instrumentation

The thermistor arrays are virtually identical in design to the sea ice units described in Chapter 3. Using an older muliplexor, only 15 thermistors and 1 standard resistor were used (rather than 22 and 2 in the ice arrays). The thermistor spacing was $\Delta z = 13.5\,\text{cm}$. YSI 44031 thermistors and Campbell CR10 data loggers were used. The thermistors have an accuracy (interchangeability) of $0.1\,^\circ\text{C}$ at $-20\,^\circ\text{C}$ but a precision better than $0.01\,^\circ\text{C}$. We stress that for all of the analytical methods we use, it is the precision that is important, not the absolute accuracy, so although not made, a one-point calibration would not have changed our results. These are a different line of thermistors to those used in the sea ice measurements, but apart from a different Steinhart-Hart temperature-resistance calibration, data processing was the same.

Sites TM1 and TM2 were core-drilled using compressed air and diamond bits [*Dickinson et al.*, 1997]. Because core recovery was only possible from the ice-cemented sediments, the dry permafrost was excavated from around the

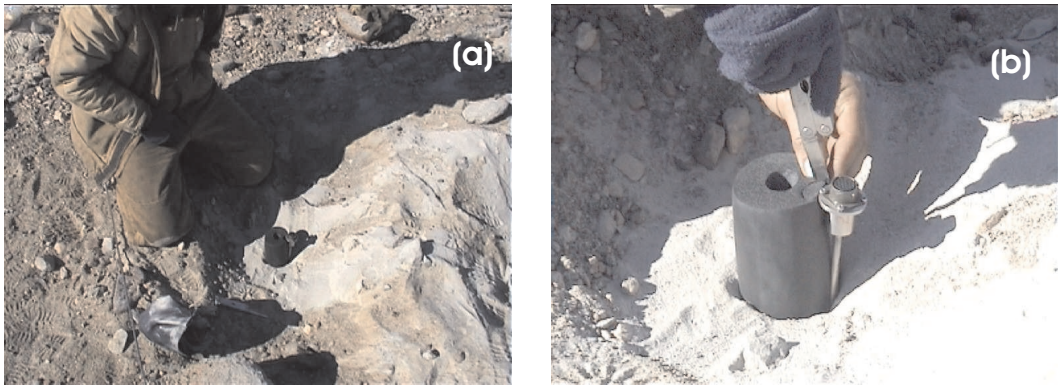

Figure 7.3: Installation of thermal array at site TM2. (a) Surface debris removed, revealing undulating ice-horizon. Black pipe lagging protruding from hole, and array just visible. (b) Cutting pipe lagging to accommodate array connector (image lightened for clarity, not true colour.)

hole before drilling. The cores were described, photographed, and analysed for particle size and ice chemistry in New Zealand. A small v-shaped notch was cut into two-meter long, 75 mm diameter polyurethane pipe insulation. The thermistor probe was placed in the notch and both were gently pushed into the 63 mm diameter hole so the pipe insulation held the probe against the side of the hole to optimise thermal contact. See figure (7.3). To minimise the disturbance to the natural heat flow caused by the array, there must be either a matching of thermal properties across the interface, or no heat flow across the boundary. With the pipe-lagging in the bore hole we approximate the latter case. This contrasts with our sea ice measurements where there is intimate contact between the array and refrozen sea water, and the thermal conductance of the array approximately matches the displaced ice, approximating the former case. Once the array was installed, the excavated area above the ice cement was re-filled and restored, as near as possible, to its original condition.

A possible variation would have been to pour water into the drill hole after installing the array and lagging. Filling the borehole, this would eliminate air voids, and improve the thermal contact. This may complicate array extraction however.

Temperatures measured at sites TM1 and TM2 are shown in figure (7.4). Between November 2000 and November 2002 the temperature profile was recorded every 4 hours, and between November 2002 and December 2003 every 1 hour.

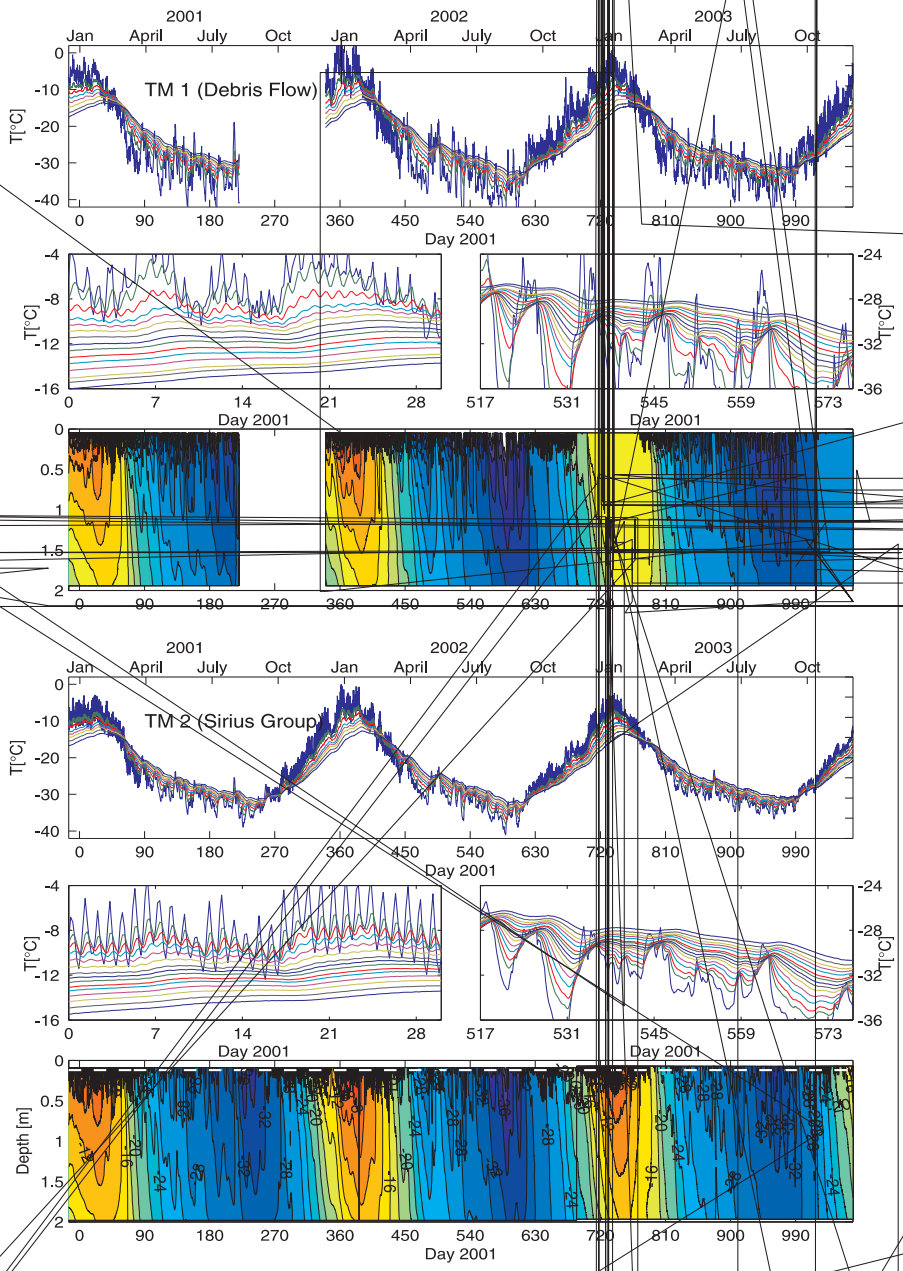

Figure 7.4: Temperatures at TM1 and TM2, 2001-03. TM1: (a) T(z,t) time series where each line is T(t) for one thermistor; top thermistor is the large-amplitude blue line. (b,c) Characteristic summer and winter variations, see text. (d) Reconstruction of temperature field; isopleth increments are 2 °C. Dashed white line is ice horizon. TM2: (e,f,g,h) similarly.

Subplots (a,e) show the temperature traces for each thermistor, which are dominated by the yearly cycle. The blue trace with the largest amplitude is the upper-most thermistor, and for clarity only every second trace is shown. The depth to ice horizon was 0.44 m at site TM1 and 0.12 m at TM2. Therefore the top 3 thermistors at TM1 were surrounded by back-filled ice free debris, as was the top thermistor at TM2. Also, in the array at site TM1 the uppermost thermistor was positioned slightly closer to the top of the tube. These two effects explain why the upper temperature traces at TM1 show larger amplitude swings than at TM2. This difference is readily identified by comparing the figure (7.3) subplots (b,c) with (f,g), which show characteristic summer and winter temperature features from the same times at the two sites. Dominant components in the summer are the daily and annual cycles. There is no daily solar cycle in the winter and the temperature record is dominated by synoptic scale events, with time scales of the order of 1-2 weeks. With a lower characteristic frequency these weekly events cause deeper-penetrating temperature disturbances than the daily cycle.

7.4 Analysis Methods

A variety of general approaches have previously been used to calculate thermal properties from ground temperature measurements, from direct time series analysis through to more sophisticated inverse problem methods. Several authors have compared subsets of these approaches, including *Persaud and Chang* [1985]; *Hinkel* [1997]; *Fuhrer* [2000]. When the thermal diffusivity is calculated from real data, assuming 1-D conductive heat flow, it is commonly termed the apparent thermal diffusivity (ATD) to acknowledge that it may include contributions from mechanisms other than 1-D conduction. We anticipate a system that is well described by 1-D conductive heat flow with no latent heat effects and seek to resolve the apparent thermal diffusivity depth profile at both sites with direct time series analysis methods.

The heat equation for conductive, linear heat flow with no latent heat effects, or other heat generation, is

$$c_V \frac{\partial T(z,t)}{\partial t} = \nabla k \cdot \nabla T + k \nabla^2 T \quad , \tag{7.1}$$

where c_V is the volumetric heat capacity and k the thermal conductivity. As the vertical temperature gradient of approximately $1 - 10$ °C/m exceeds the lateral gradient between the two sites by more than 2 orders of magnitude we

reduce equation (7.1) to 1-D;

$$c_V \frac{\partial T(z,t)}{\partial t} = \frac{\partial k}{\partial z}\frac{\partial T}{\partial z} + k\frac{\partial^2 T}{\partial z^2} \quad . \tag{7.2}$$

Equation (7.2) is in general much more readily solved when the first term on the right can be neglected, by assuming, at least locally, constant thermal properties. This gives

$$\frac{\partial T(z,t)}{\partial t} = D\frac{\partial^2 T}{\partial z^2} \quad , \tag{7.3}$$

where $D = k/c_V$ is the thermal diffusivity. We discuss our use of this assumption below.

Most Fourier methods based on the attenuation and phase lag of temperature waves derive from equation (7.3) and rely on this assumption of globally constant thermal properties, [eg. *DeVries*, 1963; *Carson*, 1963; *Nassar and Horton*, 1990]. In real situations, thermal properties invariably do vary with depth. A common way to account for this is to calculate a mean, local ATD by assuming constant thermal properties between the depths of the temperature sensors used in the calculation. However, 'perturbed Fourier' methods have been developed to accommodate non-constant thermal properties [eg. *Lettau*, 1954, 1962; *Stearns*, 1969; *Hurley and Wiltshire*, 1993]. We consider three analysis methods that require only measurements of the temperature field, and not also the heat flux, which is required in the methods of *Lettau* [1954, 1962]; *Stearns* [1969].

As we address a simple thermal regime, we limit ourselves to time-series analysis, and do not consider more sophisticated inverse problem schemes; we seek a simple but accurate method for resolving variations in the ATD. We first describe two time-series methods previously used in this context. We then show the ATD profile resolved with these methods as well as our graphical finite difference method described in Chapter 4.

Simple Fourier Method I

When the first term on the RHS is omitted, equation (7.2) admits a Fourier decomposition solution,

$$T(z,t) = \overline{T}(z) + \sum_n A_n e^{-z/d_n} e^{i(\omega_n t - z/d_n + \phi_{0,n})} \quad . \tag{7.4}$$

Here $\overline{T}(z)$ is the annual mean temperature at depth z, and n indexes the frequency components, of magnitude A_n, frequency ω_n, penetration depth $d_n =$

$(2D/\omega_n)^{1/2}$ and the phase is $\phi(z) = \phi_{0,n} - z/d_n$. In this case the mean local ATD can be estimated from both the amplitude attenuation and the phase lag of a given frequency component between two depths [Carson, 1963]:

$$D_{amp} = \frac{\omega}{2}\frac{(z_2 - z_1)^2}{ln(A_1/A_2)} \quad , \tag{7.5}$$

$$D_{phase} = \frac{\omega}{2}\frac{(z_1 - z_2)^2}{(\phi_1 - \phi_2)^2} \quad . \tag{7.6}$$

Perturbed Fourier Method II

Hurley and Wiltshire [1993] applied a perturbation approach to enable a Fourier decomposition approach whilst still retaining the $\frac{\partial k}{\partial z}$ term in equation (7.2). We adopt their approach and slightly modify the mathematics, and expand the temperature in a generalised form similar to equation (7.4),

$$T(z,t) = \overline{T}(z) + \sum_n e^{r_n(z)} e^{i(\omega_n t + \phi_n(z))} \quad , \tag{7.7}$$

where $A_n(z) = e^{r_n(z)}$ and $\phi_n(z)$ are now unknown functions of z. Inserting equation (7.7) into equation (7.2), and solving for the real and imaginary parts, gives the following expression for D:

$$D_n(z) = \omega_n \left[r'\phi' + (\phi')^2 \frac{\phi'}{r'} + \phi'' - r'' \frac{\phi'}{r'} \right]^{-1} \quad , \tag{7.8}$$

where the primes denote depth derivatives, and the index n has been dropped from all terms in the square brackets. The relevant derivatives are determined by calculating A_n and ϕ_n at the depth of each thermistor, and fitting polynomials to plots of $ln(A_n)$ vs. z and ϕ_n vs. z. For example, see figure 7.8(a), discussed in section 7.5. (This procedure requires that $\overline{T}(z)$ is constant. In our case this is a very good approximation as depth variations in $\overline{T}(z)$ are less than the absolute accuracy of the thermistors. Furthermore, when processing the data we subtracted off both $\overline{T}(z)$ and any linear trend over the period of data examined before calculating the Fourier components.)

Finite Difference Method III

Several different finite difference methods for calculating the ATD have been presented and critiqued [eg. *McGaw et al.*, 1978; *Persaud and Chang*, 1985; *Zhang and Osterkamp*, 1995; *Hinkel*, 1997]. The most direct approach is to use finite difference estimates of the derivatives in equation (7.3) and to calculate

the mean ATD by their ratio on a point-by-point basis [*McGaw et al.*, 1978; *Persaud and Chang*, 1985; *Zhang and Osterkamp*, 1995; *Hinkel*, 1997; *Westin and Zuidhoff*, 2001]. The mean ATD is then taken as the time average of these ratio values. This method suffers systematic difficulties when the temperature curvature, $\partial^2 T/\partial z^2$, passes through zero [*Zhang and Osterkamp*, 1995], and furthermore, it requires temperature measurements with both high accuracy and high precision. *Hinkel* [1997] provides a method for calculating the ATD using equation (7.5) specifically for diurnal forcing whereby the temperature amplitudes A_1 and A_2 are calculated from a finite difference estimate of the average time rate of change of temperatures. We use our graphical finite difference scheme described in Chapter 4. This does not require harmonic forcing, and is insensitive to inter-thermistor calibration offsets. As in the other finite difference methods discussed above, we make the assumption of locally constant thermal properties for the space between adjacent thermistors.

7.5 Results from 2001 Temperature Data

Based on our analysis of the 2001 data, we drew three main conclusions in *Pringle et al.* [2003]. Firstly, of the methods discussed above we considered that the graphical finite difference scheme provided the best resolution of depth variation in the ATD profile. Secondly, the depth-dependence of the ATD profiles at both sites correlates very well with the core stratigraphy and ice content profiles. And thirdly, a seasonal variation in the ATD profile was resolved at both sites which, within uncertainties, was consistent with the expected temperature dependence of the heat capacity and thermal conductivity. Based on both a re-assessment of our earlier analysis, and an improved analysis of the higher time-resolution 2003 temperatures,we reassess these conclusions below. We first present key results from the initial analysis.

The ATD profiles resolved with our graphical finite difference method are shown in figure (7.5). They start from the second thermistor frozen into the ice-cemented ground at each site, 0.63 m at TM1 and 0.36 m at TM2. These data show a thermal diffusivity which is higher in winter (1 April-1 August, blue lines) than in summer (20 November- 20 January, red lines). The range of ATD values in figure (7.5) are consistent with the diffusivity of ice and typical mineral components, $D_{ice}(-20\,^{\circ}\mathrm{C}) = 1.15 \times 10^{-6}\,\mathrm{m}^2/\mathrm{s}$, $D_{mins}(0\,^{\circ}\mathrm{C}) \approx 1.5 \times 10^{-6}\,\mathrm{m}^2/\mathrm{s}$. These values are less than that of quartz, which displays the highest diffusivity of soil minerals, $D_{quartz}(0\,^{\circ}\mathrm{C}) \approx 4.3 \times 10^{-6}\mathrm{m}^2/\mathrm{s}$ [Farouki, 1981].

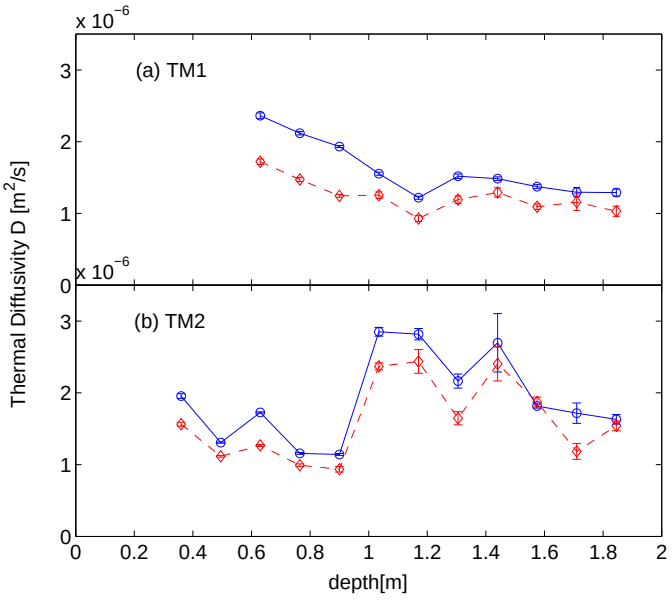

Figure 7.5: Seasonal variation in apparent thermal diffusivity profiles from original analysis of 2001 data. (a) TM1 and (b) TM2. Solid blue line: winter; dashed red line: summer. Profiles start from the second thermistor below the ice-horizon. (Figure from *Pringle et al.* [2003]).

Before seeking to explain the resolved ATD variations we note that the effective thermal diffusivity of a composite material is the ratio of the effective thermal conductivity to its volumetric heat capacity. The heat capacity is a simple volume-fraction weighted average of the components heat capacities but the effective thermal conductivity is also a function of their geometric configuration,

$$D_{eff} = \frac{k_{eff}(k_i,\, v_i)}{\sum v_i c_{V,\,i}} \quad . \tag{7.9}$$

We have discussed some of the models for $k_{eff}(k_i, v_i)$ in Chapter 1. One common feature is that they all contain only terms which are first order in the thermal conductivities of the constituents, a feature to which we refer below.

7.6 Expected Temperature-Dependence and Seasonal Variation in Thermal Diffusivity

In our earlier analysis of the 2001 data, the difference in winter- and summertime diffusivity was found to be $20 \pm 10\%$ at site TM1, $15 \pm 5\%$ at site TM2 (mistakenly transposed in *Pringle et al.* [2003]), and $18 \pm 9\%$ overall. No seasonal change was observed in the high-precision standard resistor, eliminating data logger performance as the source of the variation. From summer to win-

ter the average ground temperature in the top 2 metres decreases from −12 °C (261 K) to −27 °C (246 K), a 6% relative change.

The thermal conductivity of electrically insulating crystals is expected to vary approximately as $k \propto T^{-1}$, where T is the absolute temperature [*Ashcroft and Mermin*, 1976; *Roy et al.*, 1981], and this relationship has been recognized for rocks , minerals and ice at moderate temperatures [*Clauser and Huenges*, 1995; *Anderson and Suga*, 2002]. Thus the numerator of equation (7.9) will show a similar dependence, raising the thermal diffusivity by approximately 6% from mid-summer to mid-winter. Furthermore, the heat capacity of such materials decreases with temperature, so the diffusivity increases even faster than T^{-1} with falling temperatures. Over our temperature range the heat capacity of ice increases by 6.0% [*Weast*, 1971]. Data on the temperature dependence of the heat capacity of materials suitable for comparison with the minerals components of our cores in our temperature range are scarce. However, we note that the thermal diffusivity of Berea sandstones suggests an 11% decrease from winter to summer temperatures [*Roy et al.*, 1981], equivalent to a 5% increase in the heat capacity. This value is the highest of materials which might be appropriate for comparison. The numerator and denominator of equation (7.9) are first order in the thermal conductivities and heat capacities of ice and minerals. Consequently they will show the same relative variations as the material-specific parameters, and lead to a maximal thermal diffusivity increase of approximately 11-12% from winter to summer. Accounting for the decreasing seasonal temperature variation with depth, this figure becomes $11 \pm 3\%$ which lies within the measured uncertainties at both sites. Although the thermal conductivity of rocks and soils depend greatly on physical and diagenic factors [*Jessop*, 1990; *Clauser and Huenges*, 1995], the above comparison suggests that it is not unreasonable that the observed seasonal variation reflects the underlying temperature dependence.

7.7 Results from 2003 Temperature Data

From November 2002 - December 2003, thirteen-months of uninterrupted temperatures were recorded at both sites with a measurement interval of 1 hr. Careful analysis of these data from both sites has improved on the previous analysis, which, due to the missing data focussed on site TM2. The depth-dependence of the ATD profiles is largely unchanged, but we readdress the seasonal variation.

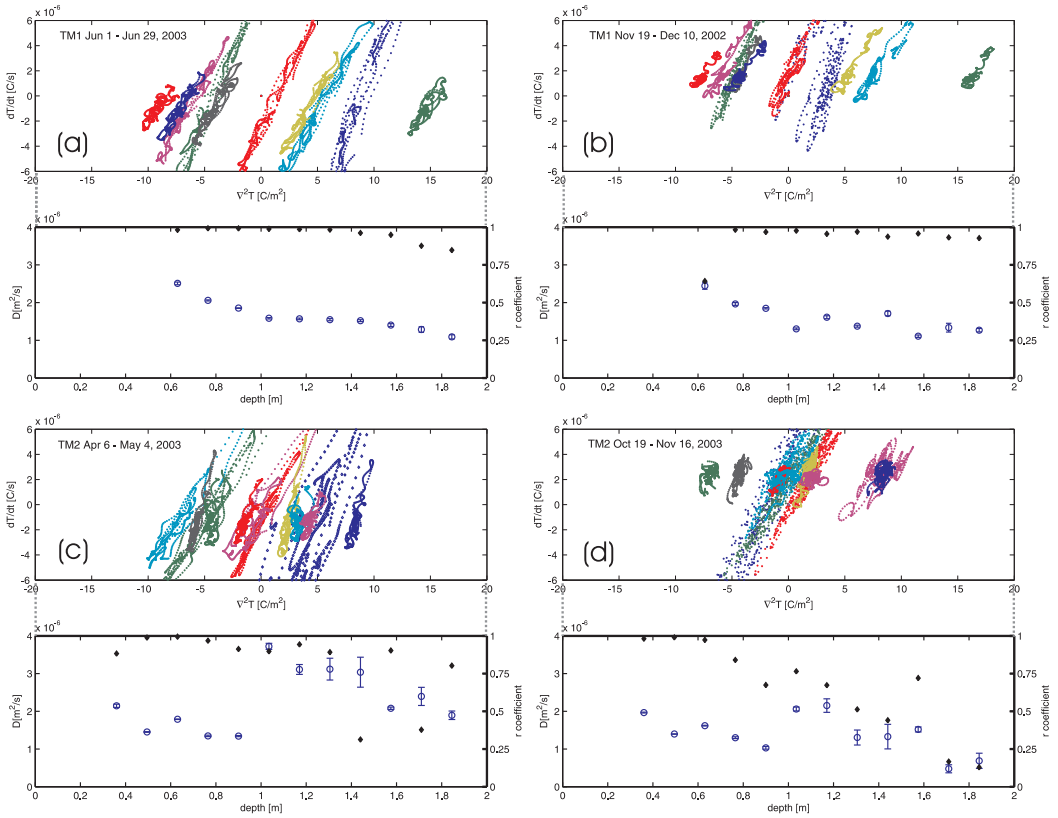

Figure 7.6: Finite difference analysis, TM1 and TM2, 2003 data. (a) TM1 winter, (b) TM1 summer. (c) TM2 winter, (d) TM2 summer. Upper plots show scatter plots for all thermsitors. Lower plots show ATD profile (blue circles, left axis), and correlation coefficients (black diamonds, right axis).

Figure (7.6) shows scatter plots and resulting diffusivity profiles for TM1 and TM2 in both summer and winter conditions. Raw temperatures were smoothed with a Gaussian filter with power spectrum half-width-half-maximum (HWHM) 24 hours, and then processed in 28 day blocks. In the four cases shown the bottom sub-plot shows the diffusivity with blue circles (left axis), and correlation coefficient with black diamonds (right axis). These results are for the periods in the winter and summer at each site for which the correlation coefficients are consistently highest and the diffusivity uncertainties smallest. They represent the data best enabling a seasonal comparison at each site. The results in figure (7.6) for the two sites are quite different. At TM1 both the winter (a) and summer (b) plots show high correlation coefficients at all depths. As this implies low relative errors in the plotted variables, we have high confidence

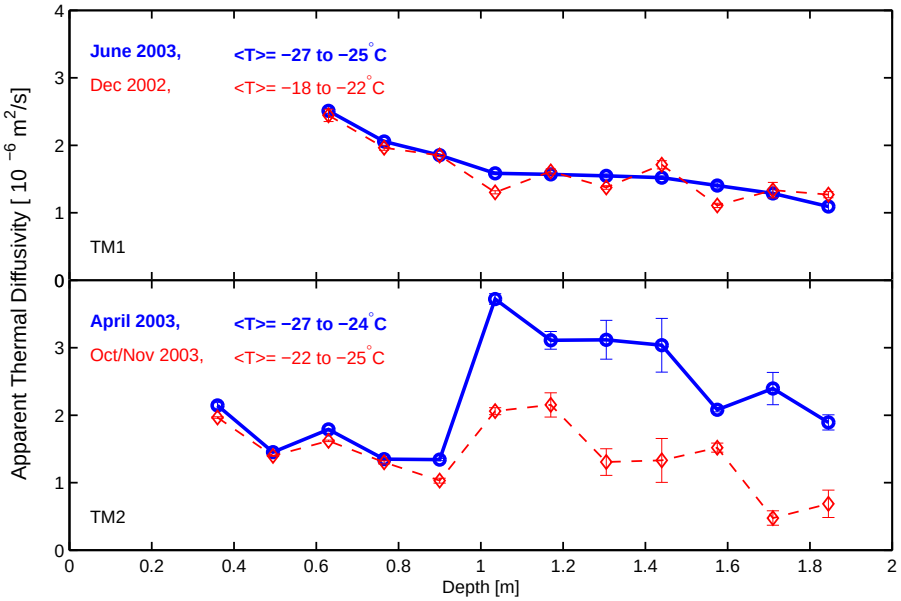

Figure 7.7: Seasonal variation in apparent thermal diffusivity profiles from analysis of 2003 data. These are the ATD profiles shown separately in figure (7.5). Top TM1; bottom TM2. Solid blue lines, winter; dashed red lines, summer. Average temperatures for top and bottom thermistors shown.

in the geometric-mean diffusivity values for both seasons, permitting a direct comparison of the seasonal ATD profiles (see below). Compared with their TM1 counterparts the TM2 scatter plots are noisier in both winter (c) and summer (d). Even in the winter when the variations are largest, the correlation coefficients are low below 1.3 m, and in the summer they are low below 0.8 m. In general, in these cases the geometric-mean ATD values are less reliable. We argue below than in the present case the ATD will be underestimated.

At site TM1 there is little variability between the profiles for the other 28 day periods, not shown. The differences are mainly in lower r-values and increased scatter in conductivity values below about 1.2 m. At site TM2, these effects are larger. We have chosen the periods for which data are shown in figure () by comparing the r-values and also the scatter plots. For some periods at site TM2, these plots were very spread, indicating an apparently large phase lag between $\partial T/\partial t$ and $\partial^2 T/\partial z^2$ values. These non-ideal features are well correlated with periods of strong variations in surface temperature. We associate this with worse thermal contact at TM2 and this is discussed further below. The conductivity values from these periods are unreliable.

Figure (7.7) shows a comparison of the seasonal ATD profiles for each site. There is very good agreement between the summer and winter profiles at TM1 where we have high confidence in the ATD results. At TM2 there is good agreement above about 0.8 m. For depths below this, where the correlation coefficients are low, the summer ATD values are consistently lower than the winter values. This behaviour is consistent with the relative spread in the scatter plots at site TM2. The winter and summer scatter plots show a similar scatter in $\partial^2 T/\partial z^2$ values, but because of the smaller summertime temperature disturbances, the relative error in $\partial^2 T/\partial z^2$ is greater at that time. As discussed in Chapter 4, the finite difference method will therefore underestimate the diffusivity. We conclude that we are unable to accurately resolve the ATD profile in the summer at TM2 below 0.8 m. The winter time profile represents our best estimate of the ATD profile using the finite difference method.

At TM1 the average decrease in the ATD profiles from the winter to summer over all depths is $3 \pm 8\%$. For the top 4 thermistors ($z > 0.8$ m) at TM2 it is $5 \pm 6\%$. We consider these results more reliable than the much higher variations reported earlier from the 2001 data [*Pringle et al.*, 2003]. Nevertheless, the 2003 results are qualitatively consistent with the expected underlying temperature dependence of diffusivity increasing in the winter. In fact larger winter values are observed at all but 3 depths below 1 m at TM1. In hindsight, we attribute the larger apparent seasonal differences in the 2003 data to underestimated summertime values.

At site TM2, the scatter plots show more scatter in $\partial^2 T/\partial z^2$ values than TM1 even in the winter months. Upon closer inspection, the increased scatter in adjacent thermistors is related and we attribute it to poor thermal contact between the array and the surrounding ground, at least for some thermistors. There will be conduction along the array between points of good thermal contact above and below regions of poor thermal contact. For dynamic temperatures the thermal profile in this region will be established by the effective thermal diffusivity of the array. The measured temperature profile will in this way be perturbed by small regions of poor contact. Although the precise effect is difficult to predict, the amplitude and phase of recorded temperature variations will differ from the actual variations at the thermistor depth. If this affects at least one of the thermistors in an adjacent triplet then the values of $\partial T/\partial t$ and $\partial^2 T/\partial z^2$, calculated at the central thermistor will be out of phase. As discussed in Chapter 4 (in the context of finite sampling intervals) this leads to loops and other features in the scatter plots, as seen in figure (7.6). Such an error will increase the relative error in $\partial^2 T/\partial z^2$ leading to a decrease in the correlation coefficient and an underestimation of the diffusivity, both of

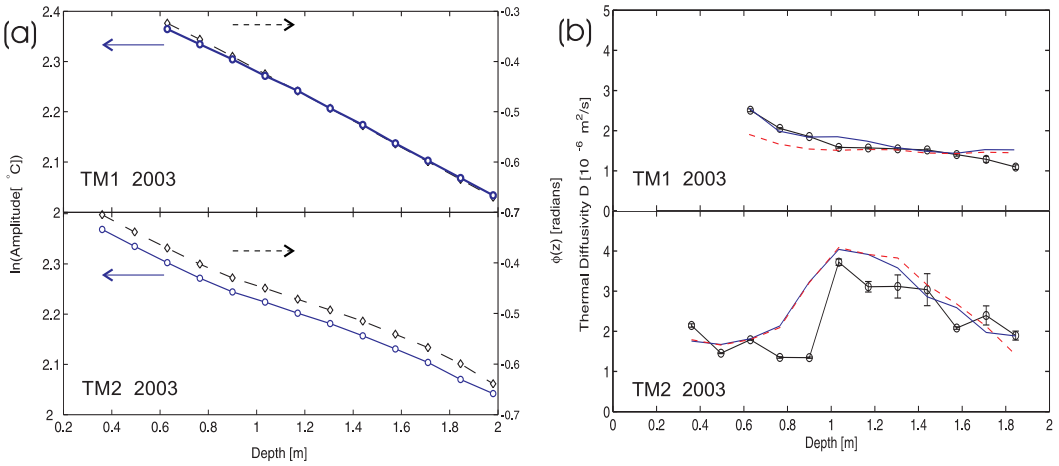

Figure 7.8: (a) Depth dependence of $r(z) = ln(A(z))$ and $\phi(z)$ for Fourier Method I, 2003 data. (b) ATD profiles at TM1 and TM2 from 2003 data. Black circles, graphical finite difference method; red solid line, Fourier Method I amplitude; red dashed line, Fourier Method I phase.

which are observed at site TM2, see figure (7.6).

From this analysis we propose that the thermal contact is generally better at TM1 than TM2, and at TM2 it is worse below about 0.8 m. This depth approximately coincides with the sharp compositional boundary at $z = 0.9\,\mathrm{m}$ between ice-cemented diamict and a Sirius sandstone unit with lower ice content. We speculate that non-uniformity in the borehole surface has led to variations in the quality of thermal contact.

7.8 Comparison of Methods

Whilst the missing data in at TM1 had restricted the application Fourier Methods I and II to TM2 in the 2001 data, they could be applied at both sites using the 2003 temperatures. Data at each depth were de-trended by subtracting the yearly-averaged temperature at each depth $\overline{T}(z)$ and any small temperature change over the one year period. The amplitude $A(z)$ and phase $\phi(z)$ of the 1 yr^{-1} component were calculated at each depth from the resulting zero-mean temperature time series.

Figure 7.8(a) shows the depth variation of $r(z) = lnA(z)$ and ϕ(z) for each site.

Figure 7.8(b) shows the corresponding ATD profiles calculated with Fourier Method I from the amplitudes (solid line) and phases (dashed line) using equations (7.5, 7.6). Also shown are the winter-time diffusivity profiles from our graphical finite difference analysis. Profiles from these methods agree quite well at site TM1 where the assumption of a globally constant diffusivity invoked in the Fourier method, is most justified. At site TM2, Fourier Method I resolves a region of enhanced diffusivity that agrees reasonably well with the graphical finite difference profile, although somewhat larger between 0.6 - 1.4 m. This is the region where the assumption of a globally constant diffusivity is least justified, so poor performance is not unexpected. Equations (7.5, 7.6) are based on the solution (7.4) which considers the downward propagation of surface disturbances, and is unable to accommodate thermal waves reflected upwards from diffusivity variations. Our method makes no such assumption and can accommodate these variations, and we expect it to outperform the simple Fourier method when there are strong depth-variations in the diffusivity.

Fourier Method II, which is mathematically robust in the presence of diffusivity variations, could be applied only at site TM2 for the 2001 temperatures. We have applied this method at both sites with the 2003 temperature data, and found it to be very prone to numerical errors. The accuracy of this method rests with the quality of the polynomial fits to $r(z) = lnA(z)$ and ϕ(z). Using equation (7.8), we obtained very different $D(z)$ profiles for 4th, 5th and 6th order polynomial fits to the data in figure (7.8). In some cases the denominator passed through zero giving a divergence in $D(z)$. As this calculation uses the first and second derivatives of these fitted polynomials, it is *very* sensitive to the quality of the fit. Given the difference in profiles returned for polynomial fits of different order, we consider the method very unreliable. Note that in *Pringle et al.* [2003] we consider this method reliable on the basis of a good agreement between the diffusivity profiles from this method and our graphical finite difference analysis. From our more thorough analysis of the 2003 data we overturn that conclusion.

A direct comparison of Fourier Method I and our graphical finite difference method is hindered by not knowing *a priori* the diffusivity structure [*Persaud and Chang*, 1985]. We show below that the conductivity values calculated from our graphical finite difference method are high, even for the high quart content of the core, so the simple Fourier method is likely to have overestimated the diffusivity between 0.6 - 1.4 m.

7.9 Composition Dependence: Depth and Site Variations

The depths of features in the ATD profiles in figure (7.8) correlate well with the composition profiles of the cores. At site TM1 the core shows little stratification consistent with the weak depth dependence shown of the ATD profiles. Below 0.6 m, the core shows a mixture of Dolerite pebbles and fragments frozen into an ice matrix. The ice content profile shows a low ice fraction nearer the ice horizon, increasing to a roughly constant value of $30 \pm 10\%$ by mass ($55 \pm 10\%$ by volume) at lower depths. The highest diffusivity ($\sim 2.5 \times 10^{-6}\,\mathrm{m}^2/\mathrm{s}$) is resolved where the ice content is lowest, ice lenses are less prevalent and the soil phase most consolidated. In the bottom 1 metre the ATD is consistent with the diffusivity of typical minerals and pure ice.

Site TM2 shows substantially more structure in both the core and the diffusivity profile. For $0.14\,\mathrm{m} < \mathrm{z} < 0.9\,\mathrm{m}$, the core is a Sirius till/ice matrix diamict with prominent ice lenses. There is a sharp transition at $z = 0.92\,\mathrm{m}$ to the quartose Sirius sandstone and little sign of segregation ice down to 1.45 m except a few lenses near 1.2 m. Below 1.45 m ice lenses become increasingly prevalent, followed by a return to a disordered regolith/ice matrix below 1.7 m. Each of these features is clearly represented in the diffusivity profile which shows a sharp transition at approximately 0.9 m, a region of enhanced diffusivity between 0.9-1.45 m and a smoother transition to lower diffusivity below this. The high ATD values in the middle of the core can be consistent only with a well-consolidated, high quartz-content mineral phase, as observed at these depths. We question the accuracy of the highest and lowest values at adjacent depth 0.9 m, 1.03 m. We have identified that the finite difference analysis can over- and under-estimate adjacent gradient estimates when the relative errors in $\partial^2 T/\partial z^2$ are not small. This can occur as follows: the temperature at three thermistors is used to calculate $\partial^2 T/\partial z^2$ at a given depth. The temperature at each thermistor is used to estimate $\partial^2 T/\partial z^2$ at three depths using equation (4.14). For three successive depths, the temperature recorded at the central thermistor enters this estimate with a weighting of (1, -2, 1). A systematic error in this temperature will therefore enter the curvature of three adjacent depths with a relative a weighting of (1, -2, 1), causing an alternating error in the conductivity estimates at adjacent depths. This is particularly evident in the summer TM1 profile in figure (7.7) which shows undulations not seen in the more accurate winter profile. The value at 1.03 m is particularly high even for a high quartz content material.

We note that the stratigraphy of this site is representative of the local ground composition. In particular, this quartose sandstone unit is not an isolated sandstone boulder but rather an extended feature, with several down-slope outcrops.

7.10 Heat Capacity and Thermal Conductivity

The most uncertain thermal parameter in this study is the effective thermal conductivity of the composite; we have a direct measure of the diffusivity and can obtain a rigorously justified estimate of the heat capacity from a volume-fraction-weighted average of the heat capacities of the constituent materials. We have used the two known parameters to determine an implied depth profile of the thermal conductivity. Using an independent quasi-static approach we have also determined the conductivity profile up to a scale factor.

We start by estimating the volumetric heat capacity of the ice-mineral diamict. The parameters required for the purpose are the densities $\{\rho_{ice},\ \rho_{min\,soil}\} = \{0.91,\ 2.65 \pm 0.05\}$ g/cm^3 and specific heats $\{c_{ice}(-20\,^\circ\mathrm{C}),\ c_{min\,soil}(-20\,^\circ\mathrm{C})\} = \{1790,\ 700 \pm 50\}$ J/kg °C [*Weast*, 1971; *Farouki*, 1981; *Roy et al.*, 1981]. The ice mass-fractions vary between approximately 10 - 35%, corresponding to volume fractions 25 - 60 % (see figure 7.2) and a volumetric heat capacity in the range $c_{soil} = 1.8 \pm 0.1 - 1.7 \pm 0.1\,\mathrm{MJ/\,^\circ C m^3}$.

The points and solid lines in figure (7.9) show the thermal conductivity profile $k(z) = D(z)c(z)$ (left axis), and the dashed line the ice content (right axis) for both sites. For each site $c(z)$ has been calculated as described above, and $D(z)$ is the wintertime ATD profile from figure (7.7). For most of TM1, and near the surface of TM2, the conductivity lies near the range expected for ice $k_{ice}(-20\,^\circ\mathrm{C}) \approx 2.4\,\mathrm{W/m\,^\circ C}$ and typical soil minerals, $k_{mins}(-20\,^\circ\mathrm{C}) \approx 3.1\,\mathrm{W/m\,^\circ C}$ (temperature-adjusted assuming $k \propto T^{-1}$ from *Farouki* [1981]. Disregarding the value at 1.03 m, the conductivity of the quartose sandstone unit between 1.17 - 1.44 m is $k_{QS} = 5.5 \pm 0.1\,\mathrm{W/m\,^\circ C}$. This region includes approximately $10-15\%$ ice by mass ($25-35\%$ ice by volume) so the conductivity of the mineral phase k_{min} must be even higher. By numerical inversion of the Maxwell model, described in Chapter 1, in the assumption of zero air content, we estimate $k_{min} = 6.8 \pm 0.5\,\mathrm{W/m\,^\circ C}$. A non-zero air content would increase this value proportionally. Such a high value is physically reasonable only for exceptionally quartz-rich materials [*Clauser and Huenges*, 1995]. We note that

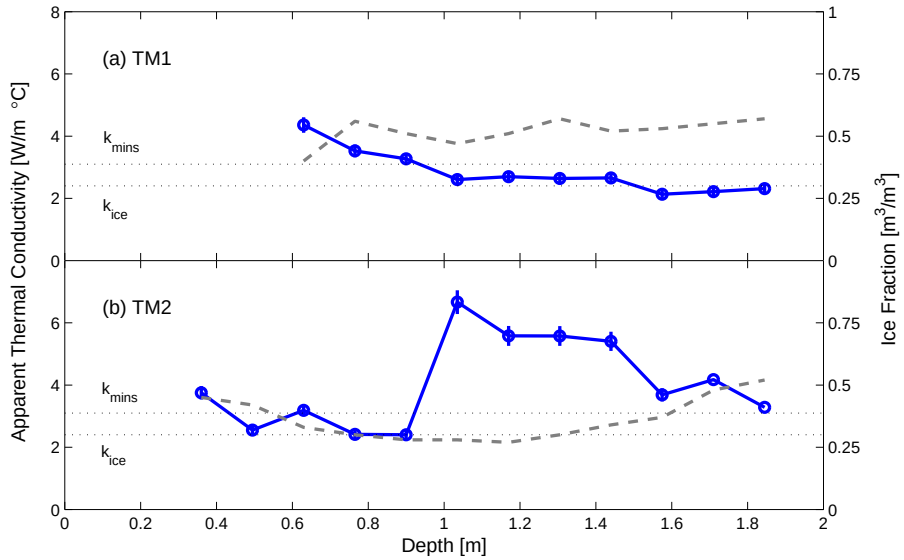

Figure 7.9: Apparent thermal conductivity profiles $k(z) = D(z)c(z)$ (blue lines, left axis), and ice content by volume (grey dashed line, right axis) at (a) TM1 and (b) TM2. $D(z)$ is the wintertime ATD profiles in figure (7.7). See text for $c(z)$ calculation. Thin lines, conductivity of ice and typical minerals at $-20\,^{\circ}\mathrm{C}$.

the quartz content is much lower in the non-Sirius units of this TM2 core, and at the TM1 site, which are characterised mainly by lower conductivity Dolerite debris.

Figure (7.10) also shows the thermal conductivity, up to a scale factor, determined directly from the temperature data with another method. In steady-state 1-D linear heat flow the temperature profile is by definition static: $\partial T/\partial t = 0$, and the heat flux $J_Q(z) = -k(z)\partial T/\partial z$ is constant, so $k(z) \propto |\partial T/\partial z|^{-1}$. Due to high frequency surface driving this situation does not apply near the surface, but at greater depths, and in the summer, the annual variation dominates and the temperatures does vary slowly over times scales of days. Quasi-static conditions are best approximated in our data at site TM2 for January 1 - 9, 2003. Each thin curve in figure (7.10) is a profile of the inverse of the daily-averaged gradient, $|\partial T/\partial z|^{-1}$ for this period (right hand axis). Temperature data were filtered as above, effectively removing sub-daily components. Because we cannot independently determine the magnitude of the local seasonal heat flow at this time, these curves give the form of the conductivity structure but not its magnitude. The agreement with the shape of

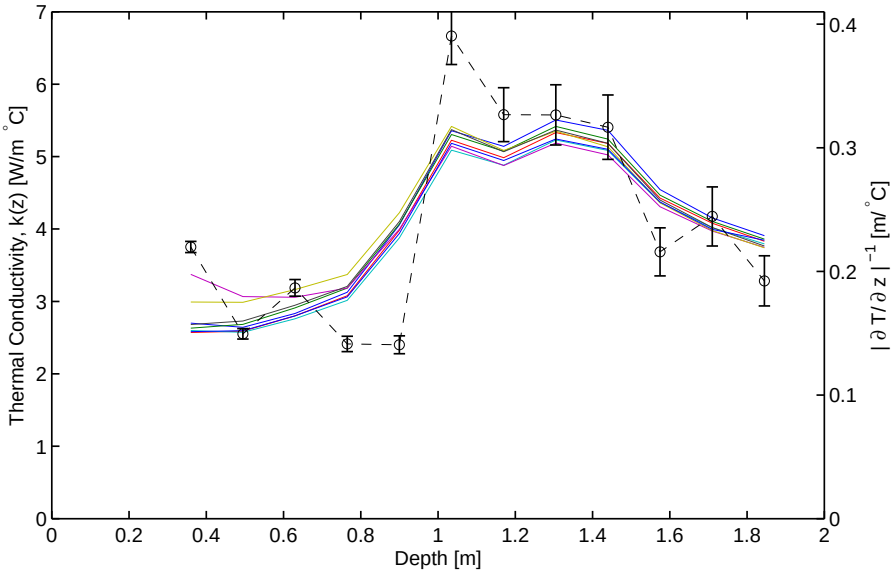

Figure 7.10: Thermal conductivity at site TM2. Circles and dashed line: $k(z) = D(z)C(z)$ from figure 7.9; series of lines: $|\partial T/\partial z|^{-1}$ profiles for days best satisfying quasi static conditions, January 1 - 9, 2003 (right hand axis).

the diffusivity-derived conductivity profile is good, providing independent and direct evidence of the region of high conductivity. The increase at 0.9 m is less abrupt than the finite difference profile, which, as discussed above, we believe to have exaggerated the step between 0.9 - 1.03 m.

Our results are consistent with the only other conductivity measurement we are aware of in the greater Dry Valley area. *McKay et al.* [1998] determined an ice-cement thermal conductivity $2.5 \pm 0.5\,\mathrm{W/m\,°C}$ just below the ice horizon at Linnaeus Terrace. However, our profiles show that due to the inhomogeneous composition, the thermal properties can vary strongly over small distances. For ice-cemented permafrost sites in the Dry Valleys with a low proportion of Sirius facies, we predict a thermal conductivity in the range $2.5 \pm 0.5\,\mathrm{W/m\,°C}$. However, the conductivity could be as much as twice as large for quartose facies of the Sirius group.

7.11 Application of Results to Patterned Ground

A detailed discussion of the factors in establishing the length scale in polygon networks is outside the scope of this work. However, in order to relate our results to the observed difference in polygon size, we provide a brief summary. Cracking of ice-rich ground occurs to relieve thermal stresses originating from large amplitude surface temperature variations, and the deeper the cracks the larger the region over which stress is relieved [*Lachenbruch*, 1962]. Over time individual cracks intersect to produce networks of crack polygons, commonly called 'polygonal patterned ground' [*Lachenbruch*, 1962; *Sletten et al.*, 2003]. Polygon size is therefore influenced by surface temperature variations, the thermal properties of the ground, and rheology and mechanical strength of the ice-rich ground itself. The build up of thermal stresses depends on the rate of temperature change, $\partial T(z)/\partial t$, which in turn depends on how the variations in surface heat flux are propagated to depth. This is measured by the thermal inertia, $I = (k\rho c)^{1/2} = D^{1/2}\rho c$. Our results show that within the permafrost at our sites, the conductivity can vary by as much as a factor of 2, but that the heat capacity is roughly constant giving a factor of about $\sqrt{2}$ variation in the thermal inertia. It is unlikely this maximal variation is a critical factor in the observed 3-fold change in polygon diameter between sites.

We find little difference, and certainly no order of magnitude difference in the distribution of $\partial T/\partial t$ values calculated at the nearest thermistors to the ice horizon at the two sites (see scatter plots, figure (7.6)). Furthermore, the age and origin of the debris flow, and the history of the depth to ice-horizon from the time of initial crack formation until now, are all unknown at both sites. We believe that the ice-rich, and heavily disordered debris flow was weaker than the surrounding, well-consolidated ground during the development of the polygon networks, which lead to deeper cracks and stress relief over larger distances, resulting in a larger scale network [*Lachenbruch*, 1962].

7.12 Summary and Conclusions

We have applied time-series analysis to high-precision temperature measurements made at two nearby sites at Table Mountain, between 2001-2003. The system is physically simple, with only 1-D conductive heat flow expected. This has enabled a comparison of the reliability of several analysis methods, and a

resolution of depth- and seasonal- variations in the apparent thermal diffusivity (ATD). From 13-months of uninterrupted temperatures recorded with a sampling time reduced from 4 hours to 1 hour, we have reassessed the conclusions of our previous analysis presented in *Pringle et al.* [2003].

We consider our graphical finite difference method to have performed better than the simple Fourier method of *Carson* [1963], based on the phase lag and attenuation of the 1 yr^{-1} temperature components, and much better than the more perturbed Fourier method of *Hurley and Wiltshire* [1993], which suffered numerical instability, being very sensitive to the quality of polynomial curve fitting required. Compared with these other time series methods, the graphical finite difference scheme is simple to implement, has depth- and time- resolution, does not require harmonic temperature variations, and can be applied to short temperature records. In this case it gave a mean local ATD profile which is consistent with an independent quasi-static analysis. Quantitatively, these profiles correlate very well with the composition of recovered cores, including a sharp two-fold increase in ATD across an abrupt compositional boundary at one site.

The graphical finite difference method has the capability to determine the time-dependence of the diffusivity profile. Compared to the summer, larger diffusivity values are measured in the winter at both sites, in all but 3 depths, with an average increase of $4 \pm 7\%$. This is consistent with the expected underlying temperature dependence. In hindsight, we attribute the much larger apparent seasonal differences in the 2001 data to a systematic effect in the analysis causing an underestimation of the summertime diffusivity values.

The volumetric heat capacity calculated from the core composition depends only weakly on ice fraction, falling in the range $c_{soil}(-20\,^{\circ}\mathrm{C}) = 1.7 \pm 0.1$ $-1.8 \pm 0.1\,\mathrm{MJ}/\,^{\circ}\mathrm{Cm}^3$. The apparent thermal conductivity, calculated as $k(z) = D(z)c(z)$, correlates very well with the core composition. The conductivity generally lies in the range $2.5 \pm 0.5\mathrm{W}/\,^{\circ}\mathrm{Cm}$, but can be as high as $5.5 \pm 0.1\mathrm{W}/\,^{\circ}\mathrm{Cm}$ for the quartose Sirius sandstone unit at site TM2.

We do not believe that the variations in thermal properties have played a critical role in the 3-fold difference in polygon size at these two sites. The surface cover and material strength at the times of debris flow creation, and polygon network development are considered to have been more critical factors.

Chapter 8

Conclusions

8.1 Conclusions

We have measured the thermal conductivity of sea ice using two methods. Using automated data loggers and thermistor strings, we measured sea ice temperatures at intervals of $\Delta z = 0.1$ m and $\Delta t = 30$ min. Measurements were made in land fast sites in FY ice in McMurdo Sound, Antarctica 2002, and in both Elson Lagoon (2001/02) and the Chukchi Sea (2003) near Point Barrow, Alaska; and in MY ice in McMurdo sound, 2003. Conductivity profiles were calculated from these temperature records using a conservation of energy analysis and a graphical finite difference scheme. Using the specific heat result of *Ono* [1968], we calculated the internal energy $U(S,T)$, and then made finite difference estimates of $\rho\partial U/\partial t$ and $\partial^2 T/\partial z^2$. The thermal conductivity was calculated as the best fit gradient to scatter plots of $\rho\partial U/\partial t$ vs. $\partial^2 T/\partial z^2$. For this we used the geometric-mean of linear least squares fits treating each variable as independent. This returns an unbiased estimate of the gradient if the relative errors in each variable are equal, but one which is biased by half the difference in their relative uncertainties if they are not. This method determines the average conductivity between the three adjacent thermistors required to estimate $\partial^2 T/\partial z^2$. From both an analytical approach and simulations with conditions appropriate to our measurements, we have established that this analysis method is unreliable near the ice surface and close to the ice/water interface, but that accurate conductivity values are expected for intermediate depths.

Our conductivity profiles show a roughly constant conductivity between a near

surface reduction of up to about 25% over the top 20-50 cm, and an increase near the ice/water interface. Due to an improved understanding of when the analysis is, and is not, reliable, the current results are more robust the previous results reported using a very similar approach [*Collins*, 1998; *McGuinness et al.*, 1998; *Trodahl et al.*, 2000, 2001]. Nevertheless, the overall conductivity profiles from which we have selected the reliable values, are similar to those previously reported, in that their departure from the expected temperature-dependence. Models of $k_{si}(T)$ predict an increase towards the colder surface due to the temperature-dependence of the conductivity of the fresh ice component, and a conductivity decreasing towards the ice/water interface due to the lower conductivity of the increasing brine fraction.

We firmly believe that the large apparent reduction in the near-surface conductivity of FY sea ice, also observed by *Collins* [1998]; *McGuinness et al.* [1998]; *Trodahl et al.* [2000, 2001], is an artifact of the analysis method. From an analysis of the harmonic driving of a 1-D semi-infinite half space, we have shown that the finite difference estimates of $\partial U/\partial t$ and $\partial^2 T/\partial z^2$ will become unreliable when there are temperature components for which $\omega\Delta t$, and/or $\Delta z\sqrt{(}\omega/2D)$ is large. In this case the derivative estimates suffer a time lag (become out of phase), resulting in loops in the scatter plots of $\partial U/\partial t$ vs. $\partial^2 T/\partial z^2$, which we clearly identify in our data. Such features have been previously observed and associated with possible hysteric effects within the ice [*Collins* [1998]; *McGuinness et al.* [1998]; *Trodahl et al.* [2000, 2001]; Karoline Frey, personal communication, 2002]. For many-component driving, this effect leads to larger relative errors in $\partial^2 T/\partial z^2$ than in $\partial U/\partial t$ so the geometric-mean least squares gradient underestimates the conductivity. Simulations show that filtering, via numerical convolution with a gaussian window, may not remove this effect very near the surface. Because the high-frequency components responsible for this effect have a short penetration depth, the effect is shallow. Temperatures near the surface are also the most prone to measurement error, due to any heat flow perturbation caused by the mismatch between the thermal conductance of the probe and the surrounding ice. We calculate that our array has a thermal conductance per unit length approximately 30% less than the ice it replaces.

We resolve an increase in the conductivity near the ice/water interface which is accompanied by a deterioration in the quality of the linear fit, as measured by the correlation coefficient (r-value). *Collins* [1998] and *McGuinness et al.* [1998] have previously associated this fall-off in r-value with depth as a signature of increasing non-linearity in the heat flow, and identified it as a possible signature of convective heat flow. We consider this an unreliable association

because the r-value naturally falls off as the signal to noise deteriorates with depth, and the conductivity estimates become unreliable. Although it is possible, and even probable, that convective heat transport occurs in the lower ice, where the brine volume is large, we have for the above reasons, been unable to clearly identify signatures of this effect. Furthermore, because of the strong salinity-dependence of the internal energy above $-5\,^{\circ}\mathrm{C}$, these temperatures were excluded from our analysis.

The conductivity profiles are approximately flat over the depths between about 50 cm and the depth at which our analysis becomes noise-limited. This is clear in the $k(z)$ profiles from two arrays in FY ice in McMurdo Sound, 2002 (site FY02). At this site, the signal to noise was good over a depth range of about 1 m due to the high precision of our custom built, 17-bit ADC, data loggers and the thick ice resulting in a deeper isothermal boundary condition. This enabled us to calculate $k(z)$ accurately to greater depths than at our other sites. We tried to determine the temperature dependence by binning these data by temperature, but found that inter-thermistor variations dominated the variation between temperature bins, and we ultimately considered this approach unreliable. Between 0.5 - 1.25 m, spanning temperatures between -25 and $-10\,^{\circ}\mathrm{C}$, we found $k = 2.29 \pm 0.07\,\mathrm{W/m\,^{\circ}C}$ at FY02. At our FY ice site in the Chukchi Sea near Point Barrow, the ice only grew to about 1.3 m and the conductivity profile showed no clear plateau. For depths 0.49 - 0.84 m, and a temperatures range -15 to $-5\,^{\circ}\mathrm{C}$ we found $k = 2.26 \pm 0.11\,\mathrm{W/m\,^{\circ}C}$. In MY ice at McMurdo Sound (site MY03) we found $k = 2.03 \pm 0.04\,\mathrm{W/m\,^{\circ}C}$, for depths 0.31 - 0.41 m in the narrow temperature window -6 to $-5\,^{\circ}\mathrm{C}$.

We also developed a parallel conductance method to measure the conductivity of small ice cores (approximately 10×2.4 cm diameter). The conductivity was measured by heating one end of a sample holder, and with the other end held at a fixed temperature, measuring the temperature gradient along it, with, and without, an ice sample loaded. The measurement was performed under high vacuum, eliminating convective and conductive heat losses. Radiative loss from the sample holder could not be eliminated but was accommodated in the analysis. We measured cores taken from $(45\,\mathrm{cm})^3$ blocks removed from near the FY02 and MY03 McMurdo Sound sites. Averaging results from several cores from each depth, we resolved no significant difference, and certainly no large reduction, in the conductivity of FY surface (0-10 cm) and sub-surface (45-55 cm) ice, being $2.14 \pm 0.11\,\mathrm{W/m\,^{\circ}C}$ and $2.09 \pm 0.12\,\mathrm{W/m\,^{\circ}C}$ respectively. (The 45-55 cm value is $2.16 \pm 0.13\,\mathrm{W/m\,^{\circ}C}$ if one low-valued outlier is discarded.) This result provides direct evidence that the near-surface reduction in the array measurements is not genuine. Although from only three measurements,

the conductivity of surface MY ice, $1.88 \pm 0.13\,\mathrm{W/m\,^\circ C}$ was just within our prediction. This large reduction is consistent with the very low density of this ice, $0.82 \pm 0.01\,\mathrm{g/cm^3}$. The high number density of small round bubbles suggests that this ice froze quickly, and it may be re-frozen surface melt. This ice is not typical of the bulk ice at the MY site for which we determined k_{si} from our array measurements, so a comparison of conductivities is not appropriate.

We compared the conductivity results from both of our methods with previous experimental values and with our theoretical predictions and the modelers' parameterisation, usually cited from *Maykut and Untersteiner* [1971]. Within a roughly ±5% scatter we found good agreement between results from both our measurements and our theoretical prediction of $k_{si}(T)$ for typical FY salinity $4 - 6\,{}^0/_{00}$ and density $\rho = 0.90 - 0.92\,\mathrm{g/cm^3}$. Some historical results also agreed quite well with our prediction, particularly in the region above $-5\,^\circ\mathrm{C}$, where we are unable to resolve the strong predicted temperature dependence. Taken together, these results suggest a conductivity about 10% higher than that predicted by the modeling parameterisation, which was based on scant experimental data for k_{si}, and also for k_i used in the theoretical models of the time. Notably, the near-surface values of *Lewis* [1967] are higher our prediction, and those of *Malmgren* [1927] are much lower.

We tentatively proposed a new three-term parameterisation to capture both the decrease near the melting point as the brine volume increases, and increase with falling temperature due to the intrinsic temperature dependence of the pure ice component. It is

$$k_{si} = 2.09 - 0.011\,T + 0.117\,S/T \qquad [\mathrm{W/m\,^\circ C}] \quad , \tag{8.1}$$

where S is salinity $[\,{}^0/_{00}\,]$ and T temperature $[\,^\circ\mathrm{C}]$. We have retained the S/T term from *Maykut and Untersteiner* [1971], and the temperature coefficient from the pure ice data of *Slack* [1980]. The constant term was chosen to fit the curve between the bounds predicted by our model, which fit the experimental data quite well. This is therefore an empirical fit, in the same sense as the original parameterisation of *Untersteiner* [1961], which pre-dated the availability of all of the data available here except those of *Malmgren* [1927], which, as noted, did show comparatively low conductivity values. If a single conductivity value is required, consideration should be taken of the expected density, salinity and temperature. The often-used constant value, 2.03 $\mathrm{W/m\,^\circ C}$ originating from *Untersteiner* [1961], is considered too low. For temperatures like those measured at our FY Antarctic sites we suggest $2.2\,\mathrm{W/m\,^\circ C}$, but values as low as $2.05\,\mathrm{W/m\,^\circ C}$ might be appropriate at warmer sites. We emphasise that our parameterisation above should not be considered a robust result. As

outlined in the following section, we expect a more reliable parameterisation, based on additional thermal array data from both Antarctica and Alaska, to be formulated in the near future.

Using measurement and analysis methods similar to the sea ice work, we have also conducted a separate study of the thermal properties of the cold, dry permafrost at two sites at Table Mountain, Antarctica. A full summary of this work, and the conclusions are presented in section (7.12). Briefly, we determined thermal diffusivity values from temperature measurements using our graphical finite difference method, which proved more reliable than Fourier analysis methods, although care was required in its application. Thermal conductivity profiles were calculated as the product of profiles of the diffusivity, and the heat capacity determined from the composition of recovered cores. The conductivity generally lies in the range $2.5 \pm 0.5\mathrm{W}/^{\circ}\mathrm{Cm}$, but was as as high as $5.5 \pm 0.1\mathrm{W}/^{\circ}\mathrm{Cm}$ for the quartose Sirius sandstone unit at one site. These profiles were consistent with a quasi-static analysis. We resolved a consistent, but weak, seasonal variation in the thermal diffusivity, that is consistent with the expected underlying temperature dependence of the thermal properties. Following a more thorough understanding of the analysis, this effect is now considered to be smaller than what we published earlier in *Pringle et al.* [2003]. Finally, variations in the thermal properties were not considered to have been critical in establishing the factor-of-three difference in the size of polygonal ground patterning at these sites. We speculate that the difference instead reflects a difference in mechanical properties at the sites for the times at which the networks were established.

8.2 Future Directions and Related Work

We anticipate that by the end of 2005, two papers stemming form this work will be in review. The first paper will settle the question of an apparent conductivity reduction near the surface. We will discuss why the reduction seen in the earlier thermal array determinations is now considered erroneous, and present the bench top results, showing no reduction over the top 50 cm. In the second paper, we will collate results from the many array measurements made by UAF and VUW in both Alaska and Antarctica. Conductivity results will be presented for the circumstances in which we have confidence in the accuracy of the analysis. a study of the sensitivity of sea ice models to changes in the k_{si} parameterisation, is to be undertaken in 2005 by members of the VUW and UAF groups.

Two observations in our temperature measurements invite further investigation. We observed 24 hour peaks at both our MY McMurdo Sound (2003), and FY Chukchi Sea (2003) sites which are not due to conductive heat flow and are believed to be to be associated with direct solar heating of the ice at depth. The peaks occur at between 3-4 pm local time, whereas a theoretical treatment of this problem [*Trodahl et al.*, 2000] suggests a $\pi/2$ phase shift from the local insolation maximum, and therefore peaks at about 6 pm. The magnitude is also higher than expected. These two results suggest a larger in-phase absorption than expected for sea ice. We speculate that this might be caused by algae in McMurdo Sound, and/or debris at Barrow. The problem of solar heating of sea ice is currently being revisited by Mark McGuinness and a student at Victoria University, to whom our temperature data are available.

The observed diurnal variations in the water temperatures in the shallow Elson Lagoon, appear to be tied to the tidal cycle. Temperature maxima corresponded roughly with predicted high water times, suggesting the interpretation that the tides are flushing the more saline lagoon with the colder, lower salinity sea water. Coordinated measurements of tidal flow and water temperature may answer this question. Results from a tide gauge being installed for other reasons in the Chukchi Sea, in 2005, by UAF graduate student Andy Mahoney, may be of interest here.

UAF graduate student Lars Backström is analysing dielectric array measurements made in FY Chukchi Sea ice, 2003. These measurements are sensitive to the seasonal evolution of the salinity and brine volume profiles. The measurements show correlations in these parameters with the temperature anomalies observed in our thermal array measurements at this site (section 5.3.2).

Thermal array measurements have been performed in Antarctica by Victoria University since 1996. We don't consider that further measurements are necessary, except as auxiliary measurements for other studies, unless improved analysis methods can be developed, for example to identify convective heat transport near the ice/water interface. The question of the convective contribution to the overall heat flow, and its possible inclusion in an 'effective heat flow coefficient' has not been resolved. It remains an experimental challenge to measure any such contribution. Possible directions include tank experiments in which sea ice growth rates can be used to determine heat flux through the ice. Varying the underwater flow rate in such small scale experiments has illustrated the flow rate control of the formation of brine channels in the 'mushy layer' [eg. *Worster and Wettlaufer*, 1997]. Measuring a flow rate dependence of the growth rate would in principle enable an estimation of the convective

contribution to the heat flow.

Epilogue

After the acceptance of this thesis, and shortly before its final submission, an error was discovered. Although this error does not significantly affect the final conductivity results presented here, it provides an unequivocal partial explanation of the apparent reduction in near-surface conductivity. The theoretical expression of *Ono* [1967] for $c(S,T)$ was misrepresented in the review articles of *Yen* [1981]; *Yen et al.* [1991], in which the last term in equation (2.18) was a factor of ten too large. The incorrect expression given by *Yen* [1981] was referenced by *McGuinness et al.* [1998]; *Trodahl et al.* [2000, 2001] and used in their analysis. It remained undetected, and was used in the analysis presented in this thesis. The incorrect expression underestimates the specific heat by an amount that increases with salinity and decreasing temperature - both of which obtain towards the ice surface. This leads to underestimated values for $\partial U/\partial t$, and hence also the conductivity, being the scatter plot best-fit gradient. The size of this reduction for S=6 at $-25\,^{\circ}$C and $-10\,^{\circ}$C is 5% and 1% respectively ($\sim 0.11 and 0.02$ W/m $^{\circ}$C).

In the above analysis, we have limited the conductivity analysis to depths which did not show a clear surface reduction. If the above correction were made, it would increase these values by approximately $2 \pm 1\%$. It does however provide a larger correction, and explanation, for the previously-reported surface reduction. This matter is addressed in two papers in preparation at the present time (March 2005).

Appendix A

CR10X Logger Details

A.1 CR10X Data Logger Program

An annotated CR10X Data Logger program is listed below, and the measurement circuit shown in figure (A.1). The program was written using Campbell's software PC 208W Version 3.3, and based on the routine developed by *Collins* [1998] for similar array measurements, but included changes in both detail and structure. Most notably is the averaging over 20 reverse polarity measurements (10 forward, 10 reverse), and the delay time used in the individual measurements. Apart from this averaging, no data manipulation was performed, and the output written to storage was the averaged fractional voltage drop over the reference resistor, $|V/V_0|$ where $V_0 = \pm 2500$ mV is the excitation voltage, and V is the voltage drop measured over the reference resistor R_{ref}. The battery voltage is output once a day.

The program has three 'tables'. Table 1: performs a series of measurements every 30 min by calling the single measurement sub-routine in Table 3. Table 2 executes every minute, and if a storage module is present automatically transmits accumulated array data . If it is the second minute of the day, the battery voltage is output to the storage module. There is also a loop to click through all relays, so logger operation can be audibly verified when retrieving data storage modules without having to wait 30 minutes. Table 3 is the measurement sub-routine using the CR10X 'p4' program - excite, delay, measure. Reverse polarity measurements are made with 10 separate measurements with each of + 2500 mV and -2500 mV. A running total of the absolute value of (V/V_0) is kept and then averaged.

The array/logger time constant for capacitive settling was measured to be $\tau \approx 150\,\mu$s. The reverse polarity command 'p7' was not used as it has no provision for a time delay greater than the default of $450\,\mu\text{s} \approx 3\tau$. The 10 ms ($\approx 60\,\tau$) delay used in command 'p4' is easily sufficient to overcome the effect of lead capacitance. The entire measurement sequences takes approximately 5 seconds.

```
CR10X Program

This program was written in PC 208W Version 3.3

UAF30M.dld  : UAF Experiment with 30 minute execution

;{CR10X} ; *Table 1 Program
  01: 1800      Execution Interval (seconds)

1:  Do (P86)
 1: 41       Set Port 1 High

2:  Beginning of Loop (P87)
 1: 0        Delay
 2: 22       Loop Count

3:  Do (P86)
 1: 72       Pulse Port 2

4:  Do (P86)
 1: 1        Call Subroutine 1

5:  Z=X (P31)
 1: 2        X Loc [ Tot$\_$B     ]
 2: 4     -- Z Loc [ Therms_B  ]

6:  End (P95)

7:  Do (P86)
 1: 51       Set Port 1 Low

8:  Do (P86)
 1: 51       Set Port 1 Low
```

```
9:  Do (P86)
 1: 10       Set Output Flag High (Flag 0)

10:  Set Active Storage Area (P80)
 1: 1        Final Storage Area 1
 2: 100      Array ID

11:  Real Time (P77)
 1: 1110     Year,Day,Hour/Minute (midnight = 0000)

12:  Resolution (P78)
 1: 1        High Resolution

13:  Sample (P70)
 1: 22       Reps
 2: 4        Loc [ Therms_B  ]

14:  Serial Out (P96)
 1: 71       Storage Module

*Table 2 Program
  02: 60        Execution Interval (seconds)

1:  Serial Out (P96)
 1: 71       Storage Module

2:  Time (P18)
 1: 1        Minutes into current day (maximum 1440)
 2: 0        Mod/By
 3: 3        Loc [ Clck_mins ]

3:  If (X<=>F) (P89)
 1: 3        X Loc [ Clck_mins ]
 2: 1        =
 3: 2        F
 4: 13       Set Flag 3 High

4:  If Flag/Port (P91)
 1: 13       Do if Flag 3 is High
 2: 30       Then Do
```

```
5:  Batt Voltage (P10)
 1: 21       Loc [ Batt_V    ]

6:  Do (P86)
 1: 41       Set Port 1 High

7:  Beginning of Loop (P87)
 1: 0        Delay
 2: 22       Loop Count

8:  Do (P86)
 1: 72       Pulse Port 2

9:  Beginning of Loop (P87)
 1: 0        Delay
 2: 20       Loop Count

10:  End (P95)

11:  End (P95)

12:  Do (P86)
 1: 51       Set Port 1 Low

13:  Do (P86)
 1: 23       Set Flag 3 Low

14:  Do (P86)
 1: 10       Set Output Flag High (Flag 0)

15:  Set Active Storage Area (P80)
 1: 1        Final Storage Area 1
 2: 120      Array ID

16:  Sample (P70)
 1: 1        Reps
 2: 21       Loc [ Batt_V    ]

17:  Serial Out (P96)
 1: 71       Storage Module
```

```
18:  End (P95)


*Table 3 Subroutines

1:  Beginning of Subroutine (P85)
 1: 1        Subroutine 1

2:  Resolution (P78)
 1: 1        High Resolution

3:  Z=F (P30)
 1: 0        F
 2: 0        Exponent of 10
 3: 2        Z Loc [ Tot_B     ]

4:  Beginning of Loop (P87)
 1: 0        Delay
 2: 10       Loop Count

5:  Excite-Delay (SE) (P4)
 1: 1        Reps
 2: 5        2500 mV Slow Range
 3: 3        SE Channel
 4: 1        Excite all reps w/Exchan 1
 5: 1        Delay (units 0.01 sec)
 6: 2500     mV Excitation
 7: 1        Loc [ Therm_B   ]
 8: 0.0004   Mult
 9: 0        Offset

6:  Z=X+Y (P33)
 1: 2        X Loc [ Tot_B     ]
 2: 1        Y Loc [ Therm_B   ]
 3: 2        Z Loc [ Tot_B     ]

7:  Excite-Delay (SE) (P4)
 1: 1        Reps
 2: 5        2500 mV Slow Range
 3: 3        SE Channel
```

```
 4: 1        Excite all reps w/Exchan 1
 5: 1        Delay (units 0.01 sec)
 6: 2500  -- mV Excitation
 7: 1        Loc [ Therm_B   ]
 8: -0.0004  Mult
 9: 0        Offset

8:  Z=X+Y (P33)
 1: 2        X Loc [ Tot_B     ]
 2: 1        Y Loc [ Therm_B   ]
 3: 2        Z Loc [ Tot_B     ]

9:  End (P95)

10:  Z=X*F (P37)
 1: 2        X Loc [ Tot_B     ]
 2: 0.05     F
 3: 2        Z Loc [ Tot_B     ]

11:  End (P95)

End Program
```

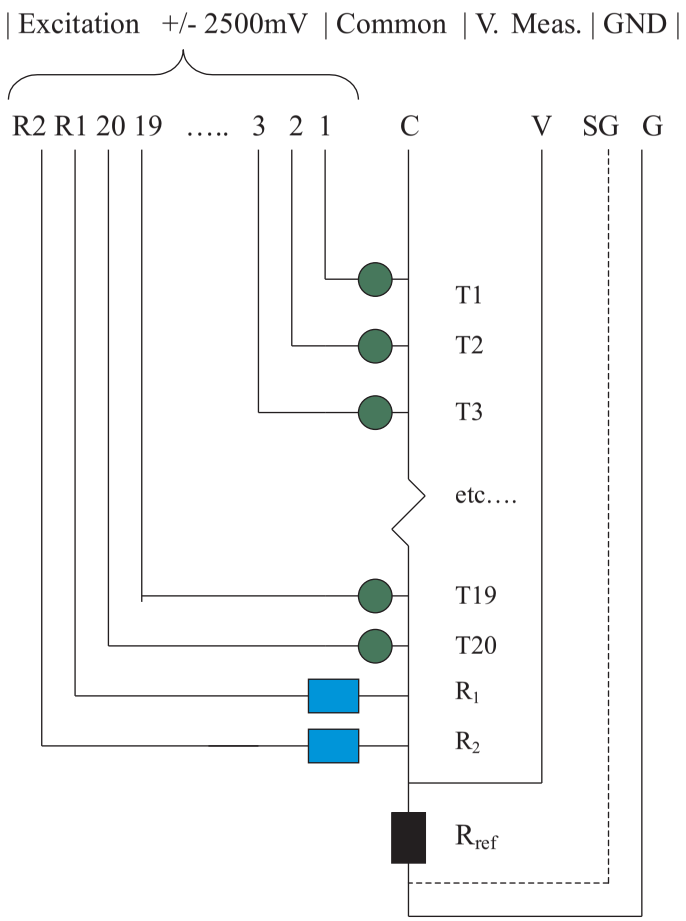

LINE	PIN (ARRAY HEAD)	COLOUR IN BOX	MULTIPLEXOR POSITION
1	H	BLUE/red	AM16/32 LO 1
2	J	GREEN	2
3	K	ORANGE/ green	3
4	X	WHITE/red	4
5	Y	BLACK/red	5
6	L	RED/green	6
7	G	RED	7
8	W	ORANGE/ red	8
9	F	WHITE	9
10	M	BLACK/red+white	10
11	Z	ORANGE	11
12	c (little sea)	BLACK	12
13	V	ORANGE/black	13
14	E	BLUE/white	14
15	N	WHITE/red+black	15
16	a (little, eh?)	BLUE	16
17	b (little bee)	GREEN/white+black	17
18	U	GREEN/black	18
19	D	GREEN/white	19
20	P	RED/black+white	20
R1	S	RED/black	21
R2	T	RED/white	22
V	R	WHITE/black	CR10X SE3
G	A	BLACK/white	CR10X AG
C	B	BLUE/black	CR10X 32 (not used)
SG not connected	C - wired into fox-proof cable just in case..	not connected	-

Battery input (12 V) to multiplexor at removable green plug.

Multiplexor Posn	CR10X Posn
12V GND (12 V)	12 V continuous GND (continuous)
Reset Clck	C1 C2
Common LO (EXCITE) Common GND	E1 GND

Figure A.1: Schematic wiring diagram and connections between Campbell CR10X Data logger, AM16/32 Multiplexor and array. The separate signal ground (SG) was for use with the custom built loggers, and is left unconnected when CR10X loggers were used.

A.2 Reference Resistor Optimisation

We here derive the result quoted in section (3.3) for optimisation of R_{ref} ,in order to minimise the average temperature uncertainty in the thermistor measurements. The starting points are equations (3.3, 3.5),

$$R = R_0 exp\left(\frac{\beta}{T}\right) \quad , \tag{A.1}$$

$$R = (R_{ref} + R_L)\left(\frac{V_0}{\overline{V}_m} - 1\right) - R_L \quad . \tag{A.2}$$

For this analysis we ignore the lead resistance $R_L << R$. Differentiating Equation (A.2) with respect to V_m with $R_L = 0$ gives the sensitivity of the thermistor resistance to the uncertainty in measured voltage:

$$\delta R = \frac{-\delta V_m}{V_0}\left(\frac{R^{\ 2}}{R_{ref}} + 2R + R_{ref}\right). \tag{A.3}$$

To convert this resistance resolution to a temperature resolution requires a functional form for the thermistor characteristic, $T(R)$. For the present analysis (but not the actual temperature conversion) the mathematics are simplified with no significant loss in accuracy by using (equation A.1) so that

$$T = \frac{\beta}{ln(R/R_0)} \quad . \tag{A.4}$$

Here for YSI 55031 thermistors between $-50\,^{\circ}\mathrm{C} - 0\,^{\circ}\mathrm{C}$, $R_0 \approx 0.16\,\Omega$ and $\beta \approx 3300\,K$. The uncertainty in temperature δT for voltage measurement uncertainty δV_m is found by differentiating equation (A.4) and substituting equation (A.3):

$$\delta T = \frac{-\delta V_m}{V_0}\left(\frac{R^{\ 2}}{R_{ref}} + 2R + R_{ref}\right)\frac{\beta}{(ln(R/R_0))^2} \tag{A.5}$$

The best choice of R_{ref} is that which minimises this sensitivity. Setting to zero the derivative of equation (A.5) with respect to R_{ref} gives the condition $R_{ref} = R_T$. For a single measurement it is best to match the reference resistor to the resistance of the thermistor. In our measurements the thermistor resistance is not constant but varies over the range $30 - 80\,\mathrm{k}\Omega$. Over this range the average temperature uncertainty can be written as:

$$< \delta T > \ = \ \frac{1}{R_2 - R_1}\int_{R_1}^{R_2} dR\,\frac{-\delta V_m}{V_0}\left(\frac{R}{R_{ref}} + 2 + \frac{R_{ref}}{R}\right)\frac{\beta}{\left[ln(R/R_0)\right]^2} \ , \tag{A.6}$$

$$\approx \ \frac{-\beta(\delta V_m/V_0)}{(R_2 - R_1)\left[ln(\overline{R}/R_0)\right]^2}\int_{R_1}^{R_2} dR\,\left(\frac{R}{R_{ref}} + 2 + \frac{R_{ref}}{R}\right) \quad . \tag{A.7}$$

Here we have simplified the integration by noting that $[ln(R/R_0)]^{-2}$ varies slower over this range, and replacing it with its average value. The optimal value of R_{ref} found by minimising equation (A.7) with respect to R_{ref} is,

$$R_{ref}{}^{*} = \left(\frac{R_2{}^2 - R_1{}^2}{2ln(R_2/R_1)} \right)^{1/2} \quad . \tag{A.8}$$

For $R_1 = 30\,\mathrm{k}\Omega$ and $R_2 = 80\,\mathrm{k}\Omega$, $R_{ref}{}^{*} = 52\,\mathrm{k}\Omega$. We used high-precision, low-temperature coefficient resistors with nominal values $R_{ref}{}^{*} = 52.3\,\mathrm{k}\Omega$. Individual resistance values were measured for all such resistors.

Appendix B

Aspects of Finite Difference Analysis

We here present the mathematical basis behind least squares fitting, and show how errors in the variable treated as independent bias the least squares slope by the relative error in that variable. For data and noise, with both Gaussian and uniform distributions, we show that the geometric mean of the two slope estimates obtained by treated each variable as independent, is biased by the difference in the relative error of the variables.

B.1 Least Squares Fitting with Measurement Errors

For a collection of data points (X_i, Y_i) the Least Squares method of linear curve fitting finds the best fit gradient m and y-axis intercept c by minimising the average squared vertical difference between the measured Y_i values and the corresponding best fit values $mX_i + c$. The method is formulated by finding the c and m that minimise this sum,

$$\begin{aligned} \frac{\partial}{\partial m}\sum_i^N (mX_i + c - Y_i)^2 &= 0 \quad , \\ \frac{\partial}{\partial c}\sum_i^N (mX_i + c - Y_i)^2 &= 0 \quad . \end{aligned} \tag{B.1}$$

This dual minimisation is formulated most easily in matrix notation using determinants [*Young*, 1962],

$$m = \frac{\begin{vmatrix} N & \sum y_i \\ \sum x_i & \sum y_i x_i \end{vmatrix}}{\begin{vmatrix} N & \sum x_i \\ \sum x_i & \sum x_i^2 \end{vmatrix}} = \frac{N\sum y_i x_i - (\sum y_i)(\sum x_i)}{N\sum x_i^2 - (\sum x_i)^2} \quad , \tag{B.2}$$

$$c = \frac{\begin{vmatrix} \sum y_i & \sum x_i \\ \sum y_i x_i & \sum x_i^2 \end{vmatrix}}{\begin{vmatrix} N & \sum x_i \\ \sum x_i & \sum x_i^2 \end{vmatrix}} = \frac{(\sum y_i)(\sum x_i^2) - (\sum y_i x_i)(\sum x_i)}{N\sum x_i^2 - (\sum x_i)^2} \quad . \tag{B.3}$$

In this procedure it is assumed that there is no uncertainty associated with the independent variable, X_i. When there is, the value of m is underestimated (and the value of c is also in error). The degree of underestimation is proportional to the 'relative error' in the independent variable. We discuss two cases below where the relative error is defined as the ratio of measurement noise to the range of values measured.

Gaussian Distributions.
We here examine the case when the signal and noise both have gaussian distributions, largely following the treatment of *Fuller* [1987]. Consider measurements (Y_i, X_i) made from the distributions:

$$\begin{aligned} Y_i &= \beta_0 + \beta_1 x_i + e_i \qquad i = 1, 2, ...n \quad , \\ X_i &= x_i + u_i \quad . \end{aligned} \tag{B.4}$$

Here $\mathrm{e_i} \sim \mathrm{N}(0, \sigma^2_{\mathrm{ee}})$ and $\mathrm{u_i} \sim \mathrm{N}(0, \sigma^2_{\mathrm{uu}})$ are the normally distributed random measurement errors with mean $\mu = 0$ and variance σ^2. In this notation $\mathrm{x_i}$ is the actual physical value of x at the time of measurement but $\mathrm{X_i}$ is the measured value due to some measurement error $\mathrm{u_i}$. And similarly for $\mathrm{Y_i}$ where β_0 and β_1 are the true y-axis intercept and gradient. It is further assumed that $\mathrm{x_i}$ is also normally distributed, $\mathrm{x_i} \sim \mathrm{N}(\mu_{\mathrm{x}}, \sigma^2_{\mathrm{xx}})$.

In this case the vector (Y, X) is said to be distributed as a bivariate normal vector. It is described by a mean vector,

$$E(Y, X) = (\mu_Y, \mu_X) = (\beta_0 + \beta_1 \mu_x, \mu_x) \quad , \tag{B.5}$$

and a covariance matrix,

$$\begin{bmatrix} \sigma_{YY}^2 & \sigma_{YX}^2 \\ \sigma_{XY}^2 & \sigma_{XX}^2 \end{bmatrix} = \begin{bmatrix} \beta_1^2\sigma_{xx}^2 + \sigma_{ee}^2 & \beta_1\sigma_{xx}^2 \\ \beta_1\sigma_{xx}^2 & \sigma_{xx}^2 + \sigma_{uu}^2 \end{bmatrix} \quad , \tag{B.6}$$

where, eg.,

$$\sigma_{XY}^2 = \frac{1}{N}\sum_i^N (X_i - \overline{X})(Y_i - \overline{Y}) \quad . \tag{B.7}$$

The least squares gradient, equation (B.2), can be recast as:

$$m_{LS} = \frac{\sum_i^N (X_i - \overline{X})(Y_i - \overline{Y})}{\sum_i^N (X_i - \overline{X})^2} \quad . \tag{B.8}$$

In the present case the gives

$$m_1 = \frac{\sigma_{XY}^2}{\sigma_{XX}^2} = \beta_1 \left(1 + \frac{\sigma_{uu}^2}{\sigma_{xx}^2}\right)^{-1} \quad , \tag{B.9}$$

$$m_1 = \frac{\beta_1}{1 + \delta x} \quad , \tag{B.10}$$

where $\delta x = \sigma_{uu}^2/\sigma_{xx}^2$. Recalling that σ_{xx}^2 is the distribution of x values sampled, and σ_{uu}^2 the variance in the noise of individual measurements, δx is the ratio of x measurement noise over x measurement range: a measure of the relative error in x. For small normally distributed errors, the least squares gradient of regressing Y against X underestimates the gradient by a factor that is the relative error in the independent variable.

Repeating this procedure for a regression of X against Y gives:

$$m_2 = \beta_1^{-1}\left(1 + \frac{\sigma_{ee}^2}{\beta_1^2\sigma_{xx}^2}\right)^{-1} \quad . \tag{B.11}$$

Comparing the two diagonal entries in the right hand side of equation (B.6) and identifying $\sigma_{yy}^2 = \beta_1^2\sigma_{xx}^2 + \sigma_{ee}^2$, so that $\delta y = \sigma_{ee}^2/\sigma_{yy}^2$ represents the relative error in Y measurements, equation (B.11) becomes

$$m_2 = \frac{\beta_1^{-1}}{(1 + \delta y)} \quad . \tag{B.12}$$

To first order in δ the geometric mean $m_{gm} = (m_1/m_2)^{1/2}$ is therefore

$$m_{gm} = \beta_1 \left(1 + \frac{1}{2}(\delta y - \delta x)\right) \quad . \tag{B.13}$$

If the relative errors δx and δy equal this gives an unbiased slope estimate.

Uniform Distributions
An interesting second case is when rather than a gaussian distribution of measured (Y_i, X_i) values, the distribution is uniform, see figure (B.1).

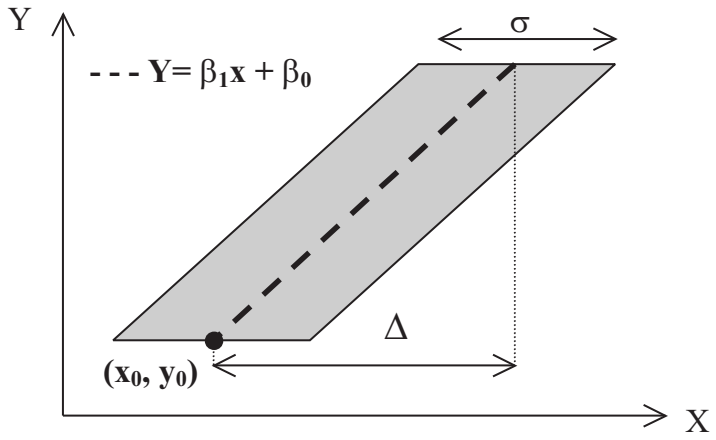

Figure B.1: Definition of Uniform Distribution parameters for effect of errors on Least Squares gradient fitting. There are errors only in the X values.

A least squares regression can be formulated as above by replacing the sums in equation (B.1) with double integrals over the shaded area in figure (B.1). This leads to the least squares slope being determined as a function of $\delta x' = (\sigma^2/\Delta^2)$, the relevant measure of relative error in the x values. For brevity, the minimisation of the double integrals is not included, just the results below.

For the regression of Y on X, where the errors are specifically in the independent variable, the least square results become,

$$m_1' = \frac{\beta_1}{1 + \delta x'} \tag{B.14}$$

$$c_1' = \beta_0 + \beta_1 \frac{(x_0 + \Delta/2)}{1 + 1/\delta x'} \tag{B.15}$$

The regression of X on Y, for which there are no errors in the independent variable, gives the ideal results as expected: $m'_2 = \beta_1$, $c'_2 = \beta_0$.

In analogy with equation (B.13), taking the geometric mean of the least squares gradients for the case of uniform errors *in both variables* gives, to first order in δ',

$$m'_{gm} = \beta_1 \left(1 + \frac{1}{2}(\delta y' - \delta x')\right) \quad . \tag{B.16}$$

The geometric mean estimates of the slope for both the gaussian and uniform distributions admit a common interpretation: the bias in the geometric mean depends on the difference in relative errors in the two plotted variables. When these relative errors are the same, the geometric mean provides an unbiased estimate of the gradient. If the relative error in both plotting variables can be identified - either in terms of the appropriate variances if the distributions can be considered gaussian, or as the widths in figure (B.1) for more uniformly distributed data - then equation (B.13) or (B.16) can be corrected to give an unbiased estimate of the gradient.

Appendix C

Conduction with Radiative Heat Loss

We here present an analytical treatment of the heat flow down a rod with radiative losses. This analysis is applied to the experimental chamber used to make the direct thermal conductivity measurements discussed in Chapter 6. It is shown that despite radiative losses as high as high as 20%, the parallel conductance method can still be used to determine the thermal conductance of our sea ice samples with an accuracy of approximately $\pm 1\%$.

C.1 Analytical Temperature Profile

Consider conductive heat flow along a homogeneous, insulated bar of density $\rho\,[\mathrm{m}^3/\mathrm{kg}]$, specific heat $c\,[\mathrm{J/kg/\,^\circ C}]$, and cross sectional area $A\,[\mathrm{m}^2]$. The net heat flow into a slice of thickness δz increases the heat content of that slice, and the change in temperature given by

$$\delta z\, kA \frac{\partial^2 T}{\partial z^2} = \rho A \delta z\, c \frac{\partial T}{\partial t} \quad . \tag{C.1}$$

For Newtonian heat loss from the surface of a rod of circumference s, at temperature T, to an isothermal surrounding T_a, the rate of heat loss is proportional to the temperature difference and the area of the rod,

$$\frac{dQ}{dt} = ns\delta z(T - T_a) \quad . \tag{C.2}$$

The 'Newtonian heat loss flux' is therefore of magnitude

$$J_N = n(T - T_a) \quad , \tag{C.3}$$

perpendicular to the rod. We call $n\,[\mathrm{W/m^2\,^\circ C}]$ the 'Newtonian heat loss coefficient'. Including equation (C.2) on the right hand side of equation (C.1) gives the appropriate heat equation,

$$\frac{\partial^2 T}{\partial z^2} = \frac{\rho C}{k}\frac{\partial T}{\partial t} + \frac{ns}{kA}(T - T_a) \quad . \tag{C.4}$$

Using excess temperature $\theta = T - T_a$, thermal diffusivity $D = \rho c/k$, and writing $\alpha^2 = (ns/kA)$ this becomes

$$\frac{\partial^2 \theta}{\partial z^2} = D\frac{\partial \theta}{\partial t} + \alpha^2\theta \quad . \tag{C.5}$$

The steady-state temperature profile for the general ($\alpha \neq 0$) case is found by solving equation (C.5) for $d\theta/dt = 0$. The general solution is:

$$\theta(z) = Me^{\alpha z} + Ne^{-\alpha z} \quad . \tag{C.6}$$

The boundary conditions in our case are:

1. $\theta(z = L) = 0$; the cold end is at the ambient temperature.
2. A small fraction, β, of the heater input is radiated away from the base of the heater. Therefore the heat flux into the tube is $J_{in} = -k\partial T/\partial z = (1 - \beta)P/A$ where $P\,[\mathrm{W}]$ is the I^2R power dissipated by the heater, and A the area perpendicular to the heat flow.

Applying these boundary conditions, the solution to equation (C.6) is

$$\theta(z) = \frac{P(1-\beta)}{\alpha L K}\frac{\sinh\left(\alpha L(1 - z/L)\right)}{\cosh(\alpha L)} \quad . \tag{C.7}$$

Here $K = kA/L$ is the thermal conductance $[\mathrm{W/\,^\circ C}]$ and $\alpha L = (nsL/K)^{1/2}$ parameterises the relative strength of radiative loss to conduction down the bar. That equation (C.7) gives the expected linear profile for no losses can be seen by expanding it in terms of the parameter (αL):

$$\begin{aligned}\theta(z) \;=\; (1-\beta)\frac{P}{K}\left(1 - \frac{z}{L}\right)\Bigg[\left(1 - \frac{(\alpha L)^2}{2}\right)\left(1 + \frac{(\alpha L)^2}{6}(1 - \frac{z}{L})^2\right) + \\ + \frac{(\alpha L)^4}{120}\left(25 + (1 - \frac{z}{L})^4\right) + \ldots\Bigg].\end{aligned} \tag{C.8}$$

For αL = 0, the term in square brackets is 1. By also setting $\beta = 0$ the no-loss linear profile is recovered. (This expansion was not used for any computations, only to illustrate here that equation (C.8) reduces to the no-loss profile for $\alpha L = \beta = 0$.)

The conducted heat flux $J_C = -k\partial T/\partial z = -k\partial\theta/\partial z$ is given by differentiating equation (C.8);

$$J_C(z) = \frac{P(1-\beta)}{A}\frac{\cosh\left(\alpha L(1-z/L)\right)}{\cosh(\alpha L} \quad . \tag{C.9}$$

We now turn to evaluating αL for our case, via the Newtonian heat loss coefficient n. The high vacuum eliminates conductive and convective losses (see section 6.3) so the only contribution to n is radiative.

The radiative heat flux emitted by a grey body (emissivity $\epsilon \neq 1$) is $\epsilon\sigma T^4$ where $\sigma = 5.67 \times 10^{-8} W/m^2K^4$ is the Stefan-Boltzman constant, and T is absolute temperature [K]. A full solution to our geometry of one grey body fully surrounded by another would involve integrating the difference $T(\mathbf{r_1})^4 - T(\mathbf{r_2})^4$ for all positions $\mathbf{r_1}$ on the sample holder and all $\mathbf{r_2}$ on the chamber wall, accounting for the geometrical view factor, F_{12}, which gives the fraction of radiation emitted at $\mathbf{r_1}$, impinging on $\mathbf{r_2}$ [*Winterton*, 1997]. The temperature distribution of the chamber, and spectral emissivity of the materials involved are not known precisely enough to justify this calculation, so we proceed by using the average temperature for each surface, and using $F_{12} = 1$ as the tube is fully enclosed by the chamber [*Winterton*, 1997]. We show below this approximation does not affect our final conclusion.

The radiative heat flux for a generalised arrangement of grey body 1 (emissivity ϵ_1, area A_1, the sample tube) fully surrounded by grey body 2 (the chamber) is [*Winterton*, 1997]:

$$J_R = \frac{\sigma {T_1}^4 - \sigma {T_2}^4}{(1-\epsilon_1)/\epsilon_1 A_1 + 1/A_1 F_{12} + (1-\epsilon_2)/\epsilon_2 A_2} \quad . \tag{C.10}$$

Substituting $F_{12} = 1$, and $\epsilon_1 = \epsilon_2 = \epsilon_{SS}$ the emissivity of stainless steel, and our values of A_1 and A_2 gives

$$J_R \approx 0.87\epsilon_{SS} A_1 \sigma \left({T_1}^4 - {T_2}^4\right) \quad . \tag{C.11}$$

The finite size of the chamber has caused a 13% reduction in the radiative flux from the case of the tube radiating into a background at T_2, for which the pre-factor would be 1, not 0.87.

The average temperature of the chamber is well controlled at the cold bath temperature $T_2 = T_a(z = L)$. The tube temperature is by definition the chamber temperature plus the excess temperature: $T_1 = T_a + \theta$. As $\theta \ll T_a$ equation (C.11) can be expanded using:

$$\left({T_1}^4 - {T_2}^4\right) = \left((T_a + \theta)^4 - {T_a}^4\right) \approx 4{T_a}^3\theta \quad . \tag{C.12}$$

This is accurate to 1% for experimental values $T_a = 260$ K and $\theta = 2$ K. By combining equations (C.11, C.12) the radiative heat loss can be written in terms of the local excess temperature;

$$J_R(z) \approx 3.5\epsilon_{SS}\sigma{T_a}^3\left(T(z) - T_a\right) \quad . \tag{C.13}$$

Recalling equation (C.3), equation (C.13) gives the Newtonian heat loss coefficient, $n = 3.5\epsilon_{SS}\sigma{T_a}^3$, and we have evaluated the parameter:

$$\alpha L = \left(\frac{sL}{K}3.5\epsilon_{SS}\sigma{T_a}^3\right)^{1/2} . \tag{C.14}$$

Equations (C.8) and (C.14) provide a full description of the temperature profile along the sample holder. We now examine the calculation of the conductance of an ice sample with this temperature profile.

C.2 Conductance Calculations with Radiative Losses

In this section we estimate the uncertainty in applying the parallel conductance method to the configuration described in Chapter 6. For no radiative losses, the conductance of the tube and a sample is additive,

$$K_{ice} = K_{ice+tube} - K_{tube} \quad . \tag{C.15}$$

For no losses the conductance can be calculated from the measured temperature gradient as

$$K = \frac{P}{L|\frac{\partial T}{\partial z}|} \quad . \tag{C.16}$$

The ice conductivity could therefore be determined as

$$k_{ice} = \frac{1}{A}\left(\frac{P'}{|\frac{\partial T}{\partial z}|'} - \frac{P}{|\frac{\partial T}{\partial z}|}\right) \quad , \tag{C.17}$$

where the unprimed variables are for runs with ice loaded, and the primed variables for tube-only measurements.

From the temperature gradient measured in the central third of the tube where the heat flow is expected to be most uniform, we calculate an 'apparent conductance',

$$K_{app} = \frac{P}{L|\frac{\partial T}{\partial z}(\frac{L}{2})|} \quad . \tag{C.18}$$

Due to radiative losses $|\frac{\partial T}{\partial z}(\frac{L}{2})|$ is smaller than it would be if all of the applied power were conducted along the tube, so K_{app} overestimates the true conductance. Furthermore, the small radiative flux from the bottom of the heater, $\beta P/A$, increases this discrepancy. We now assess the size of this effect.

Differentiating equation (C.8) and evaluating the apparent conductance with equation (C.18) gives:

$$K_{app} = \frac{K}{(1-\beta)} \frac{\cosh(\alpha L)}{\cosh(\frac{1}{2}\alpha L)}. \tag{C.19}$$

The error in calculating the ice conductance with equation (C.15) can be determined by expanding (C.19) in terms of (αL). To order $(\alpha L)^2$, we have:

$$K_{app} = \frac{1}{1-\beta}\left(K_{tube} + \frac{3}{8}qsL\right) \quad , \tag{C.20}$$

$$K'_{app} = \frac{1}{1-\beta'}\left(K_{tube} + K_{ice} + \frac{3}{8}q'sL\right) \quad . \tag{C.21}$$

Expanding to order $(\alpha L)^2$ introduces an error of less than 0.5% here. Subtracting (C.20) from (C.21) gives the apparent ice conductance,

$$\begin{aligned} K_{app}(ice) = {} & \frac{1}{1-\beta}K_{ice} + \left(\frac{1}{1-\beta} - \frac{1}{1-\beta'}\right)K_{tube} + \\ & + \frac{19}{16}\epsilon_{SS}\sigma sL\left(\frac{1}{1-\beta}{T_a}^3 - \frac{1}{1-\beta'}{T_a}'^3\right). \end{aligned} \tag{C.22}$$

Experimental values give $K_{app}(ice) \approx 10 mW/\,^\circ\mathrm{C}$. As $\beta < \beta'$, the second term on the RHS is negative. From a calculation we estimate it is approximately -0.5% of the first term. For a $\pm 5\,^\circ\mathrm{C}$ difference between T_a and T'_a (the maximum difference in operating temperatures for the ice and tube-only runs), the third term on the RHS is only $\pm 0.1\, mW/\,^\circ\mathrm{C}$, a $\pm 1\%$ effect.

We conclude that evaluating the ice conductance using the method of parallel conductance, and in particular with equation (C.16), has an associated methodical uncertainty of approximately $\pm 1\%$. This is less than the experimental variations in the measurement of the equilibrium temperature gradient.

Bibliography

Anderson, D. L. (1958), A model for determining sea ice properties, in *Arctic Sea Ice*, pp. 148–152, U.S. National Academy of Sciences - National Research Council, Pub. 598.

Anderson, O., and H. Suga (2002), Thermal conductivity of amorphous ices, *Phys. Rev. B.*, *65*(140201(R)), 1–4.

Ashcroft, N. W., and N. Mermin (1976), *Solid State Physics*, Holt, Rinehart and Winston, New York.

Assur, A. (1958), Composition of sea ice and its tensile strength, in *Arctic Sea Ice*, pp. 106–138, U.S. National Academy of Sciences - National Research Council, Pub. 598.

Atlas, 2003 (2003), *The Atlas Specialty Metals Technical Hnadbook of Stainless Steels*, Revised: July 2003. Available on line at http://www.http://www.atlas-steels.com.au/customer/downloads/technical_handbook/technical_handbook.pdf.

Bitz, C. M., and W. H. Lipscomb (1999), An energy-conserving thermodynamic model of sea ice, *J. Geophys. Res.*, *104*(C7), 15,669–16,677.

Budd, W. F. (1967), Ablation from an Antarctic Ice Surface, in *Physics of Snow and Ice: International Conference on Low Temperture Science 1966*, vol. 1(1), edited by H. Oura, pp. 431–446, Institute of Low Temperature Science, Hokkaido University, Sapporo, Japan.

Campbell Scientific, Inc., 2001 (2001), CR10X *Measurement and Control Module, Operator's Manual.*, Revision: 8/01.

Carslaw, H., and J. Jaeger (Eds.) (1959), *Conduction of Heat in Solids*, Second ed., Clarendon Press, Oxford.

Carson, J. E. (1963), Analysis of soil and air temperatures by Fourier techniques, *J. Geophys. Res.*, *68*, 2217–2232.

Cheng, B. (2002), On the Modelling of Sea Ice Thermodynamics and Air-Ice Coupling in the Bohai Sea and the Baltic Sea, Ph.D. thesis, University of Helsinki, Department of Physical Sciences, Division of Geophysics, Faculty of Science and Finnish Institute of Marine Research.

Clauser, C., and E. Huenges (1995), Thermal Conductivity of Rocks and Minerals, in *A Handbook of Physical Constants: Rock Physics and Phase Relations*, vol. 3, edited by T. Ahrens, pp. 105–126, American Geophysical Union, Washington DC.

Collins, K. A. (1998), Temperature Dependence of The Thermal Conductivity of Antarctic Sea Ice, Master's thesis, Victoria University of Wellington.

DeVries, D. A. (1963), Thermal properties of soils, in *Physics of Plant Environment*, vol. 3, edited by W. R. V. Wijk, pp. 210–235, North-Holland Publishing Co., Amsterdam.

Di Nello, A. (Ed.) (1995), *SFPE Handbook of Fire Protection Engineering*, 2nd ed., National Fire Protection Association.

Dickinson, W. W., and R. Grapes (1997), Authigenic Chabazite and Implications for Weathering in Sirius Group Diamictite, Table Mountain, Dry Valleys, Antarctica, *J. Sed. Res.*, *67*(5), 815–820.

Dickinson, W. W., P. Cooper, B. Webster, and J. Ashby (1997), A portable drilling rig for coring permafrosted sediments, *J. Sed. Res.*, *69*, 518–521.

Dieckmann, G. S., and H. H. Hellmer (2003), The importance of sea ice: An overview, in *Sea Ice - An Introduction to its Physics, Biology, Chemistry and Geology*, edited by Thomas and Dieckmann, pp. 1–21, Blackwell Science, London.

Doronin, Y. P., and D. E. Kheisin (1977), *Sea Ice*, Amerind Publishing Co. Pvt. Ltd., New Delhi, (Translation of Russian language version, originally published in 1975).

Dushman, S. (1949), *Scientific Foundations of Vacuum Technology*, Wiley & Sons.

Eicken, H. (2003), From the microscopic to the macroscopic to the regional scale: Growth, microstructure and properties of sea ice, in *Sea Ice - An*

Introduction to its Physics, Biology, Chemistry and Geology, edited by Thomas and Dieckmann, pp. 22–81, Blackwell Science, London.

Eicken, H., and P. Lemke (2001), The response of polar sea ice to climate variability and change, in *Climate of the 21st century: Changes and risks*, edited by J. L. Lozan, pp. 206–211, Wissenschaftliche Auswertungen/GEO, Hamburg.

Eicken, H., T. C. Grenfell, D. K. Perovich, J. A. Richter-Menge, and K. Frey (2004), Hydraulic controls of summer Arctic pack ice albedo, *J. Geophys. Res.*, *109*, C08,007, doi:10.1029/2003JC001989.

Farouki, O. T. (1981), Thermal Properties of Soils, *CRREL Monograph 81–1*, U.S. Army Cold Regions Research and Engineering Laboratory, Hanover, New Hampshire.

Freitag, J., and H. Eicken (2003), Melt water circulation and permeability of Arctic summer sea ice derived from hydrological field experiments, *J. Glaciol.*, *49*(166), 349–358.

Frey, K., H. Eicken, D. Perovich, T. C. Grenfell, B. Light, L. H. Shapiro, and A. P. Stierle (2001), Heat Budget and Decay of Clean and Sediment-laden Sea Ice off the Northern Coast of Alaska, in *Port and Ocean Engineering in the Arctic Conference (POAC '01) Proceedings*, vol. 3, pp. 1405–1412, Ottawa, Canada.

Fuhrer, O. (2000), Inverse heat conduction in soils: A new approach to recovering soil moisture from temperature records, *Diplom Thesis*, Swiss Federal Institute of Technology, Zürich.

Fuller, W. (1987), *Measurement Error Models*, John Wiley & Sons.

Golden, K., S. F. Ackley, and V. I. Lytle (1998), The percolation phase transition in sea ice, *Science*, *282*(5397), 2238–2241, doi:10.1126/science.282.5397.2238.

Gombosi, T. I. (1994), *Gaskinetic Theory*, Cambridge University Press.

Gough, W. A. (2001), Model tuning and its impact on modelled climate change response: Hudson Bay sea ice, a case study, *Canadian Geographer*, *45*(2), 300–305.

Hashin, Z., and S. Shtrikman (1968), A variational approach to the theory of effective magnetic permeability of multiphase materials, *J. Appl. Phys.*, *33*, 3125–3131.

Hindmarsh, R., F. van der Wateren, and A. Verbers (1998), Sublimation of ice through sediment as a constraint on ice age in Beacon Valley, East Antarctica, *Geografiska Annaler*, *80A(3-4)*, 209–219.

Hinkel, K. M. (1997), Estimating seasonal values of thermal diffusivity in thawed and frozen soils using temperature time series, *Cold Reg. Sci. Technol.*, *26*, 1–15.

Hurley, S., and R. Wiltshire (1993), Computing Thermal Diffusivity From Soil Temperature Measurements, *Geografiska Annaler*, *19*(3), 475–477.

Jessop, A. M. (1990), *Thermal Geophysics*, no. 17 in Developments in Solid Earth Geophsyics, Elsevier.

Johnson, H. L. (1989), The specific heat of sea ice, *Tech. rep.*, Victoria University of Wellington, B.Sc. Honours Thesis.

Kittel, C. (1976), *Introduction to Solid State Physics*, Fifth ed., 178 pp., Wiley & Sons.

Lachenbruch, A. H. (1962), Mechanics of Thermal Contraction Cracks and Ice-Wedge Polygons in Permafrost, *Spec. Pap. 70*, Geol. Soc. Am.

Landauer, R. (1978), Electrical Conductivity in Inhomogeneous Media, in *Electrical Transport and Optical Properties in Inhomogeneous Media*, edited by J.C. Garland, D.B. Tanner, pp. 2–45, AIP Conference Proceedings, No. 40., Ohio State University, 1977.

Lange, N. A., and G. M. Forke (1952), *Handbook of Chemistry*, Eighth ed., Handbook Publishers, Sandusky, Ohio.

Lemke, P., W. Owens, and W. H. III (1990), A coupled sea ice - mixed layer - pycnocline model for the Weddell Sea, *JGR*, *95*(C6), 9513–9525.

Lettau, H. H. (1954), Improved models of thermal diffusion in the soil, *Trans. Am. Geophys. Union*, *35*, 121–132.

Lettau, H. H. (1962), A theoretical model of thermal diffusion in nonhomogeneous conductors, *Gerlands Beitr. Geophys.*, *71*(5), 257–271.

Lewis, E. L. (1967), Heat Flow through Winter Ice, in *Physics of Snow and Ice: International Conference on Low Temperture Science 1966*, vol. 1(1), edited by H. Oura, pp. 611–631, Institute of Low Temperature Science, Hokkaido University, Sapporo, Japan.

Lide, R. T. (Ed.) (2005), *Handbook of Chemistry and Physics*, Eighty fifth ed., Chemical Rubber Company, Cleveland, Ohio.

Light, B., G. A. Maykut, and T. C. Grenfell (2003a), Effects of temperature on the micostructure of firsy-year Artic sea ice, *J. Geophys. Res.*, *108*(C2), 3051, doi:10.1029/2001JC000887.

Light, B., G. A. Maykut, and T. C. Grenfell (2003b), A temperature-dependent, structural-optical model of first-year sea ice, *J. Geophys. Res.*, *108*, C06,013, doi:10.1029/2003JC002164.

Lytle, V., and S. Ackley (1996), Heat flux through sea ice in the western Weddell Sea:Convective and conductive transfer processes, *J. Geophys. Res.*, *101*(C4), 8853–8868.

Malin, M. C., and K. S. Edgett (1998), Evidence for recent groundwater seepage and surface runoff on Mars, *Science*, *288*(5475), 2330–2335.

Malmgren, F. (1927), On the Properties of Sea Ice, in *The Norwegian North Polar Expedition with the 'Maud', 1918-1925*, vol. 1(5), pp. 1–67.

Marchant, D. R., A. Lewis, W. Phillips, E. Moore, R. Souchez, G. Denton, D. Sugden, N. Potter, and G. Landis (2002), Formation of patterned ground and sublimination till over Miocene glacier ice in Beacon Valley, southern Victoria Land, Antarctica, *Geol. Soc. Am. Bull.*, *114*, 718–730.

Matsuoka, N., K. Moriwaki, S. Iwata, and K. Hirakawa (1990), Ground Temperature Regimes and Their Relation to Periglacial Processes in the Sör Rondane Mountains, *Proc. NIPR Symp. Antarct. Geosci.*, *4*, 55–65.

Maykut, G., and N. Untersteiner (1971), Some results form a time-dependent thermodynamic model of sea ice, *J. Geophys. Res.*, *76*, 1550–1576.

Maykut, G. A. (1986), The surface heat and mass balance, in *The Geophysics of Sea Ice*, edited by N. Untersteiner, pp. 395–465, Plenum Press, New York.

McGaw, R. W., S. Outcalt, and E. Ng (1978), Thermal properties of wet tundra soils at Barrow, Alaska, in *Proc. 3rd Intl. Conf. Permafrost*, pp. 47–53.

McGuinness, M. J., K. Collins, H. J. Trodahl, and T.G.Haskell (1998), Nonlinear thermal transport and brine convection in first year sea ice, *Ann. Glaciol.*, *27*, 471–476.

McKay, C. P., M. Mellon, and E. Friedmann (1998), Soil Temperatures and stability of ice-cemented ground in the McMurdo Dry Valleys, Antarctica, *Antarctic Science*, *10*(1), 31–38.

Mellon, M. T. (1997), Small-scale polygonal features on Mars: Seasonal thermal contraction cracks in permafrost, *J. Geophys. Res.*, *102(E11)*, 25,617–25,628.

Miller, M. F., and M. Mabin (1998), Antarctic Neogene landscapes - in the refrigerator or in the deep freeze?, *GSA Today*, *8(4)*, 1–3.

Nassar, I. N., and R. Horton (1990), Determination of Soil Apparent Thermal Diffusivity from Multiharmonic Temperature Analysis for Nonuniform Soils, *Soil Sci.*, *149(3)*, 125–130.

Nazintsev, Y. L. (1959), Eksperimental'noe opredelenie teploemkosti i temperaturoprovodnosti moskogo l'da (Experimental determination of the specific heat and thermometric conductivity of sea ice), *Problemy Arktiki i Antarktiki*, *1*, 65–71, (English translation available from American Meterological Society, contract number AF 19(604)-6113).

Nazintsev, Y. L. (1964), Nekotorye dannye k raschetu teplovykh Svoistv morskogo l'da. (Some data on the calculation of thermal properties of sea ice), *Trudy Arkt. i Antarkt. Inst.*, *267*, 31–47, (Neither original or a translation could be located).

Nelson, K. H., and T. Taylor (1954), Deposition of salts from sea water by frigid concentration, *J. Marine. Res.*, *13*(2), 166–182.

Ono, N. (1965), Themal Properties of Sea Ice II. A method for determining the $K/c\rho$ value of a Non-Homogenous Ice Sheet, *Low Temperature Science, Ser. A*, *223*, 182.

Ono, N. (1967), Specific Heat and Fusion of Sea Ice, in *Physics of Snow and Ice: International Conference on Low Temperture Science 1966*, vol. 1(1), edited by H. Oura, pp. 599–610, Institute of Low Temperature Science, Hokkaido University, Sapporo, Japan.

Ono, N. (1968), Thermal Properties of Sea Ice IV. Thermal constants of sea ice, *Low-Temp. Sci.*, *A26*, 329–349.

Parkinson, C., and W. Washington (1979), A large scale numerical model of sea ice, *JGR*, *84*, 311–337.

Passchier, S., A. Verbers, F. M. van der Wateren, and F. Vermeulen (1998), Provenence, geochemistry, and grain-sizes of glacigene sediments, including the Sirius Group, and Late Cenozoic glacial history of the southern Prince Albert Mountains, Victoria Land, Antarctica, *Ann. Glaciol.*, *27*, 270–276.

Perovich, D. K., T. C. Grenfell, J. A. Richter-Menge, B. Light, W. B. Tucker, and H. Eicken (2003), Thin and thinner: Sea ice mass balance measurements during SHEBA, *J. Geophys. Res.*, *108*(C3), 8050, doi:10.1029/2001JC001079.

Persaud, N., and A. Chang (1985), Computing mean apparent soil diffusivity from daily observations of soil temperatures at two depths, *Soil Sci.*, *139(4)*, 297–304.

Péwé, T. L. (1959), Sand-wedge polygons (tessellations) in the McMurdo Sounds region, Antarctica - a progress report, *Am. Jour. Sci.*, *257*, 545–551.

Pounder, E. L. (Ed.) (1965), *The Physics of Ice*, Pergamon Press, New York.

Pringle, D. J., W. Dickinson, H. Trodahl, and A. Pyne (2003), Depth and seasonal variations in the thermal properties of Antarctic Dry Valley permafrost from temperature time series analysis, *J. Geophys. Res.*, *108(B10)*, 2474–2486, doi:10.1029/2002JB002364.

Putkonen, J., R. Sletten, and B. Hallet (2003), Atmosphere/ice energy exchange through thin debris cover in Beacon Valley, Antarctica, in Press, Proceedings of the 8th International conference on permafrost, International Permafrost Association, Zürich, Switzerland.

Ringer, W. E. (1906), De Veranderinger in Samenstelling van Zeewater by Het Bevreizen, *Chemisch Weekblad*, *3*, 223–249, (Results reported in Weeks and Ackley, 1986).

Roy, R. F., A. Beck, and Y. Touloukian (1981), Physical Properties of Rocks and Minerals, in *McGraw-Hill/CINDAS Data Series on Material Properties*, vol. II-2, edited by Y. S. Touloukian and C. Y. Ho, McGraw-Hill.

Sapoff, M. (1999), Thermistor Thermometers, in *The Measurement, Instrumentation, and Sensors Handbook*, edited by J. G. Webster, pp. **32**–25, CRC Press.

Schwerdtfeger, P. (1963), The thermal properties of sea ice, *J. Glac.*, *4*, 789–807.

Schwerdtfeger, P. (1966), On the response of a sea-ice cover to changes in surface temperature, *J. Glaciol.*, *6(45)*, 439–442.

Semtner, A. J. (1964), A Model for the Thermodynamic Growth of Sea Ice in Numerical Investigations of Climate, *J. Phys. Ocean.*, *6*, 379–389.

Slack, G. A. (1980), Thermal conductivity of ice, *Phys. Rev. B*, *22*(6), 3065–3071.

Sletten, R. S., B. Hallet, and R. Fletcher (2003), Resurfacing time of terrestrial surfaces by the formation and maturation of polygonal patterned ground, *J.Geophys. Res.*, *108*(E4), 8044, doi:10.1029/2002JE001914.

Stearns, C. R. (1969), Application of Lettau's theoretical model of thermal diffusion in soil particles of temperature and heat flux, *J. Geophys. Res.*, *74*, 532–541.

Steele, M., and G. Flato (2000), Growth, Melt, and Modelling: A Survey, in *The Freshwater Budget of the Arctic Ocean*, edited by E. L. L. et al., pp. Chapter 23, 549–587, Kluwer.

Stefan, J. (1891), ber Die Theorie der Eisbildung, Insbesondere ber die Eisbildung im Polarmeere, *Ann. Physik, N.F., 3rd Ser.*, *42*, 269–286, (Results given in Malmgren, 1927).

Steinhart, J. S., and S. Hart (1968), Calibration curves for thermistors, *Deep Sea Research*, *15*, 497.

Stierle, A. P., and H. Eicken (2002), Sediment Inclusions in Alaskan Coastal Sea Ice: Spatial Distribution, Interannual Variability and Entrainment Requirements, *Arc. Antarc. Alp. Res.*, *34*(4), 103–114.

Sturm, M., J. Holmgren, and D. K. Perovich (2002), Winter snow cover on the sea ice of the Arctic Ocean at the Surface Heat Budget of the Arctic Ocean (SHEBA): Temporal evolution and spatial variability., *J. Geophys. Res.*, *107*, doi:10.1029/2000JC000400.

Sugden, D. E., D. Marchant, N. J. Potter, R. Souchez, G. Denton, C. Swisher, and J.-L. Tison (1995), Preservation of Miocene glacier ice in East Antarctica, *Nature*, *376*, 412–414.

Thomson, D. C., R. Craig, and A. Bromley (1971), Climate and Surface Heat Balance in an Antarctic Dry Valley, *New Zealand Journal of Science*, *14*, 245–251.

Timco, G., and R. Frederking (1996), A review of sea ice density, *Cold Reg. Sci. Tech.*, *24*, 1–6.

Trodahl, H. J., and R. Buckley (1990), Enhanced Ultraviolet Transmission of Antarctic Sea Ice During The Austral Spring, *Geophys. Res. Lett.*, *17*, 2177–2179.

Trodahl, H. J., M. McGuinness, P. Langhorne, K. Collins, A. Pantoja, I. Smith, and T. Haskell (2000), Heat Transport in McMurdo Sound first-year fast ice, *J. Geophys. Res.*, *105(C5)*, 11,347–11,358.

Trodahl, H. J., S. Wilkinson, M. McGuinness, and T. Haskell (2001), Thermal Conductivity of sea ice: Dependence on temperature and depth, *Geophys. Res. Lett.*, *128*, 1279–1282.

Tuch, D. S., V. J. Wedeen, A. M. Dale, J. S. George, and J. W. Belliveau (2001), Conductivity tensor mapping of the human brain using diffusion tensor MRI, *Proc. Natl. Acad. Sci. U. S. A.*, *98*(20), 11,697–11,701, doi:10.1073/pnas.171473898 Neurobiology.

Untersteiner, N. (1961), On the mass and heat balance of arctic sea ice, *Arch. Meteor. Geophys. Bioklimatol. Ser. A,*, *12*, 151–182.

Untersteiner, N. (1964), Calculation of temperature regime and heat budget of sea ice in the Central Arctic, *J. Geophys. Res.*, *69*(22), 4755–4766.

Weast, R. (Ed.) (1971), *Handbook of Chemistry and Physics*, Fifty Second ed., Chemical Rubber Company, Cleveland, Ohio.

Weeks, W. F., and S. F. Ackley (1986), The growth, structure, and properties of sea ice, in *The Geophysics of Sea Ice*, edited by N. Untersteiner, pp. 9–165, Plenum Press, New York.

Weller, G. (1967), The Effect of Absorbed Solar Radiation on the Thermal Diffusion in Antarctic Fresh-water Ice and Sea Ice, *J. Glaciol.*, *6*(48), 859–878.

Westin, B., and F. Zuidhoff (2001), Ground Thermal Conditions in Discontinuous Permafrost, Permafrost and Periglacial Processes, *Permafrost and Periglacial Processes*, *12*, 325–335.

Wettlaufer, J. S. (2001), The Stefan Problem: Polar Exploration and the mathematics of moving boundaries, in *Festschrift 150 Jahre Inst. fur Met. und Geophysik Univ. Wien*, Styria Verlag.

Winterton, R. H. S. (1997), *Heat Transfer*, Oxford Univ. Press, Oxford.

Worster, M., and J. Wettlaufer (1997), Natural convection, solute trapping and channel formation during solidification of salt water, *J. Phys. Chem*, *B(101)*, 6132–36.

Wu, X., I. Simmonds, and W. Budd (1997), Modeling of Antarctic Sea Ice in a General Circulation Model, *J. Climate*, *10*(4), 593–609.

Yen, Y.-C. (1981), Review of thermal properties of snow, ice and sea ice, *CRREL Report 81–10*, U.S. Army Cold Regions Research and Engineering Laboratory, Hanover, New Hampshire.

Yen, Y.-C., K. C. Cheng, and S. Fukusako (1991), Review of Intrinsic Thermophysical properties of Snow, Ice, Sea Ice and Frost, in *Proceedings 3rd International Symposium on Cold Regions Heat Transfer*, edited by J. P. Zarling and S. L. Fausett, pp. 187–218, Fairbanks, Alaska.

Young, H. D. (1962), *Statistical Treatment of Data*, McGraw Hill, New York.

Zhang, T. (1993), Climate, seasonal snow cover and permafrost temperatures in Alaska north of the Brooks Range, Ph.D. thesis, University of Alaska Fairbanks.

Zhang, T., and T. Osterkamp (1995), Considerations in determining the thermal diffusivity from temperature time series using finite difference methods, *Cold Reg. Sci. Tech.*, *23*, 333–341.